

Doctoral theses at NTNU, 2016:360

Vegard Flovik

Magnetization dynamics in nanostructures

ISBN 978-82-326-2064-7 (printed version)
ISBN 978-82-326-2065-5 (electronic version)
ISSN 1503-8181

Doctoral theses at NTNU, 2016:360

NTNU
Norwegian University of
Science and Technology
Faculty of Natural
Sciences and Technology
Department of Physics

 **NTNU**
Norwegian University of
Science and Technology

 NTNU

 **NTNU**
Norwegian University of
Science and Technology

Vegard Flovik

Magnetization dynamics in nanostructures

Thesis for the degree of Philosophiae Doctor

Trondheim, November 2016

Norwegian University of Science and Technology
Faculty of Natural
Sciences and Technology
Department of Physics



Norwegian University of
Science and Technology

NTNU

Norwegian University of Science and Technology

Thesis for the degree of Philosophiae Doctor

Faculty of Natural
Sciences and Technology
Department of Physics

© Vegard Flovik

ISBN 978-82-326-2064-7 (printed version)

ISBN 978-82-326-2065-5 (electronic version)

ISSN 1503-8181

Doctoral theses at NTNU, 2016:360



Printed by Skipnes Kommunikasjon as

Magnetization dynamics in nanostructures

Abstract

Understanding the properties of magnetic structures confined to nanoscale dimensions is of both fundamental interest, as well as of importance for the development of modern electronics technology. With the ever increasing demand for downsizing devices, understanding how the magnetic properties might change when confined to the nanoscale is of great importance. At the same time, the desire for faster operation of devices also decreases the relevant timescales of the system. Thus, a fundamental understanding of the magnetodynamic properties of nanostructures is crucial.

In this thesis I have investigated the magnetodynamic properties of various systems, ranging from thin films to that of confined magnetic elements with lateral dimensions on the nanometer scale. One of the key experimental techniques utilized is that of ferromagnetic resonance (FMR) spectroscopy, which forms the experimental basis of this thesis. The investigations have been performed through a combination of FMR spectroscopy, numerical simulations as well as simplified analytical models.

A common theme in several of the papers of the thesis is the role of "effective magnetic fields", and how this determines the magnetization dynamics. This being in the form of additional Oersted fields due to induced microwave eddy currents (papers II and III), "anisotropy fields" from magnetocrystalline and shape anisotropies (paper IV) and the magnetic dipolar coupling in arrays of spin-torque oscillators (paper V). For further details, I have introduced the various research topics of the thesis in addition to a summary of the main results in chapter 5.

Preface

This thesis is submitted to the Norwegian University of Science and Technology (NTNU) for partial fulfillment of the requirements for the degree Philosophiae Doctor (PhD). It is based on 5 published papers investigating the magnetization dynamics of magnetic thin films and nanostructures.

This work has been carried out at the Department of Physics at NTNU, under the supervision of Professor Erik Wahlström and co-supervision of Professor Arne Brataas.

Trondheim, 28.09.2016

Vegard Flovik

Acknowledgements

There are a lot of people I have met during these last years, both in the "scientific world" and outside, to whom I am grateful. Firstly, I would like to thank my supervisor, Erik, for his guidance during the course of my PhD. I appreciate the freedom and encouragement to pursue own ideas and projects, and I believe this has contributed greatly on the path to becoming an independent researcher. I would like to thank Dr. Ferran Macià for being an excellent host during my visits at the University of Barcelona, both on the scientific and personal level. I have enjoyed collaborating with him on various projects during my PhD, and his input and guidance has been greatly appreciated. I am also grateful to the various fellow PhD students here at NTNU, both for the scientific discussions as well as for the more or less well earned coffee breaks to discuss topics also from "the real world" outside the physics community.

I also wish to thank my family, and my parents for teaching me the importance of hard work and dedication. For always supporting and encouraging me. Finally, I would like to thank Elisabeth, for being my lifeline to the "real world" at times when most of my time has been dedicated to the world of physics. For the support at times when progress has been scarce, and for sharing my joy and excitement when progress has been good. Thank you!

List of papers:

Paper I [1]:

Vegard Flovik, Ferran Macià, Sergi Lendínez, Joan Manel Hernández, Ingrid Hallsteinsen, Thomas Tybell, Erik Wahlström.

Thickness and temperature dependence of the magnetodynamic damping of pulsed laser deposited $La_{0.7}Sr_{0.3}MnO_3$ on (111)-oriented $SrTiO_3$.

J. Magn. Magn. Mater. 420, 280-284, (2016).

Author contributions:

V. F: Performed the FMR experiments (in collaboration with F. M., S. L. and J. M. H.). Performed the data analysis and wrote the manuscript.

I. H. and T. T: Provided the samples and characterized the films using Atomic Force Microscopy (AFM), X-ray Diffraction (XRD) and vibrating sample magnetometry (VSM).

E. W: Supervised the project.

All authors commented on the final manuscript.

Paper II [2]:

Vegard Flovik, Ferran Macià, Andrew D. Kent, Erik Wahlström.

Eddy current interactions in a ferromagnet-normal metal bilayer structure, and its impact on ferromagnetic resonance lineshapes.

J. Appl. Phys. 117, 143902 (2015).

Author contributions:

V. F: Deposited the normal metal layers, performed the FMR experiments, data analysis and wrote the manuscript.

F. M. and A. D. K: Provided the Permalloy samples.

E. W: Supervised the project.

All authors discussed the results and commented on the final manuscript.

Paper III [3]:

Vegard Flovik, Bjørn Holst Pettersen, Erik Wahlström.

Eddy-current effects on ferromagnetic resonance: Spin wave excitations and microwave screening effects.

J. Appl. Phys. 119, 163903 (2016)

Author contributions:

V. F: Performed FMR experiments and data analysis (in collaboration with B. H. P.) and wrote the manuscript.

B. H. P: Prepared the samples, and performed FMR experiments and data analysis.

E. W: Supervised the project.

All authors commented on the final manuscript.

Paper IV [4]:

Vegard Flovik, Ferran Macià, Joan Manel Hernández, Rimantas Bručas, Maj Hanson, Erik Wahlström.

Tailoring the magnetodynamic properties of nanomagnets using magnetocrystalline and shape anisotropies.

Phys. Rev. B. 92, 104406 (2015)

Author contributions:

V. F: Performed the FMR experiments, data analysis, micromagnetic simulations and wrote the manuscript.

F. M. and J. M. H: Participated in preparing the broadband FMR setup and some initial micromagnetic simulations.

R. B. and M. H: Provided the samples.

E. W: Supervised the project.

All authors commented on the final manuscript.

Paper V [5]:

Vegard Flovik, Ferran Macià, Erik Wahlström.

Describing synchronization and topological excitations in arrays of magnetic spin torque oscillators through the Kuramoto model.

Sci. Rep. 6, 32528 (2016).

Author contributions:

V. F: Initiated the project, performed the calculations/simulations and wrote the manuscript.

F. M. and E. W: Supervised the project and provided input during the analysis/discussion of results and writing of the manuscript.

Additional papers:

These papers represent work that was performed during the course of my PhD where I was not the main contributor, or the topic was considered outside the scope of the thesis:

Paper VI [6]:

Maj Hanson, Rimantas Bručas, Tomasz J. Antosiewicz, Randy K. Dumas, Björgvin Hjörvarsson, **Vegard Flovik**, and Erik Wahlström
Arrays of elliptical Fe(001) nanoparticles: Magnetization reversal, dipolar interactions, and effects of finite array sizes
Phys. Rev. B 92, 094436 (2015)

Paper VII [7]:

Vegard Flovik, Santanu Sinha, Alex Hansen
Dynamic Wettability Alteration in Immiscible Two-phase Flow in Porous Media: Effect on Transport Properties and Critical Slowing Down.
Front. Phys. 3, 00086 (2015).

Contents

Abstract	i
Preface	iii
Acknowledgements	v
List of papers:	vii
1 Introduction	1
2 Fundamentals of magnetism	7
2.1 Magnetic interaction energies	8
2.1.1 Exchange energy	8
2.1.2 Zeeman energy	9
2.1.3 Demagnetization energy	10
2.1.4 Magnetocrystalline anisotropy energy	12
2.1.5 Magnetic domains	13
2.1.6 Total free-energy density	15
2.2 Magnetization dynamics	18
2.2.1 Larmor precession	18
2.2.2 The Landau-Lifshits-Gilbert equation	20
2.2.3 Ferromagnetic resonance (FMR)	21
2.2.4 Eddy-current effects on FMR	27
2.2.5 The Smit-Suhl free-energy ansatz	31

2.2.6	Inhomogeneous spin precession: Spin waves	34
2.2.7	Magnetodynamic damping	37
2.2.8	Spin-transfer torque	42
3	Micromagnetic simulations	47
3.1	Numerical solution of the LLG equation	48
3.2	Simulation of FMR spectra	49
4	Experimental techniques	55
4.1	Thin film deposition by DC magnetron sputtering	55
4.2	FMR experimental setup	57
4.2.1	Cavity-based FMR	57
4.2.2	Broadband FMR	60
5	Main research topics	63
5.1	Magnetodynamic damping in ferromagnetic thin films . . .	64
5.1.1	Summary of paper I	66
5.2	Eddy-current effects on ferromagnetic resonance	67
5.2.1	Summary of paper II	68
5.2.2	Summary of paper III	69
5.3	Magnetodynamics of confined magnetic elements	70
5.3.1	Summary of paper IV	72
5.4	Synchronization of spin-torque oscillators	73
5.4.1	Summary of paper V	75
6	Popular science article based on paper V	77
7	Outlook	83
7.1	Final considerations	87
8	Bibliography	89
9	Papers included in the thesis:	103
9.1	Paper I	105
9.2	Paper II	113

CONTENTS

xiii

9.3 Paper III	123
9.4 Paper IV	135
9.5 Paper V	147
10 Additional papers:	165
10.1 Paper VI	167
10.2 Paper VII	181

Chapter 1

Introduction

Magnetism is something which, on some level, is probably known to all of us. At some point or another in their childhood, most kids have tried playing around with small magnets. How could it be that placing two magnets together, one feels either a repelling or attractive force? They do not even touch each other, so how could they exert this kind of invisible force as you try to put them closer together or pull them apart? The fascination of these "invisible forces" between magnets is something which is truly enchanting, and might even seem like some kind of magic. Little did I know, playing around with magnets as a child, that I would still be doing essentially the same thing at this age. Although, as I have grown larger, the magnets I play with have become smaller. While my fascination with magnetism is still present, my understanding of these phenomena has fortunately evolved quite a bit, and the explanation of magnetism as some kind of magic has been replaced by a more physically correct picture.

The fascination with magnetic phenomena is something which has occupied mankind for ages. "Understanding" magnetism however, is not at all a trivial task. Magnetism, in the form most of us know it, is a macroscopic manifestation of purely quantum mechanical effects. It is not surprising then, that mankind's understanding of magnetic phenomena has taken quite some time to reach the current level of knowledge.

The beginning,

The observation of the most primitive magnetic phenomena, like the attraction of iron to naturally occurring magnetite, Fe_3O_4 , has undoubtedly been observed already before recorded history began. Other than simple observations, the exact time and place for the first use of magnetite for functional purposes remains unclear. It is however clear that by the 12th century, the magnetic compass had gained widespread use in western Europe. This eased significantly the navigation at sea, and provided a name for the magnetic mineral that would stick for centuries; lodestone, originated from middle English for course stone, or leading stone.

In addition to the application prospects, being able to actually explain the magnetic phenomena is at the heart of scientific curiosity. The first scientific discussion on magnetism has been attributed to Thales of Miletus, one of the Greek philosophers who lived from about 625 BC to 545 BC. According to Thales, the magnetic attraction was due to the fact that magnetite has a soul. The magnetite caused movement of Iron, and at the time, the view was that movement of any kind would indicate life, or a soul.

...the present

Since then, our understanding of magnetism has fortunately evolved quite a bit, and the incorporation of technology based on magnetic phenomena has completely revolutionized our society. Examples such as the electric motor, power generators and transformers are all based on understanding magnetic phenomena, and technology we all take for granted would not exist if it were not for the combined effort and hard work of scientists over the last centuries.

Magnetism is one of the oldest scientific disciplines, but one also at the forefront of the emerging nanotechnology era. The IT revolution has been made possible by intensive research on magnetic phenomena, and research on magnetic storage devices resulted in the discovery of the giant magnetoresistance effect, GMR. This discovery awarded Albert Fert and Peter Grünberg the 2007 Nobel prize in physics [8]. In addition to being

interesting from a physics viewpoint, the GMR effect has several important applications in e.g. magnetic field sensors in hard disc drives, biosensors, microelectromechanical systems (MEMS) and other devices [9]. Subsequent discoveries led to the realization that both spin and charge properties of electrons could be utilized in electronic circuits, leading to the development of the research field of spintronics, i.e. spin-electronics [10, 11].

The ever increasing demand for processing power and storage led to the famous Moore's "law" of exponentially increasing transistor density. This is named after Gordon Moore, co-founder of Intel, who in 1965 observed an exponential increase in the number of components per integrated circuit [12]. His initial prediction that this would continue for at least another decade actually proved to be accurate for several decades, and only in recent years the pace of advancement has started to slow down.

The increase in transistor density is necessarily accompanied by a corresponding scaling in the size of the components. This shrinking process of magnetic devices has continued past the length scales of the macroscopic world, and has entered the realms of nanoscale dimensions. In the words of the famous lecture by Richard Feynman at Caltech in 1959, "There is plenty of room at the bottom". With the desire of shrinking devices to the nanoscale, it also becomes important to consider how this can affect the devices properties. One concern in the context of magnetic memory, is that of the "superparamagnetic limit". When shrinking magnetic devices, the influence of thermal fluctuations becomes increasingly important. At a certain limit, thermal fluctuations become greater than the energy required for changing the state of the magnetic bit, thus effectively erasing the stored information [13].

...and the future

Rather than just keeping on shrinking the devices, these limitations impose the need of thinking of more ingenious ways of designing them and how one could utilize other physical effects in obtaining this. One such approach is e.g. the replacement of the power-consuming magnetic-field based bit-writing by using the less intrusive spin-transfer torque effect [14].

This enables switching of the magnetization by the transfer of spin angular momentum through spin currents, and is the governing principle behind the development of Magnetic Random Access Memory, or MRAM [18].

Other possibilities includes rethinking how logic and data storage can be implemented. An emerging field of magnetism is that of magnonics [19]. Magnonics combines waves and magnetism, with the aim of investigating the behavior of spin waves in magnetic nanostructures. There is much interest in utilizing spin waves for things such as magnonic logic and data storage schemes, and follows the success of the modern hard disk. The research on these topics is concerned with the behavior of the magnetization when confined to very small length scales and very fast timescales, and improved understanding of these phenomena might lead to improvement of existing technologies, or generate new technology and computing concepts.

Another recent prospect, is that of bio-inspired computing. Here, researchers look to nature for inspiration in the development of bio-inspired chips based on natural computing architectures [20]. The brain, and biological systems in general, are able to perform high performance calculations with much higher efficiency than computers, and they do it quickly and with very low energy consumption. Interestingly, recent advances in nanotechnology and materials science finally make it possible to envisage designing and building networks based on multifunctional nanodevices approaching the complexity of biological systems [20].

This thesis:

The IT revolution has been made possible by intensive research on magnetism, and continued efforts on the investigations of novel magnetic phenomena will likely lead to new and exciting technologies in the years to come. Common for all these emerging technologies, is the need for understanding the fundamental behavior of the magnetization dynamics in systems confined to nanoscale dimensions.

This is also the common ground for the work that forms the basis of this thesis, with the title: "Magnetization dynamics in nanostructures". The thesis consists of a collection of work performed on various systems,

but with the overall aim of providing new knowledge on the magnetization dynamics in systems confined to nanoscale dimensions.

The thesis is structured as follows: I begin with a review on the fundamentals of magnetism, with special emphasis on magnetization dynamics. I then continue with an introduction to performing micromagnetic simulations, as well as the main experimental techniques utilized during the course of my PhD. In the following chapters, I provide a general overview of the main research topics and explain how the findings presented in this thesis are relevant with respect to ongoing research. Finally, I have appended the published papers that resulted from my PhD.

Chapter 2

Fundamentals of magnetism

This chapter aims to provide a general introduction to magnetism and magnetization dynamics. There are a lot of good introductory textbooks covering the fundamentals of magnetism and electromagnetism. With focus on the foundations of solid state physics, we have e.g. the classical textbooks *Introduction to solid state physics* [21] by C. Kittel and *Solid State Physics* [22] by N. W. Ashcroft & N. D. Mermin. Among books on general electromagnetism we have e.g. *Introduction to Electrodynamics* [23] by J. D. Griffiths and *Classical Electrodynamics* [24] by J. D. Jackson. The focus of this thesis is more specifically on magnetism on the nanoscale and magnetization dynamics, and some nice textbooks on these subjects are e.g. *Magnetism: From fundamentals to Nanoscale Dynamics* [13] by J. Stöhr and H. C. Siegman and *Magnetization Oscillations and Waves* [25] by A. G. Gurevich and G. A. Melkov.

The examples listed above are all books I have used during the course of my studies, and the content of these books forms the backbone of the following chapter, introducing the fundamentals of magnetism and magnetization dynamics.

2.1 Magnetic interaction energies

The following sections provide an introduction to the main magnetic interaction energies, namely exchange, Zeeman, magnetostatic and magnetocrystalline anisotropy. Emphasis is put on the implications of the various energy terms for magnetic systems confined to the nanoscale, and outcomes such as the formation of magnetic domains are introduced. By analyzing the interplay between the various energy terms, one can obtain important understanding on the properties of nanoscale magnetic systems.

2.1.1 Exchange energy

The exchange interaction is a quantum mechanical effect determined by the Pauli exclusion principle and the electrostatic Coulomb interaction, and is the fundamental force responsible for long range magnetic ordering [22]. In the Heisenberg model of magnetism, the exchange energy is given by:

$$E_{\text{ex}} = -\frac{1}{2} \sum_{i < j} J_{ij} \mathbf{S}_i \cdot \mathbf{S}_j. \quad (2.1)$$

Here, J_{ij} is the exchange integral representing the energy difference between parallel and anti-parallel states for the nearest neighbor spins \mathbf{S}_i and \mathbf{S}_j . The exchange energy given by Eq. (2.1) is isotropic, and depends only on the relative orientation of the neighboring spins.

Ferromagnetic materials are characterized by a positive exchange integral, $J_{ij} > 0$, favoring the alignment of neighboring spins, resulting in a ferromagnetic (FM) order. Antiferromagnetic (AFM) materials on the other hand, are characterized by a negative exchange integral, favoring anti-parallel alignment of neighboring spins. The difference between ferromagnetic and antiferromagnetic ordering is illustrated in Fig. 2.1. Thermal fluctuations can also affect the magnetic state, and at sufficiently high temperatures they will break the long range magnetic ordering. As the exchange interaction is the fundamental mechanism behind magnetic ordering, the magnitude of the exchange integral will determine this critical

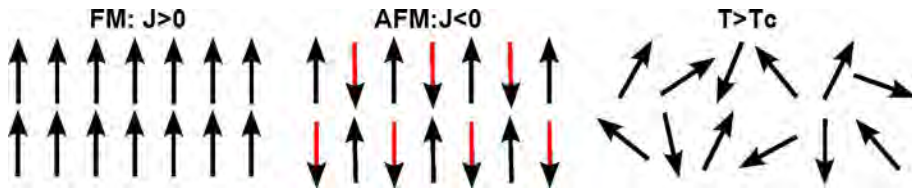


Figure 2.1: Illustration of Ferromagnetic (FM) and Antiferromagnetic (AFM) ordering below T_c and T_N respectively, depending on the sign of the exchange integral J . Above a critical temperature, where the thermal energy surpasses the exchange energy, spin fluctuations prevent long range order.

temperature, named the Curie temperature (T_C) for the FM state and the Néel temperature (T_N) for the AFM state.

Going from the discrete case of individual spins to a macroscopic treatment where the magnetization is treated as a continuous vector field rather than the sum of quantized magnetic moments, one can write the exchange energy through a phenomenological continuum description [26]:

$$E_{\text{exch}} = \frac{A}{M^2} \int (\nabla \cdot \mathbf{M})^2 dV. \quad (2.2)$$

Here, the constant A represents the exchange stiffness, which is a function of the exchange integral. Although the exchange interaction is strong, it is very local as it is determined by the overlap of the electron wave functions. As we shall see, other contributions to the magnetic energy will become gradually more important as we increase the system size from a few spins to the macroscopic scale [26]. This will also be discussed further in sections 2.1.5 and 2.1.6

2.1.2 Zeeman energy

The Zeeman energy is the interaction energy between a magnetized body and any external magnetic field, and it exerts a torque on the magnetic moment which minimizes the energy when aligned parallel to the applied field, \mathbf{H}_{ext} . For a FM with a local magnetization \mathbf{M} , the Zeeman energy is given by an integral over the magnetized body:

$$E_{\text{Zeeman}} = -\mu_0 \int_V \mathbf{H}_{\text{ext}} \cdot \mathbf{M} dV, \quad (2.3)$$

where μ_0 is the vacuum permeability.

The Zeeman interaction makes it possible to manipulate the magnetic state by applying an external magnetic field. This allows for an external switching mechanism, which is of great importance for applications in magnetic storage devices and is used in e.g. write heads on hard disc drives [27]. As we shall see in section 2.2.8, new technologies replacing the magnetic-field based bit-writing by using the less intrusive spin-transfer torque effect is also under development [18]. This allows for controlling the magnetic state locally, compared to classical memory storage which use external magnetic fields.

2.1.3 Demagnetization energy

At the surface of a magnetized body the magnetization \mathbf{M} is suddenly reduced to zero, and there is a non-zero divergence at the surface, $\nabla \cdot \mathbf{M} \neq 0$. Through Gauss' law of flux conservation ($\nabla \cdot \mathbf{B} = 0$) combined with $\mathbf{B} = (\mathbf{H} + \mathbf{M})$, this also causes a divergence of \mathbf{H} :

$$\nabla \cdot \mathbf{H} = -\nabla \cdot \mathbf{M}. \quad (2.4)$$

The result of this can be modeled as a magnetic field arising from magnetic poles located at the sample surface where $\nabla \cdot \mathbf{M} \neq 0$. The magnetic field caused by this divergence is from hereon referred to as the demagnetization field, \mathbf{H}_D . The energy associated with this field originates from Eq. (2.3), and is called the demagnetization energy:

$$E_{\text{demag}} = -\frac{\mu_0}{2} \int_V \mathbf{H}_D \cdot \mathbf{M} dV, \quad (2.5)$$

where a factor of 2 has been introduced to avoid double counting of the interaction between two magnetic dipoles.

The demagnetization energy depends on both sample geometry and on the magnetic state. For an arbitrarily shaped magnetic body, the demagnetization field generally shows a complex dependence on position, complicating the calculation of the demagnetization energy. The concentration of the magnetic poles depends on the direction of the magnetization. If the magnetization is oriented along the longest axis of the magnetized body, the poles are spread across a smaller surface, resulting in a lower demagnetization energy. This is a form of magnetic anisotropy called shape anisotropy, and is illustrated in Fig 2.2a for the case of an elliptical ferromagnet (FM).

This dependence on geometry is normally given by a demagnetization tensor $\hat{\mathbf{N}}$, such that $\mathbf{H}_D = -\hat{\mathbf{N}} \cdot \mathbf{M}$. Calculating the demagnetization tensor for an arbitrarily shaped FM is demanding, and a numerical approach is generally needed. However, for the special case of ellipsoids the demagnetization field is linearly related to the magnetization by a geometry dependent constant called the demagnetization factor.

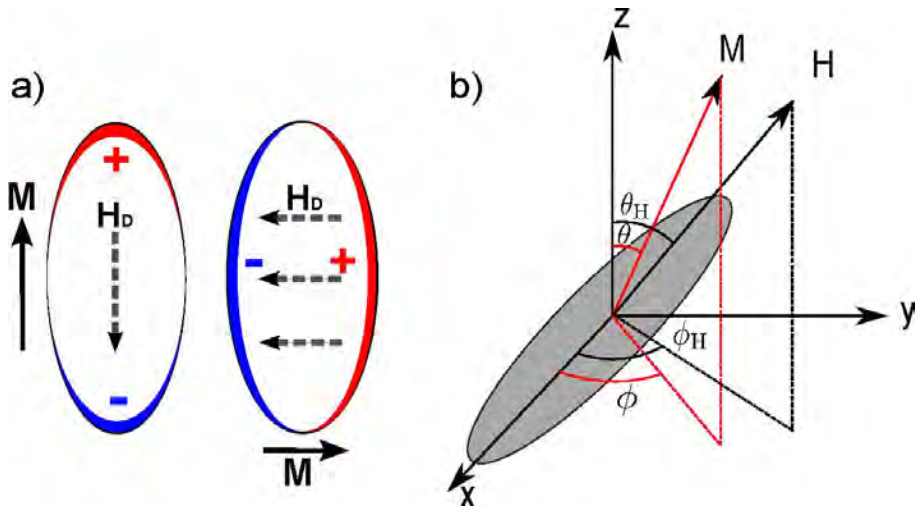


Figure 2.2: a) Illustration of the magnetic surface charges (positive and negative respectively) at the surface of a single domain elliptical FM. The direction of the magnetization is given by \mathbf{M} and the demagnetization field by \mathbf{H}_D b) Field and sample geometry for a FM with an external field \mathbf{H} and magnetization \mathbf{M} .

For an ellipsoid with principal axes aligned along the (x,y,z) coordinate axes, as illustrated in Fig 2.2b, the demagnetization tensor simplifies to only diagonal elements N_x, N_y and N_z , where $N_x + N_y + N_z = 1$. From the sample geometry illustrated in Fig. 2.2b (magnetic element in the x-y plane), one gets:

$$\begin{aligned} M_x &= M_s \sin \theta \cos \phi \\ M_y &= M_s \sin \theta \sin \phi \\ M_z &= M_s \cos \theta. \end{aligned} \tag{2.6}$$

This yields the demagnetization energy per volume for an ellipsoid:

$$\begin{aligned} E_{\text{Demag}} &= \frac{\mu_0}{2} [N_x M_x^2 + N_y M_y^2 + N_z M_z^2] \\ &= \frac{\mu_0 M_s^2}{2} [N_x \sin^2 \theta \cos^2 \phi + N_y \sin^2 \theta \sin^2 \phi + N_z \cos^2 \theta]. \end{aligned} \tag{2.7}$$

This expression contains the three extremities of a sphere (all axis equal length, $N_x = N_y = N_z = 1/3$), infinite circular cylinder (one axis infinite, $N_x = 0, N_y = N_z = 1/2$), and a plane (two axis infinite, $N_x = N_y = 0, N_z = 1$). In particular the approximation for a plane works very well for thin films, where the thickness is minute compared to the lateral dimensions.

2.1.4 Magnetocrystalline anisotropy energy

Crystalline ferromagnets are generally not isotropic, and the magnetization tends to prefer aligning along certain crystallographic axes referred to as so-called "easy axes". This energy contribution is named the magnetocrystalline anisotropy energy, and is defined through the energy required to rotate the magnetization away from an "easy axis". The magnetocrystalline anisotropy results from the spin-orbit interaction, and depends on the orientation of the electron spins relative to the crystallographic axes of the material. Given the crystalline origin, the anisotropy energy should reflect the lattice symmetry. This is normally done by an expansion of the

directional cosines of the magnetization unit vector, $\mathbf{m} = \mathbf{M}/M_s$, along the x, y and z axis, and is here denoted the m_1, m_2 and m_3 component respectively.

As an example consider Iron (Fe), which has a cubic crystalline anisotropy [28]. The anisotropy energy is symmetric under magnetization inversion, and the expansion of the directional cosines is limited to even orders of m_i . From the sample geometry defined in Fig. 2.2b, one obtains to the lowest order:

$$\begin{aligned} E_{\text{Anis}} &= K_1[m_1^2 m_2^2 + m_2^2 m_3^2 + m_3^2 m_1^2] + K_2[m_1 m_2 m_3]^2 \\ &\approx K_1 \left[\sin^4 \theta \sin^2 \phi \cos^2 \phi + \sin^2 \theta \sin^2 \phi \cos^2 \theta + \sin^2 \theta \cos^2 \phi \cos^2 \theta \right], \end{aligned} \quad (2.8)$$

where K_1 and K_2 represent material specific anisotropy constants. For Fe the K_1 term dominates [28], and as a simplification the K_2 term can be neglected.

2.1.5 Magnetic domains

A macroscopic ferromagnet does not generally consist of a single uniformly magnetized domain. Due to the complex interplay of the various energy terms introduced in the previous sections, the ferromagnet might minimize the energy by forming multiple domains with different magnetization directions. The progressive introduction of domains (Fig. 2.3a) reduces the number of surface poles and demagnetization energy (as illustrated previously in Fig. 2.2a).

The domain formation will also be influenced by magnetocrystalline anisotropy, and the domains tend to be oriented along the easy axes of the system. The transition between two domains with different orientation of the magnetization is characterized by a region with a spatial spin rotation, called a domain wall. This domain wall region is governed by a competition between the demagnetization and exchange energies. On the one hand, an abrupt realignment of the spins at the boundary between two domains is

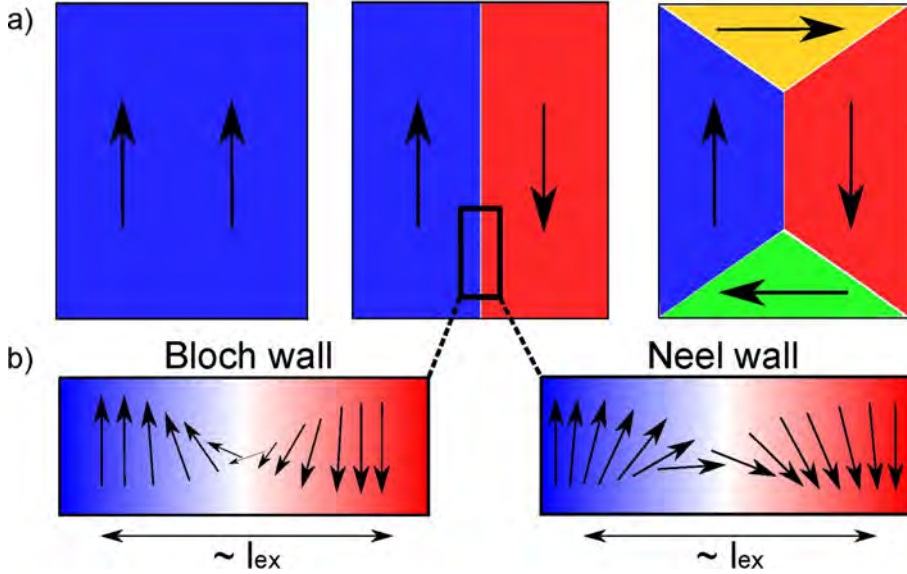


Figure 2.3: a) The formation of multiple domains results from energy minimization of the contributions from the exchange energy and demagnetization energy. b) Zoom in of a 180 degree domain wall region, showing examples of the two main groups of domain walls referred to as Bloch type and Néel type respectively.

not favorable due to the strong exchange interaction. On the other hand, a slowly varying spin orientation can be costly in terms of magnetocrystalline and magnetostatic energies. This competition can be expressed through a characteristic length scale, which determines the crossover from a regime where one or the other energy term dominates. This length scale is referred to as the exchange length, l_{ex} , determined by the ratio between the exchange stiffness A and either the magnetocrystalline or demagnetization energy density, here represented by K [29]:

$$l_{ex} = \sqrt{A/K} \quad (2.9)$$

As an example we here consider iron, using standard literature values with an exchange stiffness of $A = 21 \times 10^{-12}$ J/m and a crystalline anisotropy

constant of $K_1 = 4.3 \times 10^4 \text{ J/m}^3$. An upper limit for the demagnetization energy is given by $\frac{1}{2}\mu_0 M_s^2$, with a saturation magnetization $M_s = 1.7 \times 10^6 \text{ A/m}$. These material parameters result in the characteristic magnetic length scales of the system, $l_{\text{ex}} = 21 \text{ nm}$ and 3.5 nm for the crystalline and demagnetization energy respectively. Another example is Permalloy, which has a negligible magnetocrystalline anisotropy. In this case, the exchange length is determined by the demagnetization energy and one obtains $l_{\text{ex}} = 5 \text{ nm}$ [30].

Magnetic domain walls can be divided into two main groups, Bloch and Néel type respectively, depending on how the magnetization rotates from one domain to the other. These types of domain walls are illustrated in Fig. 2.3b, where the Bloch type wall is characterized by a spin rotation in the plane of the domain wall, with a wall width commonly defined as $w = \pi\sqrt{A/K}$ [30]. This kind of domain wall is typically found in bulk ferromagnets, where the magnetostatic energy due to stray fields at the sample surface is negligible. However, as the Bloch wall induces surface charges by its stray field, the Néel wall becomes favorable when the film thickness becomes smaller than the wall width and the magnetostatic energy from stray fields at the surface is considerable. In cases where the energy of forming a domain wall is greater than the demagnetization energy, the result is a single domain state. This is typically the case for small ferromagnets with a size of the same order as the exchange length l_{ex} , which sets the length scale of the domain wall width.

2.1.6 Total free-energy density

One can learn a lot about the properties of magnetic systems by analyzing the interplay between the various energy terms introduced in the previous sections. As an example, consider here a small Fe ellipse. Due to the size and shape of the ellipse, the magnetic element is considered to be in a single domain state (as discussed in section 2.1.5). Having a single domain state allows for using an analytical macrospin model, where the exchange energy is not considered. One can then calculate the free-energy density of the system by adding up the various energy terms, which is given by

$E_{\text{tot}} = E_{\text{Zeeman}} + E_{\text{Demag}} + E_{\text{Anis}}$. After adding the terms, one can write the total free-energy density as:

$$\begin{aligned}
 E_{\text{tot}} = & -M_s H_0 \sin \theta \cos(\phi - \phi_H) \\
 & + \frac{\mu_0 M_s^2}{2} \left[\sin^2 \theta \cos^2 \phi \left(N_x + \frac{2K_1}{\mu_0 M_s^2} \sin^2 \theta \sin^2 \phi \right) \right. \\
 & + \sin^2 \theta \sin^2 \phi \left(N_y + \frac{2K_1}{\mu_0 M_s^2} \cos^2 \theta \right) \\
 & \left. + \cos^2 \theta \left(N_z + \frac{2K_1}{\mu_0 M_s^2} \sin^2 \theta \cos^2 \phi \right) \right], \tag{2.10}
 \end{aligned}$$

where the units for the saturation magnetization and magnetic field are $[M_s] = \text{A/m}$ and $[H_0] = \text{T}$ respectively. Eq. (2.10) describes a complex energy landscape, with competing energies from the various terms.

The free-energy density for a 10 nm thick Fe film for the case of a continuous film as well as ellipses of varying lateral dimensions is shown in Fig. 2.4. This indicates how the free-energy density changes when one gradually reduces the size of the ellipse from the upper limit of a continuous film, to an ellipse of dimensions 50×150 nm. As expected, one notices that in all cases the magnetization favors an orientation in the sample plane ($\theta = 90$, from sample geometry as defined in Fig. 2.2b).

For the continuous film and the largest ellipse in Fig. 2.4a and b, one can clearly see the dominating crystalline anisotropy, with a four-fold symmetry between the energy minima along the ϕ axis. In the intermediate case of an ellipse of dimensions 150×450 nm in Fig. 2.4c, one has two dominating energy minima at $\phi = 0$ and $\phi = 180$ (magnetization oriented along the long axis of the ellipse). In addition, there is a quite flat saddle point at $\phi = 90$ (and $\phi = 270$, not included in the figure) which corresponds to the magnetization oriented along the short axis of the ellipse. These are not stable energy minima, but the flatness of the saddle point means that applying a small magnetic field along this axis will create a local energy minimum along this direction. For the smallest ellipse, in Fig. 2.4d, the

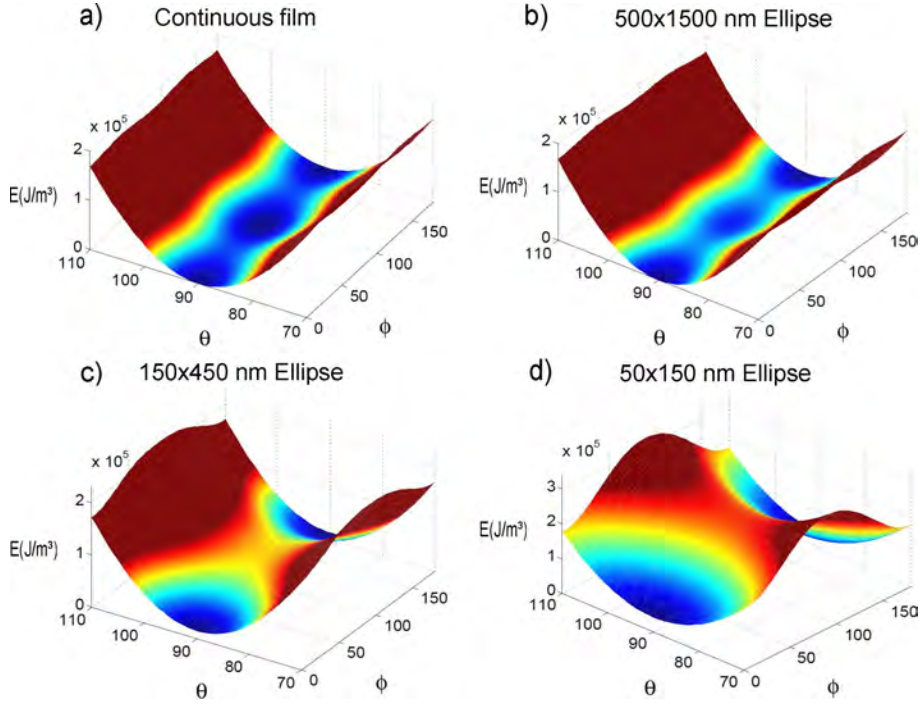


Figure 2.4: Free-energy density given by Eq. (2.10) for a) continuous film, b) 500×1500 nm ellipse, c) 150×450 nm ellipse, d) 50×150 nm ellipse. Film thickness is 10 nm in all cases. (Figure from paper IV of the thesis)

energy landscape is dominated by the two-fold shape anisotropy along the long axis of the ellipse. To align the magnetization along the short axis of the ellipse ($\phi = 90$) will thus require a quite large external magnetic field.

For a more detailed discussion on the interplay between the various energy terms, I refer to paper IV of the thesis where we investigate how the interplay between magnetocrystalline and shape anisotropies can be used to tailor the magnetodynamic properties of nanomagnets.

2.2 Magnetization dynamics

In the following sections I aim to introduce the fundamentals of magnetization dynamics, which is the common ground for the work that forms the basis of this thesis. Understanding the magnetization dynamics is important for modern world applications of magnetic phenomena, such as e.g. microwave oscillators. It is also playing an increasingly important role in "static" devices, as the switching times of current applications in e.g. magnetic memory approach the sub-ns regime where the intrinsic time scale of the magnetization dynamics is defined by the gyrotropic precession of the individual magnetic moments.

The electron spin is only fully described through quantum mechanics. However, for most purposes a quasi classical macroscopic approach is sufficient. We begin by considering a single electron spin in a static magnetic field, before dealing with the collective behavior of a collection of spins which make up the magnetization dynamics in a ferromagnet. The concept of ferromagnetic resonance is introduced, starting with the simplest case assuming a uniform spin precession. The case of inhomogeneous spin precession, spin waves, is then introduced before proceeding with a discussion on the magnetodynamic damping. Finally, I end this chapter with a brief discussion on the interplay between charge and spin degrees of freedom of electrons, and the spin-transfer torque effect.

2.2.1 Larmor precession

The energy of a single electron spin in a static magnetic field \mathbf{H} , is given by the Zeeman energy as:

$$E_s = -\boldsymbol{\mu}_s \cdot \mathbf{H}, \quad (2.11)$$

where $\boldsymbol{\mu}_s$ is the magnetic moment of the electron spin. From energy minimization, this results in the spin aligning with the magnetic field. The magnetic moment of the electron is related to the spin angular momentum \mathbf{S} :

$$\boldsymbol{\mu}_s = -\gamma_s \mathbf{S}, \quad (2.12)$$

where γ_s is the gyromagnetic ratio given by $\gamma_s = g_s e / 2m_e$. Here, e is the electron charge, g_s the electron spin g-factor and m_e the electron mass. However, the static magnetic field also exerts a torque $\boldsymbol{\tau}$ on this magnetic moment, which is given by [22]:

$$\boldsymbol{\tau} = \boldsymbol{\mu}_s \times \mathbf{H}. \quad (2.13)$$

As the torque is equal to the rate of change of angular momentum, one can combine Eqs. (2.12)-(2.13) to obtain:

$$\frac{d\boldsymbol{\mu}_s}{dt} = -\gamma_s \boldsymbol{\mu}_s \times \mathbf{H}. \quad (2.14)$$

From Eq. (2.14), one notices that rather than aligning the magnetic moment along the direction of the applied field, the torque causes a precession motion around \mathbf{H} , as illustrated in Fig. 2.5. By solving Eq. (2.14), one can obtain the precession frequency ω_L , named the Larmor frequency:

$$\omega_L = \gamma_s H. \quad (2.15)$$

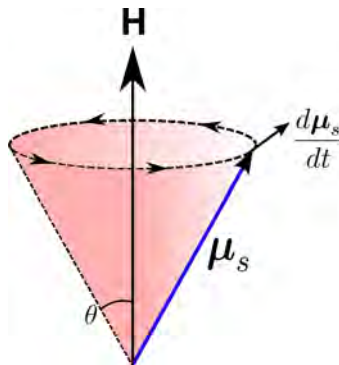


Figure 2.5: Schematic of the precession of the magnetic moment $\boldsymbol{\mu}_s$ around the external field \mathbf{H} . The precession angle θ is here severely exaggerated for illustration purposes.

The Larmor condition shows the relation between rotation frequency and magnetic field strength for a free magnetic moment. Larmor precession is the governing principle behind several important spectroscopy techniques such as nuclear magnetic resonance (NMR), electron paramagnetic resonance (EPR) and ferromagnetic resonance (FMR). In particular FMR is important for the work performed in this thesis, and this phenomena will be introduced in section 2.2.3.

2.2.2 The Landau-Lifshits-Gilbert equation

Moving on from a single electron to an ensemble of spins, we now consider a classical approach by approximating the ferromagnet as a sum of the individual spins. Following this approach, Eq. (2.14) takes the form:

$$\frac{d\mathbf{M}}{dt} = -\gamma\mathbf{M} \times \mathbf{H}. \quad (2.16)$$

Here, γ is the gyromagnetic ratio, where $\gamma/2\pi \approx 28$ GHz/T, and \mathbf{M} is the magnetization of the ferromagnet. This equation describes a uniform precession of the magnetic moments, and is a good approximation for the magnetodynamics of thin ferromagnetic films, as such uniform modes are easily obtainable experimentally. The more complicated case of non-uniform spin precession, spin waves, will be introduced in section 2.2.6

Spin dynamics is, similar to any mechanical system, always accompanied by dissipative forces (damping) during precession. To describe the damping of the precession and the alignment of the magnetic spins along the effective field, Landau and Lifshits added a phenomenological damping term to the equation for the magnetization precession [31], here written in the form of the well known Landau-Lifshitz-Gilbert (LLG) equation:

$$\frac{d\mathbf{M}}{dt} = \underbrace{-\gamma\mathbf{M} \times \mathbf{H}_{\text{eff}}}_{\text{Gyration}} + \frac{\alpha}{M_s} \underbrace{\left[\mathbf{M} \times \frac{d\mathbf{M}}{dt} \right]}_{\text{Damping}}. \quad (2.17)$$

The magnetic field \mathbf{H} is here replaced by \mathbf{H}_{eff} , containing not only the external field but also take anisotropies etc. into account. The damping is

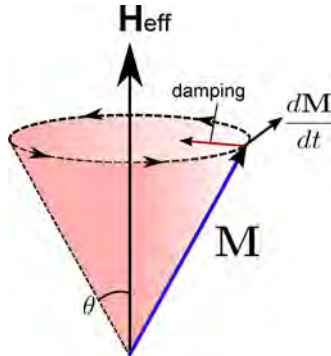


Figure 2.6: Schematic of the precession of the magnetization \mathbf{M} around the effective magnetic field \mathbf{H}_{eff} . The viscous damping, given by the Gilbert damping parameter α in Eq. (2.17), pushes the magnetization in the direction of the effective field.

included through the Gilbert damping parameter α , representing a viscous damping force that pushes the magnetization in the direction of the effective field, as illustrated in Fig. 2.6.

The various microscopic mechanisms contributing to the Gilbert damping are quite complex, and there are several processes which can cause dissipation of energy. These are commonly divided into intrinsic and extrinsic processes, and material specific Gilbert damping in real systems. Further details concerning the magnetodynamic damping will be introduced in section 2.2.7.

2.2.3 Ferromagnetic resonance (FMR)

As introduced in the previous sections, the effective magnetic field exerts a torque on the magnetization in a ferromagnet, causing a precession motion of the magnetization. The precession frequency depends on several parameters such as the shape of the ferromagnet, strength and orientation of the applied magnetic field as well as the magnetization of the sample. Applying a microwave magnetic field similar to this frequency will induce a precession motion of the magnetization where all the magnetic moments oscillate in

phase. This is the phenomenon of ferromagnetic resonance, FMR, where the ferromagnet shows a resonant absorption of the electromagnetic energy.

The dynamical response of the magnetic system can be studied through solving the LLG equation introduced in the previous section. However, as the resonance frequency depends on the effective magnetic field, which includes both the applied magnetic field as well as shape and crystalline anisotropies, this is in general a complicated problem to solve. As an initial simplification, magnetocrystalline anisotropies are neglected and an ellipsoidal sample is assumed. In this case, the demagnetization tensor simplifies to only diagonal elements, N_x, N_y and N_z , as discussed in section 2.1.3.

Taking the demagnetization effects into account and adding an oscillating magnetic field component, $\mathbf{h}(t)$, one obtains the following effective magnetic field:

$$\mathbf{H}_{\text{eff}} = \begin{pmatrix} H_0 - N_x M_0 \\ h_y(t) - N_y m_y(t) \\ h_z(t) - N_z m_z(t) \end{pmatrix}, \quad (2.18)$$

where H_0 is the external static field. The magnetization is oriented in the x -direction, and assuming a small-angle precession it can be written in the form $\mathbf{M}(t) = M_0 \hat{x} + \mathbf{m} e^{i\omega t}$, where $\mathbf{m} \perp \hat{x}$ and we assume that $h \ll H_0$ and $m \ll M_0$. The magnetic response to small excitation fields is given by the Polder susceptibility tensor $\hat{\chi}$ [32], where the elements of $\hat{\chi}$ are determined by solving Eq. (2.17) and discarding higher order terms. Introducing $\omega_H = \gamma H_0$ and $\omega_M = \gamma M_0$, one obtains the following set of coupled equations:

$$\begin{pmatrix} \omega_H + (N_y - N_x)\omega_M - i\alpha\omega & -i\omega \\ i\omega & \omega_H + (N_z - N_x)\omega_M - i\alpha\omega \end{pmatrix} \begin{pmatrix} m_y \\ m_z \end{pmatrix} = \omega_M \begin{pmatrix} h_y \\ h_z \end{pmatrix}. \quad (2.19)$$

In order to calculate the susceptibility tensor, one has to invert the matrix in Eq. (2.19) to get the expression on the form $\mathbf{m} = \hat{\chi}\mathbf{h}$. Doing this, one

obtains:

$$\hat{\chi} = \begin{pmatrix} \chi_{yy} & i\chi_{yz} \\ -i\chi_{zy} & \chi_{zz} \end{pmatrix}, \quad (2.20)$$

where the matrix elements are given by:

$$\chi_{yy/zz} = \frac{\omega_M[\omega_H + (N_{z/y} - N_x)\omega_M - i\alpha\omega]}{\omega_r^2 - \omega^2(1 + \alpha^2) - i\alpha\omega[2\omega_H + (N_y + N_z - 2N_x)\omega_M]}, \quad (2.21)$$

$$\chi_{yz/zy} = \frac{\omega\omega_M}{\omega_r^2 - \omega^2(1 + \alpha^2) - i\alpha\omega[2\omega_H + (N_y + N_z - 2N_x)\omega_M]}. \quad (2.22)$$

In these expressions, we have also introduced the resonance frequency ω_r , which was first derived by Kittel [33]:

$$\omega_r^2 = [\omega_H + (N_y - N_x)\omega_M][\omega_H + (N_z - N_x)\omega_M]. \quad (2.23)$$

Due to the damping term, the susceptibilities are complex functions and the response can be described through a real and an imaginary term, $\chi = \chi' + i\chi''$. The real term represents dispersion, or energy storage in the system, and the imaginary term represents the dissipation. From Eqs. (2.21)-(2.22) it becomes clear that the susceptibility diverges when the driving frequency, ω , matches the resonance frequency, ω_r , where the divergence is limited by the presence of the damping term given by α . This divergence of the susceptibility is the phenomenon of ferromagnetic resonance (FMR), where the ferromagnet shows a resonant absorption of the electromagnetic energy at the ferromagnetic resonance frequency. By measuring the power loss in an applied microwave magnetic field, FMR spectroscopy can thus be used as an experimental technique to probe the magnetic state. This will be discussed further in section 4.2, where the experimental FMR setups are introduced.

The absorbed power during resonance is given by the time derivative of the magnetic energy. Splitting $\hat{\chi}$ into its real and imaginary part and applying a microwave magnetic field $\mathbf{h}(t) = h_y e^{i\omega t} \hat{y}$, one obtains the absorbed power in a FM sample given by an integral over the sample volume [24]:

$$P_{\text{abs}} = -\frac{1}{2} \Re \int_V i\omega(\hat{\chi}\mathbf{h}) \cdot \mathbf{h}^* dV = \frac{1}{2} \omega h_x^2 \chi''_{yy}. \quad (2.24)$$

The measured FMR absorption is thus proportional to the imaginary part of the diagonal elements of the susceptibility tensor, χ''_{yy} . Using that the susceptibilities are written in the form $\chi = Z_1/Z_2$, where Z_i are complex numbers, one can separate the real and imaginary part by multiplying the expression by the complex conjugate of the denominator: $\chi = \frac{Z_1 Z_2^*}{Z_2 Z_2^*}$. For a thin film ($N_x = N_y = 0, N_z = 1$) and assuming low damping, ($\alpha^2 \approx 0$) this gives:

$$\chi'_{yy} = \frac{\omega_M \omega_B (\omega_r^2 - \omega^2)}{(\omega_r^2 - \omega^2)^2 + \alpha^2 \omega^2 (\omega_H + \omega_B)^2}, \quad (2.25)$$

$$\chi''_{yy} = \frac{\alpha \omega \omega_M (\omega_B^2 + \omega^2)}{(\omega_r^2 - \omega^2)^2 + \alpha^2 \omega^2 (\omega_H + \omega_B)^2}. \quad (2.26)$$

As shown through Eqs. (2.24) and (2.26), the FMR frequency, $\omega = \omega_r$, corresponds to a maximum in the power absorption. The susceptibility can thus be probed either by varying the microwave frequency ω , or by keeping the microwave frequency fixed and vary ω_r through the applied magnetic field. This latter field-sweep approach is the technique that has been utilized in this thesis (see section 4.2 for an introduction to the experimental FMR setups). When analyzing the extracted absorption curves, one then needs to relate this to the susceptibilities given by Eqs. (2.25)-(2.26). Expressing the susceptibilities in terms of the applied field strength rather than frequency is not straightforward, as the resonance field is non-linear in H_0 and M_0 . However, for curve-fitting purposes, one can obtain simplified expressions for the field-swept FMR absorption, following a few approximations.

Firstly, it is assumed that the saturation magnetization is much greater than the applied field strength, $\omega_M \gg \omega_H$. In this case, the following simplifications can be made:

$$\begin{aligned}
\omega_B &= \omega_M + \omega_H \approx \gamma M_0 \\
\omega_r^2 - \omega^2 &= \gamma^2 [H_0(H_0 + M_0) - H_r(H_r + M_0)] \\
&\approx \gamma^2 M_0(H_0 - H_r),
\end{aligned} \tag{2.27}$$

Further, when assuming a low damping, the linewidth is small compared to the resonance frequency and one does not need to deviate far from the resonance in order to observe the shape of the absorption curve:

$$\omega_r^2 + \omega^2 \approx 2\omega_r^2 \approx 2\gamma^2 M_0 H_0. \tag{2.28}$$

By applying the above approximations, the real and imaginary part of the susceptibility given by Eqs. (2.25)-(2.26) can be written as:

$$\chi'_{yy} \approx A \frac{(H_0 - H_r)/\Delta H}{(H_0 - H_r)^2 + (\Delta H/2)^2} \tag{2.29}$$

$$\chi''_{yy} \approx A \frac{1}{(H_0 - H_r)^2 + (\Delta H/2)^2}, \tag{2.30}$$

where A is an amplitude prefactor and the parameter $\Delta H = 2\alpha\omega/\gamma$ has been introduced to describe the linewidth. The imaginary part of the susceptibility has a so-called symmetric Lorentzian lineshape, whereas the real part has an antisymmetric lineshape, as illustrated in Fig. 2.7a and b respectively.

The derivation of Eq. (2.24) for the FMR absorption assumed a homogeneous microwave field, $\mathbf{h}(t) = h_y e^{i\omega t} \hat{y}$, resulting in a symmetric lineshape given by Eq. (2.30) (illustrated in Fig. 2.7a). However, having an inhomogeneous microwave field can lead to a mixing of symmetric and antisymmetric contributions to the lineshape, given by a combination of Eqs. (2.29)-(2.30). This is discussed in further detail in section 2.2.4 and papers II and III of the thesis, where we investigate how additional microwave magnetic fields due to induced eddy currents can affect the FMR excitation.

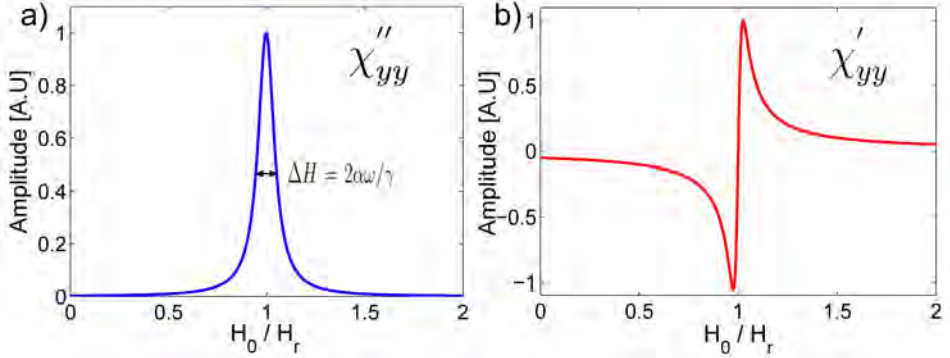


Figure 2.7: a) Imaginary part of the susceptibility, given by Eq. (2.30) b) Real part of the susceptibility, given by Eq. (2.29)

In any case, one can still extract the absorption linewidth, ΔH . As the linewidth is given by $\Delta H = 2\alpha\omega/\gamma$, one can thus estimate the magnetodynamic damping parameter α , describing the relaxation rate of the magnetization precession. The magnetization relaxation plays an important role for the magnetodynamic properties, and α is one of the key parameters obtainable from FMR spectroscopy. Further details on the various contributions to the linewidth is provided in section 2.2.7, and is also discussed in paper I of the thesis, where we investigate the damping in $\text{La}_{0.7}\text{Sr}_{0.3}\text{MnO}_3$ films.

In the above derivations, the effects of magnetocrystalline anisotropies have been neglected. The inclusion of magneocrystalline anisotropies following a similar approach was also proposed by Kittel [33]. The equilibrium orientation of the magnetization can be found by minimizing the free energy, and the idea was then to treat the free energy to act as an effective field on the magnetization, $\mathbf{H}_{\text{eff}} = -\partial E_{\text{tot}}/\partial \mathbf{M}$. From this, Kittel included both the effects of demagnetization fields and anisotropy fields in an effective demagnetization tensor, $\hat{\mathbf{N}}_{\text{eff}}$. Following this approach, one can then calculate the resonance frequency taking also magnetocrystalline anisotropies into account. Another approach for calculating the resonance

frequency from the free energy of the system, was performed by Smit, Bejers and Suhl following the Smit-Suhl free energy ansatz [34, 35], which is introduced in section 2.2.5.

2.2.4 Eddy-current effects on FMR

As mentioned in the previous section, having an inhomogeneous microwave magnetic field can lead to a mixing of symmetric and antisymmetric contributions to the FMR lineshape. A phenomenon which can cause this, is induced microwave eddy currents in conductive samples, which produce secondary phase shifted magnetic fields contributing to the microwave field exciting the FMR. In the following, I provide a brief introduction to eddy currents and the corresponding microwave magnetic fields which can influence the FMR excitation. Further details on eddy-current effects are also found in section 5.2 and papers II and III of the thesis.

A numerical approach is generally needed to calculate the distribution of induced currents and the associated magnetic fields. There are several commercial software packages capable of performing such modeling tasks, such as e.g. COMSOL [36]. However, in order to connect this to the magnetization dynamics, a numerical solution of the coupled Maxwell's and LLG equation is necessary. To my knowledge, electromagnetic modeling tools taking this coupling into account does not exist. Implementing this numerically is not a straightforward task, and due to the complexity, we rather consider simplified analytical models to provide an understanding of the basic physics involved.

Eddy current induction in a NM thin film disc

For calculating the induced eddy current, a closed form solution is obtainable for the simple case of a circular metallic film of thickness much less than the electro-magnetic skin depth. For a spatially homogeneous time harmonic magnetic field $\mathbf{B}e^{i\omega t}$ applied perpendicular to a non-magnetic circular disc, the induced current density in the thin film plane can be described by [37]:

$$J_\phi(r) = -\frac{k|\mathbf{B}|}{\mu_0} \frac{I_1(kr)}{I_0(kR)}, \quad (2.31)$$

where

$$k = \sqrt{\omega\mu_0\sigma}e^{i\pi/4}. \quad (2.32)$$

Here, R is the radius of the disc, μ_0 the vacuum permeability, σ the film conductivity and $I_n(\alpha)$ the modified Bessel function of the first kind and order n . In Fig. 2.8a the normalized current density along a circular sample calculated from Eq. (2.31) is plotted for various radii in the range $R=[0.1,1]$ mm, for a conductivity of $\sigma_{\text{py}} \approx 3 \cdot 10^6$ S/m [38] and a microwave frequency of 9.4 GHz. As shown in Fig. 2.8a, the current density is localized primarily along the sample edge as the disc size is increased. The current distribution also depends strongly on the microwave frequency, with a narrower distribution as the frequency is increased. However, here a fixed microwave frequency of 9.4 GHz is considered. As a simplification, due to the localized current distribution, the induced current is approximated by a single circular current loop in the following.

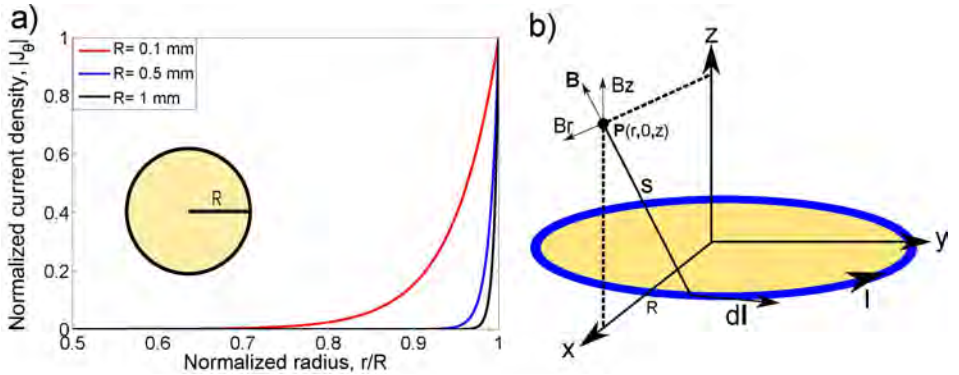


Figure 2.8: a) Calculated current density from Eq. (2.31) as a function of r for samples of radius R . b) Geometry of the circular current loop. Figure taken from paper III of the thesis

Magnetic field from a circular current loop

For a circular loop carrying a current I , the magnetic field at any point in space can be obtained from the magnetic vector potential:

$$\mathbf{A} = \frac{\mu_0 I}{4\pi} \oint \frac{d\mathbf{l}}{s}, \quad (2.33)$$

s here being the distance from a point in space, P , to the line element $d\mathbf{l}$, as illustrated in Fig. 2.8b. The general solution to Eq. (2.33) yields the vector potential [24]:

$$\mathbf{A} = A_\phi \hat{\phi} = \frac{\mu_0 I}{2\pi} [2k^{-1}r^{-1/2}(K(k) - E(k)) - kr^{-1/2}K(k)] \hat{\phi}. \quad (2.34)$$

Here, K and E represent complete elliptical integrals of the first and second kind respectively, while

$$k = \sqrt{\frac{4rR}{z^2 + (R+r)^2}}. \quad (2.35)$$

From the vector potential \mathbf{A} , one can then calculate the magnetic field ($\mathbf{B} = \nabla \times \mathbf{A}$):

$$B_z(r, z) = \frac{\mu_0 I}{2\pi \sqrt{z^2 + (R+r)^2}} \left(\frac{R^2 - z^2 - r^2}{z^2 + (r-R)^2} E(k) + K(k) \right) \quad (2.36)$$

$$B_r(r, z) = \frac{\mu_0 I z}{2\pi r \sqrt{z^2 + (R+r)^2}} \left(\frac{R^2 + z^2 + r^2}{z^2 + (r-R)^2} E(k) - K(k) \right) \quad (2.37)$$

Equations (2.36)-(2.37) give the magnetic field at any point in space produced by a current flowing in a circular loop. As discussed previously, since the eddy-current distribution is mainly localized at the sample edges, this provides a simple approximate solution for circular samples.

As an illustration, the field geometry in a circular Py/Au bilayer sample is shown in Fig. 2.9. The applied microwave field, h_{rf} , induces a circulating eddy current, I_{eddy} , which produces a microwave magnetic field, h_{ind} ,

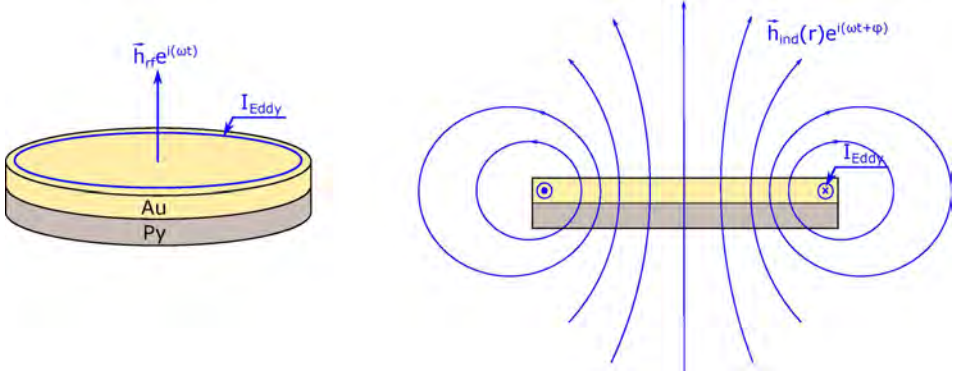


Figure 2.9: Schematic of sample and field geometry for circular Py/Au bilayers. Figure taken from paper III of the thesis.

according to Eqs. (2.36)-(2.37). The induced field has components both in the in-plane and out-of-plane direction, and will also have a phase shift, ϕ , with respect to the applied microwave field.

In paper II of the thesis, we show that phase shifted contributions to the FMR excitation produced by eddy currents results in an asymmetry of the observed lineshapes. Other studies have also shown that the relative phases of electromagnetic waves are important to consider in FMR experiments [39, 40]. Hence, the phase lag between the applied microwave field and the induced field needs to be considered.

The induced eddy currents have a relative phase lag compared to the applied microwave field, which in the ideal case is expected to be $\phi = 90$ degrees ($I_{Eddy} \propto \frac{\partial h}{\partial t}$). However, due to the inductance and resistance of the film, there will be an additional phase between the applied microwave field and the induced field. At larger film thicknesses, one also needs to take into account phase shifts due to the electro-magnetic skin effect. A complex system such as an experimental setup involving waveguides, coaxial cables etc. can also introduce a non-zero phase offset, ϕ_0 [39, 40]. Considering these effects, one can write the relative phase lag as [24]:

$$\phi = \left[90 + \tan^{-1} \left(\frac{\omega L}{R} \right) + d/\delta + \phi_0 \right]. \quad (2.38)$$

Here, ω is the microwave angular frequency, L and R are the inductance and resistance of the film, d is the film thickness and δ the electro-magnetic skin depth ($\simeq 800$ nm for Au at 10 GHz).

The derivation of the FMR absorption in the previous section which led to Eq. (2.24), indicated a symmetric Lorentzian lineshape (as illustrated in Fig. 2.7a). However, this derivation assumed a completely homogeneous microwave magnetic field. As shown in this section, induced eddy currents produce additional Oersted fields that contribute to the total microwave field driving the FMR, which can affect the observed lineshape. This change in lineshape is relevant with respect to recent experiments, where differences in the FMR lineshapes have been used to study the spin pumping from a magnetic material to a normal metal [41, 42, 43, 44, 45, 46]. In such studies, lineshape symmetry is one of the main parameters used to analyze the results. Hence, to correctly interpret experimental data involving FMR it is important to understand how eddy currents might affect the FMR excitation. For further details on eddy-current effects, I refer to section 5.2 and papers II and III of the thesis.

2.2.5 The Smit-Suhl free-energy ansatz

The fact that ferromagnetic resonance involves a small angle precession around the equilibrium position of the magnetization along the effective field, permits an approach to determine the resonance conditions using the free energy of the system. This idea was first proposed by Smit and Suhl [34, 35], and the basic ideas are the following: One important feature, is that the Landau-Lifshits (LL) equation conserves the magnitude of \mathbf{M} , i.e. the magnetization vector can be thought of as tracing the surface of a sphere. It then follows that rewriting the LL equation in spherical coordinates becomes natural:

$$\begin{aligned}\dot{\theta} &= \gamma(H_\phi + \alpha H_\theta) \\ \dot{\phi} \sin \theta &= -\gamma(H_\theta - \alpha H_\phi),\end{aligned}\tag{2.39}$$

with the spherical angles as defined previously in Fig. 2.2b. At the equilibrium orientation, the magnetization will be aligned along the effective field and the transverse components H_ϕ and H_θ vanish. However, when exciting the system with a microwave magnetic field, the magnetization is deflected away from the equilibrium orientation. The components H_ϕ and H_θ then act as restoring forces, with a strength determined by the slope of the free energy [25]:

$$\begin{aligned}H_\theta &= -\frac{1}{M_0} \frac{\partial E_{\text{tot}}}{\partial \theta} \\ H_\phi &= -\frac{1}{M_0 \sin \theta} \frac{\partial E_{\text{tot}}}{\partial \phi}.\end{aligned}\tag{2.40}$$

At the equilibrium orientation, $\partial E_{\text{tot}}/\partial \theta$ and $\partial E_{\text{tot}}/\partial \phi$ are zero, so a Taylor expansion of $\partial E_{\text{tot}}/\partial \theta$ and $\partial E_{\text{tot}}/\partial \phi$ determines the restoring force due to small displacements from equilibrium, $\delta \theta$ and $\delta \phi$. Using this, in combination with Eq. (2.40), in the equation of motion for the angular variables given by Eq. (2.39) results in a set of linear differential equations. Using the harmonic ansatz that $\delta \phi(t), \delta \theta(t) \propto e^{i\omega t}$, one can solve the equations to obtain the eigenfrequency ω_{res} [34, 35]:

$$\omega_{\text{res}} = \frac{\gamma}{M_0 \sin \theta} \sqrt{\left(\frac{\partial^2 E_{\text{tot}}}{\partial \theta^2} \frac{\partial^2 E_{\text{tot}}}{\partial \phi^2} - \left(\frac{\partial^2 E_{\text{tot}}}{\partial \theta \partial \phi} \right)^2 \right)},\tag{2.41}$$

where the double derivatives of the free energy with respect to the spherical coordinates are taken at the equilibrium orientation of the magnetization:

$$\left(\frac{\partial E_{\text{tot}}}{\partial \theta} \right)_{\theta=\theta_0, \phi=\phi_0} = \left(\frac{\partial E_{\text{tot}}}{\partial \phi} \right)_{\theta=\theta_0, \phi=\phi_0} = 0.\tag{2.42}$$

The advantage of this approach is that it is applicable to a wide range of magnetic systems with different expressions for the free energy. To find the resonance frequency of a given system, one needs an expression for the free energy as a function of the orientation of the magnetization. As an example, consider the free-energy density of the elliptical ferromagnet introduced in section 2.1.6, where $E_{\text{tot}} = E_{\text{Zeeman}} + E_{\text{Demag}} + E_{\text{Anis}}$. This system has contributions from the external field, as well as both shape anisotropy and a cubic magnetocrystalline anisotropy. Using the Smit-Suhl approach, one can then calculate the resonance frequency directly from Eq. (2.41) to obtain:

$$\begin{aligned} \left(\frac{\omega}{\gamma}\right)^2 &= \left[H \cos(\phi - \phi_H) \right. \\ &\quad \left. + \mu_0 M_s \left(N_z - \left(\frac{N_x + N_y + (N_x - N_y) \cos 2\phi}{2} \right) \right) + \frac{H_k}{4} (3 + \cos 4\phi) \right] \\ &\quad \times \left[H \cos(\phi - \phi_H) + H_k \cos 4\phi + \mu_0 M_s (N_y - N_x) \cos 2\phi \right], \end{aligned} \tag{2.43}$$

where the expression has been simplified by assuming that the magnetization is oriented in the film plane, $\theta = \pi/2$, and the anisotropy field $H_k = 2K_1/M_0$ has been introduced. Eq. (2.43) illustrates that the Smit-Suhl approach provides a way of calculating the resonance conditions for the general case of a ferromagnetic sample containing both magnetocrystalline anisotropy as well as shape anisotropy through the demagnetization factors N_i . In this example, the calculation was performed for an elliptical sample with a cubic crystalline anisotropy. In the expression for the resonance frequency given by Eq. (2.43), one can clearly identify terms with a four-fold symmetry ($\propto \cos 4\phi$) from the cubic crystalline anisotropy, in addition to terms with a two-fold symmetry ($\propto \cos 2\phi$) from the shape anisotropy along the long/short axis of the ellipse. This example of the interplay between magnetocrystalline and shape anisotropies is taken from paper IV of the thesis, and for further details I refer to the appended paper in chapter 9.

2.2.6 Inhomogeneous spin precession: Spin waves

To this point, we have only considered the precession motion of the magnetization where all spins rotate in uniform. Excitations with a finite phase shift between neighboring spins however, known as spin waves, represent the lowest-energy excitation compared to the uniform mode [22]. The spin wave is characterized by a wavevector k , determined by the wavelength λ as illustrated in Fig. 2.10. The energy of these spin waves will differ from that of the uniform precession due to a combination of exchange interaction and the dipolar interaction between neighboring dipoles. Long wavelength spin waves however, carry very little energy because the difference in direction between neighboring dipoles is very small.

The spin-wave frequency is given by the spin-wave dispersion, $\omega(k)$, which will be derived in the following. In the derivation of $\omega(k)$, a uniform precession through the thickness of the film is assumed, as in the thickness regime of interest here (thin films), spin waves with components of k perpendicular to the plane will have very high energy compared to the uniform $k = 0$ mode due to the strong exchange interaction. We start from the LL equation, $d\mathbf{M}/dt = \gamma\mathbf{M} \times \mathbf{H}$, with magnetostatic fields given by [47]:

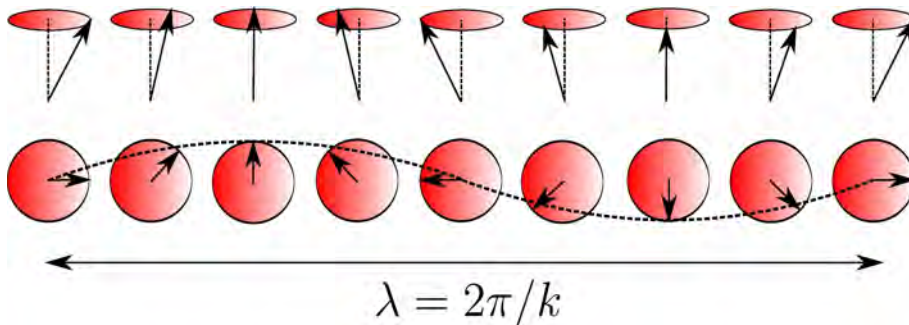


Figure 2.10: Illustration of the precession of a spinwave. The wavevector k is given by the wavelength λ through the relation. $k = 2\pi/\lambda$.

$$H_y^D(\mathbf{k}) = -N_k M_y(\mathbf{k}), \quad (2.44)$$

$$H_{x,z}^D(\mathbf{k}) = -\mathbf{k}[M_x(\mathbf{k})k_x + M_z(\mathbf{k})k_z](1 - N_k)/|k|^2, \quad (2.45)$$

where $N_k = [1 - \exp(-kd)]/kd$, and d is the film thickness. The resulting spin-wave dispersion is then given by [48]:

$$\begin{aligned} (\omega(k)/\gamma)^2 &= [H_i + Dk^2 + M(1 - N_k) \sin^2 \theta_k] \\ &\quad \times [H_i + Dk^2 + MN_k \cos^2 \phi + M(1 - N_k) \sin^2 \phi \cos^2 \theta_k] \\ &\quad - [M(1 - N_k) \cos \theta_k \sin \theta_k \sin \phi]^2, \end{aligned} \quad (2.46)$$

where H_i is the internal static field, D is the spin-wave stiffness and the angles are as defined in Fig. 2.11a.

As an example, the calculated spin-wave spectrum for a 10 nm thick Permalloy film is shown in Figs. 2.11b-d. In Fig. 2.11b, for the magnetization oriented in the sample plane, a static external field of 100 mT is assumed, which gives a resonance frequency of ≈ 9.7 GHz for the uniform $k = 0$ mode. In Figs. 2.11c-d, the static external field has been adjusted to take into account the static demagnetization fields in these geometries, in order to keep the uniform mode at the same frequency for easier comparison between the figures.

The spin-wave frequency depends on both the spin-wave propagation direction and wavelength, given by the wavevector \mathbf{k} , and the orientation of the magnetization. The calculated spin-wave spectrum is shown for the magnetization oriented in the sample plane ($\phi = 0$), 45 degrees out-of-plane ($\phi = 45$) and completely out-of-plane ($\phi = 90$). In Figs. 2.11b-c the spin-wave frequency is lowest for propagation along the magnetization direction ($\theta_k = 0$), and highest for propagation perpendicular to the magnetization ($\theta_k = 90$). For the magnetization oriented completely out-of-plane, the spin-wave frequency is independent of propagation direction (assuming an infinitely extended thin film in this case).

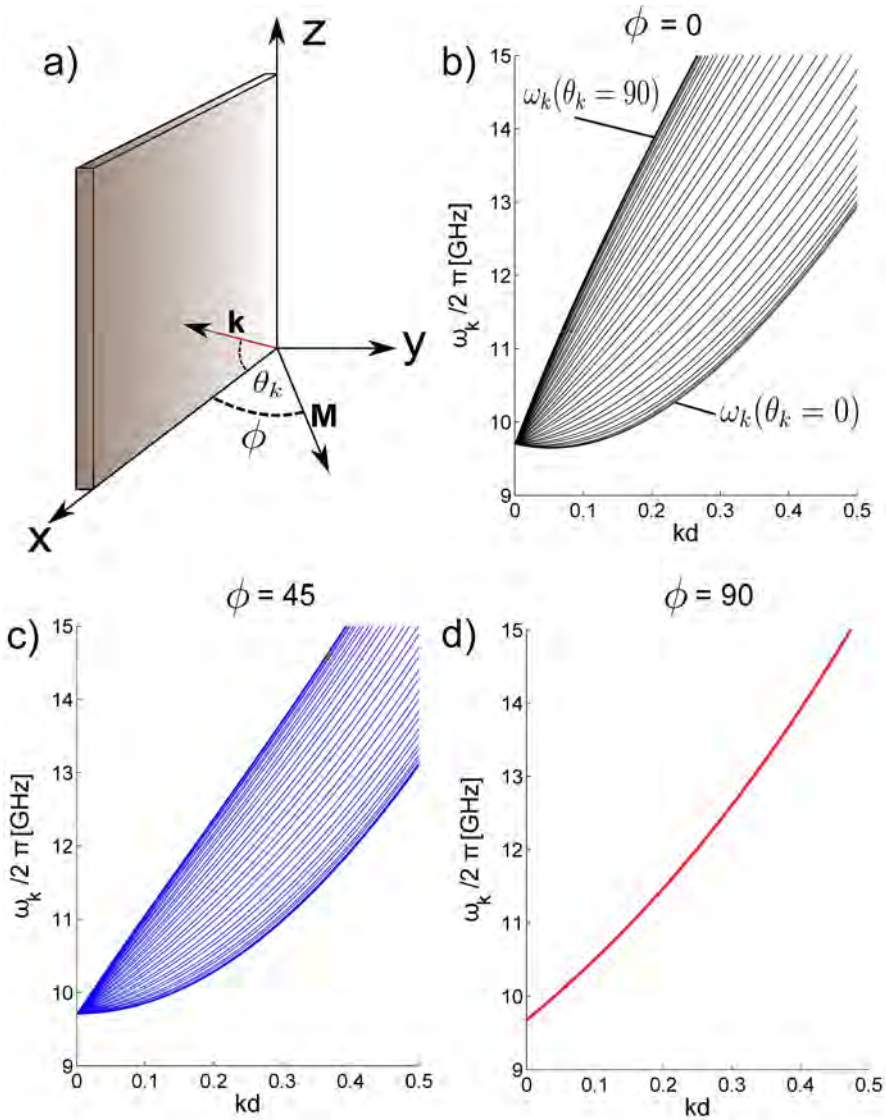


Figure 2.11: a) Geometry of a thin film where the magnetization \mathbf{M} is oriented in the x - y plane and the spin-wave wavevector \mathbf{k} lies in the x - z plane. b) Spin-wave spectrum given by Eq. (2.46) for the magnetization oriented along $\phi = 0$, c) $\phi = 45$ and d) $\phi = 90$.

The study of spin waves is at the focus of an emerging field of modern magnetism, namely that of magnonics. Magnonics combines waves and magnetism, where its main aim is to investigate the behavior of spin waves in nano-structure elements. See e.g. [19] and references therein for a nice overview of this field of research. The excitation of spin waves due to inhomogeneous microwave fields is also briefly discussed in paper III of the thesis, in that case caused by induced microwave eddy currents in conductive samples.

Another important consideration is the scattering from the uniform $k = 0$ mode into degenerate spin-wave modes through two-magnon scattering, which can be a significant contribution to the FMR linewidth. The various contributions to the linewidth will be introduced in the following section, and is also discussed in paper I of the thesis where we investigate the magnetodynamic damping in $\text{La}_{0.7}\text{Sr}_{0.3}\text{MnO}_3$ films.

2.2.7 Magnetodynamic damping

The magnetodynamic damping is one of the key material parameters governing the magnetodynamic properties. In the LLG equation this was introduced merely as a phenomenological damping parameter α , and the physical mechanisms behind the damping was not discussed further. There are several processes which can cause dissipation of energy, commonly divided into intrinsic and extrinsic processes.

As an example, the measured FMR linewidth for a 15 nm thick $\text{La}_{0.7}\text{Sr}_{0.3}\text{MnO}_3$ film is shown in Fig. 2.12 (data taken from paper I of the thesis). The linewidth, measured here in terms of field rather than frequency, can be separated into a frequency independent contribution ΔH_0 and a term proportional to the Gilbert damping parameter α [49]:

$$\Delta H = \frac{4\pi}{\gamma} \alpha f_{\text{mw}} + \Delta H_0. \quad (2.47)$$

The intrinsic Gilbert damping is a measure of the microscopic mechanism by which the absorbed microwave energy is transferred from the spin system to the lattice, and is proportional to the precession frequency. It is

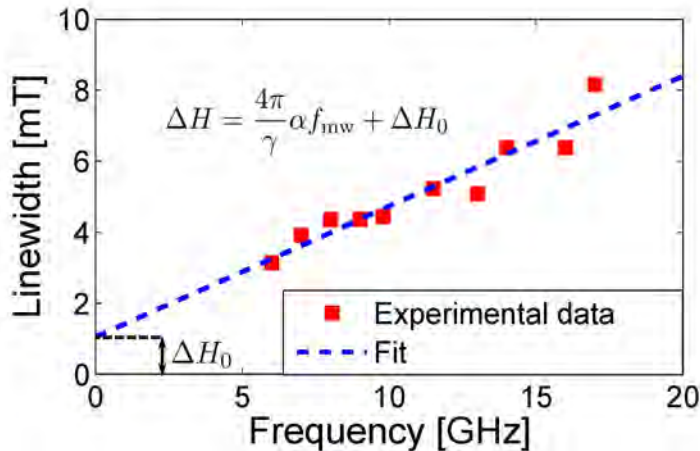


Figure 2.12: Example of measured FMR linewidth, separated into the inhomogeneous broadening ΔH_0 and a term proportional to the damping parameter α and precession frequency f_{mw} .

commonly assumed that the origin of intrinsic Gilbert damping is the spin-orbit (SO) coupling [50]. This relativistic effect leads to spin-flip scattering of electrons, which results in transfer of angular momentum from the spin system to the lattice.

However, in addition to the intrinsic Gilbert damping, the measured FMR linewidth consists of several additional contributions from e.g. two-magnon scattering, eddy-current damping and an inhomogeneous linewidth broadening [25]. In the following, we will briefly go through these various contributions and how they affect the measured FMR linewidth.

Two-magnon scattering

The two-magnon scattering contribution to the linewidth represents the loss due to scattering from the uniform FMR mode into degenerate spin-wave modes. In a uniform film, the normal modes can be described as a uniform precession mode which couples to the microwave excitation field,

and a manifold of spin-wave modes (as discussed in section 2.2.6) which are not directly excited. Non-uniformities in the sample induce a coupling between these modes, leading to a broadening of the resonance.

The two-magnon contribution to the damping treats non-uniformities in the sample as perturbations, causing transitions from the uniform mode to spin-wave modes [51]. The scattering rate for this transition can be written as [52]:

$$\lambda = \frac{2\pi}{\hbar} \sum_k |A_k|^2 \delta(\hbar\omega_0 - \hbar\omega_k), \quad (2.48)$$

where A_k is the coupling coefficient between the uniform precession and the spin-wave modes. As λ represents the decay of a population of $k = 0$ magnons, it also represents a contribution to the FMR linewidth of the driven uniform precession.

As expressed through the delta function in Eq. (2.48), the scattering process from the uniform mode into spin-wave modes is dependent on actually having degenerate spin-wave modes to scatter into. This can be illustrated by taking a closer look at the spin-wave spectrum for the 10 nm thick Permalloy film discussed in section 2.2.6. For the magnetization oriented in the sample plane (Fig. 2.13a), one notices that there are several spin-wave modes that are degenerate with the uniform $k = 0$ mode. This overlap of modes opens up the possibility of scattering into a mode with e.g. wavevector $\bar{\mathbf{k}}$. The scattering can be caused by a perturbation in the system due to defects/scattering centers of a length scale L , given by $\bar{k} = 2\pi/L$. In the context of thin films, this can e.g. be caused by inhomogeneities and defects at the sample surface, and two-magnon scattering is an effect which is usually more pronounced in thin films.

As two-magnon scattering is dependent on having degenerate modes to scatter into, this means one can suppress the effect by reducing the number of available modes. As illustrated in In Fig. 2.13b, applying a sufficiently strong external magnetic field in order to orient the magnetization out of the sample plane will strongly affect the spin-wave spectrum. As an example, one notices that with the magnetization oriented at an angle of 45 degrees

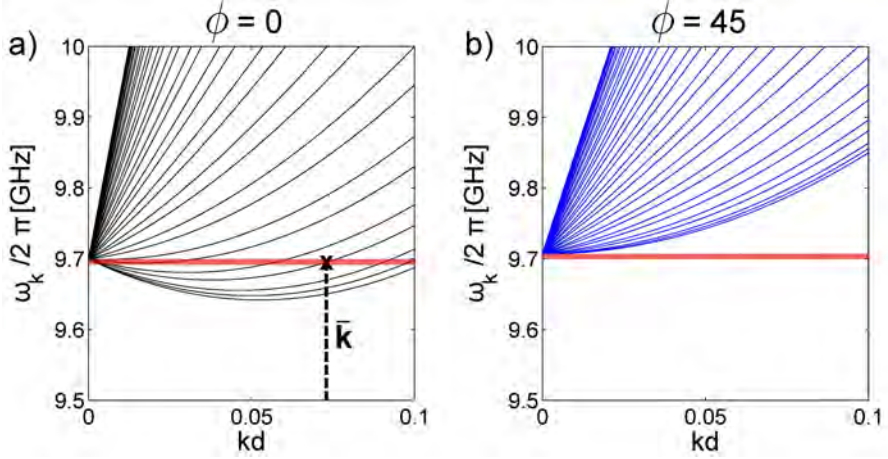


Figure 2.13: Spin wave spectrum for the magnetization oriented a) in the sample plane b) 45 degrees out of plane. The uniform $k = 0$ mode is indicated by the red line at 9.7 GHz. Overlap between the modes allows for scattering of the uniform mode into a spin-wave mode with wavevector $\bar{\mathbf{k}}$.

out of plane, there are no degenerate modes for the uniform $k = 0$ mode to scatter into. Orienting the magnetization out of the sample plane is thus an effective way of suppressing two-magnon scattering, and can be used in experiments in order to investigate the various contributions to the FMR linewidth.

Eddy-current damping

Another contribution to the damping in conductive samples, is the dissipation due to induced eddy currents. According to Faraday's law, a time varying magnetic flux induces an AC voltage in any conductive material [23]. An applied microwave magnetic field and the precessing magnetization in a conductive ferromagnet will thus induce AC currents in both the ferromagnet and any adjacent conductive layers. The dissipation of the eddy currents give rise to an additional damping of the magnetization precession, which is named eddy-current damping [53]. For the uniform FMR

mode, this additional damping contribution is given by [54]:

$$\alpha_{\text{eddy}} = \frac{C}{16} \frac{\gamma \mu_0^2 M_s \delta^2}{\rho}, \quad (2.49)$$

where ρ is the resistivity, M_s the saturation magnetization, μ_0 the vacuum permeability, γ the gyromagnetic ratio and δ the sample thickness. The constant C is a correction factor to account for details of the spatial profile of the induced eddy currents. The eddy-current damping scales with the thickness as δ^2 , and for highly conductive samples the eddy-current contribution becomes dominating for sample thicknesses of more than a few 10s of nm. In thin films of a few nm thickness however, the eddy-current damping is usually small in comparison with other contributions to the damping.

Even if the contribution to the damping is negligible, induced eddy currents in the sample can still have other effects, like spin-wave excitations due to inhomogeneous microwave fields and microwave screening effects. See also sections 2.2.4 and 5.2 as well as papers II and III of the thesis for an overview of eddy-current effects on FMR.

Inhomogeneous broadening

As the name suggests, inhomogeneous broadening originates from sample inhomogeneities. This could e.g. be spatial variations in the sample magnetization and anisotropies (both magnetocrystalline and shape anisotropies). The FMR frequency is determined by the effective magnetic field \mathbf{H}_{eff} (as introduced in section 2.2.3), and any spatial variations in the effective field will thus cause slight variations in the resonance frequency in various regions of the sample.

As an illustration of how an inhomogeneous sample would affect the FMR linewidth, the calculated absorption for a sample where the resonance frequencies ω_i vary across the sample, $\omega_{\text{res}} = \omega_0 \pm \delta\omega$, is shown in Fig. 2.14. For the sake of illustration, a quite large inhomogeneity is assumed, with a random distribution of $\delta\omega$ in the range $\delta\omega/\omega < 5\%$. The FMR absorption can then be considered as a superposition of several resonances occurring

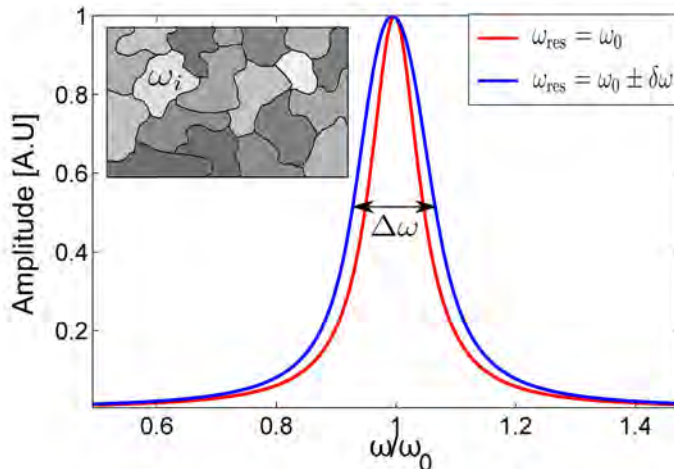


Figure 2.14: Red: Example of FMR absorption in a homogeneous sample. Blue: FMR absorption in an inhomogeneous sample modeled as a superposition of resonances occurring at slightly different frequencies, leading to an increase in the absorption linewidth. Inset: Illustration of an inhomogeneous sample where the resonance frequency, ω_i , vary across the sample.

at slightly different frequencies, which results in an apparent broadening of the FMR linewidth.

2.2.8 Spin-transfer torque

When confined to the nanoscale, the interplay between the spin and charge of electrons becomes important. On length scales similar to or smaller than the spin-diffusion length ($\approx 10^{-9} - 10^{-6}$ m [55]), the spin of the electron becomes conserved and a charge current can be considered as a sum of individual contributions from spin-up and spin-down channels. The spin dependent transport properties makes it possible to manipulate the individual spin channels, and this is the principle behind the giant magnetoresistance effect (GMR). The GMR is the change in resistance that is observed in magnetic multilayers of alternating ferromagnetic and non-magnetic layers

when the relative orientation of the magnetization in the ferromagnetic layers differ. The discovery of the GMR effect awarded Albert Fert and Peter Grünberg the 2007 Nobel prize in physics [8]. In addition to being interesting from a physics viewpoint, the GMR effect also has several important applications in e.g. magnetic field sensors in hard disc drives, biosensors, microelectromechanical systems (MEMS) and other devices [9].

However, the interplay between the spin and charge of electrons in magnetic multilayers is not limited to the effects of spin-dependent scattering on the total charge current. The inverse effect, how the layer magnetization will be affected by the spin-dependent scattering of a spin polarized current was predicted by Slonczewski and Berger in 1996 [14, 15]. This effect, named "spin-transfer torque" (STT) can cause a steady-state precession of the magnetization, excitation of spin waves, and may even result in a full reversal of the layer magnetization [16, 17]. This current-induced switching of the magnetization is particularly interesting for magnetic memory applications [18] (e.g. STT-based magnetic random access memory, STT-MRAM). The current-induced magnetization precession also enables magnetic nanostructures as a new type of tunable microwave oscillators, namely spin-torque oscillators (STO). Current controlled STO are potential generators of high frequency microwave signals, which is of interest within e.g. telecommunication technologies [20]. See also section 5.4, as well as paper V of the thesis and references therein for an introduction to STO.

The main prediction by Slonczewski, is the transfer of spin angular momentum between the layers caused by a current flowing through a magnetic multilayer. This transfer of spin angular momentum exerts a torque on the magnetic moment, causing a precession or even complete reversal of the layer magnetization. For a current flowing from the fixed layer to the free layer, the spin-polarized electrons will be scattered at the interface of the magnetic free layer. From the conservation of angular momentum, this spin-dependent scattering will transfer spin angular momentum to the free layer. The transfer of spin angular momentum results in a torque acting to align the magnetization of the free layer in parallel to that of the fixed layer, as illustrated in Fig. 2.15.

By reversing the current direction, electrons are first polarized in the

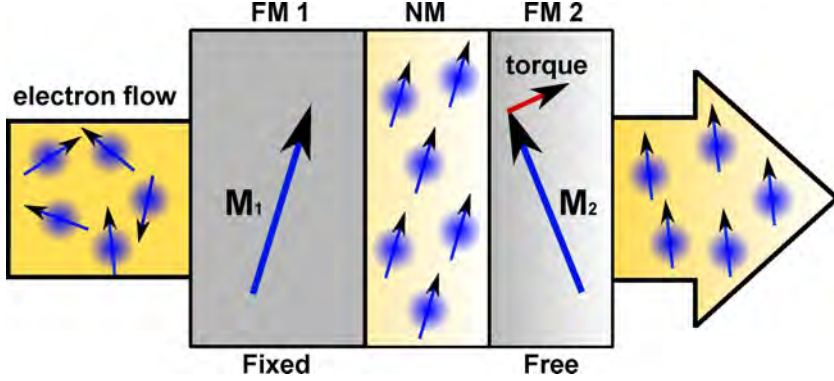


Figure 2.15: Schematic illustration of spin-transfer torque. Electrons flowing through the fixed layer become spin polarized and exert a torque on the magnetization in the free layer.

free layer and consequently scattered at the interface of the fixed layer. However, due to the greater magnetic hardness of the fixed layer, electrons of spin antiparallel to the fixed layer are reflected back to the free layer. From the conservation of angular momentum, this process exerts a torque on the free layer that tries to orient it anti-parallel to the fixed layer. This means that the direction of the current controls the stability of the relative alignment of the magnetization in the fixed and free layer.

Spin-transfer torque may be described micromagnetically through adding an additional term to the LLG equation [56]:

$$\frac{d\mathbf{M}}{dt} = \underbrace{-\gamma\mathbf{M} \times \mathbf{H}_{\text{eff}}}_{\text{Gyration}} + \underbrace{\frac{\alpha}{M_s} \left[\mathbf{M} \times \frac{d\mathbf{M}}{dt} \right]}_{\text{Damping}} - \underbrace{\frac{\chi}{d} JP(\theta)[\mathbf{M} \times (\mathbf{M} \times \mathbf{m}_f)]}_{\text{Spin Transfer Torque}}. \quad (2.50)$$

Here, $\chi = g\mu_b/(2M_s^2e)$, J is the charge current density and d the free layer thickness. $P(\theta)$ is a polarization function assumed to increase with the relative angle θ between the magnetization of the free layer and the fixed layer and \mathbf{m}_f is a unit vector in the direction of the magnetization of the fixed layer.

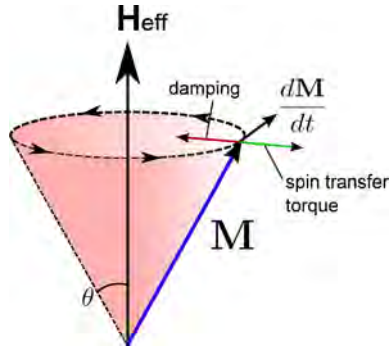


Figure 2.16: Schematic of the precession of the magnetization \mathbf{M} around the effective magnetic field \mathbf{H}_{eff} . The viscous damping given by the Gilbert damping parameter α pushes the magnetization in the direction of the effective field. The spin-transfer torque can act effectively as an "anti-damping" term, depending on the current direction and orientation of the magnetization of the fixed layer.

From the form of the STT-term in the LLG equation, it can either enhance or counteract the damping, depending on the current direction and orientation of the magnetization of the fixed layer. This results in the possibility of inducing a constant precession motion, or even a complete reversal of the free layer magnetization. By comparing the relative strengths between the damping term and the STT term, one can estimate the critical current needed to induce such excitations. The required current densities are generally quite high, and experimental observations are typically performed at current densities of the order $10^7 - 10^9$ A/cm² [57]. Such high current densities are only obtainable in point contact geometries with radiuses of the order 1-100 nm in order to avoid melting the contact due to Joule heating. Advances in nanostructuring however, has increased the possibilities of utilizing STT in physically realizable systems such as STT-MRAM and STO as mentioned previously, which are intensely studied topics in modern magnetism. See e.g. refs. [20, 56, 57] and references therein for an overview.

Chapter 3

Micromagnetic simulations

Micromagnetics as a field deals with the behavior of (ferro)magnetic materials on length scales where the atomic level theory can be approximated by a simpler micromagnetic theory. In micromagnetics, the magnetization is represented by a continuous function of position, and each spin is represented as $\mathbf{M} = M_s \mathbf{m}$, where M_s is the saturation magnetization and \mathbf{m} is the local direction of the magnetic spin [26]. This approach requires slow variations of the magnetization, on length scales such that the direction angles of the atomic spins can be approximated by a continuous function. The continuous magnetization field is a common parameter in classical electrodynamics [23]. Micromagnetism extends the classical field theory by non-classical effects such as exchange interaction, where these effects are expressed in the framework of a continuum theory. Due to the combination of classical field theory and quantum mechanical effects, micromagnetism is often referred to as a semi-classical continuum theory.

The goal of micromagnetics is to determine the local magnetization everywhere in the sample, when different components of the effective field are present. The application of numerical micromagnetics was first used as a static method in order to calculate the equilibrium orientation of the magnetization in the absence of any applied field. The goal of this method is to find the full spatial distribution of the local magnetization $\mathbf{m}(x, y, z)$ which

minimize the total free energy of the system. This energy minimization yields the equation $\mathbf{m} \times \mathbf{H}_{\text{eff}} = 0$, named Brown's magnetostatic equation [26]. This equation shows that the spins are subject to a torque given by the local effective field, where this torque equals zero at the static equilibrium configuration.

The main focus of this thesis is on the magnetodynamic properties, but it turns out that for both static and dynamic micromagnetics, the main problem to solve is that of determining the local effective field. The magnetization dynamics is described by the LLG equation (as introduced in section 2.2.2), which contains the effective field, \mathbf{H}_{eff} , governing the precession motion of the magnetization. In section 2.2.3, the effective magnetic field was defined as the field derivative of the free energy, $\mathbf{H}_{\text{eff}} = -\partial E_{\text{tot}}/\partial \mathbf{M}$. The main magnetic interaction energies was introduced in section 2.1, and includes exchange, magnetocrystalline anisotropy, demagnetization and Zeeman energy. The main objective of the micromagnetic simulation is thus to calculate the free energy of the system and obtain the local effective field governing the magnetic state. This is not at all a trivial task, and in particular calculating the contribution from the demagnetization energy is demanding and computationally time consuming due to the long range dipolar interaction.

3.1 Numerical solution of the LLG equation

The numerical solution of the LLG equation in the micromagnetic solver used in this thesis (MuMax3 [58]) employs a finite difference discretization of the magnetized region of space, using a 2D or 3D grid. When dividing the magnetized region into a grid, it is important to consider an important characteristic length scale of the material, namely the exchange length. The exchange length, as defined in section 2.1.5, describes the competition between exchange and anisotropy energies: $l_{\text{ex}} = \sqrt{A/K}$ [29], where A represents the exchange stiffness and K the magnetocrystalline or demagnetization energy. These exchange lengths limit the grid size employed in the micromagnetic model, which should be less than l_{ex} . As an example,

the exchange length of Permalloy is $l_{\text{ex}} \approx 5$ nm [30], imposing an upper limit for the grid size used in micromagnetic simulations of this material.

The volumetric quantities such as the magnetization and effective field are treated at the center of each cell in the grid, whereas coupling quantities such as exchange interaction are considered at the faces between the cells [58]. The micromagnetic solver then solves the LLG equation numerically using the local magnetization and effective field within each grid cell to obtain the magnetization \mathbf{M} for the whole magnetized region.

3.2 Simulation of FMR spectra

The main experimental technique utilized in this thesis for the investigation of magnetization dynamics is that of ferromagnetic resonance spectroscopy (FMR). Thus, being able to perform micromagnetic simulations of FMR spectra is beneficial in order to gain a better understanding of experimental results. Experimentally, the FMR is excited by a microwave magnetic field. The microwave field can either be of variable frequency while keeping the external static magnetic field fixed, or the microwave frequency can be kept constant and the magnitude of the external field swept to locate the resonances (see also sections 2.2.3 and 4.2 for an introduction to FMR spectroscopy).

An approach similar to that performed experimentally is also possible to perform in the micromagnetic simulations, with a microwave field of varying frequency as the perturbing field. This is however quite time consuming, as one needs to scan the full frequency range for each value of the applied static field in order to locate all the resonances. To obtain the full field vs. frequency map of the resonances, we rather used a field relaxation process as follows: The system is first initialized at zero applied field to obtain the magnetic ground state configuration. If a static field, \mathbf{H}_0 , is applied, the simulation is run until the system reaches the new ground state configuration. A 10 mT perturbation field, \mathbf{H}_p , is then applied along the z-axis (out of the sample plane), and the simulation is run until it reaches the ground state configuration for the field $\mathbf{H}_0 + \mathbf{H}_p$. The perturbing field

is then switched off, allowing the system to relax. This perturbation causes oscillations of the magnetization around the equilibrium position with a maximum deviation of approximately 1 degrees, avoiding any non-linear effects [59]. To obtain the resonance frequencies, we calculate the Fourier power spectrum of the m_z component the first 10 ns of the magnetization relaxation. The various excitation modes of the system will then appear as distinct peaks in the Fourier spectrum [60].

The experimental analog to this technique is that measured using a pulsed inductive microwave magnetometer (PIMM) [61]. PIMM uses a coplanar waveguide (similar to the broadband FMR setup introduced in section 4.2.2) as both a source of fast pulsed magnetic fields and as an inductive sensor for the magnetic response from the sample. A sampling oscilloscope is used to acquire the data, and using fast Fourier transform (FFT) analysis of the step-response data one can obtain the resonances of the sample.

As an example, the results of a micromagnetic simulation of a 10 nm thick Fe ellipse of lateral dimensions 150×450 nm are show in Fig. 3.1. Applying an external magnetic field of sufficient strength along the short axis of the ellipse, the magnetization orients itself along the direction of the applied field, except along the sample edges where the contribution from the demagnetization energy tries to minimize the magnetic stray fields (Fig. 3.1a). This behavior is in agreement with what one would expect from the previous discussion on demagnetization fields in section 2.1.3.

Rather than the static magnetic configuration, we are now interested in the magnetodynamic properties. The various magnetic excitation modes of the system can be investigated using the field relaxation process described previously. Applying a perturbation field along the z -axis causes oscillations of the magnetization around the equilibrium orientation, as illustrated in Fig. 3.1b. Calculating the Fourier spectrum of the magnetization oscillations, one notices several peaks corresponding to the various excitation modes of the system. The excitation modes indicated in Fig. 3.1c correspond to bulk modes located in the interior of the ellipse, in addition to edge modes that are localized along the sample edges.

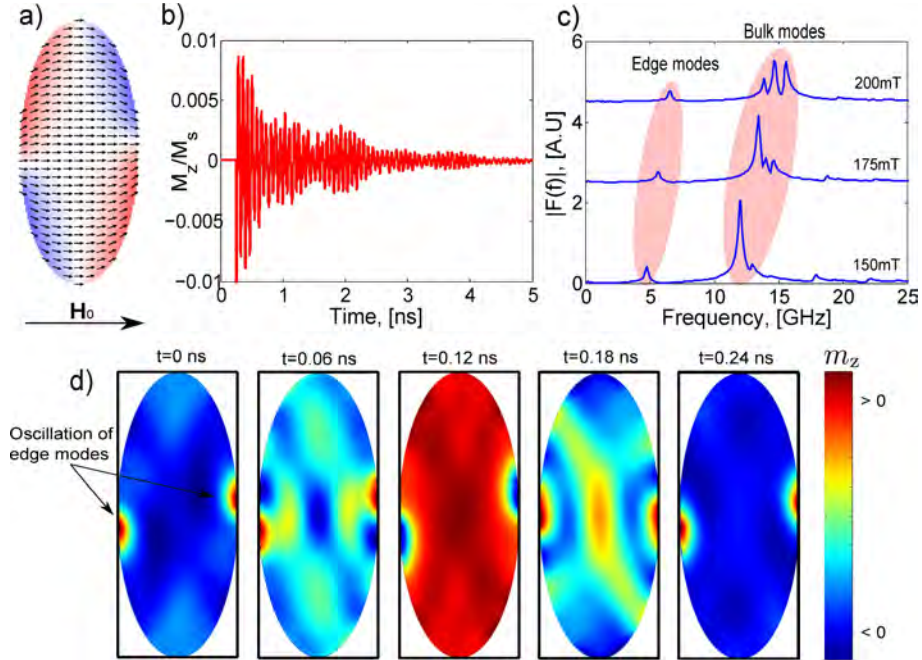


Figure 3.1: a) Magnetic state of a 10 nm thick Fe ellipse of lateral dimensions 150×450 nm for a magnetic field applied along the short axis of the ellipse. Arrows indicate the orientation of the magnetization, and the color scale indicate the m_y component along the long axis of the ellipse. b) m_z component of the magnetization after the excitation pulse. c) Fourier spectrum of the m_z component during the first 10 ns of the magnetization relaxation, showing the distinct excitation modes of the system. d) By plotting the spatial distribution of the m_z component, one can identify the edge modes as localized excitations at the sample edge.

The various modes can be identified by e.g. plotting the spatial distribution of the oscillations of the m_z component, as illustrated in Fig. 3.1d, where the edge modes are identified as localized excitations at the sample edge.

Following this approach for several values of the external static field one can obtain the full field vs. frequency map of the resonances, which in turn can be compared to the experimental FMR spectrum.

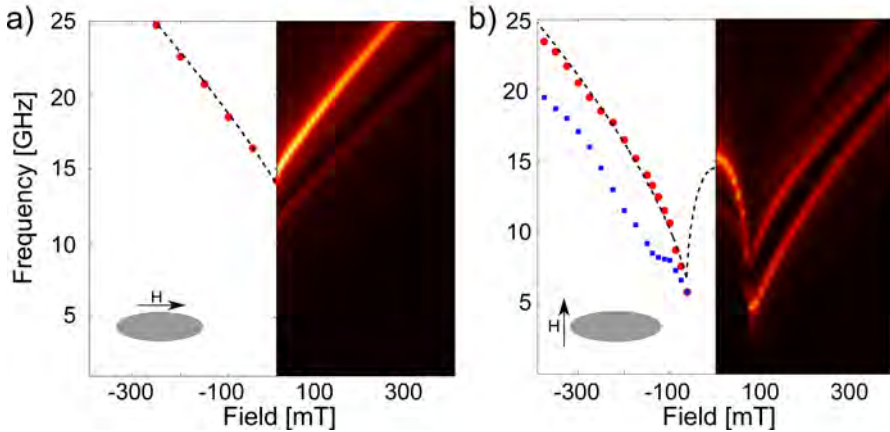


Figure 3.2: Results for the applied static field along the a) long axis and b) short axis of the ellipse. Left half: Experimental datapoints as red dots and blue squares for the main mode and edge mode respectively and analytical macrospin model as dotted black line. Right half: Micromagnetic simulations of the FMR spectrum.

As an example, Fig. 3.2 shows a comparison of the micromagnetic solution and experimental data-points (red dots and blue squares for the main mode and edge mode respectively) as well as an analytical macrospin model as dotted black line. These data are taken from paper IV of the thesis, and I refer to this paper for further details.

This example illustrates nicely that micromagnetic simulations are a valuable tool to gain a better understanding of experimental data. However, micromagnetic simulations are not limited only to this approach. Simulations can also be used for the benchmarking of analytical solutions to see if they provide accurate predictions, as well as for performing "numerical experiments", as they provide the possibility of investigating complex structures which might be time consuming or challenging to realize experimentally. This last approach is something we employed in the project which led to paper V of the thesis, where we investigate the synchronization of spin-torque oscillators (STO). Here, we performed "numerical experiments" of systems which are currently too complicated and time consuming to real-

ize experimentally, as well as using the simulation results as a benchmarking comparison for a simplified mathematical model for the coupled STO. For the applications of micromagnetic simulations in the study of these systems, I refer to paper V of the thesis for further details.

Chapter 4

Experimental techniques

In this chapter, I present the main experimental techniques used during the course of my PhD. I start with a brief introduction to the thin film deposition technique utilized for the deposition of the normal metal (NM) layers in the project that resulted in paper II of the thesis. I then move on to introducing FMR spectroscopy. This is the main experimental technique used, and in section 4.2 I introduce the FMR setups used in the projects that resulted in papers I, II, III and IV of the thesis.

4.1 Thin film deposition by DC magnetron sputtering

DC Magnetron sputtering is a physical vapor deposition (PVD) process, meaning that a target material is vaporized and transported in the form of a vapor to the substrate where it condenses, forming a coating layer [62]. A schematic of the sputtering setup is illustrated in Fig. 4.1.

The target material and the sample is placed in a vacuum chamber, where a voltage is applied between the sample and target, generating an electric field. The confining electric and magnetic field causes electrons to circulate in the field close to the target, creating a plasma region by ionizing the sputtering gas (generally an inert gas, here Argon (Ar)). The

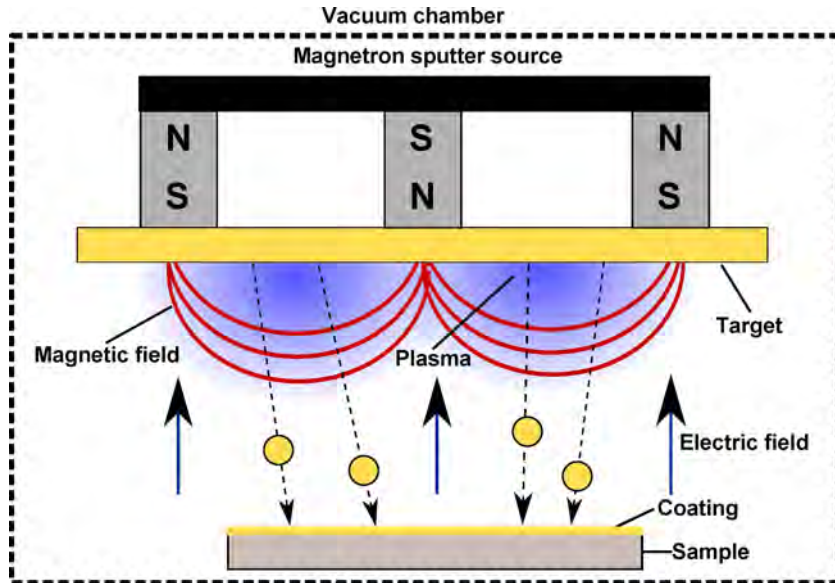


Figure 4.1: a) Schematic of the sputtering setup. Ionized Ar atoms bombard the target, ejecting target atoms which subsequently hit the substrate and coat the surface with a thin film of the target material.

Ar atoms are ionized and bombarded into the target, which leads to the ejections of atoms from the surface [62]. These ejected atoms will in turn hit the substrate and coat the surface with a thin film of the target material, where the deposition rate is controlled by the Ar pressure in the vacuum chamber and the applied plasma power.

The thickness of the deposited NM films (Au and Cu) in the project that resulted in paper II of the thesis was in the range 10 nm - 1 μm . The film thickness was monitored using a quartz crystal thickness monitor during the deposition and compared to thickness measurements using a profilometer subsequent to the deposition.

4.2 FMR experimental setup

Ferromagnetic resonance spectroscopy (FMR) is an important technique for the characterization of ferromagnetic samples, and probe static and dynamic properties of magnetic materials. The technique relies on measuring the microwave absorption associated to the precession of the magnetization, and can be used to extract valuable information about material parameters such as e.g. the effective magnetization, anisotropies and the magnetodynamic damping [25].

In an FMR experiment, a static magnetic field is applied in combination with an orthogonal microwave magnetic field. As previously discussed in section 2.2.3, this microwave magnetic field will induce a precession motion of the electron spins, provided that the frequency of the applied microwave field coincides with the ferromagnetic resonance frequency. As the resonance frequency is determined by the effective magnetic field, one can either vary the frequency of the microwave field at a fixed value of the external field, or keep the microwave frequency fixed and sweep the magnitude of the external field in order to change the resonance frequency. This latter field-sweep approach is the technique that has been utilized in this thesis, and the two different experimental setups used are presented in the following sections.

4.2.1 Cavity-based FMR

The cavity-based FMR measurements were performed using a commercial Bruker EleXsys E500 X-band EPR setup [63]. In this setup, the microwave frequency exciting the magnetization precession is kept at a fixed frequency (here 9.6 GHz), determined by the eigenmodes of the microwave cavity resonator coupled to a microwave source. A schematic of the FMR setup is illustrated in Fig. 4.2a. A microwave bridge housing a solid state radiation source is used to generate microwaves, and a waveguide connects it to the microwave cavity resonator [64]. The microwave cavity is impedance matched to the waveguide to ensure a maximal coupling. Thus, the microwave energy is mainly absorbed in the cavity and very little reflected

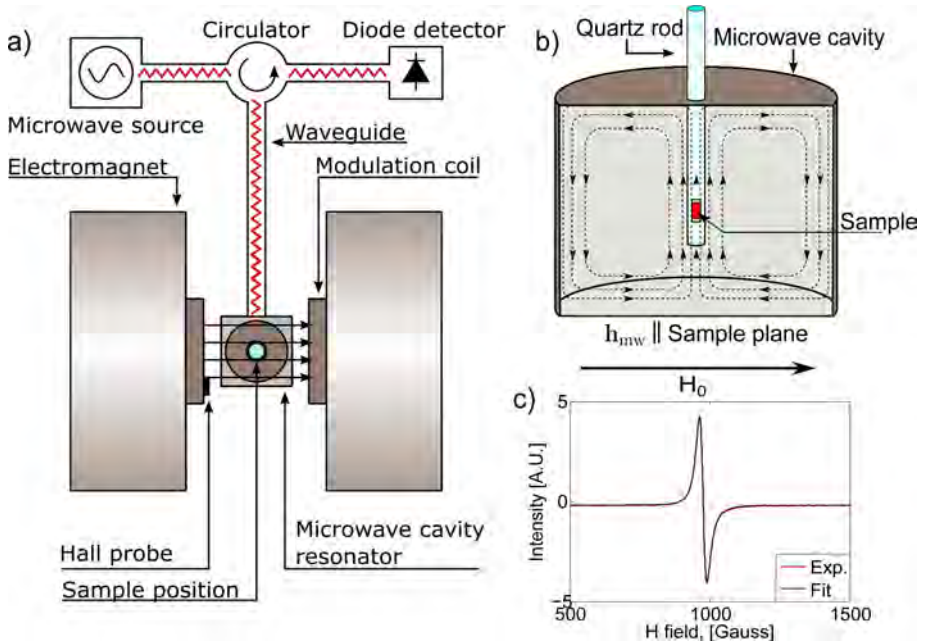


Figure 4.2: a) Schematic of the cavity based FMR setup. b) Schematic of the microwave cavity resonator. c) FMR absorption for a 10 nm thick Permalloy film and the fit to Eq. (4.2)

signal is measured at the detector diode. The microwave cavity is constructed in such a way that the standing microwave magnetic field within the cavity is located at the sample position [65], see Fig. 4.2b.

A static magnetic field perpendicular to the microwave magnetic field is provided by an electromagnet. The sample is attached to a quartz rod connected to a goniometer, allowing for a full 360 degrees rotation of the sample with respect to the external field. The field strength is swept to locate the ferromagnetic resonance while the microwave absorption in the sample is recorded by measuring the reflected microwave power from the cavity. When the resonance frequency of the sample coincides with the microwave frequency of the cavity, this causes a change in the cavity impedance. The

change in impedance results in more microwaves being reflected to the detector diode, thus providing a sensitive probe into the magnetic state of the system [65].

The measured absorption curve is proportional to the imaginary part of the magnetic susceptibility (see Eq. (2.24) in section 2.2.3 where the concept of FMR was introduced), and is often assumed to have a symmetric Lorentzian lineshape. However, in paper II and III of the thesis we show that in conductive samples, induced microwave eddy currents in the sample can affect the lineshape symmetry. In an experimental setup containing waveguides, coaxial cables etc., the relative phase between the electric and magnetic field components can also affect the lineshape [39, 40]. We thus fit the FMR absorption to a linear combination of symmetric and antisymmetric contributions, determined by the β parameter in Eq. (4.1).

$$\chi'' = A \frac{1 + \beta(H_R - H_0)/\Gamma_H}{(H_R - H_0)^2 + (\Gamma_H/2)^2}, \quad (4.1)$$

where A is an amplitude prefactor, H_R and H_0 are the resonance field and external field respectively and Γ_H the linewidth.

In order to increase the sensitivity of the measurements, a field modulation technique was used. Modulation coils are used to provide a small modulation of the static field for the use of lock-in detection [66]. The resulting recorded signal is then proportional to the field derivative of the susceptibility, and the experimental data was thus fitted to the derivative of Eq. (4.1) with respect to the external field, which is given by:

$$\frac{d\chi''}{dH_0} = A \left[\frac{-\beta/\Gamma_H}{(H_R - H_0)^2 + (\Gamma_H/2)^2} + \frac{2(H_R - H_0)[1 + \beta(H_R - H_0)/\Gamma_H]}{[(H_R - H_0)^2 + (\Gamma_H/2)^2]^2} \right]. \quad (4.2)$$

As an example, the measured FMR absorption for a 10 nm thick Permalloy film and the fit to Eq. (4.2) is shown in Fig. 4.2c

4.2.2 Broadband FMR

The broadband FMR experiments were performed using a vector network analyzer (VNA) setup in combination with a coplanar waveguide (CPW) that created microwave magnetic fields of variable frequency. A schematic of the setup is illustrated in Fig. 4.3a. A microwave current running through the center transmission line of the CPW produces a microwave magnetic field, \mathbf{h}_{mw} , as illustrated in Fig. 4.3b. The static external field, H_0 , was applied in the sample plane, and perpendicular to the microwave fields from the CPW.

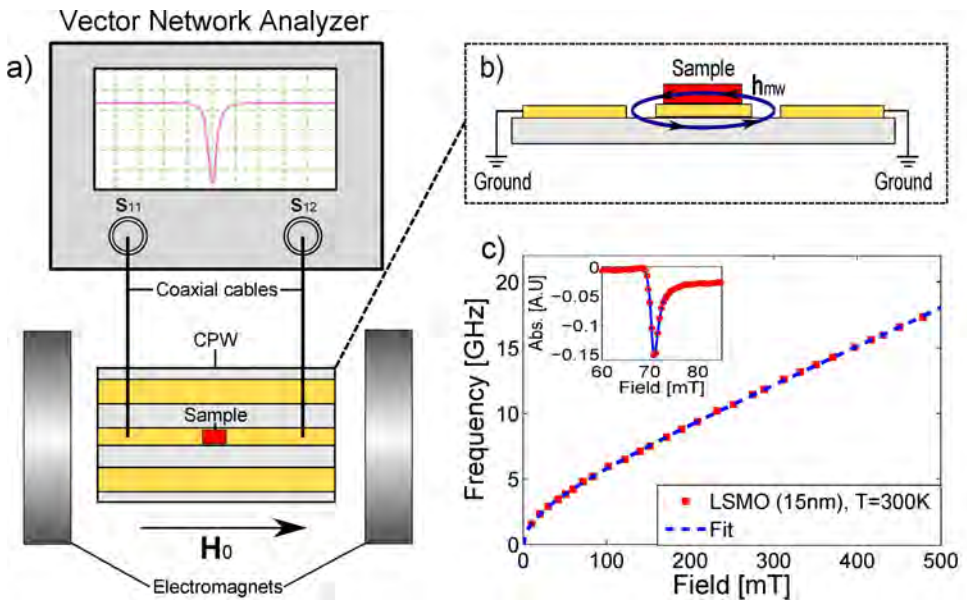


Figure 4.3: a) Schematic of the broadband FMR setup. b) Zoom in of the coplanar waveguide (CPW). c) Measured FMR dispersion for a 15 nm thick LSMO film (data taken from paper I of the thesis), with the fit to the Kittel equation as dotted line. A typical absorption lineshape and the fit to Eq. (4.1) is shown as inset.

The VNA compares the signal that leaves the analyzer with either the signal that is transmitted through the test device, or the signal that is reflected from the device input. Since it is difficult to measure the total current and voltage at high frequencies, the so-called S-parameters are used [67]. These can be used to determine common parameters such as gain, loss and reflection coefficients. The microwave transmission and reflection parameters (S_{12} and S_{11}) can then be measured as a function of the magnitude of the external field and microwave frequency in order to obtain a complete map of the ferromagnetic resonances [65].

By measuring the microwave absorption as a function of both microwave frequency and the applied external field, one can obtain the FMR dispersion. The field vs. frequency dispersion can be described by the Kittel equation (see Eq. (2.23) in section 2.2.3). As an example, the measured FMR dispersion for a 15 nm thick $\text{La}_{0.7}\text{Sr}_{0.3}\text{MnO}_3$ film is shown in Fig. 4.3c, with the fit to the Kittel equation as dotted line (data taken from paper I of the thesis). As mentioned in the previous section, the phase of the recorded signal depends on a number of external parameters. The absorption lineshape was thus fitted to a linear combination of symmetric and antisymmetric contributions, determined by the β parameter introduced in Eq. (4.1), and a typical lineshape and the fit to Eq. (4.1) is shown as inset in Fig. 4.3c

The advantage of the broadband FMR setup is the possibility of obtaining a full field vs. frequency map of the resonances, not being limited to a single frequency as with the cavity FMR setup. This becomes advantageous when e.g. characterizing a system which has multiple resonance modes, where tracking the frequency of the various modes as a function of the applied field can provide valuable information. See e.g. paper IV of the thesis, where we used a combination of broadband and cavity based FMR experiments to characterize the various resonance modes of elliptical ferromagnets of nanoscale dimensions.

The possibility of varying the microwave frequency is also a key ingredient for the ability of measuring the magnetodynamic damping parameter α , as introduced in section 2.2.7. By measuring the FMR linewidth vs. frequency, one can extract both α , which characterize the frequency depen-

dent contribution to the damping, as well as the inhomogeneous frequency independent contribution to the linewidth. Broadband FMR spectroscopy thus provides a way of measuring the damping parameter α , which is one of the key material parameters governing the magnetodynamic properties. For further details, see e.g. section 5.1 and paper I of the thesis, where we characterize the damping of $\text{La}_{0.7}\text{Sr}_{0.3}\text{MnO}_3$ films.

Chapter 5

Main research topics

This thesis consists of a collection of work performed on various systems, but with the overall aim of providing new knowledge on the magnetization dynamics in systems confined to nanoscale dimensions. In this chapter, I want to provide a brief motivation to why we have chosen to perform the studies that resulted in the papers included in this thesis. In doing this, I introduce a general overview of the main research topics and explain how the findings presented in this thesis are relevant with respect to ongoing research. In addition, I include a brief summary of the papers that resulted from these studies.

5.1 Magnetodynamic damping in ferromagnetic thin films

As the switching times of current magnetic applications approach the sub-ns regime, the intrinsic time scale of the magnetization dynamics is defined by the gyrotropic precession of the individual magnetic moments. Both static and dynamic behavior depends on the properties of the magnetic film. In response to excitations with fast varying magnetic fields, follows fundamental magnetodynamic phenomena like the movement of domain walls and switching of the magnetization [68, 69, 70]. Fundamental questions on the dissipation and magnetization damping are thus of great interest, and are intensely studied.

From a practical point of view, the most attractive materials are polycrystalline magnetic metals and alloys, which are well suited to nanofabrication techniques. Among the metallic ferromagnets, Permalloy is currently the most widely used material and is one of the prototype materials for magnetodynamic devices, with a reported damping parameter of $\alpha = 0.008$ [72]. For magnetodynamic applications, a low damping is desirable. A low damping means less dissipation of energy, which is important for several applications e.g. in magnonics, which concerns the behavior of spin waves (see e.g. ref. [19] for a nice review article). The propagation of spin waves depends crucially on a low dissipation, and the magnetic damping imposes a limit for the spin-wave propagation length due to the decay of the spin-wave amplitude.

When it comes to low magnetic damping, the insulating ferrimagnet Yttrium Iron Garnet (YIG) is often the material of choice. This provides the lowest magnetic damping recorded so far, with recently reported values of $\alpha \approx 7 \cdot 10^{-5}$ for a 20 nm thick film [73]. Although YIG is more challenging when it comes to nano-fabrication compared to other materials, fundamental insight into magnetization dynamics gained through the low damping is still transferable to other material systems. Due to this, YIG has proved to be a highly valuable material for the investigation of novel magnetodynamic phenomena. See e.g. refs. [71, 74, 75, 76] and references

therein for an overview.

For inducing a precession motion of the magnetization, or even magnetization reversal, using the aforementioned spin-transfer torque (STT) (as introduced in section 2.2.8), the damping is also a critical parameter [56]. The relative strength between the damping term and the STT term is determined by the damping parameter α and the spin current density. This means that by reducing α , one also reduces the critical current density. This is important for applications of the STT-effect, as the high current densities needed are only obtainable in point contact geometries in order to avoid melting the contacts due to Joule heating [56]. Understanding the various contributions to the magnetization relaxation is thus important, and the search for promising material systems with a low damping is an important research field.

One such group of interesting materials is the complex magnetic oxides. This source of materials exhibit intriguing phenomena such as e.g. Mott insulators, metal-insulator transitions, multiferroics and superconductivity (see e.g. refs. [77, 78, 79, 80] and references therein for an overview). The material properties of oxides are very sensitive to the structural parameters, and recent technical advances in synthesis of oxide heterostructures have provided a fertile new ground for creating novel states at their interfaces [79]. This sensitivity to structural parameters enables using thin film growth in order to engineer the magnetic properties [81], and the possibility of controlling the properties at the nm-scale makes the magnetic oxides an interesting material system for spintronics and other magnetic based applications.

Within manganites, $\text{La}_{0.7}\text{Sr}_{0.3}\text{MnO}_3$ (LSMO) has been regarded as one of the prototype model systems. Transport and static magnetic properties of LSMO are well studied, but less attention has been paid to the magnetodynamic properties. This motivates the study of LSMO as a material for magnetodynamic devices, and in doing this, characterizing the damping is one of the key properties. This is the main objective of paper I of the thesis, where we characterize the magnetodynamic damping in thin LSMO films as a function of film thickness and temperature. A summary of the main results are found in the following section, and for further details I refer to

the appended paper in chapter 9.

5.1.1 Summary of paper I

Vegard Flovik, Ferran Macià, Sergi Lendínez, Joan Manel Hernández, Ingrid Hallsteinsen, Thomas Tybell, Erik Wahlström.

Thickness and temperature dependence of the magnetodynamic damping of pulsed laser deposited $\text{La}_{0.7}\text{Sr}_{0.3}\text{MnO}_3$ on (111)-oriented SrTiO_3 .

J. Magn. Magn. Mater. 420, 280-284, (2016).

Here, we investigate the magnetodynamic properties of pulsed laser deposited LSMO films of thickness 10, 15 and 30 nm grown on (111)-oriented STO. By performing broadband FMR experiments in the temperature range 100-300 K we extract the magnetodynamic damping parameter α as a function of both temperature and film thickness, and find a minimum value of $\alpha \approx 0.002$. This damping is lower than that of e.g Permalloy ($\text{Ni}_{80}\text{Fe}_{20}$), which is one of the prototype materials for magnetodynamic devices. The low damping, in addition to other intriguing material properties and the possible coupling to the aforementioned functionalities provided by oxide electronics, indicate LSMO as a promising material for applications in magnetodynamic devices.

5.2 Eddy-current effects on ferromagnetic resonance

The microwave frequency spin dynamics in nanostructures usually involves stacks of layers combining ferromagnets (FM) and normal metals (NM) at the nanometer scale [10, 11, 19, 82]. Studies of magnetization dynamics in FM/NM structures are important within the field of microwave spintronics and magnonics, highlighted as an emerging research direction in magnetism [83]. In these structures, time varying magnetic fields will induce eddy currents in conductive layers. Eddy-current effects have often been neglected for film thicknesses below their skin depth (≈ 800 nm for Au at 10 GHz). However, the contribution of the microwave conductivity of magnetic multilayers has received increasing attention in recent years, indicating the importance of eddy-current effects also for NM films far below their skin depth [2, 3, 84, 85, 86, 87, 88, 89, 90, 91, 92, 93, 94, 95, 96].

In FM/NM bilayers, Maksymov *et al.* showed that the amplitude of the magnetization precession in the FM layer can be diminished by the shielding effect due to microwave eddy currents circulating in the NM layer [89]. A study by Kostylev also showed that in single layer and bi-layer metallic FM, the microwave screening effect results in a spatially inhomogeneous microwave field within the magnetic film [94]. The experimental manifestation of this is a strong response of higher order standing spin-wave modes due to the non-uniform microwave field across the thickness of the magnetic film.

The FMR in the FM layer is driven by the total microwave magnetic field. In conductive samples, depending on the field and sample geometry, this consists of both the external applied field and the Oersted fields from induced eddy currents. In paper II of the thesis, we show that induced eddy currents can strongly affect the FMR excitation and that the phase-shifted contribution from the induced microwave fields give rise to an asymmetry in the observed FMR lineshapes. This is relevant with respect to recent experiments, where differences in symmetry of the lineshapes have been used to study the spin pumping from a magnetic material to a normal

metal [41, 42, 43, 44, 45, 46]. In such studies, lineshape symmetry is one of the main parameters used to analyze the results. Hence, to correctly interpret experimental data involving FMR it is important to understand how eddy currents can affect the FMR excitation. This is the main focus of paper II of the thesis, where we perform a systematic study of how sample geometry and adding NM layers of various thicknesses affects the FMR lineshape.

However, rather than simply considering eddy currents a parasitic effect, one can also investigate how controlling the current paths can be used to tailor the local microwave field. The excitation of wave-vector specific spin waves in FM films using a diffraction grating has been studied by Sklenar *et. al* [97], where they show that a patterned silver antidot lattice on a thin uniform permalloy film enables coupling to spin-wave modes. In paper III of the thesis we investigate how eddy currents, in addition to the aforementioned microwave screening effects, also enables the excitation of spin-wave modes with non-zero wave vectors ($k \neq 0$), in contrast to the uniform $k = 0$ mode normally excited in FMR experiments.

The findings presented in paper II and III of the thesis points towards the importance of considering eddy-current effects not only for understanding basic experiments, but also for control of the local microwave field in thin film structures, which could be of importance for magnonics applications. A summary of the main results of paper II and III are found in the following sections, and for further details I refer to the appended papers in chapter 9

5.2.1 Summary of paper II

Vegard Flovik, Ferran Macià, Andrew D. Kent, Erik Wahlström.
Eddy current interactions in a ferromagnet-normal metal bilayer structure, and its impact on ferromagnetic resonance lineshapes
 J. Appl. Phys. 117, 143902 (2015)

In this manuscript, we show (through ferromagnetic resonance (FMR) spectroscopy) that induced eddy-current effects are important even for thin films

(10-100nm Au or Cu) in Ferromagnet/Normal metal (FM/NM) bilayers – contrary to what is usually assumed. The dynamics of such bilayers is governed by the interplay of the microwave fields from an FMR microwave cavity and the additional Oersted fields from the induced eddy currents. This coupling leads to a phase shift in the FMR excitation, measured and quantified through an asymmetry in the observed FMR lineshapes.

Further, we show that this coupling is tunable through changing the sample geometry and NM layer thickness. The tunability of the coupling opens up possibilities to use patterned NM structures to tailor the local field geometry and phase of the induced microwave fields.

5.2.2 Summary of paper III

Vegard Flovik, Bjørn Holst Pettersen, Erik Wahlström.

Eddy-current effects on ferromagnetic resonance: Spin wave excitations and microwave screening effects.

J. Appl. Phys. 119, 163903 (2016)

In this manuscript, we investigate (through ferromagnetic resonance (FMR) spectroscopy) how induced eddy-current effects in patterned FM/NM structures can be used to tailor the local microwave fields in FMR experiments. We show how induced fields from eddy currents can be used to partially compensate the applied microwave field, acting as an effective screening mechanism in selected parts of the sample. We also provide evidence that controlling the local microwave field can enable the excitation of spin-wave modes, in contrast to the uniform mode normally excited in FMR experiments. Our results suggests the possibility of actively using eddy currents to control the local microwave field excitation in thin film structures, which could be of importance for magnonics applications.

5.3 Magnetodynamics of confined magnetic elements

Confining a magnetic element to nanoscale dimensions has several important implications, and the complex interplay between the various magnetic energy terms all contribute to determining the magnetic state. The static magnetic configuration is determined by the material properties and the size and shape of the magnetic elements (as introduced in section 2.1.5), and it might become energetically favorable to form multiple magnetic domains with different orientations of the magnetization. The possibility of obtaining states where the magnetization orientation represents a bit enables the use as magnetic memory devices, and nanometer sized magnetic elements play an important role in advanced magnetic storage schemes [98, 99]. However, even for such "static" applications, as the switching times of current magnetic applications approach the sub-ns regime, understanding the magnetization dynamics is becoming increasingly important.

In addition to the importance of understanding the magnetization dynamics in terms of fast switching processes, it is also at the foundation of the emerging research field of magnonics introduced previously. The study of spin waves in nanoscale systems is of great importance, both for gaining fundamental understanding on these novel phenomena, as well as for application purposes. Due to this, the dynamic magnetic properties of nanostructures are being intensely studied, and have received extensive attention from both fundamental and applications viewpoints. See e.g. refs. [19, 83, 100, 101, 102] and references therein for an overview of recent research.

While technological applications are important, there is also significant interest in understanding the fundamental behavior of magnetic materials when they are confined to nanoscale dimensions. In confined magnetic elements, there is a complex competition between exchange, dipolar and anisotropic magnetic energies. Understanding the interplay between the various energy terms is thus of importance when investigating the magnetodynamics of such systems.

The magnetization dynamics of patterned magnetic structures has been extensively studied previously [103, 104, 105, 106, 107, 108, 109]. The spin dynamics in elliptical permalloy dots was investigated by Gubbiotti *et al.*[104]. They studied the various excitation modes as a function of dot eccentricity and in-plane orientation of the applied field, showing how the shape of the ellipses affects the spectrum of excitable modes and their frequencies. In addition to the excitation spectrum, Nembach *et. al.* also investigated the mode-and size-dependent magnetodynamic damping in magnetic nanostructures [108].

However, the above-mentioned studies of patterned magnetic structures were all performed for systems having a negligible magnetocrystalline anisotropy. Material systems with a significant crystalline anisotropy produce an effective field which also contributes to the spin dynamics. To the best of our knowledge, the dynamic properties of magnetic structures with comparable contributions from both crystalline and shape anisotropies remained unexplored.

The goal of the study that resulted in paper IV of the thesis was thus to investigate a system where the energy terms from both crystalline and shape anisotropies contribute to determine the dynamics. In order to achieve this, one needs a material system which has a significant magnetocrystalline anisotropy. In our study, we utilized epitaxial Fe thin films as the FM material, patterned to an array of elliptical nanomagnets. This resulted in a system combining the cubic crystalline anisotropy of Fe [28] with the shape anisotropy due to the elliptical shape of the magnetic elements. This allowed for a fundamental study of the magnetodynamic properties of a system where the interplay between the various energy terms could be controlled through the shape and size of the magnetic elements.

A summary of the main findings of this investigation is found in the following section, and for further details I refer to the appended paper in chapter 9.

5.3.1 Summary of paper IV

Vegard Flovik, Ferran Macià, Joan Manel Hernández, Rimantas Bručas, Maj Hanson, Erik Wahlström.

Tailoring the magnetodynamic properties of nanomagnets using magnetocrystalline and shape anisotropies.

Phys. Rev. B. 92, 104406 (2015)

In this manuscript, we investigate the interplay of magnetocrystalline and shape anisotropy in elliptical nano-magnets, and set the size range that allows controlling their dynamic properties. Through a combination of analytical calculations, micromagnetic simulations and ferromagnetic resonance (FMR) spectroscopy, we show how the size of the magnetic elements governs the balance between crystalline and shape anisotropy and how this affects their dynamic properties. From an applications viewpoint, the manuscript shows how one might utilize magnetocrystalline anisotropy in addition to the size and shape of the magnetic elements to tailor the magnetodynamic properties.

5.4 Synchronization of spin-torque oscillators

The emergence of coherent phases of interacting oscillators is a common phenomena, and is at the foundation of the cooperative functioning of a wealth of different systems in nature. Coherent phases emerge in natural systems of interacting oscillators, leading to collective synchronized states, and we are surrounded by those systems – from disease spreading to biological body rhythms [110].

Understanding the collective behavior in oscillator networks is also an intensely studied topic in modern magnetism: the synchronization of spin torque oscillators (STO). STO are strongly non-linear magnetic oscillators that can be implemented into nanoscale devices working at microwave frequencies. For a nice review on STO see e.g. refs. [111, 112] and references therein.

The functioning of STO are based on the spin-transfer torque (STT) effect and the giant magnetoresistance effect (GMR), as introduced in section 2.2.8. In a simplified picture, a nanopillar STO consists of a fixed polarizer layer and a magnetic free layer. Running a charge current through the fixed layer causes a spin polarized current which then runs through the free layer, exerting a torque on the magnetization. At sufficiently high current densities, this torque can induce a precession motion of the magnetization, characterized by a single frequency set by the applied field strength and the current density. Due to the GMR effect, as the free layer precesses at a certain frequency, the resistance of the nanopillar also oscillates at the same frequency. Thus, a direct charge current creates a microwave voltage across the STO, which is an attractive feature for applications.

STO are envisaged to be useful for a variety of advanced magnetic nanodevices, as microwave sources and for signal processing in telecommunication technologies (see e.g. refs. [20, 113] and references therein for an overview). STO have also been proposed as possible candidates for a full spintronic implementations of neural networks, based on nano-devices emulating both neurons and synapses [20, 114]. Building artificial neural networks for computation is an emerging field of research within bio-inspired computing [20, 113, 114, 115, 116, 117, 118, 119], where controlling the

collective behavior in oscillator networks is crucial.

For applications however, the ability of STO to be frequency and phase locked to external oscillatory signals or other STO is considered crucial, and is an intensely studied topic [120, 121, 122, 123, 124, 125, 126, 127, 128, 129, 130, 131, 132]. Several approaches to obtain synchronization have been investigated, such as e.g. the coupling through magnetic dipolar fields [124, 127, 128, 131], electrical connections [125, 129] and interaction mediated by spin waves [132].

In both experimental and theoretical studies, most of the work has been performed for a limited number of oscillators. Experimentally, the synchronization of STO has proven to be difficult, and the synchronization of only a few oscillators has been demonstrated [130, 132]. Theoretically, the magnetization dynamics of STO is modeled with the Landau-Lifshitz-Gilbert-Slonzewski (LLGS) equation [31, 56] (as introduced in section 2.2.8), but large number of STO lead to challenging computations. It is important to consider that in these non-linear systems, "more is different", and that the collective behavior can not be derived simply from the behavior of the individual elements. Thus, a theoretical framework capable to capture the essential dynamics would be ideal to explore those systems.

Mathematical models for understanding collective phenomena in large populations of interacting oscillators are sought after in science, and one of the more well known is the Kuramoto model. The Kuramoto model is a well known mathematical model in non-linear dynamics that describes large systems of coupled phase oscillators [133]. The model, with a remarkable simplicity, has been used to describe the essential features of collective excitations in a vast set of biological and physical phenomena [133, 134, 135, 136, 137, 138, 139, 140, 141].

Inspired by the successful use of the aforementioned Kuramoto model in describing various phenomena related to synchronization, we wanted to see if a similar simple mathematical model could be obtained for the case of a large number of interacting magnetic oscillators. This is one of the objectives of paper V of the thesis, where we show that arrays of dipolar coupled STO can be successfully described through a Kuramoto model with a coupling term mimicking the dipolar interactions. In this study,

we perform "numerical experiments" of systems which are currently too complicated and time consuming to realize experimentally. However, the results still shed new light on the synchronization of STO, and we believe that a fundamental understanding of synchronization phenomena might prove to be useful in designing new approaches to obtain synchronization of STO.

A summary of the main findings of this investigation is found in the following section, and for further details I refer to the appended paper in chapter 9.

5.4.1 Summary of paper V

Vegard Flovik, Ferran Macià, Erik Wahlström.

Describing synchronization and topological excitations in arrays of magnetic spin torque oscillators through the Kuramoto model.

Sci. Rep. 6, 32528 (2016).

Finding mathematical models that describe complex systems is not only important for a basic understanding, but it is also important in order to create and exploit such systems with all the potentiality of collective behavior. Here, we investigate the collective dynamics in large populations of magnetic vortex-based spin-torque oscillators (STO). The micromagnetic modeling of those systems is complicated and time consuming. We show that arrays of STO can be modeled using a variant of the Kuramoto model with a coupling term mimicking the magnetic dipolar fields, providing a simple theoretical framework capturing the essential dynamics to explore those systems.

By investigating the collective dynamics in large arrays of STO using the Kuramoto model as well as micromagnetic simulations, we find that the synchronization in such systems is a finite size effect. The critical coupling – for a complete synchronized state – scales with the number of oscillators, preventing global synchronization in large systems. Using realistic values of the dipolar coupling strength between STO, we show that this imposes an upper limit for the maximum number of oscillators that

can be synchronized. The ability to synchronize several STO is considered crucial for applications, and our results shed new light on the problem of mutual synchronization of a large number of oscillators.

The presented work has an interdisciplinary nature, establishing connections between different subfields such as non-linear dynamics, statistical physics and magnetization dynamics. We present an analogy between systems of interacting oscillators in biology and neuroscience to magnetic oscillators which can be implemented into nanoscale devices. This suggest, on the one hand, that the use of models from non-linear dynamics might be useful for describing synchronization of magnetic oscillators and, on the other hand, that arrays of STO may be good candidates for a spintronic implementation of neural networks or other unexplored phenomena described by the Kuramoto model.

Chapter 6

Popular science article based on paper V

As scientists, I believe we should be better at sharing our research with the public. After all, a major part of our research funding is coming from the government and the taxpayers' money. Thus, in addition to the publication of research in specialized journals, contributing to the public awareness of science should also be part of our focus. Also, I find that trying to explain complex problems in a way that is easily comprehensible and captures the interest of the "non-scientist" reader, while still providing physics insight, is an interesting challenge.

As an effort in contributing to the popular science dissemination of research, I have written an article inspired by paper V of the thesis. I have emphasized avoiding technical jargon and to keep it easy to follow, without requiring any previous physics knowledge. Slightly modified and shortened versions of this article have been published on the university blog, as well as in the Norwegian popular science magazine "Gemini" [142]. If my contribution is able to catch the interest of some "non-scientists" and get them to appreciate the joy of physics along the way, I have reached my goal.

Can we build artificial brain networks using nanoscale magnets?

Before addressing my initial question on the connection between nanoscale magnets and brain networks, let me first introduce our recent article: It has the rather technical title "*Describing synchronization and topological excitations in arrays of magnetic spin torque oscillators through the Kuramoto model*". Let us try to chop this into pieces, to make it less intimidating: The main term to understand initially is that of synchronization. The details related to topology are perhaps more suitable for the specialist reader, and will be skipped for now.

The concept of synchronization should be well known, even if you might not have thought about it that much, and do not spend your time thinking about mathematical equations on how to describe it. Synchronization basically surrounds us in all parts of nature and technology. A beautiful example of synchronization in nature includes that of e.g. fireflies. Large groups of fireflies sometimes synchronize and start flashing in unison, producing really fascinating flashing patterns. I highly recommend a quick youtube search on these phenomena. In addition to illustrating the concept of synchronization, they are simply very beautiful to look at! Another example, where you have probably contributed to the synchronization yourself, is that of rhythmic applause. The tendency of an audience to break into synchronized rhythmic applause constitutes a form of spontaneous synchronization. There are also examples of synchronized activity in the brain, and research has shown that synchronous electrical activity between neurons in distinct regions of the brain might play an important role in the performing of cognitive tasks and memory formation.

So, these phenomena are interesting, but what do they have to do with nanoscale magnets? Well, there is a common denominator in these cases of synchronized activity. As it turns out, they are connected via "the mathematics of synchronization". These vastly different phenomena can actually be described remarkably well using the same mathematical equations, all connected by the common concept of synchronization. One of the more

”famous” mathematical models to study synchronization is the Kuramoto model. The Kuramoto model has been used to describe the essential features of coupled oscillations in a vast set of biological and physical systems, where an oscillator in this sense is any system that executes periodic behavior. A swinging pendulum, for example, returns to the same point in space at regular intervals, where these intervals correspond to the oscillators frequency. You might also recognize the Kuramoto model from the title of our recent article, which I introduced in the beginning. This means we are getting closer to the content of our actual research.

So, what are the key ingredients we have introduced? Well, we have the concept of synchronization, the Kuramoto model, and the magnetic oscillators. More specifically, the focus of our latest research has been on understanding the behavior of nanoscale magnetic oscillators. These oscillators have a size of a few hundred nanometers. In comparison, a human hair has a thickness of approximately 100.000 nanometers (one nanometer is 0.000000001 meter, so they are pretty small!). They have been envisaged to be useful for a variety of magnetic nanodevices, as microwave sources and for signal processing in telecommunication technologies. Another very interesting proposal is the use of such oscillators as building blocks for the implementation of artificial neural networks, inspired by the functioning of the brain. Building artificial neural networks is an emerging field of research within bio-inspired computing. Here, researchers look to nature for inspiration in the development of bio-inspired chips based on natural computing architectures. The brain, and biological systems in general, are able to perform high performance calculations with much higher efficiency than computers, and they do it quickly and with very low energy consumption. Interestingly, recent advances in nanotechnology and materials science finally make it possible to envisage designing and building networks based on multifunctional nanodevices approaching the complexity of biological systems.

We are now getting closer to our initial question: *Can we build artificial brain networks using nanoscale magnets?* As an effort in achieving this, understanding what happens when you put a lot of these magnetic oscillators together, allowing them to interact with each other is crucial. This

is what we have been studying recently. When fabricating such nanoscale oscillators they will all be slightly different from the fabrication process, and due to this they tend to oscillate at slightly different frequencies. This is bad news for several of the interesting applications mentioned previously, where the ability of the oscillators to synchronize and oscillate at a common frequency is crucial. As a means to solve this, one can try to put several of these oscillators closely packed together, allowing them to interact and "talk" to each other. By doing this, they tend to adjust their individual frequencies and "agree" on a common rhythm with their neighbors: i.e. they become synchronized.

This synchronization transition is similar to something you have probably experienced yourself: when a theater audience spontaneously starts clapping in unison. The audience "talk" to each other and interact via the clapping sounds, where people tend to adjust their own clapping rhythm to that of the surrounding audience. This can sometimes spontaneously result in the well-known rhythmic applause. The crucial ingredient here, is that they are able to interact by hearing the clapping of the neighboring audience. Without this kind of interaction, it is highly unlikely that everyone in the audience spontaneously start clapping at exactly the same pace. This is similar also for the magnetic oscillators: In order for them to "agree" on a common frequency, they need to be able to interact with each other. In their case, the interaction is of course not through clapping, but through the magnetic fields produced by the individual oscillators. This means that by putting several of them closely packed together, the interactions among them could result in a collective behavior of all the oscillators.

This is where things get interesting: Understanding the behavior of a single oscillator is not that hard (although it can be complicated enough!), it is the collective behavior when you put a lot of them together which is the real challenge to understand. The study of such phenomena belongs to what scientists refer to as non-linear dynamics. The main consideration is that in these non-linear systems, "more is different", and the collective behavior cannot be derived simply from the behavior of the individual elements. Putting a lot of "simple" elements which are well understood on their individual level together and allowing them to interact, it gets very

complicated and non-intuitive to understand how they will behave collectively. At the same time, this complicated collective behavior is also what makes these systems interesting! This leads us to one of the main question we wanted to address in our research: What happens when you put a lot of these oscillators closely packed together, allowing them to interact? Will they synchronize to a collective rhythm, or will perhaps some other interesting effects occur?

The way we studied this, was through mathematical equations we could solve on our computers. However, the set of equations one must solve when the number of oscillators increases gets very complicated and time consuming. Even on powerful computers, the computation time is simply too long to obtain a sensible result in a reasonable amount of time. Inspired by the successful use of the aforementioned Kuramoto model in describing a vast set of different phenomena related to synchronization, we wanted to see if a similar "simple" mathematical model could be obtained for the case of interacting magnetic oscillators. The short answer here is: yes, we believe so. In our recent article, we show how one could use this mathematical model to describe the collective behavior in large networks of such magnetic oscillators, and present an analogy between systems of interacting oscillators in e.g. neuroscience and these magnetic oscillators, as they both can be described by similar mathematical equations.

So, returning again to our initial question: *Can we build artificial brain networks using nanoscale magnets?* Well, building an artificial brain, in the sense of a human brain, might be difficult. However, being able to build artificial neural networks which perform computations inspired by how the brain performs cognitive tasks is a more likely outcome. A part of the puzzle in achieving this goal is to identify the suitable elemental building blocks. In this context, nanoscale magnetic oscillators are one of the promising candidates for an implementation of neural networks based on nanodevices emulating neurons. At least, we find it very interesting that the mathematical equations used to study the synchronization of neural activity in the brain can also be used to study the synchronization of magnetic oscillators. However, with many issues yet to overcome and problems to solve, only continued hard work over the coming years will show whether

82 *CHAPTER 6. POPULAR SCIENCE ARTICLE BASED ON PAPER V*

such devices will become a reality in the future. In the meantime, we are just excited to contribute our small piece of the puzzle.

Chapter 7

Outlook

Advances in science is building upon the knowledge from previous research. As every contribution represents one piece of the puzzle, our combined understanding expands over the years due to the hard work and dedication of scientists all over the world. As such, this thesis represents my contribution to advancing the understanding of magnetization dynamics. It is my hope that the publications that resulted from my PhD will prove to be useful for fellow scientists, as well as sparking new ideas for future research. In this final chapter of my thesis, I would thus like to briefly summarize the main scientific findings and perspectives for future work.

Magnetodynamic damping in thin films

In paper I of the thesis, we investigated the magnetodynamic damping in LSMO thin films. In this study we found a minimum damping parameter of $\alpha = 0.002$, which is a factor of four lower than that of Permalloy, one of the prototype materials for magnetodynamic devices.

Due to limitations of our experiments, we were not able to separate the intrinsic Gilbert damping from other contributions such as eddy-current damping and two-magnon scattering. The eddy-current contribution is known to scale with the film thickness as δ^2 , and performing experiments

for a larger number of film thicknesses would enable us to extract this contribution to the damping. The contribution from two-magnon scattering could also be investigated further by measuring the damping as a function of the orientation of the magnetization with respect to the film plane. With the magnetization perpendicular to the sample plane, the two-magnon contribution should vanish, and one could get an estimate for the intrinsic Gilbert damping. Unfortunately, orienting the magnetization out of the sample plane requires higher magnetic fields than that obtainable in the experimental setup we used.

Due to this, performing additional studies where one could extract the various contributions to the damping would be interesting. Understanding the contributions to the damping better and optimizing film growth might lead to an additional reduction of the damping parameter, which would make LSMO a very interesting material system for further investigations.

Eddy-current effects on FMR

In paper II and III of the thesis, we showed how magnetic fields due to induced microwave eddy currents can affect the FMR excitation. Eddy currents produce highly localized fields due to the localization of the induced currents, which allows for generating and controlling the microwave field in small regions. The findings in these papers indicate that this can be utilized in order to tailor the local microwave field, which can be used for screening of an applied microwave field as well as the excitation of spin-wave modes. To obtain this, being able to control the current paths is an important step.

In our investigations, we used Permalloy as the ferromagnet. Using a conductive material, there will be induced currents flowing also in the ferromagnetic layer in addition to any adjacent normal metal layers. In order to obtain better control of the induced current paths, it would thus be interesting to utilize an insulating material like e.g. YIG as the ferromagnet. This is unfortunately not something we have been able to try yet, as we did not have access to high quality YIG films to perform such experiments.

By using patterned normal metal structures on top of a ferromagnetic

layer, it might be possible to excite spin waves with well defined wave vectors determined by the periodicity of the patterned structure. This could potentially be interesting for magnonics applications, where a controlled excitation of spin-wave modes is desirable. This is usually obtained using a microwave antenna, which requires nanostructuring on top of the ferromagnetic film with connections to electrical leads running a current through the antenna. The prospective of exciting well defined spin-wave modes using eddy currents would simplify the device, as electrical leads would then be obsolete. However, to investigate if this is feasible or not will require further work which is beyond what could be included in this thesis.

Magnetodynamics of confined magnetic elements

Paper IV of the thesis represents a fundamental study of the interplay between the various magnetic energies, and how they determine the magnetodynamic properties. In the data presented in this paper, we investigated arrays of elliptical magnets with a film thickness of 10 nm. For these samples, all the magnetic elements were in a single domain state. However, we also performed some initial investigations of similar samples with film thicknesses of 30 and 50 nm. In this thickness range, demagnetization effects are becoming increasingly important. At low magnitudes of the external magnetic field this resulted in the samples not being in a single domain state. Through Magnetic Force Microscopy (MFM) imaging, states with both single and two vortices in each magnetic element was observed.

It would be interesting to investigate the dynamical behavior of these vortex states, and how the magnetocrystalline anisotropy might affect the gyrotropic motion of the vortex core. However, as the formation of vortex states lowers the magnetostatic energy by reducing the magnetic stray fields, this also causes some challenges experimentally. Using a broadband FMR setup, the CPW acts as an inductive sensor for the magnetic response from the sample. With the magnetic elements being in a state that reduces the magnetic stray fields, it also reduces the sensitivity of the measurements. Due to this, we were not able to obtain a strong enough signal in the low-field regime in order to measure these excitations.

The measurements were performed using a flip-chip approach, placing the sample on top of the CPW. By rather depositing the patterned magnetic structures directly on top of the CPW, one could increase the sensitivity and perhaps obtain sufficient signal in order to measure these low-field vortex excitations. This is unfortunately not something we had the opportunity or time to investigate further during my PhD.

Synchronization of spin-torque oscillators

In paper V of the thesis we investigated the collective behavior in large arrays of dipolar coupled STO. The behavior of large populations of interacting oscillators is an intensely studied topic in non-linear dynamics, and the Kuramoto model is one of the most well known models for studying such systems. Describing interacting STO through the Kuramoto model thus suggest the possibility of tapping into this knowledge, in order to gain a better understanding of synchronization phenomena also relevant for STO.

In our investigations, we observed that the interaction strength needed to obtain a synchronized state depends on the number of STO in the array. This scaling with system size has implications for the desire of scaling up to large arrays of synchronized STO. On a more fundamental level, being able to understand the origin of this finite size scaling would also be interesting to investigate further. The similarities with the topological defects observed in the XY model of magnetism is then something which might be relevant to look into.

The coupling mechanism we have considered is due to the magnetic dipolar interaction. Other means to obtain synchronization, such as through electrical connections or spin waves, might also be studied using extensions of the Kuramoto model with different coupling topologies, phase offsets in the couplings etc. However, as this project represents the final stages of my PhD, we have unfortunately not had the time to pursue these ideas further yet.

7.1 Final considerations

The completion of this thesis, also marks the completion my PhD studies. Obtaining a PhD is hard work, but although it has been challenging at times, it has overall been an extremely rewarding experience. I have always been attracted by physics phenomena, and the joy of solving problems and learning something new about how nature works is truly a great feeling.

These last nine years mark the gradual transition from starting my physics studies back in 2007, to becoming a physicist capable of performing independent research. My PhD studies have also been a humbling experience. The more you learn about physics, the more you realize how much you do not know. However, in my opinion, the most important skillset as a physicist is not knowing everything. Rather, it is the way of thinking and how to approach problems.

It does not seem like we will run out of questions to answer and problems to solve any time soon. In this sense, the future as a physicist is looking bright, and I am looking forward to new challenges in the years to come. As such, the completion of my PhD marks the ending of one chapter of my scientific career, and the beginning of a new one. This is only the beginning!

Chapter 8

Bibliography

- [1] V. Flovik *et. al.* *Thickness and temperature dependence of the magnetodynamic damping of pulsed laser deposited $\text{La}_{0.7}\text{Sr}_{0.3}\text{MnO}_3$ on (111)-oriented SrTiO_3 .* J. Magn. Magn. Mater. 420, 280-284, (2016).
- [2] V. Flovik, F. Macià, A. D. Kent, E. Wahlström. *Eddy current interactions in a ferromagnet-normal metal bilayer structure, and its impact on ferromagnetic resonance lineshapes.* J. Appl. Phys. 117, 143902, (2015).
- [3] V. Flovik, B. H. Pettersen, E. Wahlström. *Eddy-current effects on ferromagnetic resonance: Spin wave excitations and microwave screening effects.* J. Appl. Phys. 119, 163903 (2016).
- [4] V. Flovik *et. al.* *Tailoring the magnetodynamic properties of nanomagnets using magnetocrystalline and shape anisotropies.* Phys. Rev. B. 92, 104406 (2015).
- [5] V. Flovik, F. Macià, E. Wahlström. *Describing synchronization and topological excitations in arrays of magnetic spin-torque oscillators through the Kuramoto model.* Sci. Rep. 6, 32528 (2016).

- [6] M. Hanson *et. al.* *Arrays of elliptical Fe(001) nanoparticles: Magnetization reversal, dipolar interactions, and effects of finite array sizes.* Phys. Rev. B 92, 094436 (2015).
- [7] V. Flovik, S. Sinha, A. Hansen. *Dynamic Wettability Alteration in Immiscible Two-phase Flow in Porous Media: Effect on Transport Properties and Critical Slowing Down.* Front. Phys. 3, 00086 (2015).
- [8] A. Fert. *Nobel Lecture: Origin, development, and future of spintronics* Rev. Mod. Phys. 80, 1517 (2008).
- [9] E. Hirota, H. Sakakima, K. Inomata, *Giant Magneto-resistance Devices*, Springer Series in Surface Sciences v.40, Springer-Verlag (2002).
- [10] S. A. Wolf *et. al.*. *Spintronics: A Spin-Based Electronics Vision or the Future.* Science, Vol. 294, Issue 5546, pp. 1488-1495, (2001).
- [11] I. Žutić, J. Fabian, S. D. Sarma. *Spintronics: Fundamentals and applications.* Rev. Mod. Phys. 76, 323, (2004).
- [12] G. E. Moore. *Solid-State Circuits Newsletter.* IEEE, 38, 114 (1965).
- [13] J. Stöhr, H. C. Siegman. *Magnetism: From fundamentals to Nanoscale Dynamics.* (Springer-Verlag Berlin Heidelberg, 2006).
- [14] J. C. Slonczewski. *Current-driven excitation of magnetic multilayers.* J. Magn. Magn. Mater. 159, L1 (1996).
- [15] L. Berger. *Emission of spin waves by a magnetic multilayer traversed by a current.* Phys. Rev. B. 54, 9353 (1996).
- [16] Rezende, S. M., de Aguiar, F. M., Azevedo, A. *Spin-Wave Theory for the Dynamics Induced by Direct Currents in Magnetic Multilayers.* Phys. Rev. Lett. 94, 037202. (2005).
- [17] Rezende, S. M., de Aguiar, F. M., Azevedo, A. *Magnon excitation by spin-polarized direct currents in magnetic nanostructures.* Phys. Rev. B. 73, 094402. (2006).

- [18] A. D. Kent, D. C. Worledge. *A new spin on magnetic memories* Nature Nanotech. 10, 187-191 (2015).
- [19] V. V. Kruglyak, S. O. Demokritov, D. Grundler. *Magnonics*. J. Phys. D: Appl. Phys. 43, 264001. (2010).
- [20] N. Locatelli, V. Cros, J. Grollier. *Spin-torque building blocks*. Nature Materials 13, 11-20 (2014).
- [21] C. Kittel. *Introduction to Solid State Physics*. 8th edition. (John Wiley & Sons, Inc., New York, 2004).
- [22] N. W. Ashcroft, N. D. Mermin. *Solid State Physics*. (Holt, Rinehart and Winston, New York 1976)
- [23] J. D. Griffiths, *Introduction to electrodynamics* (Prentice Hall, 1999), 3rd edition.
- [24] J. D. Jackson, *Classical Electrodynamics*. (John Wiley & Sons Ltd., 1998).
- [25] A. G. Gurevich, G. A. Melkov. *Magnetization Oscillations and Waves*. (CRC Press, 1996).
- [26] W. F. Brown, *Micromagnetism*. (Wiley, New York, 1963).
- [27] A. Moser. *et. al. Magnetic recording: advancing into the future*. J. Phys. D. Appl. Phys. 35 R157, (2002).
- [28] C. D. Graham. *Magnetocrystalline Anisotropy Constants of Iron at Room Temperature and Below*. Phys. Rev. 112, 1117, (1958).
- [29] G. S. Abo. *et. al.. Definition of magnetic exchange length*. IEEE Trans. Magn. 49, 4937-4939 (2013).
- [30] A. Hubert, R. Schäfer. *Magnetic domains: the analysis of magnetic microstructures*. Springer, Heidelberg (1998).

- [31] L. Landau, E. Lifshitz. *On the theory of the dispersion of magnetic permeability in ferromagnetic bodies*. Phys. Z. Sowjetunion, 8, 153 (1935).
- [32] D. Polder. *On the theory of ferromagnetic resonance*. Philos. Mag. 40, 99-115 (1949).
- [33] C. Kittel. *On the Theory of Ferromagnetic Resonance Absorption*. Phys. Rev. 73, 155 (1948).
- [34] J. Smit, H. G. Bejers, Philips Res. Repts. 10, 113 (1955).
- [35] H. Suhl. *Ferromagnetic Resonance in Nickel Ferrite Between One and Two Kilomegacycles*. Phys. Rev. 97, 555 (1955).
- [36] COMSOL Multiphysics Modeling Software. See www.comsol.com
- [37] M. Krakowski. *Eddy-current losses in thin circular and rectangular plates*. Arch. Electrotechnik 64, 307-311 (1982).
- [38] A. F. Mayadas, J. F. Janak, A. Gangulee. *Resistivity of Permalloy thin films*. J. Appl. Phys. 45, 2780 (1974).
- [39] M. Harder, Z. X. Cao, Y. S. Gui, X. L. Fan, and C.-M. Hu. *Analysis of the line shape of electrically detected ferromagnetic resonance*. Phys. Rev. B 84, 054423 (2011).
- [40] A. Wirthmann *et. al.* *Direct Phase Probing and Mapping via Spintronic Michelson Interferometry*. Phys. Rev. Lett. 105, 017202 (2010).
- [41] O. Mosendz *et. al.* *Detection and quantification of inverse spin Hall effect from spin pumping in permalloy/normal metal bilayers*. Phys. Rev. B 82, 214403 (2010).
- [42] O. Mosendz *et. al.* *Quantifying Spin Hall Angles from Spin Pumping: Experiments and Theory*. Phys. Rev. Lett. 104, 046601 (2010).
- [43] L. Liu, T. Moriyama, D. C. Ralph, and R. A. Buhrman. *Spin-Torque Ferromagnetic Resonance Induced by the Spin Hall Effect*. Phys. Rev. Lett. 106, 036601 (2011).

- [44] V. Vlaminck, J. E. Pearson, S. D. Bader, A. Hoffman. *Dependence of spin-pumping spin Hall effect measurements on layer thicknesses and stacking order*. Phys. Rev. B. 88, 064414, (2013)
- [45] M. Obstbaum *et. al.* *Inverse spin Hall effect in Ni81Fe19/normal-metal bilayers*. Phys. Rev. B. 89, 060407(R), (2014)
- [46] S.-I. Kim, D.-J. Kim, M.-S. Seo, B.-G. Park, S.-Y. Park. *Stacking order dependence of inverse spin Hall effect and anomalous Hall effect in spin pumping experiments*. J. Appl. Phys. 117, 17D901, (2015).
- [47] K. J. Harte. *Theory of Magnetization Ripple in Ferromagnetic Films*. J. Appl. Phys. 39, 1503, (1968).
- [48] D. D. Stancil, A. Prabhakar. *Spin Waves: Theory and Applications*, 1st ed. (Springer, New York, 2009)
- [49] S.S. Kalarickal *et. al.* *Ferromagnetic resonance linewidth in metallic thin films: Comparison of measurement methods*. J. Appl. Phys. 99, p. 093909 (2006).
- [50] M. C. Hickey, J. S. Moodera. *Origin of Intrinsic Gilbert Damping*. Phys. Rev. Lett. 102, 137601 (2009).
- [51] M. Sparks, R. Loudon, C. Kittel. *Ferromagnetic Relaxation. I. Theory of the Relaxation of the Uniform Precession and the Degenerate Spectrum in Insulators at Low Temperatures*. Phys. Rev. 122, 791, (1961).
- [52] M. J. Hurben, C. E. Patton. *Theory of two magnon scattering microwave relaxation and ferromagnetic resonance linewidth in magnetic thin films*. J. Appl. Phys. 83, 4344 (1998).
- [53] J. M. Lock. *Eddy current damping in thin metallic ferromagnetic films*. Br. J. Appl. Phys. 17, 1645 (1966).
- [54] M. A. Schoen, J. M. Shaw, H. T. Nembach, M. Weiler, T. J. Silva. *Radiative damping in waveguide-based ferromagnetic resonance mea-*

- sured via analysis of perpendicular standing spin waves in sputtered permalloy films.* Phys. Rev. B. 92, 184417 (2015)
- [55] J. Bass, W. P. Pratt. *Spin-diffusion lengths in metals and alloys, and spin-flipping at metal/metal interfaces: an experimentalist's critical review* J. Phys.: Condens. Matter 19, 183201 (2007).
- [56] M. Stiles, J. Miltat. Spin-Transfer torque and dynamics. In Hillebrands B. & Thiaville. A (eds.) *Spin Dynamics in Confined Magnetic Structures*. III Vol. 101, 225-308 (Springer Berlin Heidelberg, 2006).
- [57] D. C. Ralph, M. D. Stiles. *Spin transfer torques.* J. Magn. Magn. Mater. 320, 1190-1216, (2008).
- [58] A. Vansteenkiste *et. al.* *The design and verification of MuMax3.* AIP. Advances 4, 107133 (2014).
- [59] P. E. Wigen (Ed.) *Nonlinear Phenomena and Chaos in Magnetic Materials.* World Scientific, Singapore (1994)
- [60] R. D. McMichael, M. D. Stiles. *Magnetic normal modes of nanoelements.* J. Appl. Phys. 97, 10J901 (2005).
- [61] A. B. Kos, T. J. Silva, P. Kabos. *Pulsed inductive microwave magnetometer.* Rev. Sci. Instrum. 73, 3563 (2002).
- [62] M. Quirk, J. Serda. *Semiconductor Manufacturing Technology.* Prentice Hall, New Jersey, 2001.
- [63] See: <https://www.bruker.com/products/magnetic-resonance/epr.html>
- [64] E. J. Reijerse. *High-Frequency EPR instrumentation.* Appl. Magn. Reson 37: 795-818. (2010).
- [65] O. Yalçın. *Ferromagnetic Resonance - Theory and Applications.* 978-953-51-1186-3 InTech. Janeza Trdine, Rijeka, Croatia (2013).
- [66] J. H. Scofield. *Frequency-domain description of a lock-in amplifier* Am. J. Phys. 62, 129 (1994).

- [67] D. M. Pozar. *Microwave Engineering, 4th Edition*. John Wiley & Sons, Inc. (2012).
- [68] S. Geoffrey *et. al.* *Dynamics of field-driven domain-wall propagation in ferromagnetic nanowires*. Nature Materials 4, 741-744 (2005).
- [69] D. A. Allwood *et. al.* *Magnetic Domain-Wall logic*. Science 309, 1688-1692 (2005).
- [70] C. Thirion, W. Wernsdorfer, D. Mailly. *Switching of magnetization by nonlinear resonance studied in single nanoparticles*. Nature Materials 2, 524-527 (2003).
- [71] A. A. Serga, A. V. Chumak, B. Hillebrands. *YIG magnonics*. J. Phys. D: Appl. Phys. 43, 264002, (2010).
- [72] D. J. Twisselmann, R. D. McMichael. *Intrinsic damping and intentional ferromagnetic resonance broadening in thin Permalloy films*. J. Appl. Phys. 93, 6903 (2003).
- [73] C. Hauser *et. al.* *Yttrium Iron Garnet Thin Films with Very Low Damping Obtained by Recrystallization of Amorphous Material*. Sci. Rep. 6, 20827, (2016).
- [74] A. V. Chumak, V. I. Vasyuchka, A. A. Serga, B. Hillebrands. *Magnon spintronics*. Nature Physics 11, 453-461 (2015).
- [75] B. Lenk, H. Ulrichs, F. Garbs, M. Münzenberg. *The building blocks of magnonics*. Phys. Rep., 507, p. 107 (2011).
- [76] I. Žutić, H. Dery. *Spintronics: Taming spin currents*. Nature Materials 10, 647-648 (2011).
- [77] J. Mannhart, D. G. Schlom. *Oxide interfaces - An opportunity for electronics*. Science 327, 1607-1611 (2010).
- [78] P. Zubko *et. al.* *Interface physics in complex oxide heterostructures*. Ann. Rev. Condens. Matter Phys. 2, 141-165 (2011).

- [79] H. Y. Hwang *et. al.* *Emergent phenomena at oxide interfaces*. Nature Materials 11, 103-113 (2012).
- [80] S. W. Cheong, M. Mostovoy. *Multiferroics: a magnetic twist for ferroelectricity*. Nature Materials 6, 13-20 (2007).
- [81] I. Hallsteinsen *et. al.* *Crystalline symmetry controlled magnetic switching in epitaxial (111) $\text{La}_{0.7}\text{Sr}_{0.3}\text{MnO}_3$ thin films*. APL Mater. 3, 062501 (2015)
- [82] Y. Tserkovnyak, A. Brataas, G. E. W. Bauer, B. I. Helperin. *Nonlocal magnetization dynamics in ferromagnetic heterostructures*. Rev. Mod. Phys. 77, 1375 (2005).
- [83] R. L. Stamps *et al.* *The 2014 Magnetism Roadmap*. J. Phys. D: Appl. Phys. 47 333001 (2014)
- [84] S. Fahy, C. Kittel, S. G. Louie. *Electromagnetic screening by metals*. Am. J. Phys. 56, 989 (1988).
- [85] I. V. Antonets, L. N. Kotov, S. V. Nekipelov, and E. N. Karpushov. *Conducting and reflecting properties of thin metal films*. Technical Physics, November 2004, Volume 49, Issue 11, pp 1496-1500
- [86] M. Bailleul. *Shielding of the electromagnetic field of a coplanar waveguide by a metal film: Implications for broadband ferromagnetic resonance measurements*. Appl. Phys. Lett. 103, 192405 (2013)
- [87] M. Kostylev. *Strong asymmetry of microwave absorption by bilayer conducting ferromagnetic films in the microstrip-line based broadband ferromagnetic resonance*. J. Appl. Phys. 106, 043903 (2009).
- [88] I. S. Maksymov and M. Kostylev. *Microwave eddy-current shielding effect in metallic films and periodic nanostructures of sub-skin-depth thicknesses and its impact on stripline ferromagnetic resonance spectroscopy*. J. Appl Phys. 116, 173905 (2014).

- [89] I. S. Maksymov, Z. Zhang, C. Chang, and M. Kostylev. *Strong Eddy-Current Shielding of Ferromagnetic Resonance Response in Sub-Skin-Depth-Thick Conducting Magnetic Multilayers*. IEEE Magn. Lett. Volume 5 (2014).
- [90] W. E. Bailey *et. al.* *Detection of microwave phase variation in nanometre-scale magnetic heterostructures*. Nat. Commun. 4, 2025 (2013).
- [91] Y. V. Khivintsev *et. al.* *Spin wave resonance excitation in ferromagnetic films using planar waveguide structures*. J. Appl. Phys. 108, 023907 (2010).
- [92] H. Glowinski, M. Schmidt, I. Gościańska, J-Ph. Ansermet, J. Dubowik. *Coplanar waveguide based ferromagnetic resonance in ultrathin film magnetic nanostructures: Impact of conducting layers*. J. Appl. Phys. 116, 053901 (2014)
- [93] Z. Lin, M. Kostylev. *A rigorous two-dimensional model for the stripline ferromagnetic resonance response of metallic ferromagnetic films*. J. Appl. Phys. 117, 053908 (2015).
- [94] M. Kostylev. *Waveguide-based ferromagnetic resonance measurements of metallic ferromagnetic films in transmission and reflection*. J. Appl. Phys. 113, 053908 (2013).
- [95] I. S. Maksymov and M. Kostylev. *Impact of eddy currents on the dispersion relation of surface spin waves in thin conducting magnetic films*. J. Phys. D: Appl. Phys. 46 495001, (2013).
- [96] G. Council *et. al.* *Spin wave contributions to the high-frequency magnetic response of thin films obtained with inductive methods*. J. Appl. Phys. 95, 5646 (2004).
- [97] J. Sklenar, V. S. Bhat, C. C. Tsai, L. E. DeLong, J. B. Ketterson. *Generating wave vector specific Damon-Eshbach spin waves in Py using a diffraction grating*. Appl. Phys. Lett. 101, 052404 (2012).

- [98] A. Moser *et. al.* *Magnetic recording: advancing into the future.* J. Phys. D: Appl. Phys. 35 R157, (2002)
- [99] S. S. P. Parkin *et. al.* *Exchange-biased magnetic tunnel junctions and application to nonvolatile magnetic random access memory.* J. Appl. Phys. 85, 5828, (1999)
- [100] J. Åkerman. *Toward a Universal Memory.* Science 308, 508 (2005)
- [101] S. D. Bader. *Colloquium: Opportunities in nanomagnetism.* Rev. Mod. Phys. 78, 1 (2006)
- [102] M. Krawczyk, D. Grundler. *Review and prospects of magnonic crystals and devices with reprogrammable band structure.* J. Phys.: Condens. Matter 26 123202 (2014)
- [103] R. D. McMichael, M. D. Stiles. *Magnetic normal modes of nanoelements.* J. Appl. Phys. 97, 10J901 (2005).
- [104] G. Gubbiotti *et. al.* *Spin dynamics in thin nanometric elliptical Permalloy dots: A Brillouin light scattering investigation as a function of dot eccentricity.* Phys. Rev. B. 72, 184419, (2005)
- [105] F. Montoncello *et. al.* *Soft spin waves and magnetization reversal in elliptical Permalloy nanodots: Experiments and dynamical matrix results.* Phys. Rev. B 76, 024426 (2007)
- [106] O. F. Xiao, J. Rudge, B. C. Choi, Y. K. Hong, G. Donohoe. *Dynamics of ultrafast magnetization reversal in submicron elliptical Permalloy thin film elements.* Phys. Rev. B 73, 104425 (2006)
- [107] M. L. Schneider *et. al.* *Spin dynamics and damping in nanomagnets measured directly by frequency-resolved magneto-optic Kerr effect.* J. Appl. Phys. 102, 103909, (2007)
- [108] H. T. Nembach, J. M. Shaw, C. T. Boone, T. J. Silva. *Mode- and Size-Dependent Landau-Lifshitz Damping in Magnetic Nanostructures: Evidence for Nonlocal Damping.* Phys. Rev. Lett. 110, 117201, (2013)

- [109] Y. Yahagi, C. R. Berk, B. D. Harteneck, S. D. Cabrini, H. Schmidt. *Dynamic separation of nanomagnet sublattices by orientation of elliptical elements*. Appl. Phys. Lett. 104, 162406, (2014)
- [110] S. H. Strogatz, I Stewart. *Coupled oscillators and biological synchronization*. Sci. Am. 269(6), 102-109 (1993).
- [111] T. Silva, W. Rippard. *Developments in nano-oscillators based upon spin-transfer point-contact devices*. J. Magn. Magn. Mater. 320, 1260-1271 (2010).
- [112] J.-V. Kim. *Spin-Torque Oscillators*. Solid State Physics 63, 217-294 (2012).
- [113] Bonetti, S., Åkerman, J. *Nano-Contact Spin-Torque Oscillators as Magnonic Building Blocks*. Magnonics: From Fundamentals to Applications. Springer-Verlag, 2013.
- [114] Csaba, G., Porod, W. *Computational Study of Spin-Torque Oscillator Interactions for Non-Boolean Computing Applications*. IEEE Trans. Magn. vol. 49, no. 7, pp.4447-4451, (2013).
- [115] Macià, F., Kent, A. D., Hoppensteadt, F. C. *Spin-wave interference patterns created by spin-torque nano-oscillators for memory and computation*. Nanotechnology 22 (9), 095301, (2011).
- [116] Hoppensteadt, F. C., Izhikevich, E. M. *Oscillatory Neurocomputers with Dynamic Connectivity*. Phys. Rev. Lett. 82, 2983, (1999).
- [117] Maffezzoni, P., Bahr, B., Zheng, Z., Daniel, L. *Oscillator Array Models for Associative Memory and Pattern Recognition*. IEEE Trans. Circuits Syst. I, Reg. Papers, vol. 62, no. 6, pp. 1591-1598, (2015).
- [118] Locatelli, N. *et. al. Spintronic devices as key elements for energy-efficient neuroinspired architectures*. Proceedings of the 2015 Design, Automation & Test in Europe Conference & Exhibition

- [119] Vincent, A. F. *et. al.* *Spin-transfer torque magnetic memory as a stochastic memristive synapse for neuromorphic systems*. IEEE Transactions on Biomedical Circuits and Systems. Vol 9, Issue 2. (2015).
- [120] Rippard, W. H. *et. al.* *Injection Locking and Phase Control of Spin Transfer Nano-oscillators*. Phys. Rev. Lett. 95 067203, (2005).
- [121] Kaka, S. *et. al.* *Mutual phase-locking of microwave spin torque nano-oscillators*. Nature, 437 389-392 (2005).
- [122] Mancoff, F. B., Rizzo, N. D., Engel, B. N., Tehrani, S. *Phase-locking in double-point-contact spin-transfer devices*. Nature 437 393-395 (2005).
- [123] Pufall, M. R., Rippard, W. H., Russek, S. E., Kaka, S., Katine, J. A. *Electrical Measurement of Spin-Wave Interactions of Proximate Spin Transfer Nanooscillators*. Phys. Rev. Lett. 97, 087206, (2006).
- [124] Bonin, R., Bertotti, G., Serpico, C., Mayergoyz, I. D., d'Aquino, M. *Analytical treatment of synchronization of spin-torque oscillators by microwave magnetic fields*. Eur. Phys. J. B. 68, 221 (2009).
- [125] Zhou, Y., Person, J., Åkerman, J. *Intrinsic phase shift between a spin torque oscillator and an alternating current*. J. Appl. Phys. 101, 09A510 (2007).
- [126] Slavin, A. N., Tiberkevich, V. S. *Theory of mutual phase locking of spin-torque nanosized oscillators*. Phys. Rev. B. 74, 104401 (2006).
- [127] Belanovsky, A. D. *et. al.* *Numerical and analytical investigation of the synchronization of dipolarly coupled vortex spin-torque nano-oscillators*. Appl. Phys. Lett. 103, 122405 (2013).
- [128] Belanovsky, A. D. *et. al.* *Phase locking dynamics of dipolarly coupled vortex-based spin transfer oscillators*. Phys. Rev. B, 85, 100409(R) (2012).

- [129] Georges, B., Grollier, J., Cros, V., Fert, A. *Impact of the electrical connection of spin transfer nano-oscillators on their synchronization: an analytical study*. Appl. Phys. Lett 92, 232504 (2008).
- [130] Ruotolo, A. *et. al.* *Phase-locking of magnetic vortices mediated by antivortices*. Nature Nanotechnology 4, 528-532 (2009).
- [131] Locatelli, N. *et. al.* *Efficient Synchronization of Dipolarly Coupled Vortex-Based Spin Transfer Nano-Oscillators*. Sci. Rep. 5, 17039 (2015).
- [132] Houshang, A. *et. al.* *Spin-wave-beam driven synchronization of nanocontact spin-torque oscillators*. Nature Nanotechnology 11, 280-286 (2016).
- [133] Kuramoto, Y., Nishikawa, I. *Statistical macrodynamics of large dynamical systems. Case of a phase transition in oscillator communities*. J. Stat. Phys. 49, 569, (1987).
- [134] Acebrón, J. A. *et. al.* *The Kuramoto model: A simple paradigm for synchronization phenomena*. Rev. Mod. Phys. 77, 137, (2005).
- [135] Filatrella, G., Nielsen, A. H., Pedersen, N. F. *Analysis of a power grid using a Kuramoto-like model*. The European Physical Journal B. Volume 61, Issue 4, pp 485-491, (2008).
- [136] Daniels, B. C., Dissanayake, S. T. M., Trees, B. R. *Synchronization of coupled rotators: Josephson junction ladders and the locally coupled Kuramoto model*. Phys. Rev. E 67, 026216 (2003).
- [137] Wiesenfeld, K., Colet, P., Strogatz, S. H. *Frequency locking in Josephson arrays: Connection with the Kuramoto model*. Phys. Rev. E 57, 1563 (1998).
- [138] Néda, Z., Ravasz, E., Vicsek, T., Brechet, T., Barabási, A. L. *Physics of the rhythmic applause*. Phys. Rev. E 61, 6987 (2000).

- [139] Heinrich, G., Ludwig, M., Qian, J., Kubala, B., Marquardt, F. *Collective Dynamics in Optomechanical Arrays*. Phys. Rev. Lett. 107, 043603 (2011).
- [140] Cumin, D., Unsworth, C. P. *Generalising the Kuramoto model for the study of neuronal synchronisation in the brain*. Physica D: Nonlinear Phenomena, Volume 226, Issue 2, 181-196, (2007)
- [141] Timms, L., English, L. Q. *Synchronization in phase-coupled Kuramoto oscillator networks with axonal delay and synaptic plasticity*. Phys. Rev. E. 89, 032906, (2014).
- [142] Published text available at:
geminiresearchnews.com/blog/blog-can-build-artificial-brain-networks-using-nanoscale-magnets/

Chapter 9

Papers included in the thesis:

In the following sections I have appended the five published papers that make up the basis of this thesis.

9.1 Paper I

Vegard Flovik, Ferran Macià, Sergi Lendínez, Joan Manel Hernández, Ingrid Hallsteinsen, Thomas Tybell, Erik Wahlström.

Thickness and temperature dependence of the magnetodynamic damping of pulsed laser deposited $La_{0.7}Sr_{0.3}MnO_3$ on (111)-oriented $SrTiO_3$.

J. Magn. Magn. Mater. 420, 280-284, (2016).



Thickness and temperature dependence of the magnetodynamic damping of pulsed laser deposited $\text{La}_{0.7}\text{Sr}_{0.3}\text{MnO}_3$ on (111)-oriented SrTiO_3



Vegard Flovik^{a,*}, Ferran Macià^{b,c}, Sergi Lendínez^b, Joan Manel Hernández^b, Ingrid Hallsteinsen^d, Thomas Tybell^d, Erik Wahlström^a

^a Department of Physics, NTNU, Norwegian University of Science and Technology, Trondheim, N-7491, Norway

^b Grup de Magnetisme, Dept. de Física Fonamental, Universitat de Barcelona, Spain

^c Institut de Ciència de Materials de Barcelona (ICMAB-CSIC), Campus UAB, Bellaterra, 08193, Spain

^d Department of Electronics and Telecommunications, NTNU, Norwegian University of Science and Technology, Trondheim, N-7491, Norway

ARTICLE INFO

Article history:

Received 26 May 2016

Received in revised form

29 June 2016

Accepted 13 July 2016

Available online 15 July 2016

ABSTRACT

We have investigated the magnetodynamic properties of $\text{La}_{0.7}\text{Sr}_{0.3}\text{MnO}_3$ (LSMO) films of thickness 10, 15 and 30 nm grown on (111)-oriented SrTiO_3 (STO) substrates by pulsed laser deposition. Ferromagnetic resonance (FMR) experiments were performed in the temperature range 100–300 K, and the magnetodynamic damping parameter α was extracted as a function of both film thickness and temperature. We found that the damping is lowest for the intermediate film thickness of 15 nm with $\alpha \approx 2 \cdot 10^{-3}$, where α is relatively constant as a function of temperature well below the Curie temperature of the respective films.

© 2016 Elsevier B.V. All rights reserved.

1. Introduction

The magnetodynamic properties of nanostructures have received extensive attention, from both fundamental and applications viewpoints [1–3]. Nanometer sized magnetic elements play an important role in advanced magnetic storage schemes [4,5], and their static and most importantly their dynamic magnetic properties are being intensely studied [6–8].

Complex magnetic oxides display intriguing properties that make these materials promising candidates for spintronics and other magnetic applications [9]. Manganites have received attention due to a large spin polarization, the appearance of colossal magneto-resistance and a Curie temperature above room temperature [10–13]. Within manganites, LSMO has been regarded as one of the prototype model systems. Transport and static magnetic properties of LSMO are well studied, but less attention has been paid to the magnetodynamic properties. For applications in magnetodynamic devices a low magnetic damping is desirable, and having well defined magnetic properties when confined to nanoscale dimensions is crucial.

The dynamic properties can be investigated by ferromagnetic resonance spectroscopy (FMR), which can be used to extract

information about e.g. the effective magnetization, anisotropies and the magnetodynamic damping. Earlier studies on LSMO have investigated the dynamic properties of the magnetic anisotropies [14], also providing evidence for well defined resonance lines, which is a prerequisite for magnetodynamic devices.

The magnetodynamic damping is an important material parameter that can be obtained through FMR spectroscopy by measuring the resonance linewidth as a function of frequency. The linewidth of the resonance peaks has two contributions; an inhomogeneous contribution that does not depend on the frequency, and the dynamic contribution that is proportional to the precession frequency and to the damping parameter α .

Earlier studies by Luo et al. have investigated the magnetic damping in LSMO films grown on (001)-oriented STO capped by a normal metal layer [15,16], and found a damping parameter of $\alpha \approx 1.6 \cdot 10^{-3}$ for a 20 nm thick LSMO film at room temperature. Typical ferromagnetic metals have damping values of $\alpha \approx 10^{-2}$, and the low damping indicate LSMO as a promising material for applications in magnetodynamic devices. The studies by Luo et al. were performed at room temperature, whereas the Curie temperature of LSMO is around 350 K. However, the Curie temperature depends strongly on film thickness and approaches room temperature as the thickness is decreased. Being able to control the temperature is thus important in order to accurately characterize the damping in thin LSMO films.

* Corresponding author.

E-mail address: vflovik@gmail.com (V. Flovik).

The thickness and temperature dependence of static and dynamic magnetic properties of thin film LSMO grown on (001)-oriented STO have been investigated in a previous study by Monsen et al. [17]. The dynamic properties were characterized from the FMR linewidth measured in a cavity based FMR setup at a fixed frequency of 9.4 GHz, and provided evidence that the magnetic damping is dominated by extrinsic effects for thin films.

The properties of complex magnetic oxides are very sensitive to the structural parameters, hence thin film growth can be used to engineer the magnetic properties. We have previously shown that LSMO grown on (001)-oriented STO results in a biaxial crystalline anisotropy, compared with almost complete in-plane isotropy for LSMO grown on (111)-oriented STO [18]. The possibility to control the functional properties at the nm-scale make these materials promising for spintronics and other magnetic based applications. Hence, detailed studies on how film thickness affect the magnetic properties is important.

Here, we investigate the magnetodynamic properties of pulsed laser deposited LSMO films of thickness 10, 15 and 30 nm grown on (111)-oriented STO (in contrast to the previous study by Monsen et al. for LSMO grown on (001)-oriented STO [17]). By performing broadband FMR experiments we separate the inhomogeneous linewidth broadening and the dynamic contribution to the FMR linewidth, and extract the magnetodynamic damping parameter α . The main objective of our study is to characterize α for the various film thicknesses. However, as T_c changes with film thickness, it is difficult to compare the absolute values at a single temperature. We thus performed experiments in the temperature range $T=100\text{--}300$ K using the FMR setup described in Section 2.2, allowing us to extract α as a function of both temperature and film thickness.

2. Sample growth and experimental setup

2.1. Sample growth and characterization

$\text{La}_{0.7}\text{Sr}_{0.3}\text{MnO}_3$ thin films were deposited by pulsed laser deposition on (111)-oriented SrTiO_3 substrates. A KrF excimer laser ($\lambda = 248$ nm) with a fluency of ≈ 2 J cm^{-2} and repetition rate 1 Hz was employed, impinging on a stoichiometric $\text{La}_{0.7}\text{Sr}_{0.3}\text{MnO}_3$ target. The deposition took place in a 0.35 mbar oxygen ambient, at 500 °C and the substrate-to-target separation was 45 mm, resulting in thermalized ad-atoms [19,20]. After the deposition, the films were cooled to room temperature in 100 mbar of oxygen at a rate of 15 K/min. Atomic force microscopy (AFM) was used to study the surface topography. The AFM topography images shown in Fig. 1a confirm the step and terrace morphology of the films after growth for the 10 nm and 15 nm thick films. For the 30 nm film, we observe a surface relaxation and transition to a more 3 dimensional growth and rougher surface compared to the 2 dimensional layer by layer growth for thinner films.

The crystalline structure of the films was investigated using x-ray diffraction (XRD), and the XRD scans of the respective films are shown in Fig. 1b.

Magnetic moment measurements were performed with a vibrating sample magnetometer (VSM). In Fig. 1c the temperature dependence of the saturation magnetization is plotted against temperature, taken during warm-up after field cooling in 2 T. Both saturated moment and T_c increase with film thickness as expected for thin films, and the values are comparable to similar thicknesses of LSMO films grown on (001)-oriented SrTiO_3 [17].

2.2. FMR experiments

The FMR experiments were performed using a vector network

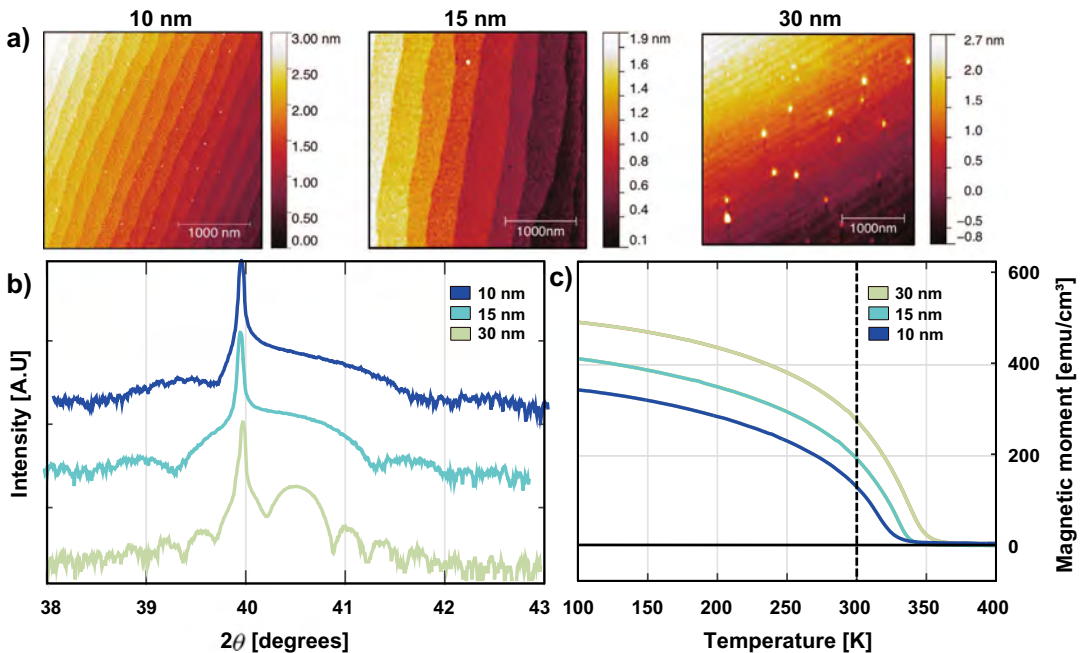


Fig. 1. (a) AFM topography for films of thickness 10 nm, 15 nm and 30 nm. (b) XRD $\theta - 2\theta$ scans of the Bragg reflection for the respective film thicknesses. (c) Magnetic moment measurements (performed with a vibrating sample magnetometer, (VSM)), showing the difference in magnetic moment and Curie temperature for the various film thicknesses.

analyzer (VNA) setup in combination with a coplanar waveguide (CPW) that created microwave magnetic fields of different frequencies to the film's structure. We used a He cryostat with a superconducting magnet capable of producing bipolar bias fields up to 5 T. The experiments were performed in the temperature range $T = 100 - 300$ K using a CPW designed specially for the cryostat and using semi-rigid coaxial cables capable to carry up to 50 GHz electrical signals.

The static external field, H_0 , was applied in the sample plane, and perpendicular to the microwave fields from the CPW. We measured the microwave transmission and reflection parameters as a function of field and frequency in order to obtain a complete map of the ferromagnetic resonances. Magnetic fields were varied from -500 to 500 mT, and microwave frequencies from 1 to 20 GHz.

By measuring the microwave absorption as a function of both microwave frequency and the applied external field, one can obtain the FMR dispersion. The field vs. frequency dispersion when the field is applied in the film plane is described by the Kittel equation [21] given by the following:

$$f_{\text{FMR}} = \frac{\gamma}{2\pi} \sqrt{H_0(H_0 + H_{\text{eff}})}. \quad (1)$$

Here, f_{FMR} is the FMR frequency and γ is the gyromagnetic ratio, where $\gamma/2\pi \approx 28$ GHz/T. H_0 is the applied external field and $H_{\text{eff}} = 4\pi M_s - H_k$ is the effective field given by the saturation magnetization M_s and the anisotropy field H_k .

The FMR absorption lineshape is often assumed to have a symmetric Lorentzian lineshape. However, in conductive samples, induced microwave eddy currents in the film can affect the lineshape symmetry [22,23]. In an experimental setup containing waveguides, coaxial cables etc., the relative phase between the electric and magnetic field components can also affect the lineshape [24,25]. We thus fit the FMR absorption, χ , to a linear combination of symmetric and antisymmetric contributions, determined by the β parameter in Eq. (2).

$$\chi = A \frac{1 + \beta(H_R - H_0)\Delta H}{(H_R - H_0)^2 + (\Delta H/2)^2}. \quad (2)$$

Here A is an amplitude prefactor, H_R and H_0 are the resonance field and external field respectively and ΔH the full linewidth at half maximum (FWHM). By measuring the FMR linewidth as a function of the microwave frequency f_{mw} , we extract the damping parameter α and the inhomogeneous linewidth broadening ΔH_0 from the following relation [26]:

$$\Delta H = \frac{4\pi}{\gamma} \alpha f_{\text{mw}} + \Delta H_0. \quad (3)$$

3. Results and discussion

The measured FMR absorption shows a good agreement with the Kittel dispersion given by Eq. (1). In Fig. 2a we show as an example the FMR dispersion for the 15 nm film measured at room temperature, with the fit to Eq. (1) as dotted line. A typical absorption lineshape and the fit to Eq. (2) is shown as inset. Fitting the FMR dispersion to Eq. (1) allows us to extract the effective field H_{eff} , given by the saturation magnetization M_s and the anisotropy field H_k through the relation $H_{\text{eff}} = 4\pi M_s - H_k$. The extracted values of H_{eff} for the various films are shown in Fig. 2b. From H_{eff} and M_s (shown in Fig. 1c) we calculate the anisotropy field H_k . The obtained values for H_k are shown in Fig. 2c and indicate a strain induced negative perpendicular magnetocrystalline anisotropy (PMA), as expected for epitaxial films. The negative PMA is in agreement with that observed in LSMO grown on (001)-oriented STO [27]. As indicated in Fig. 2c, the PMA is strongest for the thinnest film and decreases as one approaches the Curie temperature.

The main objective of our study is to characterize the magnetodynamic damping, as measured through the FMR linewidth. As an example we show in Fig. 2d the linewidth vs. frequency for the 15 nm sample at $T = 300$ K. The linear relation between linewidth

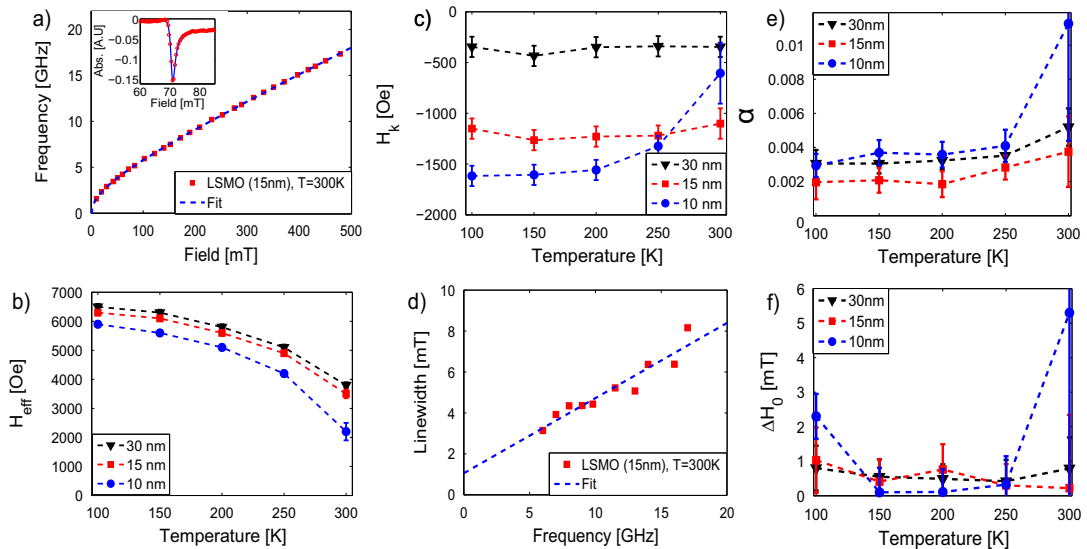


Fig. 2. (a) FMR frequency vs. external magnetic field. Experimental datapoints as red squares, and fit to Eq. (1) as dotted line. Inset: typical absorption lineshape and the fit to Eq. (2). (b) Extracted values of H_{eff} from the fit to Eq. (1). (c) Calculated anisotropy fields H_k . (d) FMR absorption linewidth vs. frequency. Experimental datapoints shown as red squares, and the fit to Eq. (3) as dotted line. (e) Extracted damping parameter α and (f) inhomogeneous linewidth broadening ΔH_0 as a function of film thickness and temperature. (For interpretation of the references to color in this figure legend, the reader is referred to the web version of this article.)

and frequency from Eq. (3) allows us to extract the damping parameter α and the inhomogeneous linewidth broadening ΔH_0 .

To ensure all samples are in a fully ferromagnetic (FM) state, we first compare the damping well below T_c of the respective films. We find that the damping is relatively constant as a function of temperature well below T_c , as shown in Fig. 2e, and the lowest damping was found for the intermediate film thickness of 15 nm with $\alpha \approx 2 \cdot 10^{-3}$. This value of α is comparable to that found in a previous study by Luo et. al. [15] for an LSMO film of thickness 20 nm, but in their case grown on (001)-oriented STO.

We observe an increased damping as the temperature approaches the Curie temperature of the respective films, which we attribute to the coexistence of ferromagnetic and paramagnetic domains as $T \rightarrow T_c$. The increase in damping is largest for the 10 nm film, in agreement with the reduced T_c for this film compared to the thicker 15 nm and 30 nm films, as shown in Fig. 1c. This behavior is consistent with data from LSMO single crystals [28], and with previous work by Monsen et. al. [17] for LSMO films grown on (001)-oriented STO.

The difference in damping for the various film thicknesses is observed well below T_c (see Fig. 2e), and is thus not caused by the coexistence of ferromagnetic and paramagnetic domains. The increased damping for the 10 nm film compared to the 15 nm film is rather attributed to the increased importance of surface defects for the thinnest film. Surface/interface imperfections/scatterers induce a direct thickness dependent broadening due to local variations in resonance field, or indirectly through two-magnon processes, as these contributions become more dominating as the film thickness is reduced [29]. Previous studies of the thickness dependence of the FMR linewidth in LSMO films grown on (001)-oriented STO by Monsen et. al. [17] show similar behavior, with a minimum in the linewidth for an intermediate film thickness and increased linewidth for thicknesses below approximately 10 nm.

For the 30 nm film we also observe an increased damping compared to the 15 nm film. Interface effects should be less important for the 30 nm film, and the increased damping is attributed to other effects as the thickness is increased. It is known that LSMO films can experience strain relief relaxation as the film thickness is increased [30,31], and for the 30 nm film we observe a rougher surface compared to the thinner films. This change in film structure can be observed in the AFM topography images in Fig. 1a, and the difference in film structure could thus cause an increased damping for the thickest film. Another consideration is the eddy-current contribution to the damping in conducting films [32]. The eddy-current contribution scales with the film thickness d , as d^2 , and separating the various contributions to the damping would thus require a more detailed study of the scaling of damping vs. film thickness.

In a homogeneous strain-free ferromagnet one expects that the inhomogeneous linewidth broadening, ΔH_0 , should be independent of temperature well below T_c [33]. The relatively temperature independence of ΔH_0 for the 15 nm and 30 nm films shown in Fig. 2f indicate high quality samples, with $\Delta H_0 < 1$ mT. For the 10 nm film there is a slight increase in ΔH_0 at low temperature, with an inhomogeneous broadening of $\Delta H_0 \approx 2$ mT. The increase in ΔH_0 at 300 K is attributed to the reduced T_c of the 10 nm film compared to the 15 and 30 nm films, and the coexistence of ferromagnetic and paramagnetic domains as $T \rightarrow T_c$.

4. Summary

We have characterized the magnetic damping parameter α in 10, 15 and 30 nm thick LSMO films grown on (111)-oriented STO for temperatures $T=100\text{--}300$ K. We found that α is relatively independent of temperature well below the Curie temperature of

the respective films, with a significant increase as $T \rightarrow T_c$ due to the coexistence of ferromagnetic and paramagnetic domains. The lowest damping was found for the intermediate film thickness of 15 nm, with $\alpha \approx 2 \cdot 10^{-3}$. For the 10 nm film, we attribute the increased damping to the increased importance of surface/interface imperfections/scatterers for thinner films. For the 30 nm film the increased damping is attributed to changes in the film structure with an increased surface roughness compared to the thinner films, as well as additional eddy-current contributions to the damping as the film thickness is increased.

The damping of $\alpha \approx 2 \cdot 10^{-3}$ for the 15 nm film is lower than that of e.g. Permalloy ($\text{Ni}_{80}\text{Fe}_{20}$) which is one of the prototype materials for magnetodynamic devices. The low damping, in addition to other intriguing material properties like large spin polarization, indicate LSMO as a promising material for applications in magnetodynamic devices.

Acknowledgments

This work was supported by the Norwegian Research Council (NFR), project number 216700. V.F acknowledge partial funding obtained from the Norwegian Ph.D. Network on Nanotechnology for Microsystems, which is sponsored by the Research Council of Norway, Division for Science, under contract no. 221860/F40. F.M. acknowledges financial support from RYC-2014-16515 and from the MINECO through the Severo Ochoa Program (SEV- 2015-0496). J.M and F.M also acknowledge funding from MINECO through MAT2015-69144.

References

- [1] R.L. Stamps, et al., J. Phys. D: Appl. Phys. 47 (2014) 333001.
- [2] J. Åkerman, Science 308 (2005) 508.
- [3] S.D. Bader, Rev. Mod. Phys. 78 (2006) 1.
- [4] A. Moser, K. Takano, D.T. Margulies, M. Albrecht, Y. Sonobe, T. Ikeda, S. Sun, E. E. Fullerton, J. Phys. D: Appl. Phys. 35 (2002) R157.
- [5] S.S.P. Parkin, K.P. Roche, M.G. Samant, P.M. Rice, R.B. Beyers, R.E. Scheuerein, E. J. O'Sullivan, S.L. Brown, J. Bucchigano, D.W. Abraham, Y. Lu, M. Rooks, P. L. Trouilloud, R.A. Wanner, W.J. Gallagher, J. Appl. Phys. 85 (1999) 5828.
- [6] R.L. Stamps, et al., J. Phys. D: Appl. Phys. 47 (2014) 333001.
- [7] V.V. Kruglak, S.O. Demokritov, D. Grundler, J. Phys. D: Appl. Phys. 43 (2010) 264001.
- [8] V. Flovik, F. Macià, J.M. Hernández, R. Bručas, M. Hanson, E. Wahlström, Phys. Rev. B 92 (2015) 104406.
- [9] M. Bibes, A. Barthelemy, IEEE Trans. Electron Devices 54 (5) (2007) 1003–1023.
- [10] J.-H. Park, E. Vescovo, H.-J. Kim, C. Kwon, R. Ramesh, T. Venkatesan, Nature 392 (1998) 794–796.
- [11] M. Bowen, M. Bibes, A. Barthélemy, J.-P. Contour, A. Anane, Y. Lemaître, A. Fert, Appl. Phys. Lett. 82 (2003) 233.
- [12] Y. Tokura, Y. Tomioka, J. Magn. Magn. Mater. 200 (1999) 1.
- [13] S. Jin, T.H. Tiefel, M. McCormack, R.A. Fastnacht, R. Ramesh, L.H. Chen, Science 264 (1994) 413.
- [14] M. Belmeguenai, S. Mercone, C. Adamo, L. Méchin, C. Fur, P. Monod, P. Moch, D. G. Schlom, Phys. Rev. B 81 (2010) 054410.
- [15] G.Y. Luo, M. Belmeguenai, Y. Roussigné, C.R. Chang, J.G. Lin, S.M. Chérif, AIP Adv. 5 (2015) 097148.
- [16] G.Y. Luo, C.R. Chang, J.G. Lin, J. Appl. Phys. 115 (2014) 17C508.
- [17] Å. Monsen, J.E. Boshker, F. Macià, J.W. Wells, P. Nordblad, A.D. Kent, R. Mathieu, T. Tybell, E. Wahlström, J. Magn. Magn. Mater. 369 (2014).
- [18] I. Hallsteinsen, E. Folven, F.K. Olsen, R.V. Chopdekar, M.S. Rzczowski, C.B. Eom, J.K. Grepstad, T. Tybell, APL Mater. 3 (2015) 062501.
- [19] I. Hallsteinsen, M. Nord, T. Bolstad, P.-E. Vullum, J.E. Boshker, R. Takahasi, R. Holmestad, M. Lippmaa, T. Tybell, Cryst. Growth Des. 16 (4) (2016) 2357, <http://dx.doi.org/10.1021/acs.cgd.6b00143>.
- [20] J.E. Boshker, E. Folven, Å. Monsen, E. Wahlström, J.K. Grepstad, T. Tybell, Cryst. Growth Des. 12 (563-566) (2012).
- [21] C. Kittel, Phys. Rev. 73 (1948) 155.
- [22] V. Flovik, F. Macià, A.D. Kent, E. Wahlström, J. Appl. Phys. 117 (2015) 143902.
- [23] V. Flovik, B.H. Pettersen, E. Wahlström, J. Appl. Phys. 119 (2016) 163903.
- [24] M. Harder, Z.X. Cao, Y.S. Gui, X.L. Fan, C.-M. Hu, Phys. Rev. B 84 (2011) 054423.
- [25] A. Wirthmann, X. Fan, Y.S. Gui, K. Martens, G. Williams, J. Dietrich, G.E. Bridges, C.-M. Hu, Phys. Rev. Lett. 105 (2010) 017202.
- [26] S.S. Kalarickal, P. Krivosik, M. Wu, C.E. Patton, M.L. Schneider, P. Kabos, T.

- J. Silva, J.P. Nibarger, *J. Appl. Phys.* 99 (2006) 093909.
- [27] H.K. Lee, I. Barsukov, A.G. Swartz, B. Kim, L. Yang, H.Y. Hwang, I.N. Krivorotov, *AIP Adv.* 6 (2016) 055212.
- [28] S.E. Lofland, P. Kim, P. Dahirol, S.M. Bhagat, S.D. Tyagi, S.G. Kerbashev, D. A. Shulyatev, A.A. Arsenov, Y. Mukovskii, *Phys. Lett. A* 233 (4–6) (1997).
- [29] A.Yu. Dobin, R.H. Victora, *Phys. Rev. Lett.* 92 (2004) 257204.
- [30] Y.C. Liang, Y.C. Liang, *J. Cryst. Growth* 304 (2007) 275.
- [31] I. Hallsteinsen, J.E. Boschker, M. Nord, S. Lee, M. Rzechowski, P.E. Vullum, J. K. Grepstad, R. Holmestad, C.B. Eom, T. Tybell, *J. Appl. Phys.* 113 (2013) 183512.
- [32] M. Kostylev, *J. Appl. Phys.* 119 (2016) 013901.
- [33] S.E. Lofland, S.M. Bhagat, C. Kwon, S.D. Tyagi, Y.M. Mukovskii, S.G. Karbashev, A.M. Balbashov, *J. Appl. Phys.* 81 (1997) 5737.

9.2 Paper II

Vegard Flovik, Ferran Macià, Andrew D. Kent, Erik Wahlström.

Eddy current interactions in a ferromagnet-normal metal bilayer structure, and its impact on ferromagnetic resonance lineshapes

J. Appl. Phys. 117, 143902 (2015)

Eddy current interactions in a ferromagnet-normal metal bilayer structure, and its impact on ferromagnetic resonance lineshapes

Vegard Flovik,^{1,a)} Ferran Macià,² Andrew D. Kent,³ and Erik Wahlström¹

¹*Department of Physics, Norwegian University of Science and Technology, N-7491 Trondheim, Norway*

²*Grup de Magnetisme, Dept. de Física Fonamental, Universitat de Barcelona, Barcelona, Spain*

³*Department of Physics, New York University, 4 Washington Place, New York, New York 10003, USA*

(Received 22 January 2015; accepted 31 March 2015; published online 8 April 2015)

We investigate the effect of eddy currents on ferromagnetic resonance (FMR) in ferromagnet-normal metal (FM/NM) bilayer structures. Eddy-current effects are usually neglected for NM layer thicknesses below the microwave (MW) skin depth (≈ 800 nm for Au at 10 GHz). However, we show that in much thinner NM layers (10–100 nm of Au or Cu) they induce a phase shift in the FMR excitation when the MW driving field has a component perpendicular to the sample plane. This results in a strong asymmetry of the measured absorption lines. In contrast to typical eddy-current effects, the asymmetry is larger for thinner NM layers and is tunable through changing the sample geometry and the NM layer thickness. © 2015 AIP Publishing LLC.

[<http://dx.doi.org/10.1063/1.4917285>]

I. INTRODUCTION

Eddy currents are induced currents in conductors by changing magnetic fields. These currents flow in closed loops perpendicular to the driving fields, and produce additional Oersted fields that partially compensate the external driving fields. The effects of eddy currents on ferromagnetic resonance (FMR) in conducting films are well known in the limit of film thickness approaching their electro-magnetic skin depth (≈ 800 nm for bulk Au at 10 GHz). In those cases, eddy-current effects can lead to linewidth broadening and give rise to spin-wave excitations due to inhomogeneous microwave fields.^{1,2}

The microwave frequency spin dynamics in nanostructures usually involves stacks of layers combining FM and NM at the nanometer scale.^{3,4} Although eddy-current effects are usually neglected in metals with thicknesses below their skin depth, some studies have shown that this may be important also for normal metal (NM) films far below their skin depth.^{5–10} In these studies, it was predominantly microwave-screening effects that were considered, and little attention was paid to how the induced Oersted fields can affect the magnetization dynamics in an adjacent ferromagnetic thin film.

FMR spectroscopy experiments probe static and dynamic properties of magnetic materials. The technique relies on measuring the microwave absorption associated to the precession of the magnetization. In FMR experiments, position and width of absorption lines carry valuable information about material parameters such as anisotropy fields and magnetic damping.¹¹

Many experimental setups used for such studies have the main component of the MW driving field oriented in the sample plane (coplanar waveguide (CPW)/stripline FMR). Non-uniformity of the MW field, and sample position with

respect to the CPW/stripline center would still lead to field components perpendicular to the sample plane, which would enhance the effects of eddy currents. On the other hand, in cavity-FMR setups, the MW fields can be oriented either parallel or perpendicular to the sample plane depending on the cavity.

Differences in symmetry of FMR lines have been used to study the spin pumping from a magnetic material to a normal metal.^{12–14} We notice here that a recent study has reported different values for the voltage induced by the inverse spin hall effect, depending on the cavity mode used.¹⁵ In such studies, lineshape symmetry is one of the main parameters used to analyze the results.

Hence, to correctly interpret experimental data involving FMR it is important to understand how eddy currents—even in very thin films—can cause modifications in the measured FMR lineshape.

In this study, we investigate the contribution of eddy currents to the FMR absorption lineshapes in ferromagnet-normal metal (FM/NM) bilayer structures. We have systematically studied how the sample geometry and NM thickness affect the coupling between microwave (MW) fields and eddy-current-induced fields, and we show that this coupling is tunable through changing the sample geometry and the NM layer thickness.

II. THEORETICAL MODEL FOR THE OBSERVED LINESHAPES

The ferromagnetic resonance is usually driven directly by the MW field from a cavity or from a coplanar waveguide/microstrip line. However, capping a FM sample with a NM layer leads to circulating eddy currents in the NM, and additional Oersted fields in the FM. These Oersted fields have a different phase with respect to the MW fields—there is a relative phase lag between the MW fields and the Oersted fields from the induced currents—and this results in a distortion of the FMR lineshape. A sketch of the FM/NM

^{a)}Electronic mail: vegard.flovik@ntnu.no

bilayer geometry and the path of the induced eddy currents are shown in Fig. 1(a). The induced currents flow in closed loops in the sample plane, with highest current density along the sample edges.^{16,17} Figures 1(b) and 1(c) compare two representative FMR lineshapes for a 10 nm Py sample before and after capping it with 10 nm Au; although resonance frequency and linewidth stay constant, the lineshape changes considerably.

To understand the origin of the distorted lineshapes due to the induced eddy currents, we consider a model describing the magnetization dynamics of the FM, starting from the Landau Lifshitz Gilbert equation¹⁸

$$\frac{\partial \mathbf{M}}{\partial t} = -\gamma \mathbf{M} \times \mathbf{H}_{\text{eff}} + \frac{\alpha}{M_s} \left(\mathbf{M} \times \frac{\partial \mathbf{M}}{\partial t} \right), \quad (1)$$

where γ is the gyromagnetic ratio, α is the Gilbert damping parameter, and M_s is the saturation magnetization. The effective magnetic field, \mathbf{H}_{eff} , includes the external field \mathbf{H}_0 , the anisotropy field, \mathbf{H}_A (we neglect the effects of dipole and exchange fields), and a driving oscillatory field, \mathbf{h}_{ac} , composed of MW fields and fields from the eddy currents. In the following, the contribution from the anisotropy field to the effective field is neglected, as this is negligible compared to the resonance field for Py.

We assume the external applied field, \mathbf{H}_0 , is along \mathbf{z} in the film plane (see Fig. 1(a)) and only consider perturbations of the oscillatory field, \mathbf{h}_{ac} , in the x-y plane, perpendicular to the external applied field (the components in the direction of the applied field do not directly perturb the dynamics of \mathbf{M}).

The phase of the microwave excitation in any FMR experiment is arbitrary and can depend on many factors. However, as we are only interested in relative phase differences, we can set the reference phase of the MW field to zero. The combined driving field can thus be written in the form

$$\begin{aligned} \mathbf{h}_{\text{ac}}(t) &= \mathbf{h}_{\text{MW}} e^{i\omega t} + \mathbf{h}_{\text{ind}} e^{i(\omega t - \phi)} \\ &= [\mathbf{h}_{\text{MW}} + \mathbf{h}_{\text{ind}}(\cos \phi - i \sin \phi)] e^{i\omega t} \equiv \mathbf{h} e^{i\omega t} [1 - \beta i], \end{aligned} \quad (2)$$

where ϕ is the relative phase difference between the MW field and the induced field, and $\mathbf{h} = \mathbf{h}_{\text{MW}} + \mathbf{h}_{\text{ind}} \cos \phi$. The parameter β is thus defined as

$$\beta = (\mathbf{h}_{\text{ind}} \sin \phi) / (\mathbf{h}_{\text{MW}} + \mathbf{h}_{\text{ind}} \cos \phi) = (\beta_x, \beta_y), \quad (3)$$

and accounts for the relative magnitude of the two fields and their phases in the x/y direction, respectively. The parameter β will thus approach zero when the induced field is small compared to the MW field, or the phase difference between the MW field and the induced field is close to 0° . There will also be maxima for β for some value of the phase difference in the range between 90° and 180° , which depends on the magnitude of the induced field compared to the MW field.

The magnetization $\mathbf{M}(t)$ is then taken the form $\mathbf{M}(t) = M_0 \mathbf{z} + \mathbf{m} e^{i\omega t}$, where $\mathbf{m} \perp \mathbf{z}$. The magnetic response to small excitation fields, $\mathbf{m} = \boldsymbol{\chi} \mathbf{h}$, is determined by the Polder susceptibility tensor $\boldsymbol{\chi}$.¹⁹

The elements of $\boldsymbol{\chi}$ were determined by solving Eq. (1), and discarding higher order terms. Setting $\mathbf{m} = \boldsymbol{\chi} \mathbf{h}$ and introducing $\omega_0 = \gamma H$ and $\omega_M = \gamma M_0$, one obtains

$$\boldsymbol{\chi} = \begin{pmatrix} \chi_{xx} & i\chi_{xy} \\ -i\chi_{yx} & \chi_{yy} \end{pmatrix}, \quad (4)$$

where the matrix elements are given by

$$\chi_{xx/yy} = \frac{(1 - i\beta_{x/y})\omega_M(\omega_0 + i\alpha\omega)}{\omega_0^2 - \omega^2(1 + \alpha^2) + 2i\alpha\omega\omega_0}, \quad (5)$$

$$\chi_{xy/yx} = \frac{(1 - i\beta_{y/x})\omega\omega_M}{\omega_0^2 - \omega^2(1 + \alpha^2) + 2i\alpha\omega\omega_0}. \quad (6)$$

The observable quantity in our FMR experiments is the MW power absorption, which is given by an integral over the sample volume V ²⁶

$$P_{\text{abs}} = \frac{1}{2} \Re \int_V i\omega(\boldsymbol{\chi} \mathbf{h}) \cdot \mathbf{h}^* dV. \quad (7)$$

Splitting $\boldsymbol{\chi}$ into its real and imaginary part and using that h_x and h_y are orthogonal, one obtains

$$\begin{aligned} P_{\text{abs}} &= \frac{1}{2} \Re \int_V i\omega [\boldsymbol{\chi}' + i\boldsymbol{\chi}''] \begin{pmatrix} h_x \\ h_y \end{pmatrix} \cdot (h_x^*, h_y^*) dV \\ &= -\frac{1}{2} \int_V \omega \begin{pmatrix} \chi''_{xx} h_x + \chi''_{xy} h_y \\ \chi''_{yx} h_x + \chi''_{yy} h_y \end{pmatrix} \cdot (h_x^*, h_y^*) dV \\ &\propto \omega (\chi''_{xx} h_x^2 + \chi''_{yy} h_y^2). \end{aligned} \quad (8)$$

The MW power absorption is thus given by the imaginary part of the diagonal elements χ''_{xx} and χ''_{yy} , for the field components in the x/y direction, respectively.

Using that $\chi_{yy/xx}$ is written in the form $\chi_{yy/xx} = Z_1/Z_2$, where Z_i are complex numbers, one can separate the real and imaginary parts by multiplying the expression by the

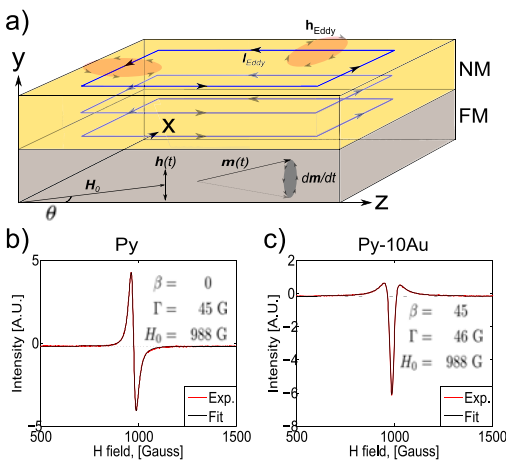


FIG. 1. (a) A schematic of the sample geometry showing the path of the induced eddy currents flowing in closed loops around the sample, with highest current density along the sample edges.^{16,17} (b) and (c) FMR lineshapes and fitted parameters from Eq. (14) for a sample with 10 nm Py (b), and the same sample after being capped with 10 nm Au (c).

complex conjugate of the denominator: $\chi_{yy}/\chi_{xx} = \frac{z_1 z_2}{z_2 z_1}$. Assuming low damping, ($\alpha^2 \approx 0$) this gives

$$\Re(\chi_{xx}/\chi_{yy}) = \frac{\omega_0 \omega_M (\omega_0^2 - \omega^2) - \beta_{x/y} \alpha \omega \omega_M (\omega_0^2 + \omega^2)}{(\omega_0^2 - \omega^2)^2 + (2\alpha \omega \omega_0)^2}, \quad (9)$$

$$\Im(\chi_{xx}/\chi_{yy}) = \frac{-\alpha \omega \omega_M (\omega_0^2 + \omega^2) - \beta_{x/y} \omega_0 \omega_M (\omega_0^2 - \omega^2)}{(\omega_0^2 - \omega^2)^2 + (2\alpha \omega \omega_0)^2}. \quad (10)$$

As the FMR linewidth for permalloy films is small compared to the resonance frequency, one can assume that one does not need to deviate far from the resonance in order to observe the shape of the curve. That being the case, $\omega_0^2 + \omega^2 \approx 2\omega_0^2$, and

$$(\omega_0^2 - \omega^2)^2 = (\omega_0 + \omega)^2 (\omega_0 - \omega)^2 \approx 4\omega_0^2 (\omega_0 - \omega)^2. \quad (11)$$

Hence, for narrow linewidths, Eq. (10) is well approximated by

$$\Im(\chi_{xx}/\chi_{yy}) \approx \left(\frac{-\omega_M \Gamma_w}{4} \right) \frac{1 + \beta_{x/y} (\omega_0 - \omega) / \Gamma_w}{(\omega_0 - \omega)^2 + (\Gamma_w/2)^2}, \quad (12)$$

where the parameter $\Gamma_w = 2\alpha\omega$ has been introduced to describe the linewidth. This expression consists of two components: a symmetric absorption lineshape arising from the in-phase driving fields, and an antisymmetric dispersive lineshape proportional to β arising from out-of-phase driving fields. The β parameter is thus determined by the ratio between the absorptive and dispersive contributions to the FMR lineshape.^{20,21}

In our set-up the microwave frequency is fixed at 9.4 GHz, and the magnetic field H_0 is then swept to locate the ferromagnetic resonance at the resonance field, $H_0 = H_R$, satisfying the condition for the resonance frequency, $\omega_R = \gamma \sqrt{H_R(H_R + 4\pi M_s)}$. To extract β from our experiments, we thus use an expression of same functional form as Eq. (12), but expressed in terms of field rather than frequency

$$\Im(\chi_{xx}/\chi_{yy}) = A \frac{1 + \beta_{x/y} (H_R - H_0) / \Gamma_H}{(H_R - H_0)^2 + (\Gamma_H/2)^2}, \quad (13)$$

where A is an unimportant proportionality factor and Γ_H has been introduced to describe the linewidth. In this form, Eq. (13) describes what is known in the literature as Dysonian lineshapes.²⁰⁻²²

In our experiments, we measure the field derivative of the MW absorption. The experimental data is thus fitted to the derivative of Eq. (13) with respect to the external field, which is given by

$$\frac{d}{dH_0} \Im(\chi_{xx}/\chi_{yy}) = A \left[\frac{-\beta_{x/y} / \Gamma_H}{(H_R - H_0)^2 + (\Gamma_H/2)^2} + \frac{2(H_R - H_0)[1 + \beta_{x/y} (H_R - H_0) / \Gamma_H]}{[(H_R - H_0)^2 + (\Gamma_H/2)^2]^2} \right]. \quad (14)$$

Through the β parameter, FMR lineshapes in an otherwise unperturbed system is thus a measure of the amplitudes

and relative phase of the MW field and the induced fields from eddy currents.

III. EXPERIMENTAL SETUP

Experiments were performed with Permalloy (Py = Fe₂₀Ni₈₀) as the ferromagnet layers, and gold (Au) and copper (Cu) as NM layers. The Py was grown by E-beam evaporation on oxidized silicon substrates, and the Au and Cu layers were grown by DC Magnetron sputter deposition. We controlled the thickness of the deposited NM layers using a Veeco Dektak 150 profilometer, and we cut our samples using a Dynatex DX-III combined scribe and breaker to obtain well defined sample geometries. Ferromagnetic resonance measurements were carried out in a commercial Electron Paramagnetic Resonance setup (Bruker Bio-spin ELEXSYS 500, with a cylindrical TE-011 microwave cavity).

The sample is attached to a quartz rod connected to a goniometer, allowing to rotate the sample 360°. The MW field is oriented perpendicular to the sample plane and is rotationally symmetric due to the cylindrical shape of the cavity, as shown in Fig. 2.

Our FMR experiments were performed with a low amplitude ac modulation of the static field, which allows lock-in detection to be used in order to increase the signal to noise ratio. The measured FMR signal is then proportional to the field derivative of the imaginary part of the susceptibility. The experimental data was thus fitted to Eq. (14), $d\chi/dH_0$ (i.e., we obtained an absorption line as in Fig. 1(b) when the driving field had only the MW component; we obtained an absorption line as in Fig. 1(c) when the driving field had a strong component from the eddy-current induced fields).

IV. RESULTS AND DISCUSSION

A. Effect of sample geometry

We first focus on the effect of the sample geometry. A full in-plane 360° rotation of a sample of dimensions

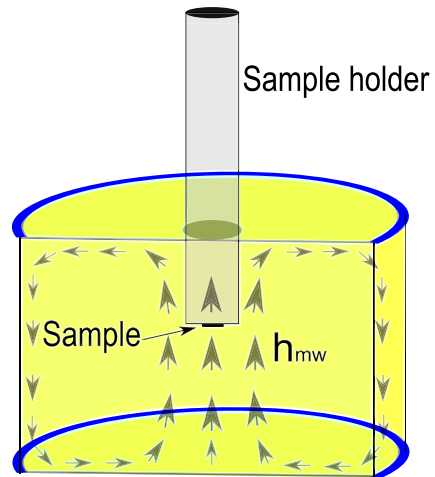


FIG. 2. Schematic of the cylindrical TE-011 microwave cavity, showing the sample position and field geometry.

1×3 mm with a thickness of 10 nm Py capped with 10 nm Au is shown in Fig. 3(a), where $\theta = 0$ corresponds to an applied field, H_0 , parallel to the short side of the sample. We note that although capping the sample with a thin NM layer affects the lineshape asymmetry considerably, the resonance field H_R and linewidth Γ stay constant. Thicker NM layers of materials with considerable spin orbit coupling would lead to a linewidth broadening due to loss of spin angular momentum through spin pumping effects, but for thin Cu/Au layers this effect is negligible.^{23,24}

The microwave field in the cavity can be considered uniform on the length scale of the sample, and rotationally symmetric due to its cylindrical shape. If the microwave excitation is inhomogeneous when rotating a long sample, it could be possible to excite magnetostatic modes in the FM film.²⁵ However, if this was the case in our experiments, one should observe the same asymmetry for the FM without the NM capping layer. To rule out conclusively this as a cause

of the asymmetry, we performed control experiments where we re-positioned the sample with an offset from the centre of the cavity (offset of the same order as the sample dimension). This did not affect the asymmetry of the lineshape, indicating that an inhomogeneous MW field in the cavity could not be the cause of the observed effect.

To investigate the effect of sample geometry further, a set of samples of dimensions $1 \times L$ mm, where L ranged from 0.5 to 4 mm was studied. The samples were again of 10 nm Py capped with 10 nm Cu and 5 nm Ta to prevent oxidation. We notice that the sample length in the direction parallel to the applied field is the main parameter that determines the asymmetry of the FMR lineshapes, given by the parameter β . Figure 3(b) shows the dependence of sample length when the varying dimension is parallel to the applied field. We see that the asymmetry increases with the sample's length and reaches a value where β appears to diverge at a length of about 3.3 mm. Samples with a length below 1 mm have lineshapes almost identical to samples with no NM capping.

We consider now the basic physics to describe the above results. The induced eddy currents flow in closed loops in planes perpendicular to the MW magnetic field, which is perpendicular to the film plane in our experiment. Thus, to obtain circulating eddy currents as shown in Fig. 1(a), it is required to have the MW field perpendicular to the film plane. We have conducted control experiments where the MW fields were applied in the film plane and we observed that the FMR lineshapes were always symmetric, indicating there were no observable effect of the eddy currents.

In our experimental geometry, the induced eddy currents flow mainly in circulating paths, with highest current density along the sample edges.^{16,17} The induced O_e fields have a component in the film plane and another perpendicular to the film plane. As indicated in Fig. 1(a), for the sample edges that are parallel to the applied field, the O_e fields will have the main in-plane component perpendicular to the applied field and could thus affect the FMR of the Py film. On the other hand, currents along sample edges perpendicular to the applied field will give rise to an in-plane Oersted field that is parallel to the applied field, and should not affect the FMR response.

The observed strong rotational dependence (see Fig. 3(a)) suggest that the effective driving field has the dominating contribution oriented in the sample plane; the contribution from the component perpendicular to the sample plane should not depend on the direction of the sample edges with respect to the applied field. As the effective driving field appears to be dominated by the in plane components, this indicates that the induced local field perturbing the FM is larger than the external field. This could be possible due to the close proximity to the induced currents at the FM/NM interface.

We now compare the length series with the rotational measurements by using a simple geometric approximation: we consider that the length of the sample parallel to the applied field is given by $L(\theta) = l \sin(\theta) + w \cos(\theta)$, where l and w are the length (3 mm) and width (1 mm) of the sample, and $\theta = 0$ corresponds to the applied field parallel to the short side of the sample. We have plotted in Fig. 3(b) the

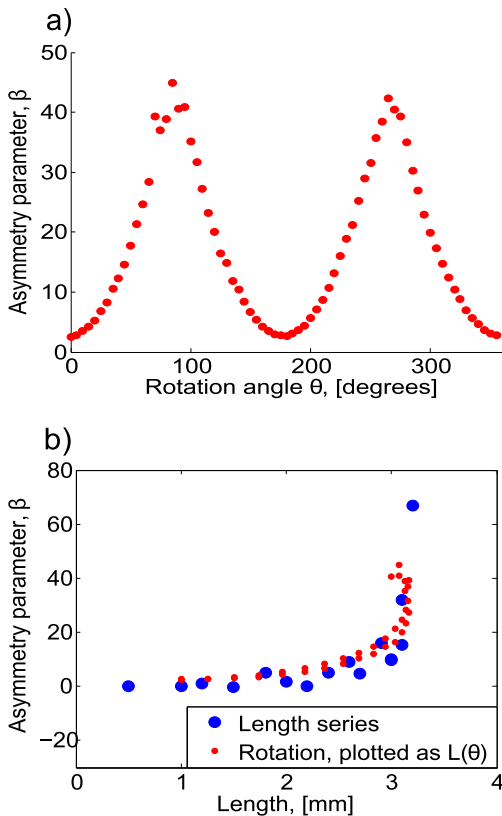


FIG. 3. (a) Angular dependence of the β parameter describing the FMR lineshape for a sample of 10 nm Py capped with 10 nm Au of dimension 1×3 mm; the applied field is rotated 360° in the film plane. (b) Sample length dependence of β for samples of 10 nm Py capped with 10 nm Cu (and 5 nm Ta to prevent oxidation) of dimensions $1 \times L$ mm, i.e., each datapoint in the "Length series" corresponds to a separate sample of length L . We also plotted in (b) the rotational measurements shown in (a) for a single sample, considering that the effective length in the direction of the applied field, H_0 , is approximated by $L(\theta) = l \sin(\theta) + w \cos(\theta)$, $l = 3$ mm and $w = 1$ mm.

rotational measurements following this approach and we can see that the resulting curve is almost identical to the length series.

To investigate the effect of sample size closer, we designed a control experiment that consisted of taking a large sample of dimensions 1×3 mm and dividing it into electrically isolated regions of 1×1 mm. This was performed using an automated scriber that scratched the sample without breaking it—we limited the size of the possible current loops (as illustrated in Fig. 4).

We tested this for samples with no NM capping, and the FMR signal was not affected. However, the same procedure on a sample capped with 10 nm Au presented a remarkable effect: the lineshape before scratching the sample was strongly asymmetric, but after scratching the film it returned to being symmetric again and matched the lineshapes for a sample of dimensions 1×1 mm.

The asymptotic behaviour of β as the sample length increases can be understood by considering how the sample size affects the magnitude of the induced field. As a simplified model, we approximate the current path as a rectangular loop around a sample of length l and width w . The induced electromotive force (EMF) is then given by the rate of change of magnetic flux through the area enclosed by the loop; its absolute value is given by $|\epsilon| = lw \left| \frac{\partial h}{\partial t} \right| \propto lw h_{MW} 2\pi f$, where f and h_{MW} are the MW frequency and amplitude, respectively. The resistance of such a loop is given by $R = 2R_s(l + w)/\zeta$, where R_s is the sheet resistance and ζ is the width of the current path. The induced current is finally given by $I = \epsilon/R$. We consider as an approximation that the magnetic field resulting from a current I in such a plane is given by $h_{ind} = \mu_0 I / 2\zeta$, where μ_0 is the vacuum permeability. The expression for the induced field is thus proportional to the sample size.

As an estimate for the strength of the induced field, we calculated this for a square sample, $w = l$, using the above expression for h_{ind} . The sheet resistance was measured to be $R_s \approx 50 \Omega$ for samples with 10 nm Py capped by 10 nm Cu and 5 nm Ta. Considering the width of the current path along the sample edge as $\zeta = w/4$, one can estimate the sample size where $h_{ind} = h_{MW}$. In the presence of a MW field of 9.4 GHz and $6 \mu T$ (values used during our experiments), we obtained that at a dimension of about 2×2 mm the induced field equals the MW field. Our estimate corresponds with what we see in the experiments: when the sample size approaches the mm scale, the effects become increasingly important.

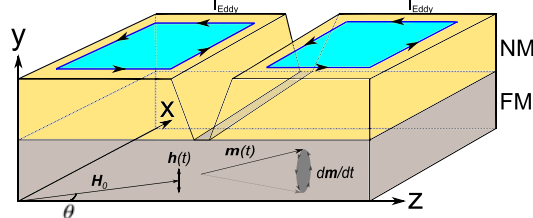


FIG. 4. Scratching the sample limits the size of the possible current loops, reducing the magnitude of the induced fields.

B. Thickness of NM layer

Next, we focus on another important parameter that governs the effect of eddy currents: the thickness of the NM layer. We prepared samples with a NM (both with Au and Cu) thickness ranging from 10 nm to $1 \mu m$ (Au) and 10–50 nm (Cu). (The experiments presented here were also performed in two more samples, where we obtained the same results. The measured asymmetry parameter β as a function of NM thickness is shown in Fig. 5 for a sample of dimensions 1×3 mm, with the applied field parallel to the long side of the sample. Replacing the Au layer by Cu in the range of 10–50 nm shows a similar behavior; the thicker the NM, the more symmetric the FMR lineshapes. In the thick film limit one observes asymmetric lineshapes again, but with an opposite sign of the β parameter.

To explain the thickness dependence, we use a simplified model where we assume that the induced eddy currents circulate in two dimensional planes in the NM layer. The Oersted fields originated by the eddy currents have a relative phase lag, ϕ , compared to the external MW field, which in the ideal case of no inductance is expected to be $\phi = -90$ deg ($I_{Eddy} \propto \frac{\partial h}{\partial t}$). However, due to the inductance and resistance of the NM film, there will be an additional phase between the MW field and the induced field that depends strongly on the NM thickness (due to the low conductivity of Py compared to Au/Cu, we consider the currents to circulate mainly in the NM layer). At larger thicknesses, one also needs to take into account phase shifts due to the skin effect. Considering this, one can write the relative phase lag as a function of NM thickness as²⁶

$$\phi(d) = - \left[90 + \tan^{-1} \left(\frac{\omega L(d)}{R(d)} \right) + d/\delta \right], \quad (15)$$

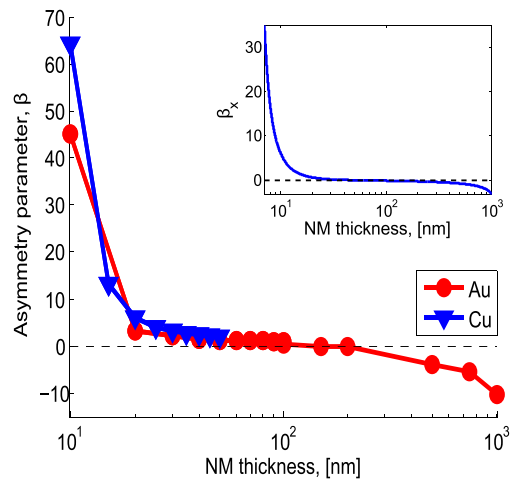


FIG. 5. NM thickness dependence of the β parameter describing the FMR lineshape for a sample of dimension 1×3 mm, with the applied field parallel to the long side of the sample. Comparing Au and Cu as NM layer in the region 0–50 nm. Inset: Calculated thickness dependence of β_x , given by Eqs. (3) and (15).

where ω is the microwave angular frequency, L and R are the inductance and resistance of the film, d is the NM thickness, and δ is the MW skin depth (≈ 800 nm for Au at 10 GHz).

To estimate values for the inductance, we consider a rectangular current path along the edges of the NM layer,²⁷ and sample dimensions of $w = 1$ mm, $l = 3$ mm with thickness d ($L \approx 10^{-8}$ H for a thickness of 10 nm).

$$L(d) = \frac{\mu_0 \mu_r}{\pi} \left[-2(w+l) + 2\sqrt{l^2 + w^2} - l \cdot \ln\left(\frac{l + \sqrt{l^2 + w^2}}{w}\right) - w \cdot \ln\left(\frac{w + \sqrt{l^2 + w^2}}{l}\right) + l \cdot \ln\left(\frac{2l}{\zeta d}\right) + w \cdot \ln\left(\frac{2w}{\zeta d}\right) \right], \quad (16)$$

where μ_r is the relative permeability of the NM film (≈ 1), and ζ is the width of the current path, set to $w/2$ in this calculation.

As mentioned in Sec. IV A, we measured a sheet resistance of $R_s \approx 50 \Omega$ for samples with 10 nm Py capped by 10 nm Cu and 5 nm Ta. However, for NM layers in this thickness regime, the conductivity depends strongly on the thickness. This is due to increased interface scattering in thin films when the thickness is of the same order as the electron mean free path. Due to this we estimate the film resistance, $R(d)$, as a function of thickness by introducing a correction factor, η , which describes a correction to the film conductivity compared to its bulk value. In Ref. 6 it was found that the increase in conductivity is close to linear in film thickness below 20–30 nm, before reaching an asymptotic value for thicker films. In our calculations we thus considered η to be a linear function of the film thickness below 20 nm: $\eta = \min\left(1, \frac{d}{l_{\text{mfp}}}\right)$, where d is the NM thickness and we set $l_{\text{mfp}} = 20$ nm.

From the rotational measurements, we argued that the effective driving field is dominated by the in plane component of the induced field. For thicker NM layers the sheet resistance is reduced, and the magnitude of the induced field should thus increase, as $|h_{\text{ind}}| \propto 1/R_s$. Due to this, the effective driving field should be dominated by the in plane component, h_x , also for thicker NM layers. From Eqs. (8) and (14), the asymmetry of the lineshape is then given by the parameter β_x .

Using these approximations, we computed the phase shift between the MW field and the induced field, and calculated the thickness dependence of β_x , given by Eqs. (3) and (15), illustrated in the inset of Fig. 5. As the NM thickness increase, the phase difference approaches a value of 180° , which then corresponds to $\beta_x = 0$ (i.e., the asymmetric lineshapes disappear quickly as the NM thickness increases). For thicker NM layers, one gets an additional contribution to the phase difference due to the skin effect. At a certain thickness the phase shift will thus be larger than 180° , which corresponds to an opposite sign of β_x .

These main features of our simple model agree well with the experimental data in Fig. 5, where the asymmetry drops off quickly with the thickness for thin NM layers. As

the thickness of the NM layer is increased further, one also observes the expected transition to asymmetric lineshapes again, but with an opposite sign of the β parameter. The thick film limit corresponds to the regime where one usually assumes eddy-current effects to become important, i.e., when the NM thickness approach its MW skin depth.

Experimentally, we observed the strongest lineshape asymmetry in films with a NM thickness of 10 nm. We also investigated thinner NM layers of 5 nm, and the FMR lineshapes were similar to single Py films. We believe this is because we had non-continuous metal films for these thicknesses; Au films tend to be granular and the Cu films might have oxidized.

V. SUMMARY

To summarize, we have shown that induced eddy currents can play an important role in FM/NM bilayer structures for certain sample geometries. In contrast to what is usually assumed about eddy currents, our results indicate that these effects can be important also for film thicknesses far below their skin depth. In FMR measurements, the influence on lineshape asymmetries has to be taken into account for NM layers below 50 nm and sample dimensions above approx. 1 mm^2 when the MW field has a significant component perpendicular to the film plane.

The dynamics of the system is determined by the interplay of the MW fields and induced fields by eddy currents, and we have shown that this coupling is tunable through changing the sample geometry and the NM layer thickness. The tunability of the coupling opens up possibilities to use patterned NM structures to tailor the local field geometry and phase of the induced microwave fields, which could be of importance for magnonics applications.

ACKNOWLEDGMENTS

We are grateful for insightful discussions with A. Brataas and H. Skarsvåg. This work was supported by the Norwegian Research Council (NFR), Project No. 216700. V.F. acknowledges long term support from NorFab Norway, and partial funding obtained from the Norwegian Ph.D. Network on Nanotechnology for Microsystems, which is sponsored by the Research Council of Norway, Division for Science, under Contract No. 221860/F40. F.M. acknowledges support from Catalan Government through COFUND-FP7 and support from MAT2011-23698. A.D.K. acknowledges support through the US-National Science Foundation, NSF-DMR-1309202.

¹C. Kittel, *Phys. Rev.* **73**, 155 (1948).

²P. Pincus, *Phys. Rev.* **118**, 658 (1960).

³Y. Tserkovnyak, A. Brataas, G. E. W. Bauer, and B. I. Halperin, *Rev. Mod. Phys.* **77**, 1375 (2005).

⁴V. V. Kruglak, S. O. Demokritov, and D. Grundler, *J. Phys. D: Appl. Phys.* **43**, 264001 (2010).

⁵S. Fahy, C. Kittel, and S. G. Louie, *Am. J. Phys.* **56**, 989 (1988).

⁶I. V. Antonets, L. N. Kotov, S. V. Nekipelov, and E. N. Karpuhov, *Tech. Phys.* **49**(11), 1496–1500 (2004).

⁷M. Bailleul, *Appl. Phys. Lett.* **103**, 192405 (2013).

⁸M. Kostylev, *J. Appl. Phys.* **106**, 043903 (2009).

⁹I. S. Maksymov and M. Kostylev, *J. Appl. Phys.* **116**, 173905 (2014).

- ¹⁰I. S. Maksymov, Z. Zhang, C. Chang, and M. Kostylev, *IEEE Magn. Lett.* **5** (2014).
- ¹¹M. Harder, Z. X. Cao, Y. S. Gui, X. L. Fan, and C.-M. Hu, *Phys. Rev. B* **84**, 054423 (2011).
- ¹²O. Mosendz, V. Vlaminck, J. E. Pearson, F. Y. Fradin, G. E. W. Bauer, S. D. Bader, and A. Hoffmann, *Phys. Rev. B* **82**, 214403 (2010).
- ¹³O. Mosendz, J. E. Pearson, F. Y. Fradin, G. E. W. Bauer, S. D. Bader, and A. Hoffmann, *Phys. Rev. Lett.* **104**, 046601 (2010).
- ¹⁴L. Liu, T. Moriyama, D. C. Ralph, and R. A. Buhrman, *Phys. Rev. Lett.* **106**, 036601 (2011).
- ¹⁵S. I. Kim, M. S. Seo, and S. Y. Park, *J. Appl. Phys.* **115**, 17C501 (2014).
- ¹⁶M. Krakowski, *Arch. Elektrotech.* **64**, 307–311 (1982).
- ¹⁷G. De Mey, *Arch. Elektrotech.* **56**(3), 137–140 (1974).
- ¹⁸L. Landau and E. Lifshitz, *Phys. Z. Sowjetunion* **8**, 153 (1935).
- ¹⁹D. Polder, *Philos. Mag.* **40**, 99–115 (1949).
- ²⁰C. J. Oates, F. Y. Ogrin, S. L. Lee, P. C. Riedi, G. M. Smith, and T. Thomson, *J. Appl. Phys.* **91**, 1417 (2002).
- ²¹C. P. Poole, *Electron Spin Resonance: A Comprehensive Treatise on Experimental Techniques* (Wiley, New York, 1967).
- ²²F. J. Dyson, *Phys. Rev.* **98**, 349 (1955).
- ²³Y. Tserkovnyak, A. Brataas, and G. W. Bauer, *Phys. Rev. B* **66**, 224403 (2002).
- ²⁴S. Mizukami, Y. Ando, and T. Miyazak, *Phys. Rev. B* **66**, 104413 (2002).
- ²⁵P. Wolf, *Zeit. fuer Angew. Phys.* **14**, 212 (1962).
- ²⁶J. D. Jackson, *Classical Electrodynamics* (John Wiley & Sons Ltd., 1998).
- ²⁷F. W. Grover, *Inductance Calculations* (Dover Publications, INC., 2004).

9.3 Paper III

Vegard Flovik, Bjørn Holst Pettersen, Erik Wahlström.

Eddy-current effects on ferromagnetic resonance: Spin wave excitations and microwave screening effects.

J. Appl. Phys. 119, 163903 (2016)

Eddy-current effects on ferromagnetic resonance: Spin wave excitations and microwave screening effects

Vegard Flovik,^{a)} Bjørn Holst Pettersen, and Erik Wahlström

Department of Physics, Norwegian University of Science and Technology, N-7491 Trondheim, Norway

(Received 24 February 2016; accepted 16 April 2016; published online 29 April 2016)

We investigate how controlling induced eddy currents in thin film ferromagnet-normal metal (FM/NM) structures can be used to tailor the local microwave (MW) fields in ferromagnetic resonance (FMR) experiments. The MW fields produced by eddy currents will in general have a relative phase shift with respect to the applied MW field which depends on the sample geometry. The induced fields can thus partially compensate the applied MW field, effectively screening the FM in selected parts of the sample. The highly localized fields produced by eddy currents enable the excitation of spin wave modes with non-zero wave vectors ($k \neq 0$), in contrast to the uniform $k = 0$ mode normally excited in FMR experiments. We find that the orientation of the applied MW field is one of the key parameters controlling the eddy-current effects. The induced currents are maximized when the applied MW field is oriented perpendicular to the sample plane. Increasing the magnitude of the eddy currents results in a stronger induced MW field, enabling a more effective screening of the applied MW field as well as an enhanced excitation of spin wave modes. This investigation underlines that eddy currents can be used to control the magnitude and phase of the local MW fields in thin film structures. *Published by AIP Publishing.* [<http://dx.doi.org/10.1063/1.4948302>]

I. INTRODUCTION

The microwave (MW) frequency spin dynamics in nanostructures usually involves stacks of layers combining ferromagnets (FM) and normal metals (NM) at the nanometer scale.^{1,2} A time varying magnetic field with a component perpendicular to a conductive thin film induces circulating currents in the thin film plane. These currents, commonly referred to as eddy currents, produce secondary phase shifted magnetic fields in close proximity to the conductor. The effects of eddy currents on ferromagnetic resonance (FMR) in conducting films are well known in the limit of film thickness approaching their electro-magnetic skin depth (≈ 800 nm for bulk Au at 10 GHz). In those cases eddy-current effects can lead to FMR linewidth broadening, and spin-wave excitations due to inhomogeneous microwave fields.^{3,4}

Eddy-current effects have often been neglected for film thicknesses below their skin depth. However, the contribution of the microwave conductivity of magnetic multilayers has received increasing attention in recent years, indicating the importance of eddy-current effects also for NM films far below their skin depth.^{5–18} In FM/NM bilayers, Maksymov *et al.* showed that the amplitude of the magnetization precession in the FM layer can be diminished by the shielding effect due to microwave eddy currents circulating in the NM layer.¹⁰ A study by Kostylev also showed that in single layer and bi-layer metallic FM the MW screening effect results in a spatially inhomogeneous MW field within the magnetic film.¹⁵ The experimental manifestation of this is a strong response of higher order standing spin wave modes due to the non-uniform MW field across the thickness of the magnetic film.

In a recent study, Flovik *et al.*¹⁸ investigated the effects of the induced Oersted fields in FM/NM bilayer structures. They show that the induced fields can strongly affect the FMR excitation, resulting in significant changes to the symmetry of the FMR lineshape. Differences in symmetry of FMR lines have been used to study the spin pumping from a magnetic material to a normal metal.^{19–24} In such studies, lineshape symmetry is one of the main parameters used to analyze the results. Hence, to correctly interpret experimental data involving FMR it is important to understand how eddy currents affect the FMR excitation.

However, rather than considering eddy currents a parasitic effect, we here investigate how controlling the current paths can be used to tailor the local MW fields. By using lithographically fabricated samples, we have systematically studied how sample and field geometry affect the coupling between the applied MW fields and eddy-current-induced fields. We show that eddy-current effects can have a significant impact on the FMR excitation even in very thin metallic FM (~ 10 nm Py), determined by the sample and MW field geometry. The induced MW fields from eddy currents can partially compensate the applied MW field, effectively screening the FM layer in selected parts of the sample. In contrast to the screening effects previously observed for continuous FM/NM bilayers by Maksymov *et al.*,¹⁰ we here consider the screening also in samples consisting of patterned NM structures.

Controlling the current paths by patterned NM structures generates highly localized MW fields. We provide evidence that this enables the excitation of spin wave modes with non-zero wave vectors ($k \neq 0$), in contrast to the uniform $k = 0$ mode normally excited in FMR experiments. As we are considering very thin metallic FM (~ 10 nm Py), we do not observe the aforementioned standing spin wave modes across the film thickness studied by Kostylev.¹⁵ Here, we

^{a)}Electronic mail: vflovik@gmail.com

argue that the inhomogeneous MW field produced by the induced eddy currents excites Damon–Eshbach surface spin wave modes.²⁵

The excitation of wave vector specific Damon–Eshbach spin waves in FM films using a diffraction grating has been studied by Sklenar *et al.*²⁶ They showed that a patterned silver antidot lattice on a thin uniform permalloy film enables coupling to spin wave modes. The amplitude of the spin wave excitations was however very small compared with the uniform FMR mode.

Here, we show that the orientation of the applied MW field with respect to the sample plane is one of the key parameters controlling eddy-current effects. The induced currents are maximized when the applied MW field is oriented perpendicular to the sample plane. Increasing the magnitude of the eddy currents results in a stronger induced MW field, enabling a more effective screening of the applied MW field as well as an enhanced excitation of spin wave modes. This points toward the importance of considering eddy-current effects not only for understanding basic experiments, but also for control of the local MW field in thin film structures.

II. EXPERIMENTAL SETUP AND SAMPLE PREPARATION

A. FMR experiments

Ferromagnetic resonance experiments were carried out in a commercial X-band electron paramagnetic resonance (EPR) setup with a fixed microwave frequency of 9.4 GHz (Bruker Bio-spin ELEXSYS 500, with a cylindrical TE-011 microwave cavity). The measurements were performed with an MW power of 0.65 mW, resulting in an MW field amplitude of $h_{mw} \approx 6 \mu\text{T}$ at the sample position. The magnitude of the external field is then swept to locate the resonance field, H_R . The sample is attached to a quartz rod connected to a goniometer, which allows for a 360° rotation of the sample with respect to the external static field. The applied MW field is oriented either parallel (Fig. 1(a)) or perpendicular (Fig. 1(b)) to the sample plane depending on sample mounting. The MW field in the cavity can be considered uniform on the length scale of the sample, and rotationally symmetric due to the cylindrical shape of the cavity.

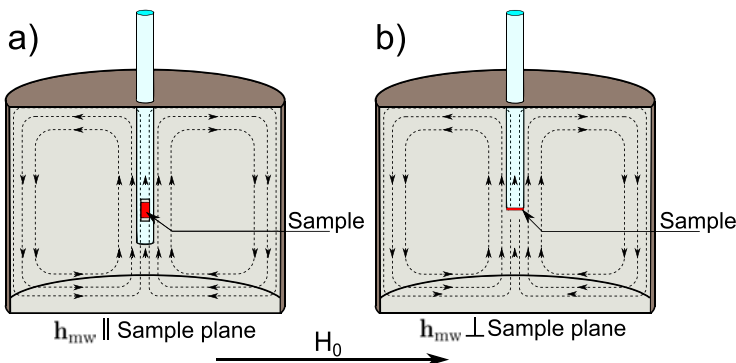


FIG. 1. Schematic of the cylindrical TE-011 microwave cavity, showing the sample position and field geometry for (a) vertical sample mounting resulting in h_{mw} parallel to the sample plane, and (b) horizontal sample mounting resulting in h_{mw} perpendicular to the sample plane. A goniometer allows for a 360° rotation of the sample with respect to the external static field, H_0 .

The ferromagnetic resonance is usually driven directly by the MW field from a cavity or from a coplanar waveguide/microstrip line. However, a time varying magnetic field component perpendicular to the sample plane will induce circulating eddy currents in conducting samples, and additional Oersted fields perturbing the FM. The FMR is often assumed to have a symmetric Lorentzian lineshape, but previous work by Flovik *et al.*¹⁸ show that eddy-current effects can strongly affect the lineshape symmetry. We thus fit the FMR lineshapes to a linear combination of symmetric and antisymmetric contributions, determined by the β parameter in Eq. (1)

$$\chi = A \frac{1 + \beta(H_0 - H_R)/\Gamma}{(H_0 - H_R)^2 + (\Gamma/2)^2}. \quad (1)$$

Here, A is a general amplitude prefactor, H_0 and H_R are the external field and resonance field, respectively, and Γ the FMR full linewidth at half maximum (FWHM). This expression consists of two components: a symmetric absorption lineshape arising from the in-phase driving fields, and an antisymmetric dispersive lineshape proportional to β arising from out-of-phase driving fields from the induced eddy currents. In this form, Eq. (1) describes what is known in the literature as Dysonian lineshapes.^{27–29}

The FMR experiments were performed with a low amplitude ac modulation of the static field, which allows lock-in detection to be used in order to increase the signal-to-noise ratio. The measured FMR signal is then proportional to the field derivative of the absorption, and the experimental data were thus fitted to Eq. (2), $d\chi/dH_0$

$$\frac{d\chi}{dH_0} = A \left[\frac{\beta/\Gamma}{(H_0 - H_R)^2 + (\Gamma/2)^2} - \frac{2(H_0 - H_R)[1 + \beta(H_0 - H_R)/\Gamma]}{[(H_0 - H_R)^2 + (\Gamma/2)^2]^2} \right]. \quad (2)$$

B. Sample preparation

Experiments were performed with Permalloy (Py = $\text{Fe}_{20}\text{Ni}_{80}$) as the FM layer and gold (Au) as the NM layer. The thin film structures were prepared using a lift off process

combining optical lithography, DC magnetron sputter deposition, and electron beam evaporation.

A thin layer of AZ5214E image reversal resist was first applied to a clean silicon support. To enhance the resolution of the lithographic pattern transfer, edge beads corresponding to resist thickness variations along the sample edge are removed before transferring the pattern from a photomask to the resist layer. Before loading the resist covered substrates into the sputtering chamber a hard baking step was performed to reduce water content in the photoresist, thereby increasing its etch resistance. After loading the patterned substrate into the vacuum chamber an argon pre-sputtering step was performed to remove contaminants from the sample surface, thus improving the quality of the final thin film. Permalloy was deposited using DC magnetron sputtering. The steps following Py deposition depended on the number of lithography steps used to define the final thin film structure. In the single mask process, gold was deposited directly on top of Py by E-beam evaporation. A lift off process was performed to dissolve the photoresist, leaving only the thin film stacks in direct contact with the substrate. In the multi mask process, lift off was performed directly after Py deposition followed by a second lithography process transferring a secondary pattern to the substrate, thus allowing one to vary the geometry of the gold layer independently of the Py layer. After completing the final lift off process all samples were inspected by optical microscopy to reveal defective samples. Atomic force microscopy (AFM) was used to measure the height of deposited thin films, and the individual samples produced on the same silicon support were separated using an automated scribe and breaker.

III. THEORETICAL CONSIDERATIONS

A. Eddy current induction in an NM thin film disc

A numerical approach is generally needed to calculate the distribution of induced currents and the associated magnetic fields. However, a closed form solution is obtainable for the simple case of a circular metallic film of thickness much less than the electro-magnetic skin depth. For a spatially homogeneous time harmonic magnetic field $\mathbf{B}e^{i\omega t}$ applied perpendicular to a non-magnetic circular disc, the induced current density in the thin film plane can be described by Ref. 30

$$J_{\phi}(r) = -\frac{k|\mathbf{B}| I_1(kr)}{\mu_0 I_0(kR)}, \quad (3)$$

where

$$k = \sqrt{\omega\mu_0\sigma}e^{i\pi/4}. \quad (4)$$

Here, R is the radius of the disc, μ_0 the vacuum permeability, σ the film conductivity, and $I_n(x)$ the modified Bessel function of the first kind and order n . In Fig. 2(a), we plot the normalized current density calculated from Eq. (3) along a circular sample for various radii in the range $r = [0,1]$ mm, for a conductivity of $\sigma_{py} \approx 3 \cdot 10^6$ S/m (Ref. 31) and a microwave frequency of 9.4 GHz.

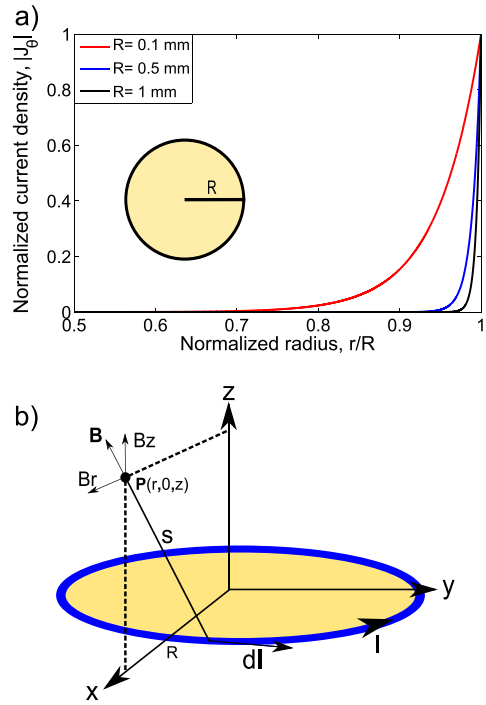


FIG. 2. (a) Calculated current density from Eq. (3) as a function of r for samples of radius R . (b) Geometry of the circular current loop.

As shown in Fig. 2(a), the current density is localized primarily along the sample edge as the disc size is increased. The current distribution also depends strongly on MW frequency, with a narrower distribution as the frequency is increased. However, in this work we consider a fixed microwave frequency of 9.4 GHz. Due to the localized current distribution, we approximate to first order the induced current as a single circular current loop along the sample edge.

B. Magnetic field from a circular current loop

For a circular loop carrying a current I , the magnetic field at any point in space can be obtained from the magnetic vector potential

$$\mathbf{A} = \frac{\mu_0 I}{4\pi} \oint \frac{d\mathbf{l}}{s}, \quad (5)$$

with s here being the distance from a point in space, P , to the line element $d\mathbf{l}$, as shown in Fig. 2(b). The general solution to Eq. (5) yields the vector potential³²

$$\mathbf{A} = A_{\phi} \hat{\phi} = \frac{\mu_0 I}{2\pi} [2k^{-1}r^{-1/2}(K(k) - E(k)) - kr^{-1/2}K(k)] \hat{\phi}. \quad (6)$$

Here K and E represent complete elliptical integrals of the first and second kind, respectively, while

$$k = \sqrt{\frac{4rR}{z^2 + (R+r)^2}} \tag{7}$$

From the vector potential \mathbf{A} , one can calculate the magnetic field ($\mathbf{B} = \nabla \times \mathbf{A}$)

$$B_z(r, z) = \frac{\mu_0 I}{2\pi\sqrt{z^2 + (R+r)^2}} \left(\frac{R^2 - z^2 - r^2}{z^2 + (r-R)^2} E(k) + K(k) \right), \tag{8}$$

$$B_r(r, z) = \frac{\mu_0 I z}{2\pi r\sqrt{z^2 + (R+r)^2}} \left(\frac{R^2 + z^2 + r^2}{z^2 + (r-R)^2} E(k) - K(k) \right). \tag{9}$$

In previous work by Flovik *et al.*,¹⁸ it was shown that phase shifted contributions to the FMR excitation produced by eddy currents result in an asymmetry of the observed lineshapes. Other studies have also shown that the relative phases of electromagnetic waves are important to consider in the FMR experiments.^{33,34} Hence, the phase lag between the applied MW field and the induced field needs to be considered. The Oersted fields produced by the eddy currents have a relative phase lag, ϕ , compared with the applied MW field, which in the ideal case is expected to be $\phi = -90^\circ$ ($I_{\text{Eddy}} \propto \frac{\partial h}{\partial t}$). However, due to the inductance and resistance of the film, there will be an additional phase between the applied MW field and the induced field. At larger film thicknesses, one also needs to take into account phase shifts due to the skin effect. A complex system such as an experimental setup involving waveguides, coaxial cables, etc., can also introduce a non-zero phase offset, ϕ_0 .^{33,34} Considering this, one can write the relative phase lag as³²

$$\phi = - \left[90 + \tan^{-1} \left(\frac{\omega L}{R} \right) + d/\delta + \phi_0 \right]. \tag{10}$$

Here, ω is the microwave angular frequency, L and R are the inductance and resistance of the film, respectively, d is the film thickness, and δ is the MW skin depth (≈ 800 nm for Au at 10 GHz).

IV. RESULTS AND DISCUSSION

The effects of eddy currents on the FMR excitation depend on both sample and field geometry. In Sec. IV A, we investigate the effects of the MW field geometry and show that eddy-current effects are significant also for thin FM layers (~ 10 nm Py). In Sec. IV B, we add NM layers with a high conductivity compared with the Py layer. The induced currents in the NM layer produce localized MW fields, enabling the excitation of spin wave modes with a non-zero wavevector ($k \neq 0$). In Sec. IV C, we investigate how patterned NM structures can be used to control the induced current paths, and by this the local MW field in thin film structures.

A. Circular Py discs: Effect of MW field geometry

We first characterize the simplest case of samples consisting of a single layer of Py and investigate the FMR absorption in a series of Py discs with a thickness of 10 nm and radius in the range 0.15–1.3 mm.

By fitting the FMR lineshape to Eq. (2), we plot the absorption amplitude, resonance field, lineshape asymmetry parameter β , and linewidth as a function of disc area in Fig. 3. Results are shown for the applied MW field oriented both parallel and perpendicular to the sample plane. Having the MW field oriented perpendicular to the sample plane will, according to Faraday’s law, maximize the induced currents in the sample, while rotating the MW field parallel to the sample plane should minimize any eddy-current effects. The FMR absorption amplitude is proportional to the energy dissipation in the sample. For the MW field oriented in the sample plane such that eddy-current effects are minimized,

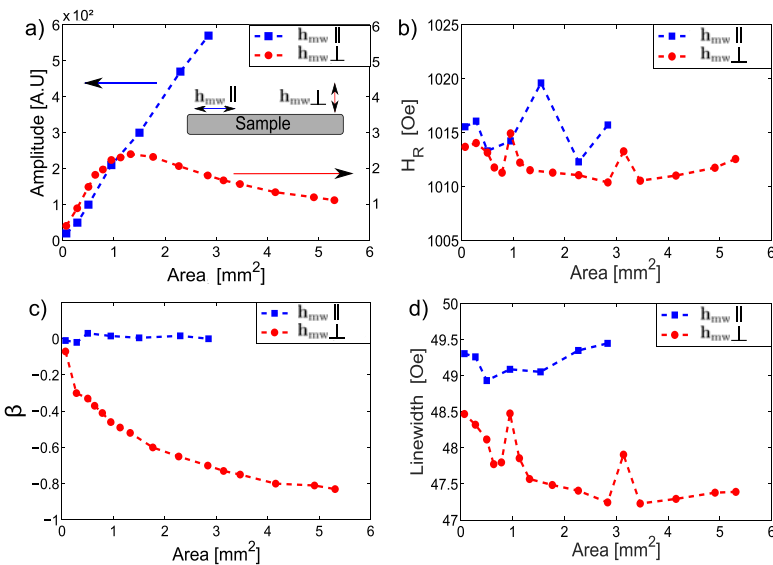


FIG. 3. (a) FMR absorption amplitude as a function of disc area for the MW field oriented parallel and perpendicular to the sample plane, respectively. Inset: Geometry for MW field oriented parallel and perpendicular to the sample plane. (b) Resonance field; (c) Lineshape asymmetry parameter β ; and (d) Linewidth for the same field geometries.

we observe the expected behavior that the FMR absorption amplitude increases linearly with sample volume (blue squares in Fig. 3(a)). The lineshape also remains symmetric for all sample sizes with an asymmetry parameter $\beta \approx 0$ for the field geometry that minimizes eddy-current effects (blue squares in Fig. 3(c)). The lineshape asymmetry in the geometry that maximizes eddy currents (red dots in Fig. 3(c)) is due to the contribution of phase shifted induced fields from eddy currents to the FMR excitation, as discussed in Sec. III B and in a previous study.¹⁸

The differences in resonance field and linewidth (Figs. 3(b) and 3(d)) between the two geometries can be explained by effects which we do not attribute to eddy currents. Due to different sample holders for the two geometries there could be a slight misalignment of the external static field with respect to the sample plane, resulting in a small shift in resonance field and linewidth. Another consideration is that the magnetization precession in thin films is not circular but elliptical due to strong demagnetizing fields, which force the magnetization into the film-plane. Having the applied MW field oriented along the long/short elliptic trajectory in the two geometries will affect how effectively the FMR is excited. This determines the cone angle of the magnetization precession, which could also cause a small shift in resonance field and linewidth.

The significant difference between the two MW field geometries is thus the FMR absorption amplitude and lineshape asymmetry. Comparing the results, one notice that for small samples the amplitude increases with sample size in both cases, until the sample reaches an area of approximately 1 mm² (Fig. 3(a)). Above this size, the amplitude starts to decrease as the sample size is increased when the MW field is oriented perpendicular to the sample plane. The lineshape asymmetry β also increases with sample size, reaching a limiting value of $|\beta| < 1$ for large samples (Fig. 3(c)).

While these trends present strong evidence for the effects of eddy currents on FMR in a single layer of Py, care should be taken when comparing the absorption amplitude for the two field geometries. As shown in Fig. 3(a), an in-plane orientation of the MW field results in an increase in amplitude compared with the same samples measured with an out-of-plane MW field. This is partially attributed to the screening effect of the applied MW field by the induced fields from eddy currents, but there are additional factors which also need to be considered. In the two measurement geometries the sample orientation with respect to the magnetic mode in the cavity is different, which could affect the detector coupling coefficient κ . As the recorded signal amplitude is proportional to κ , this would introduce a scaling offset in the signal amplitudes. Another consideration is the aforementioned ellipticity of the magnetization precession in thin films. Having the MW field oriented along the long/short elliptic trajectory in the two geometries will affect the FMR excitation, and by this the absorption amplitude. The difference in amplitudes between the two geometries could thus be caused by a combination of several factors. The main point to note is rather the dependence of absorption amplitude vs. sample area, whether a linear trend is observed or not. To explain the observed trend in the FMR absorption

amplitude vs. disc radius in Fig. 3(a), which shows a maximum for an intermediate disc radius, we consider a simple current loop model:

From electromagnetic theory we know that the induced electromotive force (EMF), ϵ , is proportional to the time derivative of the magnetic flux enclosed by the sample, and ϵ will thus increase proportional to the sample area. At the same time, approximating the current path as a circular loop around the edges of the sample, the resistance, R , of the loop scales linearly with the radius r . This means that the magnitude of the induced current should scale linearly with the sample radius, as $|I_{\text{ind}}| = |\epsilon|/R \propto \pi r^2/2\pi r$. As the simplest case we consider the magnetic field from a circular current loop, given by Eqs. (8) and (9). For a single layer of Py, we are interested in the magnetic field in the sample plane. Calculating the magnetic field at the center of the current loop in the x-y plane, the expressions simplify to the well known result for the magnetic field from a circular current loop: $B_z = \mu_0 I_{\text{ind}}/2\pi r$. As mentioned previously, the magnitude of the induced current should scale linearly with the disk radius. Using these approximations results in that the magnetic field at the center of the loop is independent of the loop radius. This cannot simply explain the observed maximum in the FMR absorption amplitude for an intermediate disc radius in Fig. 3(a). However, one of the approximations used was that one could consider the induced current as a single current loop localized at the sample edge. As shown in Fig. 2(a), this approximation is not independent of the disc radius. For small discs, even if the current density is highest along the edges, it is still more evenly distributed throughout the sample. The current distribution also determines the balance between in-plane and out-of-plane components of the corresponding induced MW field perturbing the FM.

Determining the relative magnitude of the MW field components is in general a complicated problem, and would require a simultaneous numerical solution of the coupled Maxwells and LLG equations³⁵ for the various sample geometries. However, previous observations indicate that the induced field perturbing the FM can be comparable and in some cases even larger than the applied MW field, due to the close proximity to the induced currents at the FM/NM interface.¹⁸ Two limiting cases are worth considering: A uniform current distribution in the sample would result in induced field components having only in-plane components (analogous to the magnetic field from a current in an infinite conducting plane). On the other hand, a localized current at the sample edge would produce mainly out of plane components of the corresponding magnetic field in the sample plane. As the applied MW field is oriented perpendicular to the sample plane, having induced field components perpendicular to the plane is needed in order to partially compensate the applied field. This could thus explain the observed behavior in Fig. 3(a): For the smallest samples, having a more uniform current distribution, the induced field components will have significant components in the sample plane. As the sample size is increased and the current density more localized along the sample edge, the induced fields will have the main component perpendicular to the sample plane, and could thus partially compensate the applied MW field. A compensation

effect, reducing the effective MW field exciting the FMR, would lead to the decrease in the absorption amplitude which is observed for the larger samples.

B. Circular Py discs with Au capping: Spin wave excitations

By adding NM layers with a high conductivity compared with the Py layer one can control the dominant current paths, and thus also the induced MW fields. We fabricated two separate set of samples consisting of Py discs capped with a 10 nm Au layer, as shown in Fig. 4. The conductivity of Au is significantly higher than for Py, with $\sigma_{Au}/\sigma_{Py} \approx 6 - 7$.³¹ This results in larger induced currents in the sample, mainly flowing in the Au layer.

The two set of samples both give similar results. Starting with the absorption amplitude in Fig. 5(a), it does not follow the same trend as for the single layer Py samples (Fig. 3(a)). For a disc area below 0.5mm², there is an initial region where the signal amplitude increases slowly with sample size, whereas for larger samples a clear increase in amplitude with sample size is observed. This initial region corresponds with the size range where a peak in both lineshape asymmetry β and linewidth is observed (Figs. 5(c) and 5(d)). There is also a shift in the resonance field of ≈ 5 Oe, before remaining relatively constant for larger samples (Fig. 5(b)). The shift in resonance field and linewidth between the two sample series can be explained by a slight variation in material properties, as the samples were deposited at two separate occasions.

Compared with the case of a single layer of Py, there are some important factors that differ: With a circulating current flowing in the Au layer, the Py layer will experience MW field components in both the in-plane and out-of-plane orientations, as indicated in Fig. 4. The balance between in-plane vs. out-of-plane components is determined by the current distribution in the sample, as regions directly below the current paths will be dominated by in-plane components. As the sample size is increased, the current paths will be gradually more localized along the sample edge (Fig. 2(a)). As this occurs, the induced field will gradually be dominated by out-of-plane components (Fig. 4). This means that one should expect three different size regimes governing the influence by eddy-current effects.

For the smallest samples the induced currents are low due to the small size of the sample, as well as having a more uniformly distributed current density (Fig. 2(a)). Still, there

are observable eddy-current effects. For a disc area below $\approx 0.5\text{mm}^2$, there is an initial region where the signal amplitude increases slowly with sample size compared with larger samples (Fig. 5(a)). This behavior is attributed to screening effects, reducing the amplitude of the magnetization precession in the FM layer.

For increasing sample sizes the current density becomes gradually more localized along the sample edges (Fig. 2(a)). The FM will experience both in-plane and out-of-plane MW field components, and this regime corresponds to where we observe significant changes in behavior for amplitude, resonance field, lineshape asymmetry, and linewidth (Figs. 5(a)–5(d)). It has been shown that non-uniform MW fields can excite spin waves with a non-zero wave vector ($k \neq 0$), and that this can cause a shift in resonance frequency and broadening of the FMR linewidth.^{16,17} Here, the region which has dominant contributions from both in-plane and out-of-plane MW field components, and thus a non-uniform MW field, is localized along the sample edge. The width of this edge region will thus determine the range of possible wave vectors of spin wave excitations. The excitation of Damon–Eshbach surface spin wave modes is dominating in this field geometry,^{25,36} and the spin wave frequency is determined by the magnetostatic spin wave dispersion given by the following:³⁷

$$w(k) = \gamma\mu_0 \left[H_0(H_0 + M_s) + M_s^2 \frac{(1 - e^{-2kd})}{4} \right]^{1/2}, \quad (11)$$

where γ is the gyromagnetic ratio, μ_0 the vacuum permeability, H_0 the external field, M_s the saturation magnetization of Py, k the spin wave vector, and d the thickness of the Py film.

If we denote the width of the edge region by Δ , the maximum spin wave vector will be determined by $k_{\max} \propto \pi/\Delta$. From the radial current density in Fig. 2(a), the area with highest current density is localized in an edge region of width $\Delta \approx 10\text{--}50 \mu\text{m}$. As a simple estimate we calculate the spin wave dispersion from Eq. (11) for the uniform $k=0$ mode as well as the spin wave modes for k_{\max} when $\Delta = 10 \mu\text{m}$ and $\Delta = 50 \mu\text{m}$. The results are shown in Fig. 6, where the FMR cavity resonance frequency is indicated by the solid line at 9.4 GHz. Shown as inset is a zoom-in of the same plot, where the splitting between the various modes is visible. The calculated splitting between the $k=0$ mode and the spin wave mode is 3 and 13 Oe, respectively, determined by the width of the edge region, for $\Delta = 50 \mu\text{m}$ and $\Delta = 10 \mu\text{m}$.

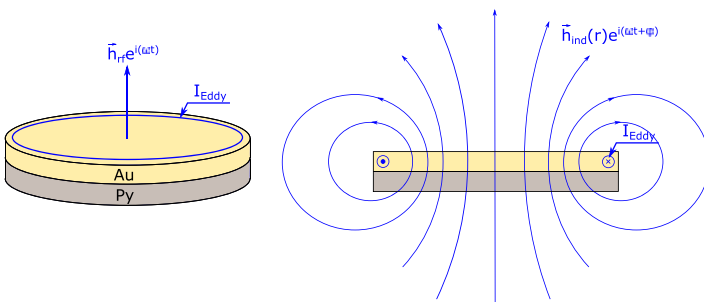


FIG. 4. Sample and field geometry, Py/Au bilayers.

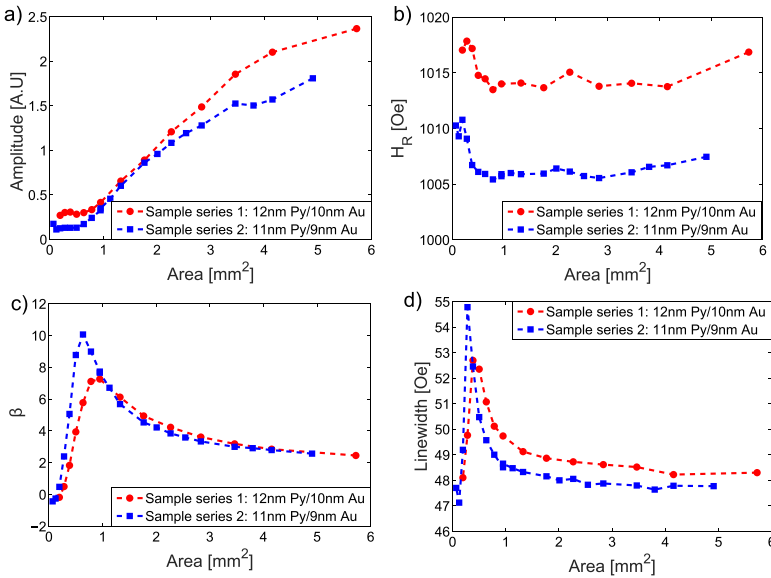


FIG. 5. Comparing two set of samples of Py capped with a thin Au layer. (a) FMR absorption amplitude; (b) Resonance field; (c) Lineshape asymmetry parameter β ; and (d) Linewidth.

The excitable spin wave modes vary over a continuous range, $0 < k < k_{\max}$. In the linear response regime, the total FMR response can be taken as the sum of all excitable states. As shown in the inset of Fig. 6, for such long wavelength spin waves the shift in resonance field between excitations in the range $0 < k < k_{\max}$ is too small to be observed as separate peaks in the FMR spectrum. Summing the FMR response over a continuum of closely spaced states would thus rather appear as an apparent broadening of the FMR linewidth, where the broadening will be in the order of the shift in resonance field between the modes. This suggests that the observed linewidth broadening of ≈ 5 Oe in Fig. 5(d) for intermediate sample sizes is related to the excitation of spin wave modes with $k \neq 0$, due to the mixing of in-plane and out-of-plane MW field components for these sample sizes. By further increasing the sample size the FM will experience mainly out-of-plane field components, and one would no longer expect significant contributions from spin wave excitations to the total FMR absorption. This corresponds well with the experimental observations, where the resonance field and linewidth approach constant values for large samples.

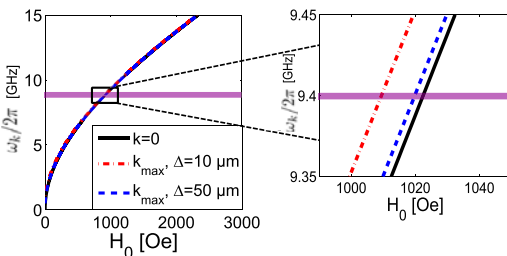


FIG. 6. Calculated spin wave dispersion, $\omega(k)$ from Eq. (11) for spin waves with wave vectors k_{\max} , determined by the width of the edge region, Δ . The cavity FMR frequency of 9.4 GHz is shown as solid line.

For the lineshape asymmetry in Fig. 5(c) we observe a similar trend as for the linewidth, with a maxima for intermediate sample sizes. As mentioned previously, the lineshape asymmetry results from several phase shifted contributions to the FMR excitation. One would thus expect a maxima in β in the size range where the FM experience a mixing of several MW field components, which is consistent with the experimental observations. The asymmetry parameter can have both positive and negative signs, depending on sample geometry and the phase shifts between the applied MW field and the induced fields. In this geometry, we observe a sign change in β compared with the case of single Py discs in Sec. IV A. This is caused by the change in sample geometry where the current in this case is mainly flowing in the adjacent NM layer, compared with in the FM layer for the first samples. The different sample geometry introduces an effective phase shift to the induced field perturbing the FM, and thus a sign change in β . In general, determining the magnitudes and phases of the MW fields exciting the FMR is a non-trivial problem to solve even with a numerical approach. However, the lineshape asymmetry is not our main focus, and we refer to earlier work investigating the effects of eddy currents on the FMR lineshape.¹⁸

Our results indicate that by modifying the conductivity one can control the dominant current paths in the sample, and thus the induced MW fields. As a model system to investigate this further, we fabricated patterned NM structures which enable better control of the current paths.

C. Circular Py discs enclosed by Au ring: MW screening effects

As a final set of samples, we fabricated structures consisting of Py discs enclosed by an Au ring, as shown in Fig. 7. The high conductivity of Au compared with Py, as well as the

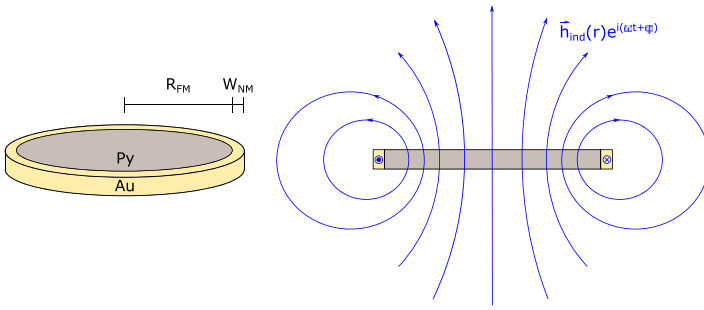


FIG. 7. Sample and field geometry Py/Au ring series.

radial current density distribution shown in Fig. 2(a), results in that the induced current is mainly flowing in the Au ring. In this case the induced MW field perturbing the FM will have only out-of-plane components, as the radial component vanishes due to the sample geometry. The fabricated samples consist of series where both the radius of the FM disk, as well as the width of the NM ring, is varied. Increasing the NM ring width reduces its resistance, resulting in stronger eddy-current effects.

In Fig. 8(a), we plot the FMR absorption amplitude for several samples of different size as a function of NM ring width, ranging from 10 to 250 μm . A clear trend is observed where the amplitude drops as the width of the NM ring is increased. For an NM ring of 250 μm , where the eddy currents should be strongest, the amplitude approaches zero. We interpret this as an almost complete compensation of the applied MW field by the induced fields from eddy currents in the NM ring, suggesting a strong screening effect.

For the resonance field (Fig. 8(b)) we observe an increase of $\approx 70\text{Oe}$ compared with that of the previous sample series, which indicates a reduction in the saturation magnetization. The preparation of this sample series involves an extra lithography step, as mentioned in Sec. II B, and this could cause a

reduced film quality compared with the other samples. A reduced film quality is consistent with the increased linewidth (Fig. 8(d)), which is in the order of 10 Oe larger than that for the other samples. However, we do not observe any clear trend in the linewidth as a function of disc size or NM ring width. This corresponds well with what one would expect if the change in linewidth for the PyAu bilayers in Fig. 5(d) is caused by the excitation of spin waves. In this last series, due to the sample geometry shown in Fig. 7, there will be no in-plane field components. Without any mixing of in-plane vs. out-of-plane field components, one should thus not expect any spin wave excitations and corresponding FMR linewidth broadening.

By investigating the lineshape asymmetry in Fig. 8(c) for an NM ring width ranging from 10 to 100 μm , we observe that the asymmetry increases with both the NM ring width and the FM disc radius. (For an NM ring width of 250 μm , the absorption amplitude was too low to get a good estimate of the linewidth and lineshape asymmetry.) As mentioned previously in Sec. IV B the sign of β depends on the sample geometry, and we note here that β has a negative sign, same as for the single Py discs in Sec. IV A. This is due to the similar sample geometry where the current loop (flowing mainly

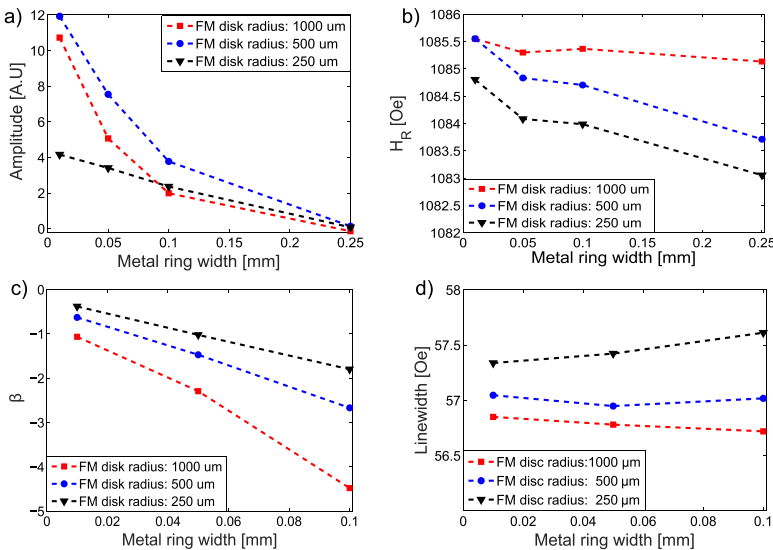


FIG. 8. (a) FMR absorption amplitude, (b) resonance field, (c) lineshape asymmetry, β and (d) linewidth as a function of FM disc radius and metal ring width.

in the NM ring) is in the same plane as the FM disc. This is in contrast to the PyAu bilayers in Sec. IV B where the current is flowing mainly in the adjacent Au layer, and a positive β is observed.

The most interesting observation for this sample series is the significant screening effect. The FMR absorption amplitude in Fig. 8(a) indicates that the induced fields from eddy currents in the NM ring are able to almost completely compensate the applied MW field for an NM ring width of 250 μm , where the absorption amplitude drops to near zero. To estimate the compensation of the applied MW field by induced fields from eddy currents, we consider a simple current loop model: The induced electromotive force (EMF) ϵ is given by the rate of change of the magnetic flux through the area enclosed by the current loop; its absolute value is given by $|\epsilon| = \pi r^2 |\frac{\partial h_{\text{mw}}}{\partial t}|$. The induced current is then given by $I_{\text{ind}} = \epsilon/R$, where R is the resistance of the current loop. The resistance of the Au ring is given by $R = 2\pi r \rho_{\text{Au}}/w\delta$, where ρ_{Au} is the resistivity of Au, w is the width of the NM ring, and δ is the thickness of the Au layer. As discussed previously in Section IV B, the expressions for the magnetic field at the center of a circular current loop of radius r in the x - y plane given by Eqs. (8) and (9) simplify to the well-known expression: $h_{\text{ind}} = \mu_0 I_{\text{ind}}/2\pi r$. We are here interested in the condition where the induced field is comparable in strength with the applied MW field, $h_{\text{ind}} \approx h_{\text{mw}}$. Fulfilling this relation, one obtains the following expression for the NM ring width:

$$w = \frac{2\rho_{\text{Au}}}{\mu_0 f_{\text{mw}} \delta}. \quad (12)$$

A microwave frequency $f_{\text{mw}} = 9.4$ GHz, Au thickness of $\delta = 10$ nm, and the standard textbook value of resistivity, ρ_{Au} , results in an NM ring width of $w \approx 400$ μm . Comparing the model calculation with experimental data, we observe such a compensation already at $w \approx 250$ μm . However, in this simplified model we only consider induced fields from currents in the NM ring. As we have discussed previously in Section IV A, and shown in Fig. 3(a), induced currents in the Py disc also affect the absorption amplitude. Taking the compensation effect from the Py disc into account would result in that a thinner NM ring width is needed to compensate the applied MW field. This is consistent with the results from our simplified current loop model, which overestimate the NM ring width compared with the experimental result.

V. SUMMARY

To summarize, we have shown that eddy-current effects can have a significant impact on the FMR excitation even in very thin metallic FM (~ 10 nm Py), determined by the sample and MW field geometry. Our results indicate how patterned FM/NM structures can be used to control the induced current paths. The corresponding MW fields have a relative phase shift with respect to the applied MW field, which depends on the sample geometry. The induced fields produced by eddy currents can thus be used to compensate the applied MW field, as an effective screening of the FM in

selected parts of the sample. We also provide evidence that controlling the local MW field enables the excitation of spin wave modes with a non-zero wave vector ($k \neq 0$), in contrast to the uniform ($k = 0$) mode normally excited in the FMR experiments.

What is not contained within this study is a proper investigation on the linearity of these effects. The induced current density given by Eq. (3) depends linearly on the microwave magnetic field. At some point, however, the magnitude of induced currents will be limited by the conductivity and thickness of the NM film. This will limit the MW fields produced by eddy currents, and will thus introduce a threshold for when eddy-current effects will affect the system.

Developing a more detailed theoretical model involving a numerical solution of the coupled Maxwells and LLG equation would also be beneficial. A numerical model would enable the investigation of the interplay between applied and induced MW fields for various sample geometries. This is however outside the scope of our current work.

For applications, combining the effects of eddy currents could be used for canceling of MW fields in different geometries, and providing highly localized fields due to the localization of the eddy currents. This allows for generating and controlling the MW field in small regions. In more complicated geometries, as often found in devices, the findings point toward that care should be taken in design, and that eddy-current effects can yield both FMR lineshape changes, unwanted or wanted screening/amplification of the local MW field, as well as the FMR excitation of spin waves with non-zero wave vectors. However, rather than treating eddy currents as a parasitic effect, our results suggest the possibility of actively using eddy currents to control the MW field excitation in thin film structures, which could be of importance for magnonics applications.

ACKNOWLEDGMENTS

This work was supported by the Norwegian Research Council (NFR), Project No. 216700. V.F. acknowledges long-term support from NorFab Norway, and partial funding obtained from the Norwegian Ph.D. Network on Nanotechnology for Microsystems, which is sponsored by the Research Council of Norway, Division for Science, under Contract No. 221860/F40.

¹Y. Tserkovnyak, A. Brataas, G. E. W. Bauer, and B. I. Halperin, *Rev. Mod. Phys.* **77**, 1375 (2005).

²V. V. Kruglyak, S. O. Demokritov, and D. Grundler, *J. Phys. D: Appl. Phys.* **43**, 264001 (2010).

³C. Kittel, *Phys. Rev.* **73**, 155 (1948).

⁴P. Pincus, *Phys. Rev.* **118**, 658 (1960).

⁵S. Fahy, C. Kittel, and S. G. Louie, *Am. J. Phys.* **56**, 989 (1988).

⁶I. V. Antonets, L. N. Kotov, S. V. Nekipelov, and E. N. Karpushov, *Tech. Phys.* **49**(11), 1496–1500 (2004).

⁷M. Bailleul, *Appl. Phys. Lett.* **103**, 192405 (2013).

⁸M. Kostylev, *J. Appl. Phys.* **106**, 043903 (2009).

⁹I. S. Maksymov and M. Kostylev, *J. Appl. Phys.* **116**, 173905 (2014).

¹⁰I. S. Maksymov, Z. Zhang, C. Chang, and M. Kostylev, *IEEE Magn. Lett.* **5**, 3500104 (2014).

¹¹W. E. Bailey, C. Cheng, R. Knut, O. Karis, A. Auffret, S. Zohar, D. Keavney, P. Warnicke, J. S. Lee, and D. A. Arena, *Nat. Commun.* **4**, 2025 (2013).

- ¹²Y. V. Khivintsev, L. Reisman, J. Lovejoy, R. Adam, C. M. Schneider, R. E. Camley, and Z. J. Celinski, *J. Appl. Phys.* **108**, 023907 (2010).
- ¹³H. Glowński, M. Schmidt, I. Gościńska, J.-Ph. Ansermet, and J. Dubowik, *J. Appl. Phys.* **116**, 053901 (2014).
- ¹⁴Z. Lin and M. Kostylev, *J. Appl. Phys.* **117**, 053908 (2015).
- ¹⁵M. Kostylev, *J. Appl. Phys.* **113**, 053908 (2013).
- ¹⁶I. S. Maksymov and M. Kostylev, *J. Phys. D: Appl. Phys.* **46**, 495001 (2013).
- ¹⁷G. Council, J. V. Kim, T. Devolder, C. Chappert, K. Shigeto, and Y. Otani, *J. Appl. Phys.* **95**, 5646 (2004).
- ¹⁸V. Flovik, F. Macià, A. D. Kent, and E. Wahlström, *J. Appl. Phys.* **117**, 143902 (2015).
- ¹⁹O. Mosendz, V. Vlaminck, J. E. Pearson, F. Y. Fradin, G. E. W. Bauer, S. D. Bader, and A. Hoffmann, *Phys. Rev. B* **82**, 214403 (2010).
- ²⁰O. Mosendz, J. E. Pearson, F. Y. Fradin, G. E. W. Bauer, S. D. Bader, and A. Hoffmann, *Phys. Rev. Lett.* **104**, 046601 (2010).
- ²¹L. Liu, T. Moriyama, D. C. Ralph, and R. A. Buhrman, *Phys. Rev. Lett.* **106**, 036601 (2011).
- ²²V. Vlaminck, J. E. Pearson, S. D. Bader, and A. Hoffman, *Phys. Rev. B* **88**, 064414 (2013).
- ²³M. Obstbaum, M. Härtinger, H. G. Bauer, T. Meier, F. Swientek, C. H. Back, and G. Woltersdorf, *Phys. Rev. B* **89**, 060407(R) (2014).
- ²⁴S.-I. Kim, D.-J. Kim, M.-S. Seo, B.-G. Park, and S.-Y. Park, *J. Appl. Phys.* **117**, 17D901 (2015).
- ²⁵R. W. Damon and J. R. Eshbach, *J. Phys. Chem. Solids* **19**, 308 (1961).
- ²⁶J. Sklenar, V. S. Bhat, C. C. Tsai, L. E. DeLong, and J. B. Ketterson, *Appl. Phys. Lett.* **101**, 052404 (2012).
- ²⁷F. J. Dyson, *Phys. Rev.* **98**, 349 (1955).
- ²⁸C. J. Oates, F. Y. Ogrin, S. L. Lee, P. C. Riedi, G. M. Smith, and T. Thomson, *J. Appl. Phys.* **91**, 1417 (2002).
- ²⁹C. P. Poole, *Electron Spin Resonance: A Comprehensive Treatise on Experimental Techniques* (Wiley, New York, 1967).
- ³⁰M. Krakowski, *Arch. Elektrotechnik* **64**, 307–311 (1982).
- ³¹A. F. Mayadas, J. F. Janak, and A. Gangulee, *J. Appl. Phys.* **45**, 2780 (1974).
- ³²J. D. Jackson, *Classical Electrodynamics* (Wiley-VCH, 1998), Vol. 1.
- ³³M. Harder, Z. X. Cao, Y. S. Gui, X. L. Fan, and C.-M. Hu, *Phys. Rev. B* **84**, 054423 (2011).
- ³⁴A. Wirthmann, X. Fan, Y. S. Gui, K. Martens, G. Williams, J. Dietrich, G. E. Bridges, and C.-M. Hu, *Phys. Rev. Lett.* **105**, 017202 (2010).
- ³⁵L. Landau and E. Lifshitz, *Phys. Z. Sowjetunion* **8**, 153 (1935).
- ³⁶H. J. J. Liu, G. A. Riley, and K. S. Buchanan, *IEEE Magn. Lett.* **6**, 4000304 (2015).
- ³⁷D. D. Stancil and A. Prabhakar, *Spin Waves: Theory and Applications*, 1st ed. (Springer, New York, 2009).

9.4 Paper IV

Vegard Flovik, Ferran Macià, Joan Manel Hernández, Rimantas Bručas, Maj Hanson, Erik Wahlström.

Tailoring the magnetodynamic properties of nanomagnets using magnetocrystalline and shape anisotropies.

Phys. Rev. B. 92, 104406 (2015)

Tailoring the magnetodynamic properties of nanomagnets using magnetocrystalline and shape anisotropies

Vegard Flovik,^{1,*} Ferran Macià,² Joan Manel Hernández,² Rimantas Bručas,³ Maj Hanson,⁴ and Erik Wahlström¹

¹*Department of Physics, Norwegian University of Science and Technology, N-7491 Trondheim, Norway*

²*Grup de Magnetisme, Departament de Física Fonamental, Universitat de Barcelona, Spain*

³*Department of Engineering Sciences, Uppsala University, SE-751 21 Uppsala, Sweden*

⁴*Department of Applied Physics, Chalmers University of Technology, SE-412 96 Gothenburg, Sweden*

(Received 21 April 2015; revised manuscript received 25 August 2015; published 10 September 2015)

Magnetodynamical properties of nanomagnets are affected by the demagnetizing fields created by the same nanoelements. In addition, magnetocrystalline anisotropy produces an effective field that also contributes to the spin dynamics. We show how the dimensions of magnetic elements can be used to balance crystalline and shape anisotropies, and that this can be used to tailor the magnetodynamic properties. We study ferromagnetic ellipses patterned from a 10-nm-thick epitaxial Fe film with dimensions ranging from 50×150 to 150×450 nm. The study combines ferromagnetic resonance (FMR) spectroscopy with analytical calculations and micromagnetic simulations, and proves that the dynamical properties can be effectively controlled by changing the size of the nanomagnets. We also show how edge defects in the samples influence the magnetization dynamics. Dynamical edge modes localized along the sample edges are strongly influenced by edge defects, and this needs to be taken into account in understanding the full FMR spectrum.

DOI: [10.1103/PhysRevB.92.104406](https://doi.org/10.1103/PhysRevB.92.104406)

PACS number(s): 75.75.Jn, 75.78.-n, 76.50.+g

I. INTRODUCTION

The magnetodynamic properties of nanostructures have received extensive attention, from both fundamental and applications viewpoints [1–5]. Nanometer-size magnetic elements play an important role in advanced magnetic storage schemes [6,7], and their static and, most importantly, their dynamic magnetic properties are being intensely studied. While technological applications are important, there is also significant interest in understanding the fundamental behavior of magnetic materials when they are confined to nanoscale dimensions. In confined magnetic elements, there is a complex competition between exchange, dipolar, and anisotropic magnetic energies. Understanding the interplay between the various energy terms is thus of importance when investigating the magnetodynamics of such systems.

The magnetization dynamics in patterned magnetic structures has been extensively studied [8–14]. The spin dynamics in elliptical permalloy dots was investigated by Gubbiotti *et al.* [9]. They studied the various excitation modes as a function of dot eccentricity and in-plane orientation of the applied field, showing how the shape of the ellipses affects the spectrum of excitable modes and their frequencies.

However, the above-mentioned studies of patterned magnetic structures were all performed for systems having a negligible magnetocrystalline anisotropy. Material systems with a significant crystalline anisotropy produce an effective field which also contributes to the spin dynamics. The combination of shape and crystalline anisotropy results in a complex energy landscape, where the interplay of these energy terms determines the magnetodynamic properties of the system.

The influence of shape and crystalline anisotropy on magnetic hysteresis and domain structures in submicron-size Fe particles has been investigated by Hanson *et al.* [15].

However, here we explore the dynamic properties of magnetic structures utilizing both crystalline and shape anisotropies. The goal of this study is to investigate a system where the energy terms from both crystalline and shape anisotropy contribute to determine the dynamics of the system.

We have investigated a system utilizing epitaxial Fe as the ferromagnetic (FM) material, patterned to an array of elliptical nanomagnets. This results in a system combining the cubic crystalline anisotropy of Fe with the shape anisotropy due to the elliptical shape of the confined magnetic elements.

The dynamic properties were investigated by ferromagnetic resonance (FMR) experiments for ellipses with a thickness of 10 nm and lateral dimensions of 50×150 , 100×300 , and 150×450 nm. The experimental results are compared with micromagnetic simulations and a macrospin model considering the total free-energy density of a ferromagnetic structure containing both crystalline and shape anisotropies. The macrospin model is then used to explore the properties of ellipses with lateral dimensions ranging from 50×150 to 500×1500 nm, showing how the ellipse size governs the balance between crystalline and shape anisotropy.

During the fabrication of such structures, the magnetic properties may be affected by edge defects and shape distortions [16–19]. As the size of the magnetic elements are reduced, the edge regions become increasingly important. Understanding how edge defects affect the magnetodynamic properties of the elements is thus of importance in nanomagnets, where the edge region covers a significant amount of the total sample area. We show how this affects the magnetization dynamics, and that edge defects need to be taken into account in understanding the full FMR spectrum.

II. EXPERIMENTAL SETUP

The samples are based on a single-crystalline Fe film epitaxially grown on MgO(001) substrates. The ferromagnetic

*vegard.flovik@ntnu.no

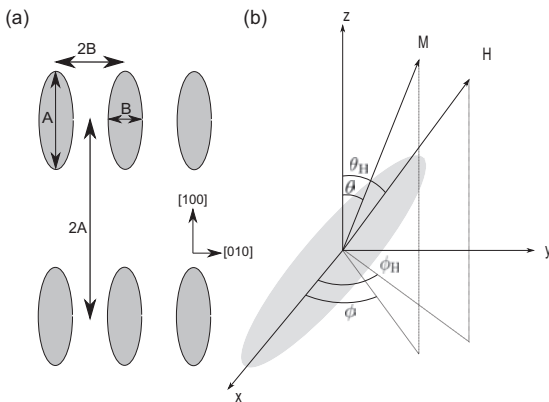


FIG. 1. (a) Array of ellipses with dimension $A \times B$, an aspect ratio of $A/B = 3$, and interparticle spacing of two times the corresponding ellipse dimension in each direction. The $[100]$ and $[010]$ crystallographic axis of Fe is oriented along the long/short ellipse axis. (b) Field geometry of the individual ellipses.

ellipses were patterned by electron-beam lithography and ion-beam milling from a 10-nm-thick Fe layer, and have lateral dimensions of 50×150 , 100×300 , and 150×450 nm. The crystalline easy axis $[100]$ and $[010]$ of the Fe film are oriented along the long/short axis of the ellipses, as indicated in Fig. 1(a). Further details concerning sample growth and processing are similar to that described earlier [20].

The FMR experiments were performed using two complementary setups. The cavity FMR measurements were carried out in a commercial X-band electron paramagnetic resonance (EPR) setup with a fixed microwave frequency of 9.4 GHz (Bruker Bio-spin ELEXSYS 500, with a cylindrical TE-011 microwave cavity). The magnitude of the external field is then swept to locate the resonance field, H_R . The sample is attached to a quartz rod connected to a goniometer, allowing one to rotate the sample 360 degrees in order to accurately resolve the angular dependence. The FMR measurements were performed with a low-amplitude ac modulation of the static field, which allows lock-in detection to be used in order to increase the signal-to-noise ratio.

For the broadband FMR measurements, we used a vector network analyzer (VNA) FMR setup with a coplanar waveguide (CPW) excitation structure. The static external field H_0 was applied in the sample plane, and perpendicular to the microwave field from the CPW. This was used to obtain the standard microwave S parameters as a function of frequency for various fixed values of the static field. This allows for a complete field-versus-frequency map of the resonance absorption, not being limited to a fixed frequency as for the cavity measurements. Data was then collected in a field range of ± 500 mT and a frequency range of 1–25 GHz. Typical absorption maps had a step size of $\Delta f = 0.1$ GHz and $\Delta H_0 = 5$ mT.

III. MICROMAGNETIC SIMULATIONS

The micromagnetic calculations were performed using MuMax [21]. The simulated ellipses have a dimension of

150×450 nm, with a thickness of 10 nm. In order to have mesh independence, the discretization cells should have sides of the same order, or less than, the two characteristic magnetic length scales of the system. The exchange length is $l_{\text{exch}} = (\frac{A}{K_1})^{1/2}$ and the magnetostatic exchange length is $l_{\text{dem}} = (\frac{A}{K_d})^{1/2}$. Here, A is the exchange stiffness constant, K_1 is the first-order anisotropy constant, K_d is the energy density of the stray field, and an upper limit for K_d is given by $\frac{1}{2}\mu_0 M_s^2$.

Material parameters used in the simulations are standard literature values, with a saturation magnetization, $M_s = 1.7 \times 10^6$ A/m, and a crystalline anisotropy constant of $K_1 = 4.3 \times 10^4$ J/m³, with the easy axis oriented along the long and short axis of the ellipse. The exchange stiffness was set to a value of $A = 21 \times 10^{-12}$ J m⁻¹ and the damping coefficient to $\alpha = 0.01$.

Performing simulations for a $3d$ model and a $2d$ model, we obtained the same results, and varying the grid size it was found that the results converge at a grid size of 2×2 nm. To save computation time, the simulation model was thus implemented as a $2d$ model with a grid size of 2×2 nm, which is well below the characteristic magnetic length scales of the system ($l_{\text{exch}} = 21$ nm, $l_{\text{dem}} = 3.5$ nm).

Simulations of the FMR spectra were performed by using a field relaxation process. The system is first initialized at zero applied field. If a static field H_0 is applied, the simulations are run until the system reaches the new ground-state configuration. A 10 mT perturbation field H_p is then applied along the z axis (out of plane), and the simulation is run until it reaches the ground-state configuration for the field $H_0 + H_p$. The perturbation field is then switched off, allowing the system to relax. The perturbation causes oscillations of the magnetization around the equilibrium position with a maximum deviation of approximately 1 degree, avoiding any nonlinear effects. To obtain the resonance frequencies, we take the Fourier power spectrum of the m_z component the first 10 ns of the magnetization relaxation. The various excitation modes of the system will then appear as distinct peaks in the Fourier spectrum [8].

Simulations with an ac field of varying frequency as the perturbing field were also performed, and we obtained the same results as for the field relaxation procedure. The ac approach is, however, more time consuming, as one has to scan the full frequency range for each value of the applied static field in order to locate all of the resonances. To obtain the full field-versus-frequency map of the excitation modes in the system, we thus used the field relaxation process.

IV. FREE-ENERGY DENSITY AND THEORETICAL FMR SPECTRUM

Due to the size and shape of the ellipses, we consider the individual magnetic elements to be in a single domain state. This was also confirmed by magnetic force microscopy (MFM) imaging of similar samples [22], where all particles were found to be in a single domain state for a thickness of 10 nm. Increasing the thickness makes it energetically favorable to form flux closure domains, and already at a thickness of 30 nm some of the particles were found to be in such multidomain states. This means that to make sure the magnetic elements are in single domain states, one has to keep the film thickness

well below 30 nm for ellipses of the dimensions we have investigated. Having a single domain state allows us to use an analytical macrospin model to investigate the ferromagnetic resonance properties of the system.

The array of ellipses has an interparticle spacing of two times the corresponding ellipse dimension in each direction, as illustrated in Fig. 1(a). This spacing is sufficient to significantly reduce the dipolar coupling between the individual elements, and as a first approximation we consider the ellipses as uncoupled magnetic elements.

We start by defining the geometry of the system and consider the free-energy density of the individual magnetic elements. From the sample geometry illustrated in Fig. 1(b) (magnetic element in the xy plane), one gets

$$\begin{aligned} M_x &= M_s \sin \theta \cos \phi, \\ M_y &= M_s \sin \theta \sin \phi, \\ M_z &= M_s \cos \theta, \end{aligned} \quad (1)$$

where M_s is the saturation magnetization. Assuming the external applied field \mathbf{H}_0 is oriented in the sample plane, $\theta_H = \pi/2$, gives

$$\begin{aligned} H_x &= H_0 \cos \phi_H, \\ H_y &= H_0 \sin \phi_H. \end{aligned} \quad (2)$$

After defining the geometry, one can calculate the free-energy density of the system by adding up the various energy terms. Using a macrospin model, we do not consider the exchange energy. The total free-energy density of the system is then given by $E_{\text{tot}} = E_{\text{Zeeman}} + E_{\text{demagnetization}} + E_{\text{anisotropy}}$,

$$\begin{aligned} E_{\text{Zeeman}} &= -\vec{M} \cdot \vec{H} \\ &= -M_s H_0 [\sin \theta \cos \phi \cos \phi_H + \sin \theta \sin \phi \sin \phi_H] \\ &= -M_s H_0 \sin \theta \cos(\phi - \phi_H), \end{aligned} \quad (3)$$

$$\begin{aligned} E_{\text{demagnetization}} &= \frac{\mu_0}{2} [N_x M_x^2 + N_y M_y^2 + N_z M_z^2] \\ &= \frac{\mu_0 M_s^2}{2} [N_x \sin^2 \theta \cos^2 \phi + N_y \sin^2 \theta \sin^2 \phi \\ &\quad + N_z \cos^2 \theta], \end{aligned} \quad (4)$$

where μ_0 is the vacuum permeability, N_i are the demagnetization factors, and $N_x + N_y + N_z = 1$. The units for the saturation magnetization and magnetic field are $[M_s] = \text{A/m}$ and $[H] = \text{T}$, respectively. We assume cubic crystalline anisotropy for the epitaxial Fe film, with the easy axis oriented parallel to the long/short axis of the ellipse, as indicated in Fig. 1(a). The lowest-order term in the crystalline anisotropy energy is then the fourth-order term,

$$\begin{aligned} E_{\text{anisotropy}} &= K_1 [\alpha_x^2 \alpha_y^2 + \alpha_y^2 \alpha_z^2 + \alpha_z^2 \alpha_x^2] \\ &= K_1 [\sin^4 \theta \sin^2 \phi \cos^2 \phi + \sin^2 \theta \sin^2 \phi \cos^2 \theta \\ &\quad + \sin^2 \theta \cos^2 \phi \cos^2 \theta], \end{aligned} \quad (5)$$

where K_1 is the magnetocrystalline anisotropy constant and $\alpha_i = M_i/M_s$. After adding the terms, one can write the total

free-energy density as

$$\begin{aligned} E_{\text{tot}} &= -M_s H_0 \sin \theta \cos(\phi - \phi_H) \\ &\quad + \frac{\mu_0 M_s^2}{2} \left[\sin^2 \theta \cos^2 \phi \left(N_x + \frac{2K_1}{\mu_0 M_s^2} \sin^2 \theta \sin^2 \phi \right) \right. \\ &\quad + \sin^2 \theta \sin^2 \phi \left(N_y + \frac{2K_1}{\mu_0 M_s^2} \cos^2 \theta \right) \\ &\quad \left. + \cos^2 \theta \left(N_z + \frac{2K_1}{\mu_0 M_s^2} \sin^2 \theta \cos^2 \phi \right) \right]. \end{aligned} \quad (6)$$

Equation (6) describes a complex energy landscape, with competing energies from the various terms. It is important to note that the orientation of the magnetization, given by ϕ , might not be parallel to the applied field, ϕ_H . Thus, to investigate the resonance conditions of the system, one must first find the equilibrium orientation of the magnetization. The equilibrium orientation was found by minimizing the free-energy density of the system given by Eq. (6) for each value of H and ϕ_H , and was performed numerically. After obtaining the equilibrium orientation of the magnetization, one can calculate the resonance frequency ω given by [23]

$$\omega = \frac{\gamma}{\mu_0 M_s \sin \theta} \sqrt{\left[\frac{\partial^2 E_{\text{tot}}}{\partial \theta^2} \frac{\partial^2 E_{\text{tot}}}{\partial \phi^2} - \left(\frac{\partial^2 E_{\text{tot}}}{\partial \theta \partial \phi} \right)^2 \right]}. \quad (7)$$

By solving Eq. (7), one can obtain the resonance frequency as a function of magnitude and direction of the applied field, $\omega(H, \phi_H)$. By calculating the various terms in Eq. (7), one obtains

$$\begin{aligned} \frac{\partial^2 E_{\text{tot}}}{\partial \theta^2} &= M_s H \sin \theta \cos(\phi - \phi_H) \\ &\quad + \frac{K_1}{4} \left(\cos 2\theta \left\{ 1 - \cos 4\phi - 4\mu_0 M_s^2 N_z / K_1 \right. \right. \\ &\quad \left. \left. + \frac{2\mu_0 M_s^2}{K_1} [N_x + N_y + (N_x - N_y) \cos 2\phi] \right\} \right. \\ &\quad \left. + (\cos 4\phi + 7) \cos 4\theta \right), \end{aligned} \quad (8)$$

$$\begin{aligned} \frac{\partial^2 E_{\text{tot}}}{\partial \phi^2} &= M_s H \sin \theta \cos(\phi - \phi_H) + 2K_1 \sin^2 \theta \\ &\quad \times \left[\cos 4\phi \sin^2 \theta + \frac{\mu_0 M_s^2 (N_y - N_x)}{2K_1} \cos 2\phi \right], \end{aligned} \quad (9)$$

$$\begin{aligned} \frac{\partial^2 E_{\text{tot}}}{\partial \theta \partial \phi} &= M_s H \cos \theta \sin(\phi - \phi_H) + 8K_1 \sin \phi \cos \phi \sin \theta \cos \theta \\ &\quad \times \left[\cos 2\phi \sin^2 \theta + \frac{\mu_0 M_s^2 (N_y - N_x)}{4K_1} \right]. \end{aligned} \quad (10)$$

For thin films, one can simplify these expressions by assuming that the magnetization is oriented in the film plane, $\theta = \pi/2$. After introducing the anisotropy field, $H_k = 2K_1/M_s$, one obtains the resonance frequency given by

Eq. (7),

$$\left(\frac{\omega}{\gamma}\right)^2 = \left[H \cos(\phi - \phi_H) + \mu_0 M_s \left\{ N_z - \left[\frac{N_x + N_y + (N_x - N_y) \cos 2\phi}{2} \right] \right\} + \frac{H_k}{4} (3 + \cos 4\phi) \right] \times [H \cos(\phi - \phi_H) + H_k \cos 4\phi + \mu_0 M_s (N_y - N_x) \cos 2\phi]. \quad (11)$$

Equation (11) gives the resonance frequency for the general case, with the assumption that the magnetization is oriented in the sample plane. Depending on the shape and size of the magnetic elements, one can then adjust the demagnetization factors N_i to obtain the resonance conditions for various samples.

In addition to the fourfold symmetry from the cubic anisotropy, one notices that in this case there are additional terms of twofold symmetry due to the shape anisotropy along the long/short axis of the ellipse. The resonance conditions of the system are thus more complicated and are determined by the interplay of shape and crystalline anisotropies. This brings us to the main topic of the study, which is to investigate how tuning the various energy terms changes the magnetodynamic properties of the system.

V. RESULTS AND DISCUSSION

A. Cavity FMR measurements

The experiments to investigate the angular dependence were performed in the X-band cavity FMR setup described in Sec. II. This gives an angular FMR spectrum for both the continuous film and an array of ellipses of dimension 150×450 nm, as shown in Fig. 2.

Going from a continuous film to a patterned array of ellipses, there is a significant difference. For the continuous film, the fourfold symmetry due to the cubic crystalline anisotropy in Fe is dominating. For the ellipses, the situation is more complicated, as there are competing energies also from the shape anisotropy.

To investigate this, we compare the experimental and theoretical results. By solving Eq. (11) after first minimizing the free-energy density for each value of H and ϕ_H , one gets the FMR dispersion relations shown in the lower panel of Fig. 3. From Eq. (11), the relevant parameters determining the dispersion are the demagnetization factors N_i , the anisotropy field H_k , and the saturation magnetization M_s . In nanometer-

dimension magnetic structures, estimates of the demagnetization factors using ellipsoidal formulas are considered to represent the anisotropy fields well [24,25]. The factors N_i were found from [24] and, for an ellipse of dimension $10 \times 150 \times 450$ nm, they are $N_x \approx 0.005$, $N_y \approx 0.05$, and $N_z = 1 - N_x - N_y$. The anisotropy field H_k was determined from the experimental FMR spectrum in Fig. 2(a) and was found to be approximately 50 mT. In the calculations, M_s was adjusted to obtain the best fit between the experimental and theoretical spectrum, and the best fit was found for $M_s = 1.5 \times 10^6$ A/m (a reduction of approximately 10% compared to textbook values of M_s for Fe).

To compare the angular dependence of the theoretical spectrum with experimental results from the cavity measurements shown in Fig. 2, one can invert the solution. This instead gives the resonance field H_R as a function of rotation angle for a fixed excitation frequency of 9.4 GHz, and the inverted solution is shown in the upper panel of Fig. 3. To distinguish the effect of crystalline anisotropy and shape anisotropy, the same calculations were also performed assuming polycrystalline Fe, setting $H_k = 0$.

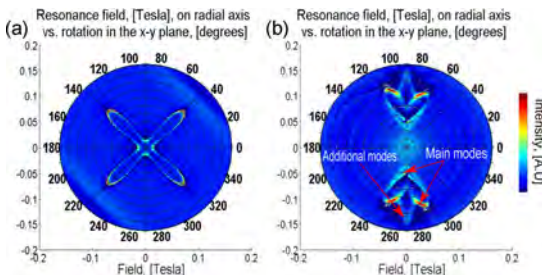


FIG. 2. (Color online) Experimental FMR spectrum for (a) continuous film and (b) ellipses of dimension 150×450 nm from the X-band cavity FMR setup.

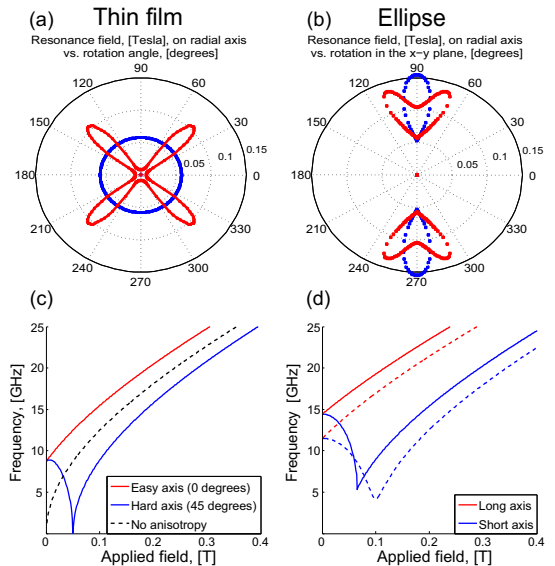


FIG. 3. (Color online) (a),(b) Theoretical data for resonance field vs rotation angle for (a) continuous film and (b) ellipse of dimension $10 \times 150 \times 450$ nm, with (red) and without (blue) crystalline anisotropy. (c),(d) Dispersion for (c) continuous film and (d) ellipse of dimension $10 \times 150 \times 450$ nm, with (solid lines) and without (dotted lines) crystalline anisotropy.

Comparing theory and experiment in Figs. 2 and 3, one notices that for the continuous film, both show the expected fourfold cubic symmetry. For the ellipses, the theory replicates the “heart shape” of the resonance well. In the experimental data in Fig. 2(b), there are also some additional weak resonance lines. It is known that regions along the sample edges could lead to a spectrum of additional edge modes [9,10,16]. However, from our experiments, we observe that the main mode is dominating, and thus focus on this in the following. The other resonances are characterized and discussed in detail in Sec. V C.

B. Size of the ellipses

To investigate the interplay of shape anisotropy and crystalline anisotropy, we studied ellipses of various lateral dimensions, but with the same aspect ratio of 1:3. Changing the sample size affects the balance between crystalline and shape anisotropy in the free-energy density. As shown using our macrospin model for the main FMR mode, this will in turn change the resonance frequency. There are two limiting cases worth noticing: in the limit of a very large ellipse, one should expect a behavior close to that of a continuous film, where crystalline anisotropy is dominating. By gradually reducing the size of the ellipse, shape anisotropy becomes increasingly important. This means that one can use the size of the magnetic elements to tune the ratio between crystalline and shape anisotropies, and thus change the magnetodynamic properties of the system.

Changing the dimensions of the ellipse affects the free-energy density of the system, given by Eq. (6). The transition from a continuous film to a small ellipse can be observed by considering the energy landscape of the system as a function of the ellipse dimension, as shown in Fig. 4.

Figure 4 indicates how the free-energy density changes when one gradually reduces the size of the ellipse from the upper limit of a continuous film to an ellipse of dimension

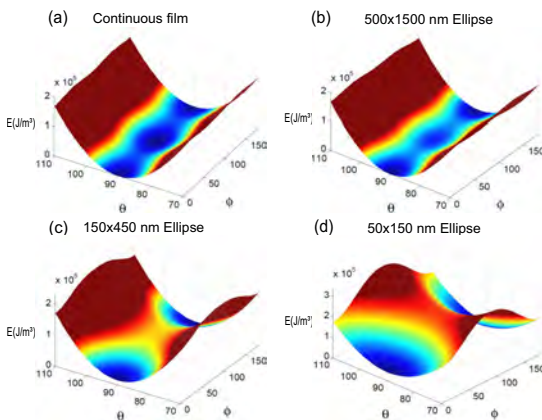


FIG. 4. (Color online) Free-energy density given by Eq. (6) for (a) continuous film, (b) 500×1500 nm ellipse, (c) 150×450 nm ellipse, and (d) 50×150 nm ellipse. Film thickness is 10 nm in all cases.

50×150 nm. As expected, one notices that in all cases, the magnetization favors an orientation in the sample plane [$\theta = 90$, from sample geometry as defined in Fig. 1(b)]. For the continuous film and the largest ellipse in Figs. 4(a) and 4(b), one can clearly see the dominating crystalline anisotropy, with a fourfold symmetry between the energy minima along the ϕ axis.

In the intermediate case for an ellipse of dimension 150×450 nm, one has two dominating energy minima at $\phi = 0$ and $\phi = 180$ (magnetization along the long axis of the ellipse). In addition, there is a quite flat saddle point at $\phi = 90$ (which corresponds to a magnetization along the short axis of the ellipse). This is not a stable energy minimum, but the flatness of the saddle point means that applying a small magnetic field along this axis will create a local energy minimum along this direction.

For the smallest ellipse, the energy landscape is dominated by the twofold shape anisotropy along the long axis of the ellipse. To align the magnetization along the short axis of the ellipse ($\phi = 90$) will thus require a quite large external field.

As shown in Sec. IV, the FMR frequency given by Eq. (11) is determined by the free-energy density of the system. Adjusting the lateral dimensions of the ellipse is thus an important parameter controlling the FMR frequency. From Eq. (11), one notices that the resonance frequency is determined by contributions of both twofold and fourfold symmetry. From this expression, the relevant ratio to determine which term will dominate is given by $H_K / \mu_0 M_s (N_x - N_y)$. Changing the ellipse dimensions, and thus the demagnetization factors N_i , affects the resonance frequency significantly, as shown in the upper panel of Fig. 5.

Figures 5(a) and 5(b) compare the theoretical FMR spectrum for ellipses of dimension 150×450 , 100×300 , and

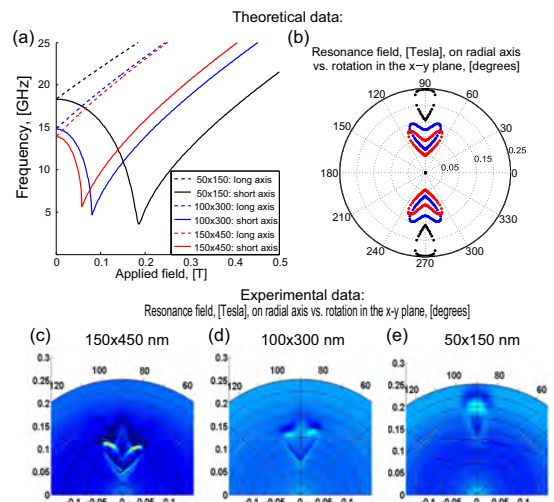


FIG. 5. (Color online) (a) Theoretical dispersion for ellipses of dimension 50×150 nm (black), 100×300 nm (blue), and 150×450 nm (red). (b) Angular dependence of same data. Experimental data for ellipse of dimension (c) 150×450 nm, (d) 100×300 nm, and (e) 50×150 nm.

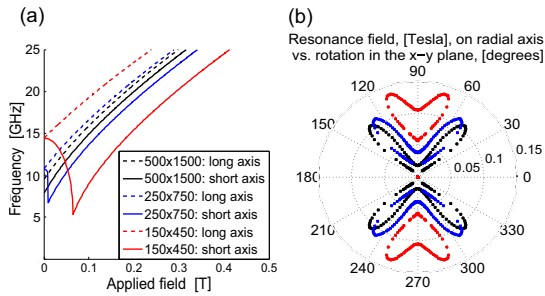


FIG. 6. (Color online) (a) Theoretical dispersion for ellipses of dimension 500×1500 nm (black), 250×750 nm (blue), and 150×450 nm (red). (b) Angular dependence of same data.

50×150 nm. As the dimensions of the ellipse are reduced, the twofold shape anisotropy tends to dominate over the crystalline anisotropy, and the heart shape of the spectrum in Fig. 5(b) due to the cubic crystalline anisotropy is suppressed. Comparing the theoretical results with the experimental data in the lower panel of Fig. 5, they follow the same trend. As the size is reduced, the resonance is shifted to slightly higher fields, and the heart shape of the resonance gets suppressed.

Investigating the opposite limit, one can determine when the crystalline anisotropy starts to dominate. Comparing the theoretical FMR spectrum for ellipses of dimension 150×450 , 250×750 , and 500×1500 nm in Fig. 6, one notices that by increasing the size, the effect of shape anisotropy is suppressed compared to that of crystalline anisotropy.

For an ellipse of dimension 500×1500 nm, the dispersion starts to look similar along the long/short axis of the ellipse, as indicated in Fig. 6(a). If the only contribution was from the crystalline anisotropy, the dispersion should be identical along the long/short axis due to the fourfold symmetry. Comparing the FMR spectrum for the largest ellipse in Fig. 6(b) to that of a continuous film in Fig. 3(a), they look very similar. This indicates that as the sample dimensions approach the micrometric scale, shape anisotropies play a minor role compared to the crystalline anisotropy.

To summarize the size dependence, we have shown that for sample dimensions above approximately $1 \mu\text{m}$, crystalline anisotropy will dominate. In the opposite size limit, shape anisotropy will dominate for sample dimensions below approximately 50×150 nm. In this intermediate regime, one can thus effectively use the sample size as a parameter to tune the balance between crystalline and shape anisotropies.

C. Broadband FMR measurements and micromagnetic simulations

The assumption that the magnetization in the individual ellipses is uniform is a good approximation at the center of the ellipse, but along the edges the magnetization will be less uniform due to the demagnetizing fields. Regions along the sample edges could lead to a spectrum of additional edge modes [9,16]. In addition, there could be other spin-wave excitations with nonzero wave vectors, and correspondingly varying frequencies [9,10]. To characterize the various resonances,

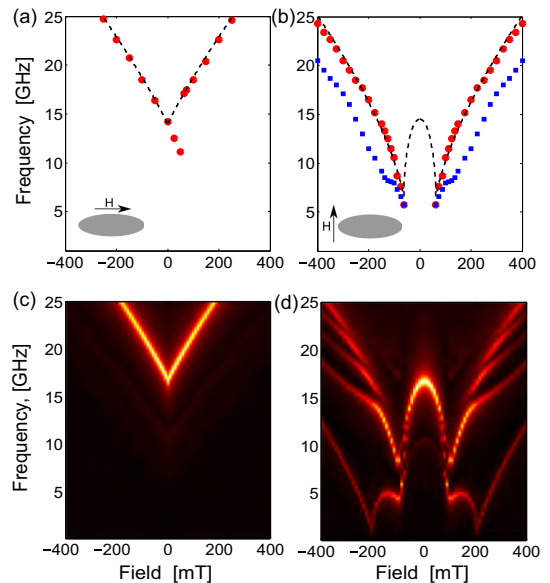


FIG. 7. (Color online) (a),(b) Experimental FMR spectrum for ellipses with field oriented along long/short axis. Experimental data is shown as red dots/blue squares, and theoretical spectrum as dotted black line. (a) Field sweep from the negative to positive field along the long axis, also showing the switching of the magnetization at approximately 75 mT. (b) Similar measurement along the short axis, showing the main mode (red dots) and an additional weak resonance at lower frequency (blue squares). (c),(d) Simulated FMR spectrum for a single ellipse of dimension 150×450 nm with the field oriented along the (c) long and (d) short axis.

we thus performed a series of broadband FMR measurements in combination with micromagnetic simulations.

To obtain a complete field-versus-frequency map of the FMR absorption, we performed experiments using the broadband setup described in Sec. II. The experimental FMR absorption peaks were extracted and are shown in the upper panel of Fig. 7. Red dots represent the main FMR mode and the blue squares represent the additional weaker mode. For clarity, only a few selected data points are included, where the uncertainty in determining the absorption peak position is of the order of the dot size. The experimental results are then compared with the theoretical FMR spectrum from the macrospin model, shown as dotted black lines.

The agreement between theory and experiment is good for an applied field oriented along the long axis of the ellipse, as indicated in Fig. 7(a). Sweeping the field from negative to positive, one also notices the switching of the magnetization. As the field is swept from negative to zero, the FMR frequency decreases as expected. This continues also for positive fields until the external field is strong enough to overcome the anisotropy favoring the magnetization along the long axis of the ellipse. The switching is then observed as an abrupt jump in the FMR spectrum.

When applying the field along the short axis, there are two parallel dispersing lines, as shown in Fig. 7(b): a

high-frequency resonance and an additional weaker resonance at lower frequency, which corresponds well to the additional resonance also seen in the cavity measurements [see Fig. 2(b)]. Comparing the measurements along the short axis with the theoretical dispersion, one does not observe the low field resonance in Fig. 7(b) (the black dotted line below 100 mT). In this field range, the magnetization is not saturated and it is still oriented along the long axis of the ellipse, being parallel to the microwave (MW) pumping field from the CPW. However, in the cavity measurements, we observed both resonances because the pumping field is, in this case, oriented out of the sample plane and thus perpendicular to the magnetization. The first resonance is observed at a field of ~ 50 mT [see Fig. 2(b)] and a second one is observed at ~ 100 mT, which agrees well with the expected resonance fields from the theoretical curves shown in Fig. 7(b) at a frequency of 9.4 GHz. At higher fields, the magnetization in the ellipse saturates in the direction of the external field, being perpendicular to the MW pumping field from the CPW, and thus the theoretical spectrum corresponds well with the high-frequency branch of the experimental data.

Using a macrospin model, one accounts only for the main FMR mode. In order to investigate the observed low-frequency resonance, we performed micromagnetic simulations. The model was implemented as a single ellipse of dimensions 150×450 nm with a thickness of 10 nm, and the simulated FMR spectrums are shown in the lower panel of Fig. 7. Comparing the experimental data with the micromagnetic simulations, we notice a few differences. Applying the field along the long axis of the ellipse, the simulated and experimental data both show a single dispersing resonance. The simulated FMR frequency is, however, noticeably higher than the experimental results. Applying the field along the short axis of the ellipse, the differences between the experimental and simulated FMR spectrum are more significant. The experimental data show two parallel dispersing lines, whereas the simulated spectrum shows a whole range of various excitation modes.

A similar splitting of the main mode has been observed experimentally in elliptical permalloy dots, and was attributed to a hybridization of the main mode with other spin-wave modes [9,10]. A study of the excitation modes in permalloy dots as a function of dot eccentricity has been performed by Gubiotti *et al.* [9], where they found a large range of possible modes depending on the orientation of the external field with respect to the axis of the dots. The number of modes in our system compared to theirs may be smaller because of the different material parameters and sample size. The exchange stiffness in Fe is almost twice that of permalloy and, combined with a smaller sample size, this results in a reduction in the number of excitation modes due to the increased exchange energy. This was also confirmed in our simulations, where the mode splitting disappears when reducing the sample size or increasing the exchange stiffness.

The low-frequency branch in Fig. 7(d) was identified by imaging the m_z component from the micromagnetic simulations (out-of-plane component). From the periodic oscillations of the magnetization, we determined the low-frequency resonance to be localized along the edges of the ellipse, as indicated in Fig. 8 for an applied field of 150 mT along the short axis.

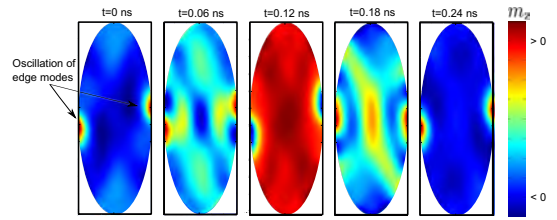


FIG. 8. (Color online) m_z component, showing one oscillation period of the edge mode at $H = 150$ mT, corresponding to a frequency of approximately 4 GHz.

After identifying the excitation modes, one needs to consider why there is a significant difference between the simulated and experimental FMR spectrum. It is known that the fabrication process of nanostructures can lead to distortions and defects at the sample edges [16–19]. To investigate how this would affect the magnetodynamic properties, the effects of edge defects need to be taken into account in the simulation model.

1. Edge modes and edge defects

In the initial simulations, the edges of the ellipse were treated as ideal. However, the samples most likely have some kind of nonideal edges, which could influence the FMR spectrum. The effects of nonideal edges on the dynamics have been investigated theoretically by McMichael *et al.* [16]. It was shown that several cases, such as edge geometry, reduced edge magnetization and surface anisotropy on the edge surface all had similar effects. The main effect was to reduce the edge saturation field, which is the field needed to align the magnetization at the edge nearly parallel to the applied field. A reduced edge magnetization will also lead to a smaller effective demagnetization field along the edges. This would cause a significant increase of the edge mode resonance frequency compared to that of an ideal edge, and the shift could be of the order of several GHz [16]. Such effects would be less important when the field is oriented along the easy axis of the ellipse, explaining the better agreement between the simulated and experimental spectrum in that geometry.

To account for edge defects in the simulations, we made a model where the material properties were changed along the edges of the ellipse. In a real sample, the variation of the material properties when approaching the sample edge should be gradual, but as a first approximation the model was defined with two distinct regions. The width of the edge region was set to 10 nm and is within the same width range as that investigated theoretically by McMichael *et al.* [16]. A schematic of the model including edge defects is shown in Fig. 9(b).

As mentioned in Sec. II, the samples were defined by ion-beam milling. This can affect the magnetic properties of the sample [19], and a more disordered edge region could lead to an increased damping of the FMR modes. Two kinds of defects have thus been considered in the simulations: increased damping α and reduced M_s .

In the initial simulation model with ideal edges, excited spin waves would be reflected at the edges of the sample.

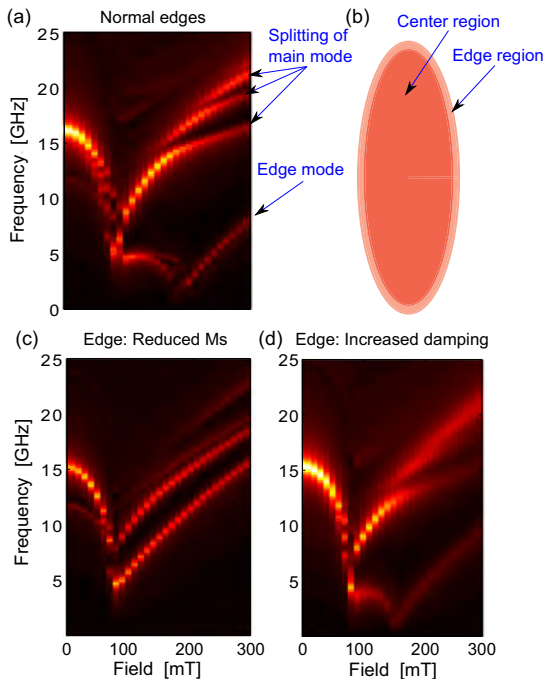


FIG. 9. (Color online) (a) Simulation using normal edges, showing the edge mode and splitting of the main mode. (b) Schematic of simulation model with a defined edge region. (c) Simulation with reduced M_s in the edge region (reduction of 40%). (d) Simulation with increased damping α in the edge region (from 0.01 to 0.1).

This explains the multiple excitation modes observed in the simulations, due to a hybridization of the main mode with other spin-wave modes [9,10] [see Fig. 9(a)]. As a disordered edge region could lead to increased damping of the FMR modes, we introduced an edge region where the damping was increased from $\alpha = 0.01$ to $\alpha = 0.1$. This would absorb the propagation of spin waves, reducing the spin-wave reflection at the sample edges. As seen in Fig. 9(d), the increased damping leads to a broadening of the FMR modes and suppresses some of the splitting of the main mode. The low-frequency edge mode, however, remains relatively unaffected.

The edge magnetization M_s was found to be the most important parameter, and we made simulation models where the outer region of the ellipse had a significantly reduced M_s from $M_s = 1.7 \times 10^6$ to $M_s = 1 \times 10^6$ A/m. Reducing M_s in the edge region changes the FMR spectrum considerably, as seen when comparing Figs. 9(a) and 9(c). The splitting of the main mode is suppressed and the resonance frequency of the edge mode is shifted significantly. The resulting spectrum now resembles the experimental data, showing mainly two parallel dispersing modes.

Another important effect to consider in arrays of nanomagnets is the dipolar interaction among the individual particles. In order to take this into account, we performed simulations for arrays of interacting ellipses.

2. Dipolar interactions

The simulations so far have been performed for single ellipses. However, due to the periodic array of ellipses [as shown in Fig. 1(a)], there will be some degree of dipolar interaction between the individual ellipses. The dipolar interaction in arrays of magnetic particles can have both static and dynamic contributions. The effects of static dipolar interaction on the magnetization reversal of the same samples were investigated previously, and an interaction field in the order of tens of mT was found [22]. The dynamic interaction can couple the magnetization dynamics of adjacent dots through the stray field generated by the precessing magnetization, forming collective spin excitations in the system [4,5].

Interactions were included in the simulations by using periodic boundary conditions (bc), with the same periodicity as that indicated in Fig. 1(a). In the limit of strong dipolar interaction, one could also expect collective modes in the system. A simple model of a single ellipse with periodic bc would not be sufficient to resolve such modes, as the neighboring ellipses could rotate either in phase (acoustic mode) or out of phase (optic mode) [26,27]. To take this into account, we compared the simulation results for a single ellipse with periodic bc versus arrays of 3×3 , 5×5 , and 10×10 ellipses. Comparing the simulated FMR spectrums for the various array sizes, we found no indication of such collective modes in our system. In the following simulations, the dipolar interaction was thus taken into account by using a simple model for a single ellipse with periodic bc.

Comparing the simulated spectrums for a single ellipse versus an array of ellipses, we found that the dipolar interaction changes the effective field felt by the individual ellipses. At zero applied field, the magnetization is oriented along the long axis of the ellipses. The overall dipolar field caused by the array geometry will then oppose the magnetization direction. As seen in Fig. 10(a), the dipolar field reduces the resonance frequency at zero applied field for the array compared to a single ellipse. Increasing the field along the short axis of the ellipse, the magnetization will reorient itself along the short axis at an applied field of approximately 75 mT [seen as a “dip” in the FMR spectrum in Fig. 9(c)]. At fields above this switching field, the dipolar interaction acts to increase effective magnetic field felt by the ellipses, and thus increases the FMR frequency. These shifts can be seen in Fig. 10(a) for an applied field between 150–350 mT, and are of the order of 1 GHz. These shifts in the FMR frequencies along the hard/easy axis are similar to those observed by Carlotti *et al.* [28], who studied the effects of dipolar interactions in arrays of rectangular permalloy dots.

To capture all significant effects, we thus made a simulation model with periodic bc, where edge defects were modeled as a reduced M_s at the sample edges. After including both edge defects and dipolar interactions, one can compare the simulated and experimental spectrums in Figs. 10(b) and 10(c).

We notice that the inclusion of edge defects and dipolar interactions gives a better agreement between the simulated and experimental FMR spectrum. As expected, the edge modes are strongly influenced by edge defects in the samples. To accurately capture the behavior of all the FMR modes, it is thus important to take edge defects into account in the

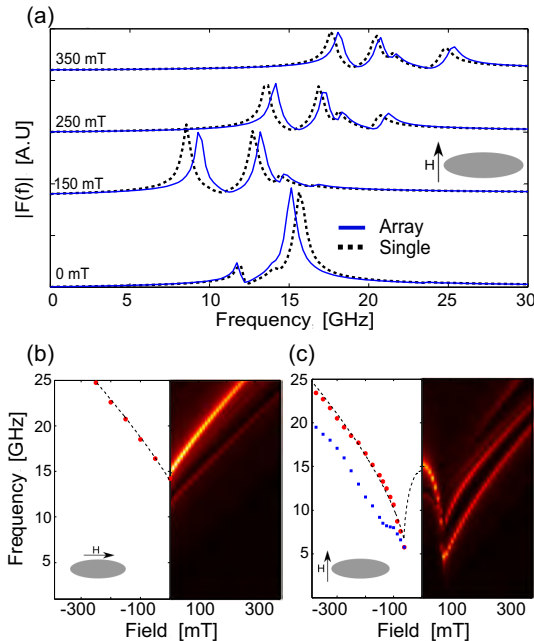


FIG. 10. (Color online) (a) Fourier power spectrum of a single ellipse (black dots) vs an array of ellipses (blue line) using periodic bc, for an applied field oriented along the short axis of the ellipse. (b) Left half: Experimental data and macrospin model as dotted black line. Right half: Micromagnetic simulation including edge defects and dipolar interactions in an array of ellipses. Data shown is for the field oriented along the long axis. (c) Same data for the field oriented along the short axis.

simulation model. Due to the large spacing between the individual ellipses in the array, the dipolar interaction is quite weak. In the simulations, we observe a small shift in the FMR frequencies, but not any indications of collective modes between neighboring ellipses.

The fact that the amplitude of the main mode dominates in the experiments, together with the weak dipolar coupling, explains the good agreement between the analytical macrospin model and experimental data. This indicates that in the limit of weak dipolar interaction, our macrospin model can be used to estimate the FMR frequency of the main mode in magnetic elements within the investigated size range (e.g., in a single domain state). Using an analytical macrospin model compared to performing numerical simulations simplifies the analysis considerably. The various energy terms contributing to the FMR dynamics can then be separated and their relative importance investigated.

VI. CONCLUSIONS

In this study, we have investigated how the combined interplay between shape anisotropy and crystalline anisotropy affects the magnetodynamic properties of confined magnetic elements. We have shown how the dimensions of the magnetic elements can be used to balance crystalline and shape anisotropies, and that this can be used to tailor the magnetodynamic properties.

We have shown that a simple macrospin model for the FMR frequency gives good agreement with the experimental results for the main FMR mode. Comparing experimental data and model calculations, we show how changing the sample size affects the magnetodynamic properties. For the smallest ellipses, shape anisotropy is dominating, whereas for the largest ellipses, crystalline anisotropy is the dominating energy term. From Eq. (11), the relative contributions to the resonance frequency from crystalline and shape anisotropy are given by $H_k/\mu_0 M_s(N_x - N_y)$, determined by the anisotropy field H_k , the saturation magnetization M_s , and the demagnetization factors N_i . This means that for the case of a 10-nm-thick epitaxial Fe film, one has an intermediate regime between approximately 50 nm to 1 μm where one can use the sample size as an additional tuning parameter for the dynamic properties. For other materials with a different H_k and M_s , this regime can be shifted to smaller/larger sample sizes.

The effects of nonideal sample edges and dipolar interaction in the array of ellipses were investigated using micromagnetic simulations. We found that edge defects in the form of a reduced edge magnetization had to be included in the micromagnetic model, and that this needs to be taken into account in understanding the full FMR spectrum. The static dipolar interaction in the array was found to shift the FMR frequency of the order of 1 GHz compared to that of a single ellipse. From the simulated FMR spectrums, we found no indications of collective spin excitations due to the dynamic dipolar interaction between neighboring ellipses.

The tunability of the relative contributions from crystalline and shape anisotropies means that by changing the material parameters and sample size, one can tailor the magnetodynamic properties of the magnetic elements, which could be of importance for magnonics applications.

ACKNOWLEDGMENTS

This work was supported by the Research council of Norway, Project No. 216700. V.F. acknowledges partial funding obtained from the Norwegian Ph.D. Network on Nanotechnology for Microsystems, which is sponsored by the Research Council of Norway, Division for Science, under Contract No. 221860/F40. F.M. acknowledges support from Catalan Government COFUND-FP7. J.M.H. and F.M. also thank the Spanish Government for support (Grant No. MAT2011-23698).

- [1] R. L. Stamps *et al.*, *J. Phys. D: Appl. Phys.* **47**, 333001 (2014).
- [2] J. Åkerman, *Science* **308**, 508 (2005).
- [3] S. D. Bader, *Rev. Mod. Phys.* **78**, 1 (2006).

- [4] M. Krawczyk and D. Grundler, *J. Phys.: Condens. Matter* **26**, 123202 (2014).
- [5] V. V. Kruglyak, S. O. Demokritov, and D. Grundler, *J. Phys. D: Appl. Phys.* **43**, 264001 (2010).

- [6] A. Moser, K. Takano, D. T. Margulies, M. Albrecht, Y. Sonobe, T. Ikeda, S. Sun, and E. E. Fullerton, *J. Phys. D: Appl. Phys.* **35**, R157 (2002).
- [7] S. S. P. Parkin, K. P. Roche, M. G. Samant, P. M. Rice, R. B. Beyers, R. E. Scheuerlein, E. J. O'Sullivan, S. L. Brown, J. Bucchigano, D. W. Abraham, Y. Lu, M. Rooks, P. L. Trouilloud, R. A. Wanner, and W. J. Gallagher, *J. Appl. Phys.* **85**, 5828 (1999).
- [8] R. D. McMichael and M. D. Stiles, *J. Appl. Phys.* **97**, 10J901 (2005).
- [9] G. Gubbiotti, G. Carlotti, T. Okuno, M. Grimsditch, L. Giovannini, F. Montoncello, and F. Nizzoli, *Phys. Rev. B* **72**, 184419 (2005).
- [10] F. Montoncello, L. Giovannini, F. Nizzoli, P. Vavassori, M. Grimsditch, T. Ono, G. Gubbiotti, S. Tacchi, and G. Carlotti, *Phys. Rev. B* **76**, 024426 (2007).
- [11] Q. F. Xiao, J. Rudge, B. C. Choi, Y. K. Hong, and G. Donohoe, *Phys. Rev. B* **73**, 104425 (2006).
- [12] M. L. Schneider, J. M. Shaw, A. B. Kos, Th. Gerrits, T. J. Silva, and R. D. McMichael, *J. Appl. Phys.* **102**, 103909 (2007).
- [13] H. T. Nembach, J. M. Shaw, C. T. Boone, and T. J. Silva, *Phys. Rev. Lett.* **110**, 117201 (2013).
- [14] Y. Yahagi, C. R. Berk, B. D. Harteneck, S. D. Cabrini, and H. Schmidt, *Appl. Phys. Lett.* **104**, 162406 (2014).
- [15] M. Hanson, O. Kazakova, P. Blomqvist, R. Wäppling, and B. Nilsson, *Phys. Rev. B* **66**, 144419 (2002).
- [16] R. D. McMichael and B. B. Maranville, *Phys. Rev. B* **74**, 024424 (2006).
- [17] H. T. Nembach, J. M. Shaw, T. J. Silva, W. L. Johnson, S. Kim, R. D. McMichael, and P. Kabos, *Phys. Rev. B* **83**, 094427 (2011).
- [18] J. M. Shaw, S. E. Russek, T. Thomson, M. J. Donahue, B. D. Terris, O. Hellwig, E. Dobisz, and M. L. Schneider, *Phys. Rev. B* **78**, 024414 (2008).
- [19] J. Fassbender, D. Ravelosona, and Y. Samson, *J. Phys. D: Appl. Phys.* **37**, R179 (2004).
- [20] M. Hanson, C. Johanson, B. Nilsson, P. Isberg, and R. Wäppling, *J. Appl. Phys.* **85**, 2793 (1999).
- [21] A. Vansteenkiste, J. Leliaert, M. Dvornik, M. Helsen, F. G. Sanchez, and B. V. Waeyenberge, *AIP Adv.* **4**, 107133 (2014).
- [22] M. Hanson, R. Bručas, T. J. Antosiewicz, R. K. Dumas, B. Hjörvarson, V. Flovik, and E. Wahlström [Phys. Rev. B (to be published)].
- [23] H. Suhl, *Phys. Rev.* **97**, 555 (1955).
- [24] J. A. Osborn, *Phys. Rev.* **67**, 351 (1945).
- [25] Y. Li, Y. Lu, and W. E. Bailey, *J. Appl. Phys.* **113**, 17B506 (2013).
- [26] M. Dvornik, P. V. Bondarenko, B. A. Ivanov, and V. V. Kruglyak, *J. Appl. Phys.* **109**, 07B912 (2011).
- [27] O. Dmytriiev, V. V. Kruglyak, M. Franchin, H. Fangohr, L. Giovannini, and F. Montoncello, *Phys. Rev. B* **87**, 174422 (2013).
- [28] G. Carlotti, S. Tacchi, G. Gubbiotti, M. Madami, H. Dey, G. Csaba, and W. Porod, *J. Appl. Phys.* **117**, 17A316 (2015).


9.5 Paper V

Vegard Flovik, Ferran Macià, Erik Wahlström.

Describing synchronization and topological excitations in arrays of magnetic spin torque oscillators through the Kuramoto model.

Sci. Rep. 6, 32528 (2016).

SCIENTIFIC REPORTS



OPEN

Describing synchronization and topological excitations in arrays of magnetic spin torque oscillators through the Kuramoto model

Vegard Flovik¹, Ferran Macià² & Erik Wahlström¹

Received: 26 April 2016

Accepted: 10 August 2016

Published: 01 September 2016

The collective dynamics in populations of magnetic spin torque oscillators (STO) is an intensely studied topic in modern magnetism. Here, we show that arrays of STO coupled via dipolar fields can be modeled using a variant of the Kuramoto model, a well-known mathematical model in non-linear dynamics. By investigating the collective dynamics in arrays of STO we find that the synchronization in such systems is a finite size effect and show that the critical coupling—for a complete synchronized state—scales with the number of oscillators. Using realistic values of the dipolar coupling strength between STO we show that this imposes an upper limit for the maximum number of oscillators that can be synchronized. Further, we show that the lack of long range order is associated with the formation of topological defects in the phase field similar to the two-dimensional XY model of ferromagnetism. Our results shed new light on the synchronization of STO, where controlling the mutual synchronization of several oscillators is considered crucial for applications.

The emergence of coherent phases of interacting oscillators is at the foundation of the cooperative functioning of a wealth of different systems in nature¹. Examples of collective behavior can be chosen within a wide range of systems such as laser arrays², Josephson junctions³, chemical reactions⁴, synchronously flashing firefly populations⁵, disease spreading⁶, or cortical oscillations in the brain^{6,7}. Science has sought mathematical models for understanding collective phenomena in large populations of oscillators that were tractable both analytically and numerically.

The Kuramoto model is a well known mathematical model in non-linear dynamics that describes large systems of coupled phase oscillators⁸. The model, with a remarkable simplicity, has been used to describe the essential features of collective excitations in a vast set of biological and physical phenomena^{8–16}. Although the Kuramoto model originally described oscillators interacting all-to-all with the same strength, variations of the model have been used to describe systems with phase offset and time delays in the couplings, other topologies like one-dimensional structures with local couplings etc. (see e.g. ref. 9 for an overview of extensions of the Kuramoto model). In particular, two-dimensional Kuramoto networks with diffusive local coupling accept solutions consisting in waves, spirals and many other patterns¹⁷.

Understanding the collective behavior in oscillator networks is also an intensely studied topic in modern magnetism: the synchronization of spin torque oscillators (STO). STO are strongly non-linear magnetic oscillators that can be implemented into nanoscale devices working at microwave frequencies, and can be frequency and phase locked to external oscillatory signals or other STO^{18–32}. They are envisaged to be useful for a variety of advanced magnetic nanodevices, as microwave sources and for signal processing in telecommunication technologies (see e.g. refs 33–35 and references therein). STO have also been proposed as possible candidates for a full spintronic implementations of neural networks, based on nano-devices emulating both neurons and synapses^{35,36}. Building artificial neural networks for computation is an emerging field of research within bio-inspired computing^{33–40}, where controlling the collective behavior in oscillator networks is crucial.

In both experimental and theoretical studies, most of the work has been performed for limited number of oscillators. Experimentally, the synchronization of STO has proven to be difficult, and the synchronization of

¹Department of Physics, NTNU, Norwegian University of Science and Technology, N-7491 Trondheim, Norway.

²Institut de Ciència de Materials de Barcelona (ICMAB-CSIC), Campus UAB, 08193 Bellaterra, Spain. Correspondence and requests for materials should be addressed to V.F. (email: vflovik@gmail.com)

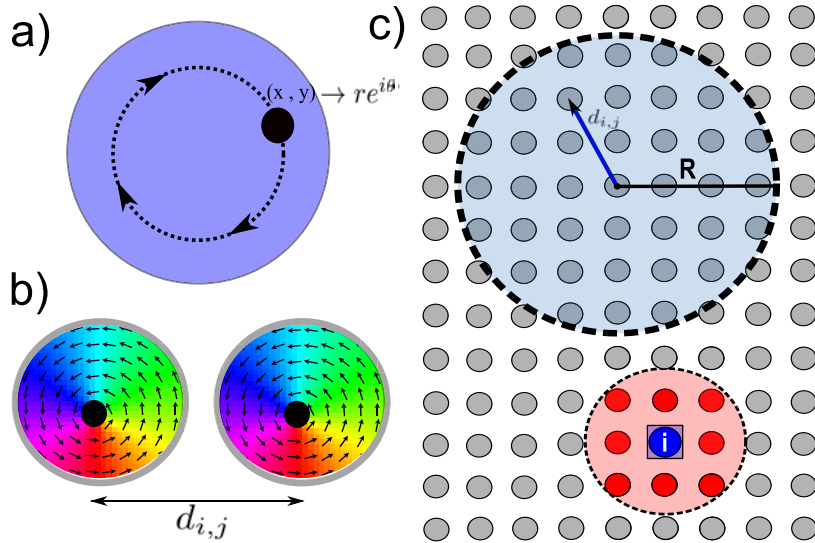


Figure 1. (a) The gyrotropic motion of the vortex core around the center of the disc can be described by the radius r and phase, θ . (b) Two vortex based STO separated by a distance $d_{i,j}$, showing the curling magnetization in the disc plane and the location of the vortex core indicated in black. (c) Network model for an array of STO. The interaction strength is determined by the spacing $d_{i,j}$ and we include interactions within a coupling radius R , indicated by the blue circle in the figure. The local correlation function β_i at position i (blue) is given by the degree of synchronization with its neighbors (red).

only a few oscillators has been demonstrated^{30,32}. Theoretically, the magnetization dynamics of STO is modeled with the Landau-Lifshitz-Gilbert-Slonzewski (LLGS) equation^{41,42}, but large number of STO lead to challenging computations caused by the non-local dipolar fields. It is important to consider that in these non-linear systems “more is different”, and that the collective behavior can not be derived simply from the behavior of its individual elements. Thus, a theoretical framework capable to capture the essential dynamics would be ideal to explore those systems.

Here, we show that two-dimensional arrays of STO coupled via dipolar fields can be modeled by a variant of the Kuramoto model. We begin with describing two coupled STO with the Thiele equation⁴³ and show that for small-amplitude oscillations the system can be described as a simple phase oscillator model. Next, we model the interactions for the case of a two-dimensional array of oscillators based on the dipolar coupling and obtain a modified Kuramoto model. Finally we compare the results from our model to the micromagnetic solution of the LLGS equation.

We find that the synchronization in two-dimensional arrays of dipolar coupled STO is purely a finite size effect and the critical coupling strength for obtaining a globally synchronized state scales with the number of oscillators N as $\lambda_{\text{crit}} \propto \log(N)$. Using realistic values of the dipolar coupling strength between STO we show that this imposes an upper limit for the maximum number of STO that can be synchronized. Further, we study the synchronization transition between the initial formation of locally synchronized clusters and the globally synchronized and phase coherent state and correlate it with a transition in the local order of the system. We also observe the emergence of topological defects and the formation of patterns in the phase field similar to the two-dimensional XY-model of magnetism—suggesting a connection between arrays of STO, systems described by a 2d Kuramoto model and the 2d XY model of statistical mechanics.

Results

From the Thiele equation to the Kuramoto model. We are considering STO whose free layer ground state configuration is a magnetic vortex. The vortex state is characterized by in-plane curling magnetization, and a small (~ 10 nm) region of the vortex core with out-of-plane magnetization⁴⁴. The gyrotropic motion of the vortex core is driven by the injection of a DC spin polarized current through the STO stack, and can be described by a gyration radius r and phase θ , as illustrated in Fig. 1a. We first model the interaction of two vortices with the Thiele equation with an extra term that accounts for the vortex interaction. These equations describe the vortices motion given by their coordinates $\mathbf{X}_{1,2}$ in their self induced gyrotropic mode, and include the spin-transfer-torque (STT) as well as a coupling term^{43,45}.

$$G(\mathbf{e}_z \times \dot{\mathbf{X}}_{1,2}) - k(\mathbf{X}_{1,2})\mathbf{X}_{1,2} - D_{1,2}\dot{\mathbf{X}}_{1,2} - \mathbf{F}_{\text{STT},1,2} - \mathbf{F}_{\text{int}}(\mathbf{X}_{2,1}) = 0. \quad (1)$$

Here, G is the gyroconstant, $k(\mathbf{X}_{1,2})$ the confining force, $D_{1,2}$ the damping coefficient and \mathbf{F}_{STT} the STT. The interaction between the neighboring STO illustrated in Fig. 1b is summarized by a dipolar coupling term given by $\mathbf{F}_{\text{int}} = -\mu(d)\mathbf{X}_{2,1}$, where $\mu(d)$ describes the interaction strength as a function of the separation d between the two STO.

Assuming a small difference in the nominal frequencies of two coupled STO described by Eq. (1), one can linearize the set of equations following the approach by Belanovsky *et al.*²⁷, showing that the dynamics of the phase difference between the STO can be described by Adler's equation⁴⁶. Following these approximations, the set of equations reduce to that of two coupled phase oscillators θ_1 and θ_2 : (see 'Supplementary information' for details).

$$\dot{\theta}_1 = \omega_1 + \lambda \sin(\theta_2 - \theta_1), \quad (2)$$

$$\dot{\theta}_2 = \omega_2 + \lambda \sin(\theta_1 - \theta_2), \quad (3)$$

where $\omega_{1,2}$ are eigenfrequencies of oscillators $\theta_{1,2}$ respectively, and λ describes the interaction strength trying to synchronize them.

To check the validity of the approximations, one can compare the results obtained using a simplified phase oscillator model to a numerical solution of Eq. (1) as well as a micromagnetic solution of the full system using the LLGS equation. This was done by Belanovsky *et al.*²⁷, where they found that for a small difference in nominal frequencies, in their case given by a difference in STO disc diameter $\Delta D/D_0 \leq 5\%$, the synchronization can be qualitatively described using the simplified model. Assuming the error in state-of-the-art fabrication processes is below this limit, the simplified equations are a valid description of the system.

The functional form of Eqs (2–3) is the same as that of the well known Kuramoto model^{8,9}, which is a generalization for the case of an ensemble of weakly coupled phase oscillators. Considering the interaction between several STO, we obtain a Kuramoto model where the single oscillator state is described through the dynamic equation of its phase θ_i due to the interaction with its surrounding oscillators θ_j :

$$\frac{d\theta_i}{dt} = \omega_i + \sum_{j \neq i} \lambda_{ij} \sin(\theta_j - \theta_i). \quad (4)$$

The coupling term is here generalized to include the interaction between several oscillators, determined by the interaction strength λ_{ij} between oscillators θ_i and θ_j . This determines the nature of the interaction, ranging from a global all-to-all coupling where $\lambda_{ij} = \lambda$ for all oscillators, to a local interaction where $\lambda_{ij} = 0$ for all but the nearest neighbors. Here, we are considering the intermediate case of a non-local coupling to mimic the dipolar interaction between neighboring STO. Starting from a macrodipole approximation for the dipolar energy between two magnetic dipoles μ_1 and μ_2 , the average interaction strength is found to decay as $\mu(d) \propto d_{ij}^{-3}$ ⁴⁷, where d_{ij} is the distance between oscillators θ_i and θ_j . We thus set the coupling strength to

$$\lambda_{ij} = \begin{cases} \lambda/d_{ij}^3 & d_{ij} < R \\ 0 & d_{ij} > R, \end{cases} \quad (5)$$

where we include interactions within a coupling radius R , indicated by the blue circle in Fig. 1c. The network model for the STO array is implemented with bi-periodic boundary conditions and the time evolution of the oscillator phases given by Eq. (4) is solved numerically. A small random disorder in the oscillator eigenfrequencies is included by setting $\omega_i = \omega_0 \pm \delta\omega_i$. Here, $\omega_0 = 1$ GHz and $\delta\omega_i$ represents a uniformly distributed random disorder where $\delta\omega_i/\omega_0 \leq 2.5\%$. The interaction strength is determined by the STO spacing and size, as well as the magnetic material properties³¹. Here, the interaction strength has been varied in the range $\lambda = 1$ –20 MHz, and is in the same range as the interaction strength extracted from micromagnetic simulations for similar STO³¹.

In order to evaluate the Kuramoto model as a valid description for arrays of STO, we compare it to a micromagnetic solution of the complete system, accounting for all dynamic dipolar terms (see 'Methods' section). To compare the Kuramoto model and the micromagnetic solution, we define a suitable order parameter to distinguish disordered and synchronized states. The phase of the individual oscillators θ_i is used to define the order parameter ρ , describing the phase coherence in a system of N oscillators:

$$\rho = \frac{1}{N} \left| \sum_j e^{i\theta_j} \right|. \quad (6)$$

The case $\rho = 0$ corresponds to the maximally disordered state, whereas $\rho = 1$ represents the state where all oscillators are perfectly synchronized and phase coherent. In addition to the global order parameter ρ , we define a local correlation function β_i :

$$\beta_i = \frac{1}{n} \left| \sum_{\langle j \rangle} e^{i\theta_j} \right|, \quad (7)$$

where the brackets indicate a summation over neighboring oscillators, and n is the number of neighbors. β_i is a measure of the phase correlation of oscillator θ_i and its neighbors, indicated by the blue and red oscillators in Fig. 1c respectively. If oscillator θ_i is located within a synchronized cluster, $\beta_i \rightarrow 1$. Calculating β thus allows for

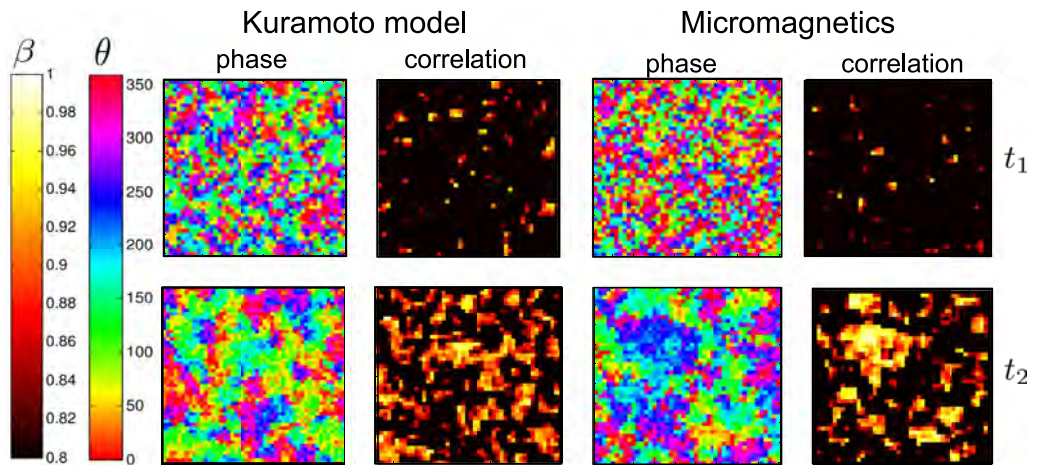


Figure 2. Snapshots of the phase map θ_i and local correlation function β_i for the Kuramoto model and the micromagnetic solution at time t_1 and $t_2 > t_1$ for a network of 45×45 oscillators.

investigating the formation of locally synchronized clusters and the emergence of patterns of synchronized states, which can not be obtained simply from the global order parameter ρ .

Kuramoto model versus micromagnetic simulations. We now compare the Kuramoto model given by Eq. (4) and the full micromagnetic solution of the LLGS equation (see ‘Methods’ section for details). Starting from a disordered initial state, we investigate the synchronization dynamics by calculating the time evolution of the phase distribution θ_i and local correlation β_i . As an example, we show in Fig. 2 snapshots of θ_i and β_i for the Kuramoto model and the micromagnetic solution for a system of 45×45 oscillators at times t_1 and $t_2 > t_1$, with random initial phases. At time t_1 , one notices the initial formation of small locally synchronized clusters, as seen through both the phase distribution and the bright areas in the correlation maps, where $\beta \rightarrow 1$. As time progresses to t_2 , these clusters grow in size and merge with neighboring clusters.

Comparing the two models, we find that they both show the same behavior. For weak interaction strengths, the system tends to be in a disordered state with no correlation between neighboring oscillators. By increasing the interaction strength above a certain threshold, synchronized clusters begin to form. The oscillators within each cluster are synchronized, but might not be phase coherent with other clusters. This can be seen in the phase maps in Fig. 2, where the individual clusters have different phases. As time progresses, the transition from a disordered to a synchronized state is governed by the growth and merging of neighboring clusters, reaching a globally synchronized and phase coherent state for sufficiently strong interactions.

Depending on the interaction strength, the system ends up in either a disordered, partially synchronized or globally synchronized state. Controlling the interaction strength is thus the key parameter to determine the system behavior. The interaction strength needed to obtain synchronization will depend on the differences in the nominal frequencies of the oscillators³¹. Another important consideration, is whether the critical interaction strength also depends on the number of oscillators. Lee *et al.*⁴⁸ have studied the synchronization in a 2d Kuramoto model with a nearest neighbor interaction. They showed that the transition to a synchronized state depends strongly on system size, and that the critical coupling strength needed to synchronize scales with the number of oscillators N as $\lambda_{\text{crit}} \propto \log(N)$. This raises the question if such a scaling law can also be observed in our models: observing the same scaling laws in both the Kuramoto model and the micromagnetic solution would strengthen the suggestion of the Kuramoto model as a valid description of arrays of STO.

We first consider our Kuramoto model, which has a non-local interaction to mimic the dipolar interaction in arrays of STO. Due to the increased complexity compared to the nearest neighbor model studied by Lee *et al.*⁴⁸, an analytical derivation of the scaling behavior with system size is to our knowledge still an open question. To investigate the scaling behavior we thus resort to a numerical solution. We performed simulations with the number of oscillators ranging from $N = 9$ to $N = 2500$, gradually increasing the interaction strength between each simulation until the system reaches a synchronized state at a critical coupling strength, λ_{crit} . 100 simulations were performed for each system size, with different initial oscillator phases and eigenfrequencies. In Fig. 3a we show a plot of λ_{crit} vs. number of oscillators, N . The results indicate that the critical coupling strength scales as $\lambda_{\text{crit}} \propto \log(N)$, same as the nearest neighbor Kuramoto model investigated by Lee *et al.*⁴⁸. The main difference compared with the nearest neighbor model is that we include interactions within a coupling radius R , as indicated by the blue circle in Fig. 1c. The imposed cutoff radius has a physical justification when considering a realistic system, which would inevitably include thermal noise. As the STO we consider are weakly coupled, and the dipolar interaction decay with distance, there will be a limiting spacing where the thermal noise level is comparable to the coupling

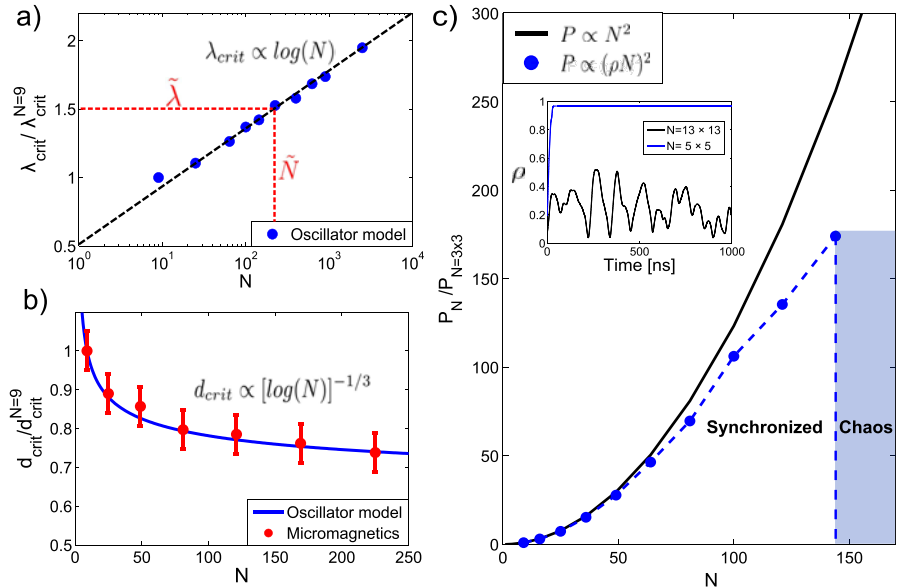


Figure 3. (a) Critical coupling strength λ_{crit} vs. number of oscillators N in the Kuramoto model, normalized to the case where $N = 3 \times 3$. Red dotted line: For a system size \tilde{N} , there is a corresponding minimum coupling strength $\tilde{\lambda}$ to obtain a synchronized state, and vice versa. (b) Blue solid line: Expected scaling between critical oscillator spacing, d_{crit} , and number of oscillators when assuming a dipolar interaction decaying as $1/d^3$. Red datapoints: Results from micromagnetic simulations. (c) Black solid line: Power output assuming an ideal scaling, $P \propto N^2$. Blue dotted line: Calculated power output for an interaction strength $\tilde{\lambda} = 7.5$ MHz, normalized to the case where $N = 3 \times 3$. Inset: Order parameter ρ for 3×3 and 13×13 STO respectively, showing the transition from a synchronized state to chaotic behavior as the number of STO is increased.

strength. In our model we observe that the results do not depend qualitatively on the range of the cutoff radius, and that the large scale behavior is dominated by the diffusive coupling. This suggests that insight from studying the analytically tractable nearest neighbor model of Lee *et al.*⁴⁸ might provide valuable insight into the behavior of STO arrays.

The coupling in the Kuramoto model is defined simply as an interaction strength given by λ in Eq. (4). In the micromagnetic model the coupling comes from dipolar interactions, determined by the magnetic material properties and the STO spacing. In order to investigate the scaling behavior in the micromagnetic solution, one thus needs to relate the critical interaction strength to a critical STO spacing. Following the aforementioned macro-dipole approximation that the effective dipolar interaction decays as $1/d^3$, one can relate the coupling strength λ_{crit} to a critical spacing d_{crit} between neighboring STO as $d_{crit} \propto [\log(N)]^{-1/3}$. Micromagnetic simulations were then performed to obtain d_{crit} vs. number of oscillators in the range $N = 3 \times 3$ to $N = 15 \times 15$. The results are shown as the red datapoints in Fig. 3b. For comparison, we show as a solid line the expected scaling from the Kuramoto model: $d_{crit} \propto [\log(N)]^{-1/3}$. The good agreement between the micromagnetics result and the Kuramoto model indicate that they both follow the same scaling law, strengthening the suggestion of the Kuramoto model as a valid description for arrays of STO.

Scaling of output power in arrays of STO. To investigate the implications of the scaling with system size, we consider a model calculation of the output power as we increase the number of STO. For applications of STO as e.g. nanoscale microwave generators, the power output of a single STO is not competitive. Decisive improvement is expected from the synchronization and phase locking of several STO, as this would result in a quadratic increase of the output power, $P \propto N^2$ for N synchronized oscillators.

The output of a single STO can be described by its amplitude and phase, $a_j e^{i\theta_j}$. In our model we have assumed a constant amplitude for all STO and the total amplitude A for an array of STO is given by: $A = \sum_j a e^{i\theta_j}$. The power output is proportional to $|A|^2$, and for N oscillators we obtain $P \propto \left| a N \frac{1}{N} \sum_j e^{i\theta_j} \right|^2 \propto (\rho N)^2$, from the definition of the order parameter ρ in Eq. (6). A quadratic scaling in the power output, $P \propto N^2$, implies a perfectly synchronized and phase coherent state, given by $\rho = 1$. However, as the coupling strength to obtain a synchronized state scales with the number of STO, this will affect the power output when scaling up to large arrays.

As an example, we consider a system of STO composed of 200 nm diameter spin valve nanopillars with 15 nm thick Permalloy as the ferromagnetic layer. The average interaction energy can be extracted from micromagnetic

simulations, and for an edge-edge spacing of 150 nm the interaction strength is found to be $\tilde{\lambda} \approx 7\text{--}8\text{ MHz}^{31}$. To increase the output power, we are now interested in scaling up to a large number of STO. We keep the same STO spacing when scaling up, e.g. keeping λ fixed. From Fig. 3a, we see that for an interaction strength $\tilde{\lambda}$, there is a corresponding number of STO, \tilde{N} , where $\lambda_{\text{crit}} > \tilde{\lambda}$. This can be illustrated by calculating the total power output as the number of STO is increased, as shown in Fig. 3c. For a small number of STO, we see that the power output follows close to the ideal N^2 scaling. However, as the number of STO is increased, the scaling with system size becomes increasingly important. For a certain number of STO, indicated by \tilde{N} in Fig. 3a, the interaction is no longer strong enough to obtain a synchronized state. This is also illustrated in the inset of Fig. 3c, where we plot the order parameter ρ for arrays of 3×3 and 13×13 STO respectively, showing the transition from a synchronized state to chaotic behavior as the number of STO is increased above \tilde{N} .

This illustrates the importance of our findings that synchronization in such 2d arrays is purely a finite size effect. The interaction strength is limited by the material properties and STO spacing, and using realistic values of the coupling strength we start to see significant deviations from the ideal $P \propto N^2$ scaling for array sizes larger than 10×10 STO (see Fig. 3c). This means that in a physical realizable system, the scaling with system size imposes an upper limit for the maximum number of STO that can be synchronized.

Topological defects. That the synchronized and phase coherent state is purely a finite size effect, is similar to that of the classical 2d XY model of magnetism. The Kuramoto model is indeed similar to the 2d XY model⁴⁹, where the direction of spin in the XY model corresponds to the oscillator phase in the Kuramoto model. In the 2d XY model a long range ordered phase is absent due to the presence of spin wave fluctuations and topological defects. The lack of long range order is a specific case of the Mermin-Wagner theorem in spin systems⁵⁰, stating that continuous symmetries cannot be spontaneously broken in systems with sufficiently short range interactions in dimensions $d \leq 2$. The fluctuations preventing long range order in the 2d XY model diverge logarithmically with system size⁴⁹, in agreement with the logarithmic scaling observed in our system of STO.

Similar topological defects at the boundaries between locally synchronized clusters have previously been observed in the nearest neighbor Kuramoto model⁴⁸ as well as in other two-dimensional oscillator network models^{17,51–53}. In oscillator networks this is associated with the appearance of topological defects in the oscillator phase field, θ_i . In the continuum limit this is expressed as:

$$\frac{1}{2\pi} \oint \nabla \theta(\mathbf{r}, t) \cdot d\mathbf{l} = \pm n, \quad (8)$$

where $d\mathbf{l}$ is an integration path enclosing the defect, and n is the topological charge.

Such topological features are observed also in our Kuramoto model for arrays of STO. The presence of vortices in the phase field is more pronounced as the system size increases. As an example we here consider an array of 50×50 oscillators. The disorder in the system is kept constant (given by the difference in the nominal frequencies of the oscillators) and the interaction strength λ is varied, acting as the inverse temperature: as coupling increases, the system becomes more ordered. Starting from a disordered initial state and varying the interaction strength between each simulation, we observe 4 different regimes: For weak interaction strengths we observe the formation of locally synchronized clusters, where cluster sizes increase with interaction strength. Apart from the localized clusters there is no long range order in the system (indicated as regime 1 in Fig. 4). Increasing λ above a certain threshold, we enter regime 2. Here we observe the formation of vortices in the phase field, and as an example we show in Fig. 4c a state with 4 vortices. The topological charge is conserved in the system, and two vortices of charge ± 1 respectively is present.

In both regime 1 and 2 long range order in the system is absent and $\rho \approx 0$, as indicated in Fig. 4a. (that $\rho > 0$ here is a result of fluctuations due to the finite array size). Increasing λ further we enter regime 3, where the transition from regime 2 \rightarrow 3 is governed by vortex annihilation processes (see ‘Supplementary information’). Here there are no topological defects in the phase field, and the lack of global phase coherence is due to spin waves in the phase field where the oscillator phases change smoothly across the array (regime 3 in Fig. 4b). For sufficiently strong interactions we enter regime 4. Increasing the interaction strength is analogous to increasing the exchange coupling in a Ferromagnetic system, resulting in a more ordered state. The result here is a gradual suppression of the spin waves in the phase field observed in regime 3 as the interaction strength is increased. Regime 4 is thus characterized as the globally phase coherent state where all oscillators are synchronized and phase coherent (regime 4 in Fig. 4b).

The growth of the order parameter ρ with increasing coupling strength λ in Fig. 4a resembles that of a phase transition. Previous work have shown that the synchronization transition in the globally coupled Kuramoto model can be described as a phase transition, where the nature of the transition can be of first or second-order depending on the frequency distribution and coupling topology^{8,54}. The Kuramoto model with finite range couplings is less studied, as these systems are difficult to analyze and solve analytically. A study of the locally coupled Kuramoto model on a d-dimensional lattice have shown that the synchronization transition depends strongly on the lattice dimensionality, and indicates $d = 4$ as the lower critical dimension for phase synchronization⁵⁵. This is in agreement with the observed scaling with system size in our model, which indicates that the synchronization transition is purely a finite size effect.

In order to investigate the synchronization transition in our model further, we calculate the spatial correlation function for the array of oscillators. The correlations decay with distance, and asymptotically the correlation function is given by: $\langle \theta(\mathbf{r}) \cdot \theta(\mathbf{R}) \rangle \propto e^{-|r-R|/\xi} / |r-R|^p$. This describes the correlation between oscillators at positions r and R respectively, and the correlation length ξ is obtained by averaging over all positions r and R in the array (an example is shown in ‘Supplementary information’ Fig. S2). From the decay of the correlation function, we

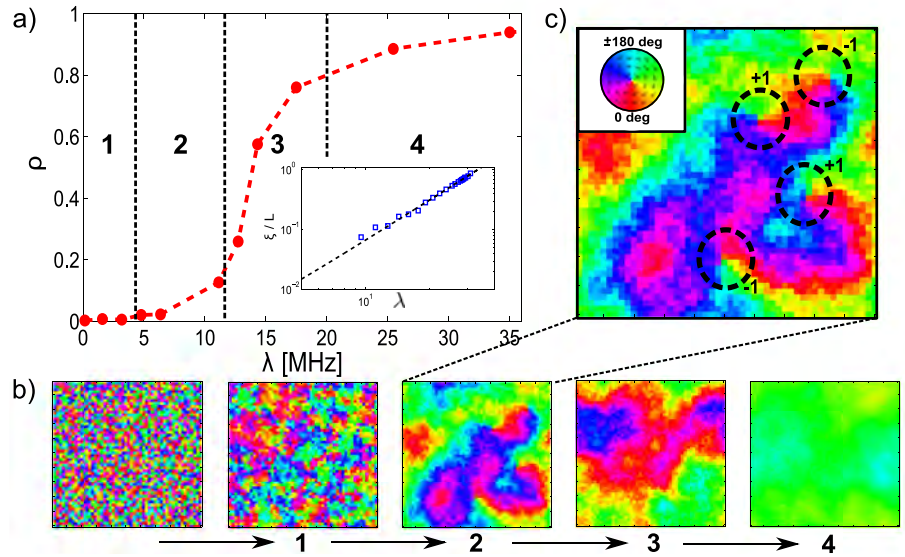


Figure 4. (a) Order parameter ρ vs. interaction strength λ in the Kuramoto model for a system of $N = 50 \times 50$ oscillators, showing the transition from a disordered ($\rho \approx 0$) to a globally synchronized and phase coherent state ($\rho \rightarrow 1$). Inset: Calculated correlation length ξ vs. interaction strength λ , where the correlation length is normalized to the system size, ξ/L ($N = L \times L$) (b) The corresponding phase maps, showing the transition from a disordered state via the formation of locally synchronized clusters (1), vortices (2), spin waves (3) and the globally phase coherent state (4). (c) Zoom in of phase map for regime 2, showing the appearance of 4 vortices of charges ± 1 respectively, as defined in Eq. (8).

obtain the correlation length ξ as a function of the interaction strength λ . Conventional phase transitions are accompanied by a diverging correlation length close to the transition. Here, we do not observe a diverging ξ going from the disordered to the phase coherent state (1 \rightarrow 4 in Fig. 4), and the correlation length remains finite. As inset in Fig. 4a we show a log-log plot of the correlation length normalized to the system size, ξ/L , ($N = L \times L$). The results indicate a power law relating the correlation length and the interaction strength as $\xi \propto \lambda^\nu$, where the exponent for this case was found to be $\nu = 2.1 \pm 0.1$. This means that the correlation length simply scales with the coupling strength, and the transition between regimes 1–4 in Fig. 4 correspond to structures of ever increasing length scales. The transition to the phase coherent state ($\rho \rightarrow 1$) occurs when the correlation length approaches the system size L , underlining the finite size effects on the synchronization transition and that the system is not undergoing a conventional phase transition. Further investigations of finite size effects, the lack of long range order in the Kuramoto model and the connection to the 2d XY model will be the subject of future work.

Discussion

To summarize, we have shown that the Kuramoto model provides a good description of arrays of STO. It provides a simple theoretical model to study large populations of coupled STO, which were previously inaccessible due to the long computation time for a full micromagnetic solution. By investigating the collective dynamics in large arrays of STO, we observed a scaling with system size indicating that the synchronization in arrays of dipolar-coupled STO is purely a finite size effect. The critical coupling strength to obtain a globally synchronized state scales with the number of oscillators, as $\lambda_{\text{crit}} \propto \log(N)$, preventing global synchronization for large system sizes. As a consequence of the scaling with system size, we showed that for realistic values of the dipolar coupling strength between STO this imposes an upper limit for the maximum number of oscillators that can be synchronized. Further, we showed that the lack of long range order and scaling with system size is associated with the emergence of topological defects and the formation of patterns in the phase field, similar to that of the 2d XY-model of magnetism.

In the present study we considered dipolar-coupled STO, where the short time delay in the coupling between neighboring oscillators compared to the oscillator frequency means that phase delay in the couplings can be neglected. However, for other coupling mechanisms, time delay can become significant. Interaction mediated by spin waves provide a different mechanism to obtain synchronization of STO³², where the finite propagation speed of the spin waves results in a phase offset in the couplings. Another recent proposal includes the use of non-local electrical couplings, where the coupling phase can be externally tuned through an electrical delay line³⁶.

From a dynamical systems point of view, the study of time delay induced modifications to the couplings is of fundamental interest, as well as of practical relevance for modeling of physical, biological and chemical systems. In such systems, time delay is associated with finite propagation velocity of the couplings via e.g latency times of

neuronal excitations, reaction times in chemical systems etc. (see e.g. ref. 9 and references therein). The possibility of designing STO arrays with a defined phase offset in the couplings suggests a real world analog to the more general Sakaguchi-Kuramoto model on a 2d lattice, which allows for a phase lag in the couplings⁵⁷.

Our study suggests, on the one hand, that the use of models from non-linear dynamics can be useful for describing synchronization of magnetic oscillators and, on the other hand, arrays of STO as a physical realizable model system for the Kuramoto model on a 2d lattice.

Methods

Micromagnetic model. The micromagnetic model is defined as arrays of discs, where the system is divided into a grid with a mesh size of 5 nm, limited by the exchange length of the ferromagnetic material (here Py). The volumetric quantities such as the magnetization \mathbf{M} and effective field \mathbf{H}_{eff} are treated at the center of each cell, whereas coupling quantities such as exchange strength are considered at the faces between cells. The numerical solution was obtained using the micromagnetic solver Mumax³⁵⁸, which uses a RKF 45 method to solve the Landau-Lifshitz-Gilbert-Slonzewski (LLGS) equation^{41,42} given by:

$$\frac{d\mathbf{M}}{dt} = \underbrace{-\gamma\mathbf{M} \times \mathbf{H}_{\text{eff}}}_{\text{Gyration}} + \underbrace{\frac{\alpha}{M_s} \left[\mathbf{M} \times \frac{d\mathbf{M}}{dt} \right]}_{\text{Damping}} - \underbrace{\frac{\chi}{d} JP(\theta) [\mathbf{M} \times (\mathbf{M} \times \mathbf{m}_f)]}_{\text{Spin-TransferTorque}} \quad (9)$$

Here, γ is the gyromagnetic ratio, α the damping parameter and M_s the saturation magnetization. The spin-transfer torque term is given by $\chi = g\mu_b/(2M_s^2 e)$, the charge current density J and the free layer thickness d . $P(\theta)$ is a polarization function assumed to increase with the relative angle θ between the magnetization of the free layer and the fixed layer and \mathbf{m}_f is a unit vector in the direction of the magnetization of the free layer.

In the model, each disc is composed by a magnetic free layer and a fixed polarizer which generates a perpendicular spin polarization p_z . The free layer in the STO is 30 nm thick Py with a disc diameter of 150 nm, and the damping parameter α was set to 0.01. A small disorder in the eigenfrequencies of the individual STO is included through a random distribution in the saturation magnetization in the range $[865, 885] \cdot 10^3$ A/m, resulting in a slight variation of STO eigenfrequencies. All discs were initialized with a vortex of same polarity and chirality, and the center-center spacing of the discs was varied to change the interaction strength. The polarizing layers are not included in the model as these layers, being uniformly magnetized in z direction have almost no influence on the vortices motion. The vortex gyration was driven by a DC spin current with a polarization $p_z = 0.3$, and current density $J \approx 4.3 \cdot 10^7$ A/m². During the simulations, a static magnetic field of 150 mT was applied along the z direction to set the vortex core polarity.

References

1. Strogatz, S. H. & Stewart, I. Coupled oscillators and biological synchronization. *Sci. Am.* **269**(6), 102–109 (1993).
2. Kourtchatov, S. Yu., Likhanski, V. V., Napartovich, A. P., Arecchi, F. T. & Lapucci, A. Theory of phase locking of globally coupled laser arrays. *Phys. Rev. A* **52**, 4089 (1995).
3. Wiesenfeld, K., Colet, P. & Strogatz, S. H. Synchronization Transitions in a Disordered Josephson Series Array. *Phys. Rev. Lett.* **76**, 404 (1996).
4. Singh, R. & Sinha, S. Spatiotemporal order, disorder, and propagating defects in homogeneous system of relaxation oscillators. *Phys. Rev. E* **87**, 012907 (2013).
5. Kuperman, M. & Abramson, G. Small World Effect in an Epidemiological Mode. *Phys. Rev. Lett.* **86**, 2909 (2001).
6. Breakspear, M., Heitmann, S. & Daffertshofer, A. Generative models of cortical oscillations: neurobiological implications of the Kuramoto model. *Front. Hum. Neurosci.* (2010).
7. Izhikevich, E. M. Which Model to Use for Cortical Spiking Neurons? *IEEE transactions on neural networks.* 15.5, 1063–1070 (2004).
8. Kuramoto, Y. & Nishikawa, I. Statistical macrodynamics of large dynamical systems. Case of a phase transition in oscillator communities. *J. Stat. Phys.* **49**, 569 (1987).
9. Acebrón, J. A. *et al.* The Kuramoto model: A simple paradigm for synchronization phenomena. *Rev. Mod. Phys.* **77**, 137 (2005).
10. Filatrella, G., Nielsen, A. H. & Pedersen, N. F. Analysis of a power grid using a Kuramoto-like model. *The European Physical Journal B.* **61**(4), 485–491 (2008).
11. Daniels, B. C., Dissanayake, S. T. M. & Trees, B. R. Synchronization of coupled rotators: Josephson junction ladders and the locally coupled Kuramoto model. *Phys. Rev. E* **67**, 026216 (2003).
12. Wiesenfeld, K., Colet, P. & Strogatz, S. H. Frequency locking in Josephson arrays: Connection with the Kuramoto model. *Phys. Rev. E* **57**, 1563 (1998).
13. Néda, Z., Ravasz, E., Vicsek, T., Brechet, T. & Barabási, A. L. Physics of the rhythmic applause. *Phys. Rev. E* **61**, 6987 (2000).
14. Heinrich, G., Ludwig, M., Qian, J., Kubala, B. & Marquardt, F. Collective Dynamics in Optomechanical Arrays. *Phys. Rev. Lett.* **107**, 043603 (2011).
15. Cumin, D. & Unsworth, C. P. Generalising the Kuramoto model for the study of neuronal synchronisation in the brain. *Physica D: Nonlinear Phenomena*, **226**(2), 181–196 (2007).
16. Timms, L. & English, L. Q. Synchronization in phase-coupled Kuramoto oscillator networks with axonal delay and synaptic plasticity. *Phys. Rev. E* **89**, 032906 (2014).
17. Lauter, R., Brendel, C., Habraken, S. J. M. & Marquardt, F. Pattern phase diagram for two-dimensional arrays of coupled limit-cycle oscillators. *Phys. Rev. E* 012902 (2015).
18. Rippard, W. H. *et al.* Injection Locking and Phase Control of Spin Transfer Nano-oscillators. *Phys. Rev. Lett.* **95** 067203 (2005).
19. Kaka, S. *et al.* Mutual phase-locking of microwave spin torque nano-oscillators. *Nature*, **437** 389–392 (2005).
20. Mancoff, F. B., Rizzo, N. D., Engel, B. N. & Tehrani, S. Phase-locking in double-point-contact spin-transfer devices. *Nature* **437** 393–395 (2005).
21. Pufall, M. R., Rippard, W. H., Russek, S. E., Kaka, S. & Katine, J. A. Electrical Measurement of Spin-Wave Interactions of Proximate Spin Transfer Nanooscillators. *Phys. Rev. Lett.* **97**, 087206 (2006).
22. Bonin, R., Bertotti, G., Serpico, C., Mayergoyz, I. D. & d'Aquino, M. Analytical treatment of synchronization of spin-torque oscillators by microwave magnetic fields. *Eur. Phys. J. B.* **68**, 221 (2009).
23. Zhou, Y., Person, J. & Åkerman, J. Intrinsic phase shift between a spin torque oscillator and an alternating current. *J. Appl. Phys.* **101**, 09A510 (2007).

24. Recende, S. M., de Aguiar, F. M. & Azevedo, A. Spin-Wave Theory for the Dynamics Induced by Direct Currents in Magnetic Multilayers. *Phys. Rev. Lett.* **94**, 037202. (2005).
25. Rezende, S. M., de Aguiar, F. M. & Azevedo, A. Spin-Wave Theory for the Dynamics Induced by Direct Currents in Magnetic Multilayers. *Phys. Rev. B* **73**, 094402 (2006).
26. Slavin, A. N. & Tiberkevich, V. S. Theory of mutual phase locking of spin-torque nanosized oscillators. *Phys. Rev. B* **74**, 104401 (2006).
27. Belanovsky, A. D. *et al.* Numerical and analytical investigation of the synchronization of dipolarly coupled vortex spin-torque nano-oscillators. *Appl. Phys. Lett.* **103**, 122405 (2013).
28. Belanovsky, A. D. *et al.* Phase locking dynamics of dipolarly coupled vortex-based spin transfer oscillators. *Phys. Rev. B* 100409(R) (2012).
29. Georges, B., Grollier, J., Cros, V. & Fert, A. Impact of the electrical connection of spin transfer nano-oscillators on their synchronization: an analytical study. *Appl. Phys. Lett.* **92**, 232504 (2008).
30. Ruotolo, A. *et al.* Phase-locking of magnetic vortices mediated by antivortices. *Nature Nanotechnology* **4**, 528–532 (2009).
31. Locatelli, N. *et al.* Efficient Synchronization of Dipolarly Coupled Vortex-Based Spin Transfer Nano-Oscillators. *Sci. Rep.* **5**, 17039 (2015).
32. Housang, A. *et al.* Spin-wave-beam driven synchronization of nanocontact spin-torque oscillators. *Nature Nanotechnology* **11**, 280–286 (2016).
33. Bonetti, S. & Åkerman, J. *Magnonics: From Fundamentals to Applications* (2013).
34. Macià, F., Kent, A. D. & Hoppensteadt, F. C. Spin-wave interference patterns created by spin-torque nano-oscillators for memory and computation. *Nanotechnology* **22**(9), 095301 (2011).
35. Locatelli, N., Cros, V. & Grollier, J. Spin-torque building blocks. *Nature Materials*, **13**, 11 (2014).
36. Csaba, G. & Porod, W. Computational Study of Spin-Torque Oscillator Interactions for Non-Boolean Computing Applications. *IEEE Trans. Magn.* **49**(7), 4447–4451 (2013).
37. Hoppensteadt, F. C. & Izhikevich, E. M. Oscillatory Neurocomputers with Dynamic Connectivity. *Phys. Rev. Lett.* **82**, 2983 (1999).
38. Maffezzoni, P., Bahr, B., Zheng, Z. & Daniel, L. Oscillator Array Models for Associative Memory and Pattern Recognition. *IEEE Trans. Circuits Syst. I, Reg. Papers*, **62**(6), 1591–1598 (2015).
39. Locatelli, N. *et al.* Spintronic devices as key elements for energy-efficient neuroinspired architectures. Proceedings of the 2015 Design, Automation & Test in Europe Conference & Exhibition.
40. Vincent, A. F. *et al.* Locking phenomena in oscillators. *Proc. IRE* **34**, 351 (1946).
41. Vincent, A. F. *et al.* Optimizing magnetodipolar interactions for synchronizing vortex based spin-torque nano-oscillators. *Phys. Rev. B* **92**, 045419 (2015).
42. Lee, T. E., Tam, H., Refael, G., Rogers, J. L. & Cross, M. C. Vortices and the entrainment transition in the two-dimensional Kuramoto model. *Phys. Rev. E* **82**, 036202 (2010).
43. Kostelitz, J. M. & Touless, D. J. Ordering, metastability and phase transitions in two-dimensional systems. *J. Phys. C* **6**, 1181 (1973).
44. Mermin, N. D. & Wagner, H. Absence of Ferromagnetism or Antiferromagnetism in One- or Two-Dimensional Isotropic Heisenberg Models. *Phys. Rev. Lett.* **17**, 1133 (1966).
45. Davidsen, J. & Kapral, R. Phase synchronization and topological defects in inhomogeneous media. *Phys. Rev. E* **66**, 055202(R) (2002).
46. Singh, R., Xu, J., Garnier, N. G., Pumir, A. & Sinha, S. Self-Organized Transition to Coherent Activity in Disordered Media. *Phys. Rev. Lett.* **108**, 068102 (2012).
47. Großmann, G., Peruani, F. & Bär, M. Superdiffusion, large-scale synchronization, and topological defects. *Phys. Rev. E* **93**, 040102(R) (2016).
48. Basnarkov, L. & Urumov, V. Phase transitions in the Kuramoto model. *Phys. Rev. E* **76**, 057201 (2007).
49. Hong, H., Park, H. & Choi, M. Y. Collective synchronization in spatially extended systems of coupled oscillators with random frequencies. *Phys. Rev. E* **72**, 036217 (2005).
50. Lebrun, R. *et al.* Mutual synchronization of spin torque nano-oscillators through a non-local and tunable electrical coupling. arXiv:1601.01247.
51. Sakaguchi, H. & Kuramoto, Y. A Soluble Active Rotator Model Showing Phase Transitions via Mutual Entertainment. *Prog. Theor. Phys.* **76**, 576 (1986).
52. Vansteenkiste, A. *et al.* The design and verification of MuMax3. *AIP Advances* **4**, 107133 (2014).

Acknowledgements

This work was supported by the Norwegian Research Council (NFR), project number 216700. V.F. acknowledge partial funding obtained from the Norwegian PhD Network on Nanotechnology for Microsystems, which is sponsored by the Research Council of Norway, Division for Science, under contract no. 221860/F40. F.M. acknowledges financial support from the Ramón y Cajal program through RYC-2014-16515 and from the MINECO through the Severo Ochoa Program for Centers of Excellence in R&D (SEV- 2015-0496).

Author Contributions

V.F. initiated the project, developed the model, performed the calculations/simulations and wrote the manuscript. F.M. and E.W. supervised the project and provided valuable input during the analysis/discussion of results and writing of the manuscript.

Additional Information

Supplementary information accompanies this paper at <http://www.nature.com/srep>

Competing financial interests: The authors declare no competing financial interests.

How to cite this article: Flovik, V. *et al.* Describing synchronization and topological excitations in arrays of magnetic spin torque oscillators through the Kuramoto model. *Sci. Rep.* **6**, 32528; doi: 10.1038/srep32528 (2016).



This work is licensed under a Creative Commons Attribution 4.0 International License. The images or other third party material in this article are included in the article's Creative Commons license, unless indicated otherwise in the credit line; if the material is not included under the Creative Commons license, users will need to obtain permission from the license holder to reproduce the material. To view a copy of this license, visit <http://creativecommons.org/licenses/by/4.0/>

© The Author(s) 2016

**Supplementary information: Describing synchronization and
topological excitations in arrays of magnetic spin torque
oscillators through the Kuramoto model**

Vegard Flovik,^{1,*} Ferran Macià,² and Erik Wahlström¹

*¹Department of Physics, NTNU, Norwegian University
of Science and Technology, N-7491 Trondheim, Norway*

*²Institut de Ciència de Materials de Barcelona (ICMAB-CSIC),
Campus UAB, 08193 Bellaterra, Spain*

From the Thiele equation to the phase oscillator model

We here provide some more details on the derivation of the Kuramoto model starting from the coupled Thiele equation:

$$G(\mathbf{e}_z \times \dot{\mathbf{X}}_{1,2}) - k(\mathbf{X}_{1,2})\mathbf{X}_{1,2} - D_{1,2}\dot{\mathbf{X}}_{1,2} - \mathbf{F}_{\text{STT},1,2} - \mathbf{F}_{\text{int}}(\mathbf{X}_{2,1}) = 0. \quad (\text{S1})$$

Here, $G = -2\pi p M_s h / \gamma$ is the gyroconstant, p is the core polarity, γ is the gyromagnetic ratio, M_s is the saturation magnetization and h is the thickness of the ferromagnetic layer. The confining force is given by $k(\mathbf{X}_{1,2}) = \omega_{01,2} G \left(1 + a \frac{\mathbf{X}_{1,2}^2}{R_{1,2}}\right)$ [1, 2], where $R_{1,2}$ are the disc radii and the gyrotronic frequency for disc 1, 2 is $\omega_{01,2} = \frac{20}{9} \gamma M_s h / R_{1,2}$. The damping coefficient $-D_{1,2} = \alpha \eta_{1,2} G$, where $\eta_{1,2} = \frac{1}{2} \ln \left(\frac{R_{1,2}}{2l_e} \right) + \frac{3}{8}$. Here, $l_e = \sqrt{\frac{A}{2\pi M_s}}$ is the exchange length given by the exchange stiffness A and the saturation magnetization M_s . Assuming a uniform perpendicularly magnetized polarizer layer, $\mathbf{F}_{\text{STT}} = \pi \gamma a_J M_s h (\mathbf{X}_{1,2} \times \mathbf{e}_z) = \varkappa (\mathbf{X}_{1,2} \times \mathbf{e}_z)$ [3], where the spin torque coefficient is given by $a_J = \hbar p_z J / (2|e| \hbar M_s)$, \hbar is the Planck's constant, J is the current density and e is the elementary charge. The interaction between the neighboring vortices is summarized by a dipolar coupling term given by $\mathbf{F}_{\text{int}} = -\mu(d)\mathbf{X}_{2,1}$, where $\mu(d)$ describes the interaction strength as a function of the separation d between the STO. A study of the dipolar interaction between neighboring vortices has been performed by Araujo *et al.* [4]. Starting from a macrodipole approximation for the dipolar energy between two magnetic dipoles μ_1 and μ_2 , they show that the average interaction energy can be written as $\langle W_{\text{int}} \rangle = \mu_{\text{eff}} C_1 C_2 X_1 X_2$. Here, C_i and X_i are the chirality and gyration radius respectively and μ_{eff} is given by:

$$\mu_{\text{eff}} = 3 \frac{\pi^2 \chi^2 R^2 h^2}{2d^3}, \quad (\text{S2})$$

where $\chi = 2/3$, R is the disc radius, h the thickness and d is the inter-disc spacing. In polar coordinates $(X_{1,2} \cos \theta_{1,2}, X_{1,2} \sin \theta_{1,2})$, the coupled equations for two neighboring vortices from Eq. (S1) can be written as:

$$\frac{\dot{X}_1}{X_1} = \alpha \eta_1 \dot{\theta}_1 - \frac{\varkappa}{G} + \frac{\mu X_2}{G X_1} \sin(\theta_1 - \theta_2) \quad (\text{S3})$$

$$\dot{\theta}_1 = -\frac{k(X_1)}{G} - \alpha\eta_1 \frac{\dot{X}_1}{X_1} - \frac{\mu X_2}{GX_1} \cos(\theta_1 - \theta_2) \quad (\text{S4})$$

$$\frac{\dot{X}_2}{X_2} = \alpha\eta_2 \dot{\theta}_2 - \frac{\varkappa}{G} - \frac{\mu X_1}{GX_2} \sin(\theta_1 - \theta_2) \quad (\text{S5})$$

$$\dot{\theta}_2 = -\frac{k(X_2)}{G} - \alpha\eta_2 \frac{\dot{X}_2}{X_2} - \frac{\mu X_1}{GX_2} \cos(\theta_1 - \theta_2) \quad (\text{S6})$$

One can then show that after a few approximations, the set of equations reduce to that of two coupled phase oscillators. We assume the same gyration radius for both vortices, $X_2 = X_1$, and that the steady state vortex gyrotropic radius is close to its mean value, X_0 . This means that Eq. (S3) can be set to zero, as $\dot{X}_1 = 0$, and we obtain:

$$\dot{\theta}_1 = \frac{\varkappa}{\alpha\eta_1 G} - \frac{\mu}{\alpha\eta_1 G} \sin(\theta_1 - \theta_2) \quad (\text{S7})$$

Setting $\dot{X}_1 = 0$ and $X_2 = X_1$ also in Eq. (S4):

$$\dot{\theta}_1 = -\frac{k(X_1)}{G} - \frac{\mu}{G} \cos(\theta_1 - \theta_2) \quad (\text{S8})$$

We then add Eqs. (S7) and (S8) to obtain:

$$\dot{\theta}_1 = \frac{\varkappa - \alpha\eta_1 k(X_1)}{2\alpha\eta_1 G} - \frac{\mu}{2\alpha\eta_1 G} [\sin(\theta_1 - \theta_2) + \alpha\eta_1 \cos(\theta_1 - \theta_2)]. \quad (\text{S9})$$

Following the same procedure for vortex nr. 2 and assuming low damping, $\alpha\eta << 1$, we obtain the equations for two coupled phase oscillators θ_1 and θ_2 :

$$\dot{\theta}_1 = \omega_1 + \lambda \sin(\theta_2 - \theta_1), \quad (\text{S10})$$

$$\dot{\theta}_2 = \omega_2 + \lambda \sin(\theta_1 - \theta_2), \quad (\text{S11})$$

Where $\omega_{1,2} = \frac{\varkappa - \alpha\eta_{1,2} k(X_{1,2})}{2\alpha\eta_{1,2} G}$ and $\lambda = \frac{\mu}{2\alpha\eta_{1,2} G}$. The functional form of Eqs. (S10)-(S11) is the same as that of the well known Kuramoto model, which is a generalization for the case of an ensemble of weakly coupled phase oscillators. Considering the interaction between several STO, determined by the interaction strength λ_{ij} between oscillators θ_i and θ_j , we obtain a

Kuramoto model for a population of N interacting oscillators:

$$\frac{d\theta_i}{dt} = \omega_i + \sum_{j \neq i} \lambda_{ij} \sin(\theta_j - \theta_i). \quad (\text{S12})$$

Vortex annihilation processes

Starting from a disordered initial condition, a number of vortices with $n = \pm 1$ is created initially, depending on the array size. Thermal fluctuations of sufficient amplitude could give rise to vortex unbinding, where free vortices proliferate due to thermal fluctuations. As we do not consider thermal effects, such vortex unbinding is not observed this in our model. Since a vortex is topological, it exists until it meets and annihilates with a vortex of opposite polarity, and the transition from disordered to a synchronized state is governed by vortex annihilation processes.

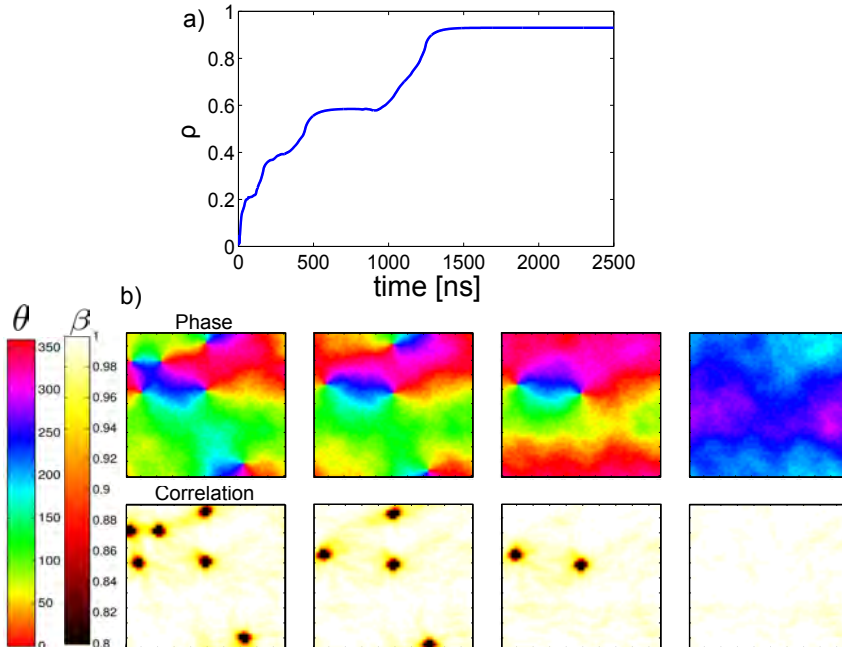


FIG. S1. a) Order parameter ρ vs. time for an interaction strength of $\lambda = 25$ MHz for a system of 50×50 oscillators, starting from a disordered initial state. b) Snapshots of phase and correlation maps at various timesteps (increasing time from left to right), showing the vortex annihilation processes.

In Fig. S1a we show the order parameter ρ vs. time, starting from a disordered initial state for a system of 50×50 oscillators using the Kuramoto model. The observed jumps in the order parameter correspond to the annihilation of vortices of charge ± 1 . This process is also illustrated in the panels of Fig. S1b, where we show snapshots of the phase map θ_i and local correlation β_i at various timesteps (with time increasing from left to right). The location and polarity ($n = \pm 1$) of the vortices can be seen in the phase maps in the upper panels. The position of the vortex core is identified by areas of low correlation ($\beta \rightarrow 0$) between neighboring oscillators, seen as the black spots in the lower panels. As time progress the vortices annihilate, resulting in a globally synchronized and phase coherent state.

Correlation function and correlation length

The spatial correlation function is given asymptotically by: $\langle \theta(r) \cdot \theta(R) \rangle \propto e^{-|r-R|/\xi} / |r-R|^\eta$. The brackets indicate the correlation between oscillators at positions r and R , and the correlation length ξ is obtained by averaging over all positions r and R in the array. An example of the decay of spatial correlations is shown in Fig. S2 for a system of 50×50 oscillators using the Kuramoto model, showing a dominating exponential decay in the correlations for increasing distances between the oscillators. The spacing $|r - R|$ is here expressed in terms of the number of lattice spacings between the oscillators. From the decay of the correlation function, we can then extract the correlation length ξ .

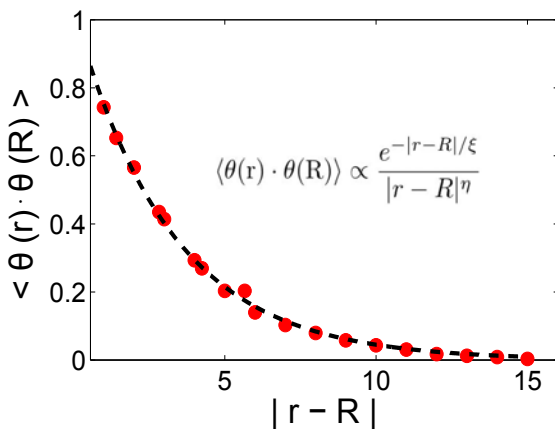


FIG. S2. Correlation as a function of oscillator spacing, $|r - R|$ for a system of 50×50 oscillators using the Kuramoto model.

* vflovik@gmail.com

- [1] Guslienko, K. Yu., Han, X. F., Keavney, D. J., Divan, R., Bader, S. D. Magnetic Vortex Core Dynamics in Cylindrical Ferromagnetic Dots. *Phys. Rev. Lett.* 96, 067205 (2006).
- [2] Ivanov, B. A., Zaspel, C. E. Excitation of Spin Dynamics by Spin-Polarized Current in Vortex State Magnetic Disks. *Phys. Rev. Lett.* 99, 247208, (2007).
- [3] Khvalkovskiy, A. V., Grollier, J., Dussaux, A., Zvezdin, A., Cros, V. Vortex oscillations induced by spin-polarized current in a magnetic nanopillar: Analytical versus micromagnetic calculations. *Phys. Rev. B* 80, 140401(R) (2009).
- [4] Araujo, F. A. *et. al.* Optimizing magnetodipolar interactions for synchronizing vortex based spin-torque nano-oscillators. *Phys. Rev. B* 92, 045419 (2015).

Chapter 10

Additional papers:

The following two papers represent work that was performed during the course of my PhD where I was not the main contributor, or the topic was considered outside the scope of the thesis.

10.1 Paper VI

Maj Hanson, Rimantas Bručas, Tomasz J. Antosiewicz, Randy K. Dumas, Björgvin Hjörvarsson, **Vegard Flovik**, and Erik Wahlström

Arrays of elliptical Fe(001) nanoparticles: Magnetization reversal, dipolar interactions, and effects of finite array sizes

Phys. Rev. B 92, 094436 (2015)

Arrays of elliptical Fe(001) nanoparticles: Magnetization reversal, dipolar interactions, and effects of finite array sizes

Maj Hanson*

Department of Applied Physics, Chalmers University of Technology, SE-412 96 Göteborg, Sweden

Rimantas Bručas

Department of Engineering Sciences and Ångström Microstructure Laboratory, Uppsala University, Box 534, SE-751 21 Uppsala, Sweden

Tomasz J. Antosiewicz

Centre of New Technologies, University of Warsaw, Banacha 2c, 02-097 Warszawa, Poland and Department of Applied Physics, Chalmers University of Technology, SE-412 96 Göteborg, Sweden

Randy K. Dumas

Physics Department, University of Gothenburg, SE-412 96 Göteborg, Sweden

Björgvin Hjörvarsson

Department of Physics and Astronomy, Uppsala University, Box 516, SE-751 20 Uppsala, Sweden

Vegard Flovik and Erik Wahlström

Department of Physics, Norwegian University of Science and Technology, N-7491 Trondheim, Norway

(Received 19 May 2015; published 22 September 2015)

The magnetic properties of arrays of nanoparticles are determined by the interplay between the individual particle properties and the dipolar interactions between them. Here we present a study of arrays of elliptical Fe(001) particles of thickness 10–50 nm. The aspect ratios of the ellipses are 1:3, their short axes $a = 50, 100,$ or 150 nm, and the periodicity of the rectangular arrays is either two or four times the corresponding axes of the ellipses. Magnetic measurements together with numerical and micromagnetic calculations yield a consistent picture of the arrays, comprising single-domain nanoparticles. We show that the magnetization reversal, occurring in the range 100–400 mT for fields applied along the long axis, is mainly determined by the properties of the corresponding single Fe ellipses. The interaction fields of the order of tens of mT can be tuned by the array configurations. For the actual arrays the interactions promote switching. For film thicknesses below the Bloch wall width parameter of Fe, $l_w = 22$ nm, magnetization reversal occurs without formation of domain walls or vortices. Within this range arrays may be tuned to obtain a well-defined switching field. Two general conclusions are drawn from the calculations: the character of the interaction, whether it promotes or delays magnetization reversal, is determined by the aspect ratio of the array grid, and the interaction strength saturates as the size of the array increases.

DOI: [10.1103/PhysRevB.92.094436](https://doi.org/10.1103/PhysRevB.92.094436)

PACS number(s): 75.60.–d, 75.75.–c

I. INTRODUCTION

The physics of arrays of small ferromagnetic particles is a topic of great interest in current research. Part of the motivation for studies of such systems lies in their potential for applications, e.g., for data storage [1], as discussed within the developing field of magnonics [2,3], or for studies of artificial spin ices [4]. The arrays are complex systems in which the individual particles as well as the interparticle interactions, introduced by the design of the arrays, must be controlled to obtain any desired static and dynamic magnetic properties of a device.

*maj.hanson@chalmers.se

Published by the American Physical Society under the terms of the Creative Commons Attribution 3.0 License. Further distribution of this work must maintain attribution to the author(s) and the published article's title, journal citation, and DOI.

In a finite two-dimensional (2D) array of magnetic particles the dipolar interactions depend on the symmetry and size of the array. Finite arrays of single domain, weakly interacting magnetic dots were investigated by Stamps and Camley [5]. They found that a resulting array anisotropy, depending on array size as well as symmetry, was induced and that this in turn controlled the hysteresis curves (comprising discrete steps) and magnetization reversal processes. Kayali and Saslow [6] applied the same model in studies extended to larger arrays and Takagaki and Ploog [7] performed similar studies adding an internal magnetocrystalline anisotropy to the individual particles. In a comment Alcántara Ortigoza *et al.* [8] pointed out that some qualitative differences between the results obtained in the two last mentioned studies could be attributed to different choices of the dipolar interaction strength in respective work. The ground state of two-dimensional lattices attracts continued interest and, as discussed in a recent work by Ewerlin *et al.* [9], its nature depends on details of the interaction and boundary conditions.

Realistic array models require the intrinsic properties and magnetic switching of the individual particles to be included in the calculations. As for the choice of materials, permalloy ($\text{Fe}_{81}\text{Ni}_{19}$) is the archetype for soft magnetic properties with low intrinsic anisotropy. Single-domain permalloy particles of circular or other shapes with low aspect ratio are often used as model systems to study the influence of array configurations. As methods for fabrication of nanostructures [10] and computation capacity develop, the number of publications in the field continues to increase. It is beyond the scope of this paper to give a comprehensive review of the current state; here we give a few examples in which also further references can be found. A system that attracted particular interest comprises nearly isotropic permalloy particles, which for a certain range of thicknesses and lateral sizes may undergo switching through vortex formation and movement. The properties of the particles were reviewed by Guslienko [11], and their sensitivity to dipolar interactions was studied for different array configurations, e.g., by Novosad *et al.* [12]. Also arrays with elliptical permalloy particles were studied, but to a lesser extent; see, e.g., the work by Wang *et al.* [13], Pardavi-Horvath [14], and references therein.

For arrays of materials with higher intrinsic magnetization and anisotropy the classic ferromagnet Fe is well suited, and such systems are less well studied. In earlier work we developed fabrication methods and studied the thickness and size dependence of the equilibrium domain structures in rectangular and circular particles of epitaxial Fe(001) films [15–17]. With the aim to study the interplay between single-particle properties and array configurations, we prepared two-dimensional (2D) arrays of smaller, single-domain (SD) elliptical particles in the same way. Magnetization measurements together with numerical and micromagnetic calculations in the quasistatic regime show how the field B_{sw} for magnetization reversal depends on film thickness and lateral extension of the individual particles, and how the interaction strength B_i and its character varies with the design of the arrays. Balancing B_{sw} and B_i makes it possible to tune the onset of switching of the arrays.

The paper is organized as follows. Section II describes the sample preparation and methods for magnetic characterization. Section III presents magnetic hysteresis, dc remanent magnetization observed by magnetic force microscopy (MFM), first-order reversal curves (FORCs), micromagnetic simulation of single particle switching, numerical analysis of the interaction field in finite array configurations, and micromagnetic calculations of magnetization reversal in finite arrays. Section IV gives account of the arguments behind our interpretation regarding magnetization reversal and influence of array configurations. Section V gives a summary of the main results of the work.

II. MATERIALS AND METHODS

A. Sample preparation

Fe films with thickness t in the range $10 \text{ nm} \leq t \leq 50 \text{ nm}$ were epitaxially grown by magnetron sputtering on $\text{MgO}(001)$ substrates, $10 \times 10 \times 0.5 \text{ (mm)}^3$. The films were capped by a 5-nm layer of Al_2O_3 to prevent oxidation. Samples with arrays of elliptical particles were patterned by electron-beam

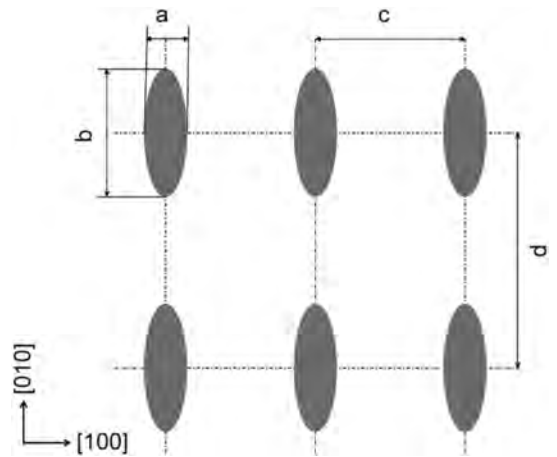


FIG. 1. Layout for patterning of arrays of ellipses. Ellipses with $a = 50, 100, \text{ or } 150 \text{ nm}$ were prepared with the axes along the in-plane easy magnetization directions [100] and [010] of the Fe(001) film. $b = 3a$. The center-to-center distances between the particles scale with the sizes of the ellipses. For narrow and wide distances $c = 2a$ and $d = 2b$ or $c = 4a$, and $d = 4b$, respectively.

lithography and ion-beam milling, as described earlier [15]. The axes of the ellipses are oriented along the easy directions of magnetization [100] and [010] in Fe; see the sketch of the layout in Fig. 1. The aspect ratio $a : b$ is 1 : 3 for all ellipses and the center-to-center interparticle distances are either two (narrow separation) or four times (wide separation) the lateral size of the corresponding ellipses. On each film up to six samples, including one circular reference with diameter 1.7 μm , were prepared. A patterned area is composed of a number of e -beam fields with area $500 \mu\text{m} \times 500 \mu\text{m}$, that form samples of rectangular areas with edges up to 3 mm. A sample comprises of the order of 5×10^6 – 10^8 ellipses.

B. Magnetic measurements

The magnetization of the samples was measured with an alternating gradient magnetometer (AGM) from Princeton Measurements Corporation. The samples were investigated at room temperature in magnetic fields B in the range $-2 \text{ T} \leq B \leq 2 \text{ T}$. Hysteresis curves and FORCs were recorded. The magnetization M was obtained after diamagnetic correction determined from the slope of the high-field hysteresis curves. It was verified that the saturation magnetization M_s of the arrays and reference samples were equal to the value for the nominal amount of Fe.

The arrays were studied by scanning force microscopy (SFM) in a Dimension3000 from Digital Instruments. Topographic and magnetic images were recorded at room temperature in zero field. The magnetic tip used for imaging has a coating of Co and Cr films yielding a resulting radius of curvature of the order of 90 nm. The switching behavior was studied during dc demagnetization, by scanning sampled areas and counting the number of switched particles in arrays that were first saturated in a field $B = +2 \text{ T}$, applied along the long

axis of the ellipses, and subsequently exposed to a field in the opposite direction. Due to tip-sample interactions and limited resolution of dense-packed patterns the demagnetization was not traced for all samples.

C. Micromagnetic simulation

The field dependence of the magnetic state of the Fe ellipses was calculated using the MicroMagus package for quasistatic micromagnetic simulations [18]. Each ellipse was discretized into layers of cubic elements. In order to obtain mesh independence the discretization cells should have sides of the same order, or better, less than, the two characteristic length scales in micromagnetics (both frequently called exchange lengths). The competition between exchange and dipolar energy is characterized by the magnetostatic exchange length $l_{\text{ex}} = (\frac{A}{K_d})^{1/2}$ and the competition between exchange and anisotropy energies is characterized by the Bloch wall width parameter $l_w = (\frac{A}{K_1})^{1/2}$ [19–22]. Here A is the exchange stiffness constant, K_d is the energy density of the stray field, and K_1 is the first-order anisotropy constant. An upper limit for K_d is $\frac{1}{2}\mu_0 M_s^2$, where μ_0 is the permeability of vacuum and M_s is the saturation magnetization. In the simulation we used the following bulk values for Fe: $A = 21 \times 10^{-12} \text{ J m}^{-1}$, $M_s = 1.7 \times 10^6 \text{ A m}^{-1}$, $K_1 = 4.3 \times 10^4 \text{ J m}^{-3}$. These yield $l_w = 22 \text{ nm}$ and $l_{\text{ex}} = 3.5 \text{ nm}$. An estimate of the width of a Bloch wall in Fe, $\delta_w = 64 \text{ nm}$, is given by Coey [22]. For the smallest ellipses simulations made with cube sides of 2 and 3 nm, respectively, yielded the same switching behavior. For the rest of the simulations we used cubic cells with sides $\Delta_x = \Delta_y = \Delta_z = 3 \text{ nm}$. Here the x and y axes are along the short and long axes of the ellipses, respectively, and the z direction is perpendicular to the film plane. To minimize computation time the number of discretization cells should be factors of low prime numbers. For example, ellipses $50 \text{ nm} \times 150 \text{ nm}$ with $t = 10 \text{ nm}$ are simulated with $a = 16\Delta_x$, $b = 48\Delta_y$, and $t = 3\Delta_z$.

III. RESULTS

A. Thickness and size dependence of magnetization reversal in arrays

To study the thickness and size dependence of the arrays, the samples were first characterized by measuring the hysteresis curves, and by MFM observation of the ellipses after dc demagnetization. Figure 2 gives an overview of hysteresis curves of arrays within the actual size and thickness range. Three different sizes of ellipses and three thicknesses are displayed. The center-to-center separation is narrow (twice the corresponding lateral size of the ellipses). For all three sizes the 30-nm particles are hardest to switch. The hysteresis curves of the two largest and thickest particles, with short axes 100 and 150 nm and $t = 50 \text{ nm}$, are characteristic for magnetization reversal through domain-wall formation and movement. The curves for samples with $t = 10$ and 30 nm have different shapes, and we will show that in these magnetization reversal occurs through formation and movement of quasingle domain configurations called *S* and *C* states [23]. The reversal processes will be further analyzed by micromagnetic simulations and FORC analysis.

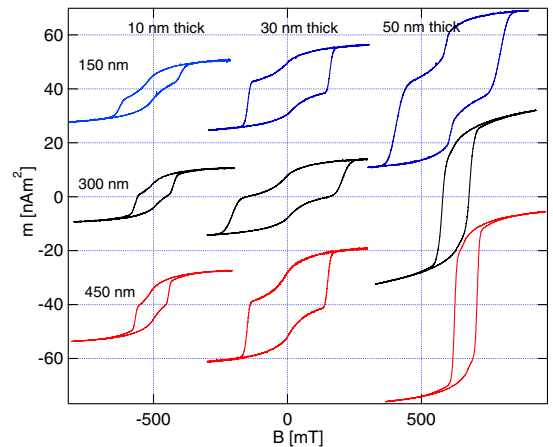


FIG. 2. (Color online) Size and thickness dependence of hysteresis curves of Fe ellipses with the field applied along the long axes. The interparticle separation is twice the lateral size of corresponding ellipses. The film thicknesses and the long axes are noted in the figure. All curves are drawn to scale with an offset for all except the central one.

In a second set of arrays, ellipses of size $50 \text{ nm} \times 150 \text{ nm}$ and $100 \text{ nm} \times 300 \text{ nm}$ were prepared with $t = 10, 20, 30,$ and 50 nm . To study the influence of interactions, samples with narrow and wide (four times the size of the ellipses) particle separation were made. All samples are hardest to switch for $t = 20 \text{ nm}$. The thickness dependence of the hysteresis is shown for $100 \text{ nm} \times 300 \text{ nm}$ ellipses with $400 \text{ nm} \times 1200 \text{ nm}$ separation in Fig. 3(a). The field region with the steep slope right until the loop closes is the range where the dominant magnetization component, along the long axis of the ellipses, is reversed. This is clearly seen in a comparison with the stepwise dc demagnetization of the sample with $t = 20 \text{ nm}$; see Fig. 4. The MFM images of the remanent state after saturation display particles of elliptical shape with stray fields of dipolar character, aligned along the saturation field. This is characteristic for a single domain (SD) state, which is without domain walls, but not necessarily with homogeneous magnetization. In the ellipses edge domains are formed to minimize the stray fields. All investigated samples follow a similar switching behavior as observed in Fig. 4. During the stepwise dc demagnetization the particles were always observed in one or the other dipolar state and the switching began with isolated particles at random positions. In the ac demagnetized state, however, the largest particles were occasionally observed in another state, e.g., the particles of size $100 \text{ nm} \times 300 \text{ nm}$ were observed in a bidomain state for $t = 30 \text{ nm}$ and thicker, but not for $t = 10 \text{ nm}$. The smallest $50 \text{ nm} \times 150 \text{ nm}$ ellipses were always observed as single domains. Thus, from the magnetic force microscopy we conclude that the particles form stable single domains and there is no long-range ordering in the arrays.

The shape of the hysteresis curves have widely differing characters; pot bellies with spreading middles, and wasp waists with constrained middles [24] can be seen, as well as curves

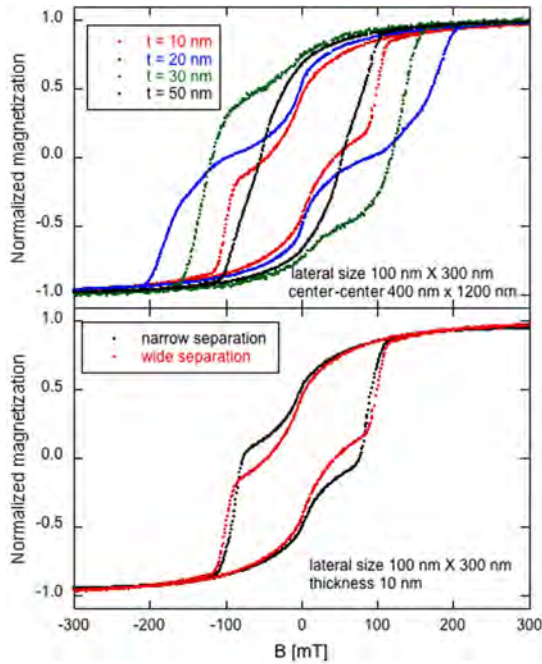


FIG. 3. (Color online) (a) The thickness dependence of hysteresis curves for Fe elliptical particles with lateral size and thicknesses as noted in the figure. Note the order of complete reversal: $t = 50, 10, 30,$ and 20 nm. (b) The influence of interactions for the 10-nm sample in (a). The field is applied along the long axis.

with a character like any polycrystalline ferromagnetic film. For these the usual coercivity B_c defined as the field at $M = 0$, is not a proper measure of the switching field, thus, for comparison the closing of the hysteresis curve at B_{cl} is used. Samples with narrow and wide separation yield very similar hysteresis curves; see Fig. 3(b). As a main influence of stronger interactions, it was found that the switching starts earlier and is completed at about the same value of B_{cl} as the sample with weaker interaction. For the samples with wide separation of $100 \text{ nm} \times 300 \text{ nm}$ ellipses the values of B_{cl} are in the range $100\text{--}200$ mT. For the $50 \text{ nm} \times 150 \text{ nm}$ ellipses (not shown here) the corresponding range is $200\text{--}400$ mT. The influence of interactions is further analyzed from the FORC curves, and numerical calculations.

In a third set of arrays ellipses of size $100 \text{ nm} \times 300 \text{ nm}$ and $150 \text{ nm} \times 450 \text{ nm}$, $t = 15, 25,$ and 30 nm, and wide separation were prepared. Of these the 25-nm sample has the highest values of B_{cl} . The hysteresis curves for the $150 \text{ nm} \times 450 \text{ nm}$ ellipses are shown in Fig. 5 and the corresponding dc remanent switching range is shown in Fig. 6. Both measurements indicate the same values of B_{cl} , being in the range $100\text{--}200$ mT. When comparing the switching field B_{sw} determined by micromagnetic simulation for an individual Fe ellipse (cf. Fig. 7), the experimentally determined value B_{cl} for an array is lower. The differences, as well as range of switching, vary between different samples. For the $150 \text{ nm} \times$

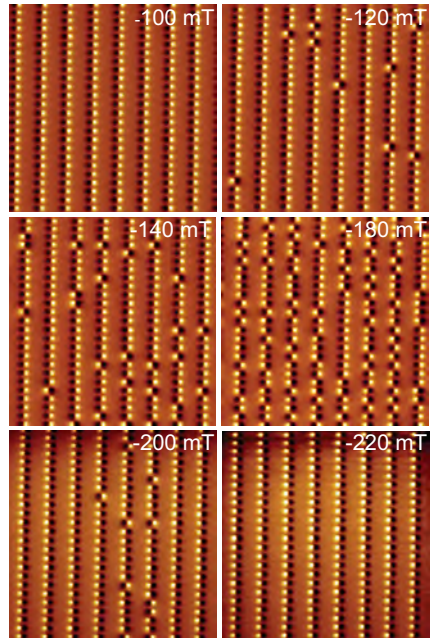


FIG. 4. (Color online) MFM images taken during stepwise dc demagnetization of the saturated state of an array of 20-nm-thick ellipses with lateral size $100 \text{ nm} \times 300 \text{ nm}$ and the separation four times the lateral size of the ellipses. The magnetization was made *ex situ*, thus the images do not represent identical areas. The sampling is made at random locations in the central part of the sample. The scan sizes are $10 \mu\text{m} \times 10 \mu\text{m}$.

450 nm ellipses, see Figs. 5 and 6, the values of B_{cl} are about 60 mT lower than the calculated B_{sw} for corresponding single Fe ellipses with thicknesses 15, 25, and 30 nm. For the $100 \text{ nm} \times 300 \text{ nm}$ ellipses made of the same films (not shown here), the corresponding difference is about 50 mT.

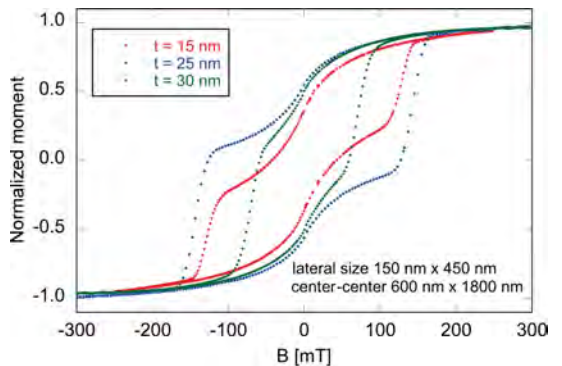


FIG. 5. (Color online) The thickness dependence of the hysteresis curves for Fe elliptical particles. The lateral size and film thicknesses are noted in the figure. The field is applied along the long axis. Note the order of complete reversal: $t = 30, 15,$ and 25 nm.

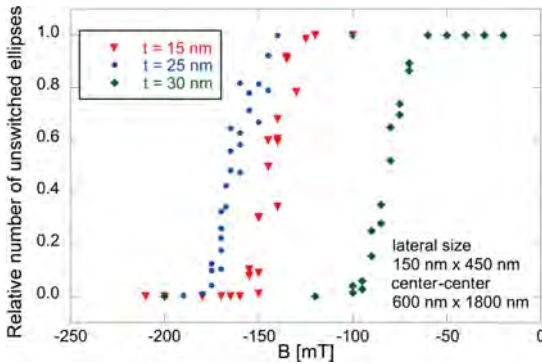


FIG. 6. (Color online) The relative number of ellipses that remained unswitched vs a reversal field applied after saturation in a field of +2 T. The lateral size and film thicknesses are noted in the figure. Note the order of complete reversal: $t = 30, 15,$ and 25 nm.

A common trait of the hysteresis curves is an initial curved slope as the field decreases to a remanent magnetization M_r significantly lower than M_s . Thus they deviate from the ideal square hysteresis behavior. This is mainly due to the initial film properties and demagnetizing effects in the particles, which occurs in a different field range. To estimate orders of magnitude, we take the demagnetizing factors from the relations applied in our earlier work [15] and obtain for the largest ellipses the values along the long axes; $N_y = 0.025, 0.041,$ and $0.050,$ for $t = 15, 25,$ and 30 nm respectively. The ratios $M_r/M_s = 0.46, 0.59,$ and 0.47 taken from the hysteresis curves in Fig. 5 increase to $0.64, 0.70,$ and $0.68,$ respectively, after demagnetization correction.

The switching field of the arrays display a systematic dependence of the thickness and size of the individual elements. This will be compared with the switching properties of the corresponding single Fe ellipses, which are analyzed in the next section.

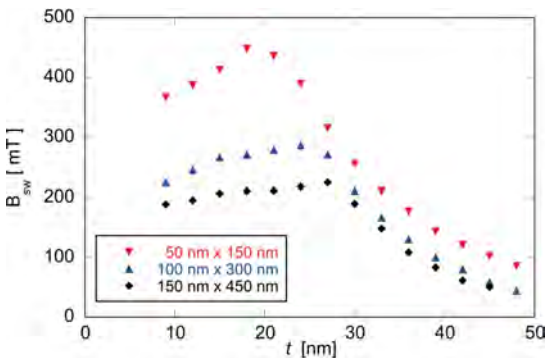


FIG. 7. (Color online) Micromagnetic simulation of the field B_{sw} for magnetization reversal of a single Fe ellipse, plotted vs film thickness t . The field is applied along the long axis of the ellipses. The lateral sizes of the ellipses are noted in the figure.

B. Micromagnetic simulation of magnetization reversal in single Fe ellipses

The field dependence of the magnetization of the Fe ellipses was studied in micromagnetic simulations. By treating the ellipses as structures composed of 3-nm-thick layers it is possible to follow the behavior of the individual layers. The switching field B_{sw} for a single Fe ellipse was simulated by starting with the single ellipse saturated in a field $+B_i$ applied along the easy axis of the ellipse, and then recording the magnetic equilibrium state as the field was decreased in steps until the magnetization was completely reversed. It is not possible to catch the reversal in a quasistatic simulation; the value of B_{sw} is taken as the first field step in showing a switched state. Figure 7 shows the thickness dependence of the switching for three lateral sizes of ellipses. B_{sw} has a maximum at t_{sw} , in the range of the wall width parameter $l_w = 22$ nm. This marks a transition between different magnetization reversal processes. For thicknesses below t_{sw} all layers undergo identical in-plane reversals, and the micromagnetic state of a single ellipse immediately before the final switching of the dominant magnetization direction is an S-like quasingle domain state. Figure 8 shows the in-plane components m_x and m_y and the out-of-plane component m_z in the field steps before and after switching of layer 1 of three. m_x and m_y are identical in all three layers. The m_z components are practically zero, except at the edges of the long axis of layers 1 and 3, which have equally large components of reversed signs, that is opposite directions. As the thickness increases, a phase shift between the in-plane rotations in different layers can be observed, together with an increasing out-of-plane component. Only in the thickest films and for the two largest particle sizes were states with clear domain walls observed during switching;

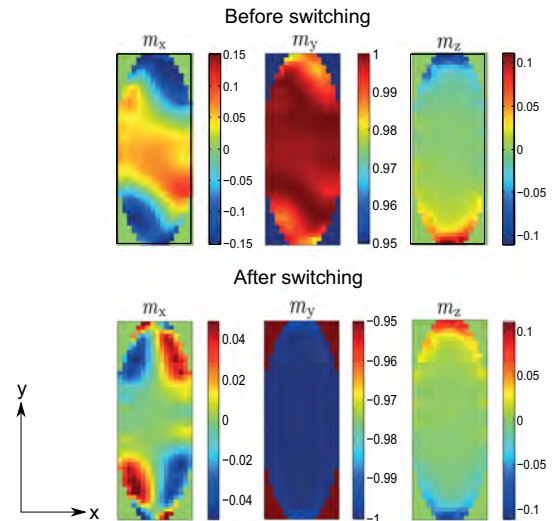


FIG. 8. (Color online) Micromagnetic simulation of a single Fe(001) ellipse with easy axes along the [100] and [010] directions. The field is applied along the long axis. In the simulation the thickness was 3×3 nm, the short axis 16×3 nm, and the long axis 48×3 nm. Layer 1 of three is plotted.

for $100\text{ nm} \times 300\text{ nm}$ with $t = 48\text{ nm}$ and for $150\text{ nm} \times 450\text{ nm}$ with $t \geq 45\text{ nm}$.

The simulated thickness dependence of the switching field is in good agreement with the experimental observations, which showed a maximum for $t = 20\text{--}25\text{ nm}$. In general the hysteresis and dc remanent demagnetization are softer than the calculated values indicate. There are several factors that can lead to such discrepancies, among which effects of disturbed particle edges and interactions are obvious. The program allows simulations of edge defects by setting an area near the element border where the magnetization is reduced. The values of B_{sw} displayed in Fig. 7 were obtained with a width of the disturbed area corresponding to one calculation cell. With a disturbance of for example two cells width, the value of B_{sw} is decreased by about 13 mT for the smallest and thinnest ellipses.

Two important results from the magnetic measurements are (i) the thickness dependence of the switching field for a given pattern shows the characteristics of the corresponding single Fe particles with a clear maximum in the range around $t = 20\text{--}25\text{ nm}$, and (ii) the switching starts in lower fields when the interactions are increased.

The following sections treat the interactions in the arrays.

C. Interactions in first-order reversal curves FORCs

1. Experimental details

In order to investigate the details of the magnetization reversal processes and in particular to gain an experimental measure of the strength of the magnetostatic interactions present within the array, the first-order reversal curve (FORC)

technique [25–27] was used. With the field H applied along the long axes of the ellipses the measurement of a FORC proceeds as follows: After positive saturation, the applied field is reduced to a given reversal field, H_R . From this reversal field the magnetization is then measured back towards positive saturation. This process is repeated for decreasing reversal fields filling the interior of the major hysteresis loop with a family of FORCs, Figs. 9(a), 9(c), and 9(e), where the magnetization is a function of both the applied and reversal fields, $M(H, H_R)$. The FORC distribution is then defined [25] as a mixed second-order derivative of the normalized magnetization:

$$\rho(H, H_R) \equiv -\frac{1}{2} \frac{\partial^2 M(H, H_R)/M_S}{\partial H \partial H_R}. \quad (1)$$

It is often convenient to perform a simple coordinate transformation and interpret the results in terms of a local coercivity $H_C = (H - H_R)/2$ and bias/interaction field $H_B = (H + H_R)/2$, as shown in Figs. 9(b), 9(d), and 9(f).

2. Analysis

The family of FORCs and corresponding FORC distribution for the median sized ($100\text{ nm} \times 300\text{ nm}$), 30-nm-thick Fe ellipses on a $400\text{ nm} \times 1200\text{ nm}$ grid are shown in Figs. 9(a) and 9(b), respectively. While the major loop, as seen by the outer boundary of the family of FORCs, shows a distinct pinching often seen in magnetic nanostructures that reverse via a vortex state [26], the FORC distribution shows no signs of vortex state reversal. In fact, the FORC distribution, which is characterized by a relatively narrow ridge centered along

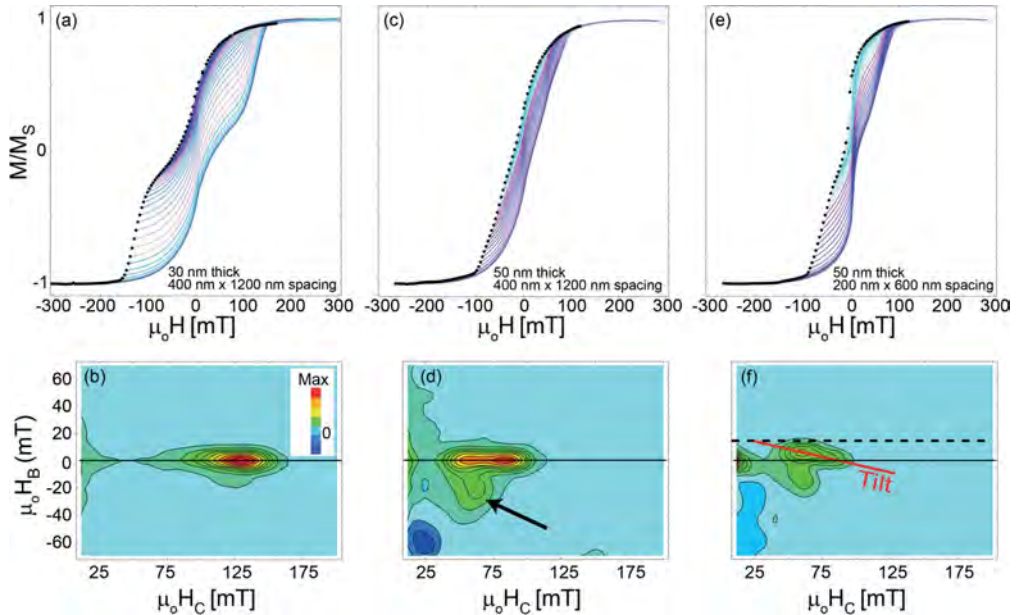


FIG. 9. (Color online) Families of FORCs, whose starting points are represented with black dots (a, c, e) and corresponding FORC distributions (b, d, f) plotted against (H_C, H_B) coordinates for $100\text{ nm} \times 300\text{ nm}$ Fe ellipses with the indicated thickness and grid spacing.

the H_C axis, is consistent with a single highly irreversible switching of the magnetization in each ellipse. However, the relatively low remanence of the major loop is consistent with a significant amount of curling or buckling preceding the switching. The extent of the ridge along the H_C axis provides a measure of the coercivity distribution while the fact that this ridge is not skewed in any manner along the H_B axis indicates that the ellipses are highly noninteracting. The FORC distribution begins to evolve as the thickness of the Fe ellipses is increased to 50 nm, Figs. 9(c) and 9(d), for the same grid spacing. The average interaction field of the ellipses should increase as they get thicker, which is observed as the FORC distribution begins to develop a clear feature for negative values along the H_B axis, indicated with an arrow. However, the primary ridge still lies predominately along the H_C axis ($H_B = 0$) indicating that the interactions are still quite weak. The interactions can be increased further by decreasing the spacing of the ellipses to 200 nm \times 600 nm, as shown in Figs. 9(e) and 9(f). Here the FORC distribution, Fig. 9(f), not only has developed a significant feature for negative values of H_B , but the ridge along the H_C axis now has a significant tilt with respect to the H_C axis. Following the analysis in earlier work [27], the maximal extent of this tilt along the positive H_B axis, shown with a horizontal dashed line, provides a direct experimental measure of the average interaction fields, namely $\mu_0 H_i \approx 18 \pm 2$ mT. This is in good agreement with the value of the interaction field 22.6 mT that was calculated at the center of a 61 \times 61 array of the same ellipses. The calculation was made as described in the following section.

D. Calculation of interaction fields in arrays

The interaction between the nanoparticles is investigated by calculating the magnetic dipolar fields at different positions in the arrays. We consider the saturated case where each nanomagnet is assumed to have a magnetic moment equal to the magnetization of iron $M_{Fe} = 1.7 \times 10^6$ A/m times the volume V . To calculate the interaction fields with high spatial accuracy we divide each ellipse into tiny cubes with $\Delta_x = \Delta_y = \Delta_z = 2$ nm. The considered magnetization is a static quantity. Each cube behaves like a tiny magnetic dipole with moment \mathbf{m} and generates a magnetic near-field according to

$$\mathbf{B} = \frac{\mu_0}{4\pi r^3} [3\mathbf{n}(\mathbf{n} \cdot \mathbf{m}) - \mathbf{m}], \quad (2)$$

where \mathbf{n} is a unit vector pointing from the cube to the place at which we calculate the field and μ_0 is the permeability of free space.

The ellipses as well as the periodicity have an aspect ratio of 3 and here we calculate the field from a square pattern of 61 \times 21 particles occupying 6 $\mu\text{m} \times 6 \mu\text{m}$ with 100 nm being the short axis periodicity. We calculate the magnetic field in the center of the array, at the corners and either edge. The positions are marked in Fig. 10. Equation (2) is used to calculate the magnetic field at desired positions for discretized ellipses from 10 to 50 nm in thickness and semiaxes 25 and 75 nm.

We begin by analyzing the magnetic field that is generated by the saturated nanomagnets. In the calculations we assume

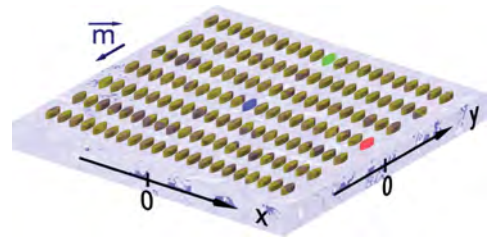


FIG. 10. (Color online) Array scheme for the calculations. A nanomagnet is in the shape of an ellipse of a given height and semiaxes 25 and 75 nm in the x and y directions, respectively. The periodicity has the same aspect ratio as that of the semiaxes and equals 100 and 300 nm. The magnetic moment of each ellipse is assumed to be in the $-y$ direction. We mark clearly the particles for which we calculate the magnetic fields acting onto them from the remainder of the array, i.e., we calculate the magnetic field at its geometrical center as if it were not present; these particles are the central particle, those at the top edge (along the x axis), and the side edge (y axis).

that the magnetic dipole moment is in the $-y$ direction. The interaction magnetic field is calculated at the geometrical center of each ellipse in question, i.e., the field acting onto the central ellipse is calculated as a sum of the fields from all ellipses except for the central one. We begin by investigating the spatial dependence of the field for 10-nm-thick ellipses in an array with a short axis periodicity of 100 nm. The results are plotted in Fig. 11. The field acting onto the central ellipse, and indeed onto most of the ellipses in the array, is approximately 10 mT. However, at the edges it deviates from this value and at each of the four corners, in Fig. 10, it is equal to 6 mT. At the side edge the field decays down to 4 mT (in the geometrical center of that edge), which is the lowest calculated value. The opposite happens at the top edge which has a dense arrangement of ellipses—the field there reaches a value of 13.5 mT. These are the B_y components which are aligned along the magnetization vector and add/subtract from the outside magnetic field applied to switch the magnetization of the ellipses. In addition to the dominant B_y component, at the center of the ellipses one can determine the cross-polarized B_x component. It is much weaker reaching a value of -2 mT at the corner (the sign depends on which corner) and for most of the array is negligible in the geometrical centers of the ellipses due to symmetry. As noted, these interaction fields are calculated at the geometrical centers of the ellipses. However, these fields within the volume of an ellipse will inevitably vary. In Fig. 12 we present the dependence of the magnetic field generated by the arrays and calculated at selected positions as a function of the array periodicity and ellipse thickness. Note, that at the onset of switching the interaction between the ellipses serves to reinforce the outside magnetic field used for switching the magnetization.

The size of the array also has an effect on the interaction strength. When the size of a square array, with lattice constant c , increases from $N \times N$ to $(N + 1) \times (N + 1)$ the number of ellipses increases by $2N + 1$ at a distance of $r \approx \frac{(2N+1)c}{2}$ from the center of the array. The near-field term decays as r^{-3} . Thus, the incremental contribution to the interaction field

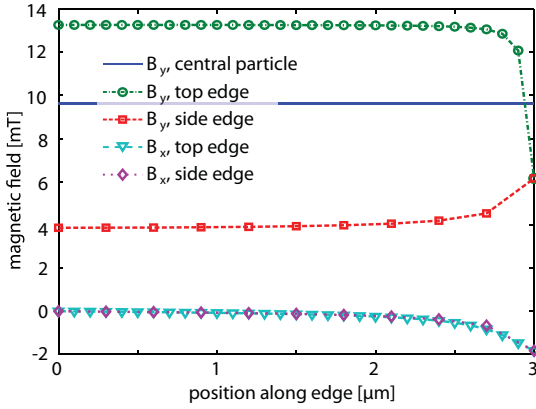


FIG. 11. (Color online) Magnetic field at the geometrical centers of $150 \text{ nm} \times 50 \text{ nm}$ ellipses in an array with a short axis period 100 nm in the x direction and thickness of 10 nm ; there are 61×21 particles in the array. The fields are plotted along the edges of the array from their respective centers ($0 \mu\text{m}$) to the corner ($3 \mu\text{m}$) with markers indicating positions of the particles along the edges (there are more particles along the top edge, hence the density of markers is larger than at the side edge). The solid line marks the magnetic field (only B_y component is nonvanishing) acting onto the central particle. At the edges the B_y field is either smaller (side edge) or larger (top edge, except corner) than at the center of the array. There is also a nonvanishing B_x component which is strongest at the corner and decays rapidly when moving away from it.

decreases as N^{-2} or r^{-2} , and the field approaches a limiting value. For example, for a 10-nm -thick ellipse the magnetic field acting onto the central particle in a square array $600 \text{ nm} \times 600 \text{ nm}$ (3×7 ellipses) is approximately 11 mT , a value which decreases when increasing the array size. In the limit of large arrays it is equal to approximately 9.3 mT . This value is reached (within a 1% accuracy) already for arrays $6 \mu\text{m} \times 6 \mu\text{m}$ (the employed 61×21 particle arrays). The magnitude of this effect as well as the trend (increase or decrease) depend on the array geometry. The above-mentioned effect (decrease of the interaction field with array size) occurs for a periodicity aspect ratio that is the same as that of the ellipse's semi-axes, namely 3 . However, for the same ellipses arranged in a square lattice with a period of, e.g., 150 nm , increasing the array size will asymptotically increase the interaction field. Moreover, the periodicity will also affect the sense of the magnetic field generated by the array. For the previously mentioned square lattice the interaction field will change qualitatively—it will reinforce the magnetization and, as mentioned, will increase in amplitude for larger arrays. Figure 13 shows how the interaction field varies with the aspect ratio for two cases of array configurations. Thus, by designing the array properly, it is possible to tailor the magnetization properties to either promote switching (by lowering the switching field via the interaction field) or inhibit it.

E. Micromagnetic simulation of arrays

To find the influence of interactions on the magnetization switching in an array it is not sufficient to simply add an

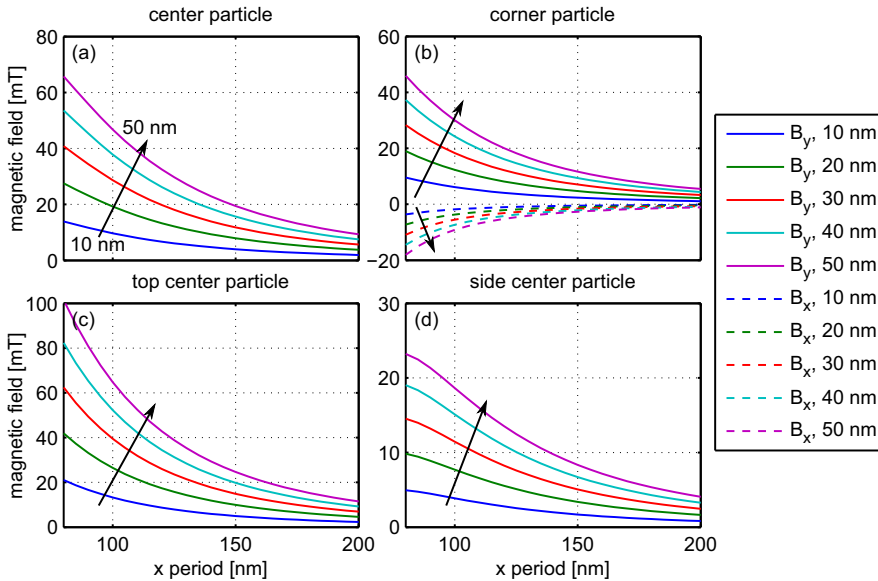


FIG. 12. (Color online) Dependence of the magnetic field acting onto the nanoellipses on the array periodicity and ellipse thickness. The field is calculated for (a) the central particle, (b) the corner particle, (c) the top central particle, and (d) the side central particle. In all cases the solid lines indicate the B_y component which is parallel to the magnetization of the ellipses and for the corner particle the dashed lines show the B_x component. The arrows indicate the direction of increasing thicknesses from 10 to 50 nm .

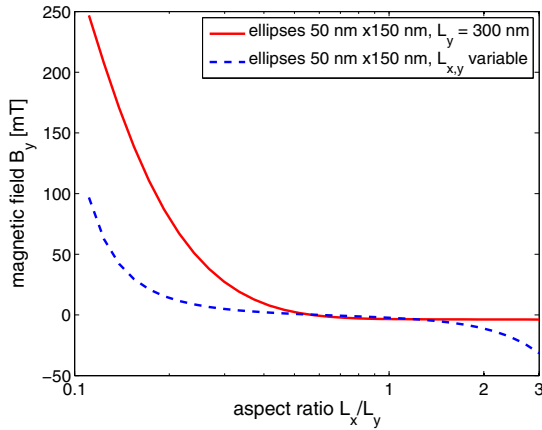


FIG. 13. (Color online) The interaction field calculated at the center of an array, for two cases of varying aspect ratios. The arrays comprise 11×11 nanoparticles, all 20 nm thick and with lateral sizes as noted in the figure. L_x and L_y are the periods in the x and y directions, respectively. The aspect ratio $A = L_x/L_y$ is varied according to the following relations. For one set of ellipses L_y is const = 300 nm and $L_x = L_y A$. In the second case, for the same size of ellipses, $60 \text{ nm} \leq L_x \leq 480 \text{ nm}$, and L_y/A . The magnetic moment of each nanoparticle is assumed to be in the $-y$ direction.

effective field to the applied field, since this does not take the local variation of the interaction into account, nor the changes of the magnetic domain structure of the ellipses during demagnetization. One method, often applied when looking for ferromagnetic resonances (FMR) in arrays, is to find the effects of dipolar interactions by simulating the array as a single ellipse under periodic boundary (PB) conditions. Figure 14(a) shows the resulting micromagnetic state at the last field step before switching for the smallest, 10-nm-thick ellipses. (The image displays one of the three identical layers in the simulation.) With open boundary (OB) conditions switching occurred at $B_{sw} = 354$ mT. Simulation with PB for wide and narrow separation yielded switching at 345 and 331 mT, respectively. This gives an estimate of interaction field strengths of 9 and 23 mT, respectively, in agreement with our calculated interaction fields. An additional, important effect of interactions can be noted in Fig. 14(a); the symmetry of the magnetic state just before switching is changed from being an S state to more like a C state.

A more realistic picture is expected from simulations of the actual array. We did not make a complete investigation to catch the statistics and all details of how array size and step length during demagnetizing influence the processes; here we give a few examples. The smallest, 10-nm-thick ellipses were studied in, e.g., small arrays with 3×3 , 5×5 , 4×6 , and 6×4 ellipses in configurations with narrow and wide separation. In all cases the first reversal occurs in fields lower than B_{sw} for the corresponding single ellipse. In arrays with wide separation the ellipses switch individually and the switching seems to always be finalized at about B_{sw} . With narrow separation the switching range is narrower.

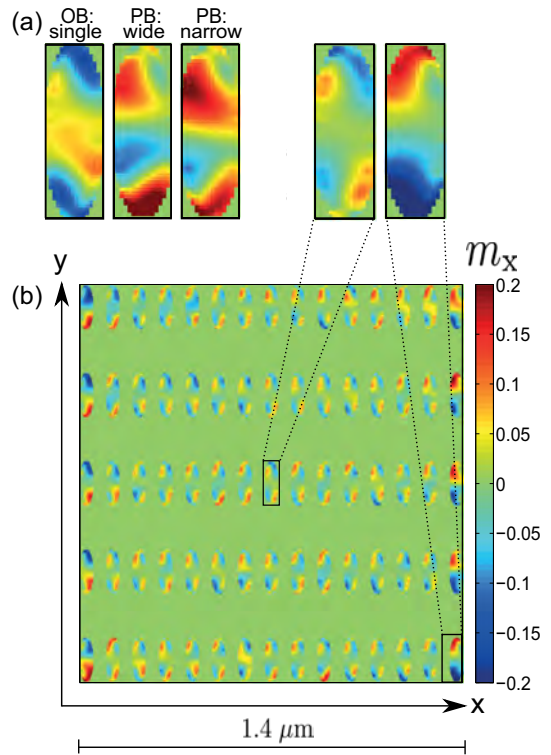


FIG. 14. (Color online) (a) Comparison of simulated states of a $48 \text{ nm} \times 144 \text{ nm}$ single ellipse with $t = 3 \times 3 \text{ nm}$, just before switching. From left to right, the x component of the magnetization was obtained with open boundary conditions and periodic boundary conditions for wide and narrow separation, respectively. (b) The x component of the magnetization in the simulated state of an array with 15×5 of the same ellipses. Layer 1 of three is shown in all figures. The field is at the point before the switching of the first ellipse, located in the lower right corner of the array.

Figure 14(b) shows one step at $B = 309.1$ mT during demagnetization of a larger array of 15×5 ellipses with narrow separation. In the next step, with $B = 311.6$ mT, the first ellipse at the lower right corner is reversed and in the following $B = 314.1$ mT all ellipses are reversed. The variations in internal structure, with strong effects at the edges of the array, can be noted. A simulation of a still larger array of the same configuration, 54×18 ellipses in field steps of 1.25 mT, displayed a switching of all ellipses at $B = 310.4$ mT. The switching fields of these two arrays are both about 40 mT lower than B_{sw} of the single Fe ellipse. The difference is larger than the calculated interactions fields, which implies that effects of variations in local interaction fields and internal domain structures are important. Although we did not perform simulations for the larger ellipses, it is interesting to note that the difference between B_{sw} and B_{cl} is of the order 50–60 mT for these, as discussed in Sec. III A. The simulations of the arrays support the conclusion drawn from the calculation of

the interaction fields, namely that the interactions saturate for arrays with sizes in these ranges.

IV. DISCUSSION

The properties of a 2D array of submicron or nanosize ferromagnetic particles are determined by the combination of, on one hand, the domain state and magnetization reversal processes of each single particle, and on the other, the array configuration. Now, the question is how well theoretical models can describe the magnetic properties of the real system, or perhaps whether an ideal system really can be fabricated.

A. Magnetization reversal

The magnetization switching field B_{cl} was determined for arrays of epitaxial Fe(001) ellipses with thickness t in the range 10–50 nm and lateral sizes in the range 50–450 nm. It was found that B_{cl} decreases with increasing particle size, and the t dependence of B_{cl} for each particle size displays a maximum in the range 20–25 nm. This thickness is of the order of the wall width parameter $l_w = 22$ nm. It is not possible to fully characterize the magnetization reversal from the major hysteresis loops only. The switching field range and remanent domain state were determined also from MFM observation of dc demagnetization. The equilibrium zero-field state during these processes was observed to be SD, except for the largest particles, which were occasionally seen as bidomains. Complementary measurements of the hysteresis with FORC analysis could clearly identify the field range for single-particle reversal and sort out effects of interactions. It can be noted that in the literature there are several examples of hysteresis curves that have similar character, but are generated by different materials and magnetization processes. Pot bellies, with spreading middles, and wasp waists, with constrained middles, were shown by Tauxe *et al.* [24] to originate from different populations of superparamagnetic and single-domain particles. Bennett and Della Torre [28] showed how two exchange coupled materials may be arranged to yield one or the other of the two shapes, and how FORC analysis could separate the two cases.

The switching field B_{sw} of single Fe ellipses was determined by micromagnetic simulations, in which the values for bulk Fe were used as input parameters. The size and thickness dependence of B_{cl} observed in the experiments is well reproduced in the behavior of the single ellipses. The absolute values display systematic deviations, with B_{cl} being lower than corresponding B_{sw} . For the 100 nm \times 300 nm ellipses with 400 nm \times 1200 nm separation B_{cl} is in the range 100–200 mT, about 50 mT lower than B_{sw} for corresponding thicknesses. For the smaller and larger ellipses the difference is smaller and larger, respectively. For the single ellipses it was shown that below the maximum of B_{sw} at t_{sw} , about equal to l_w , all layers undergo identical in-plane reversals, and the micromagnetic state of a single ellipse immediately before the final switching of the dominant magnetization direction is an S -like quasisingle domain state. When interactions are taken into account by introducing periodic boundary conditions, the symmetric S state is deformed towards a more C -like state. In simulated arrays the particles display a variety of

similar, but not identical, C - or S -like states. The FORC analysis gave evidence that, whereas details in the major loops resembled those of nanostructures reversing via vortex states, the FORC distributions showed no signs of vortex reversal. Altogether, our interpretation is that the particles undergo in-plane switching through the development of the quasisingle C or S states in which the spins finally rotate into the reversed SD state. Above t_{sw} the switching becomes more complex with a gradually increasing phase shift between the in-plane rotation in different layers, and finally also an out-of-plane component develops.

These switching processes are known to be sensitive to imperfections in the materials, as well as to interactions between the particles. The influence of interactions are discussed in the next section. The imperfections in the materials may be defects and variations—on one hand in the structure and/or surfaces of the Fe films on the other in the particle shapes and edges. Particle edge effects of the size of a discretization cell (3 nm) were found to decrease the switching by the order of 10 mT. We did not study the influence of capping layer directly, but note that in our earlier studies of larger Fe/Co particles capped with V, the relative saturation remanence was higher [23]. Fruchart *et al.* [29] showed hysteresis curves with higher squareness in their studies of Fe(110) dots. Their films were sandwiched between two Mo or W (110) layers. Our capping layers of Al₂O₃ were chosen because they prevent oxidation efficiently; examples showed identical hysteresis curves when the measurements were repeated after three years.

B. Arrays

There are two important conclusions to draw from the calculations of the interaction field in the arrays. The character of the interaction, whether it promotes or delays magnetization reversal, is determined by the aspect ratio of the array grid, and the interaction strength saturates as the size of the array increases. The dipolar interaction field was calculated for arrays with 61 \times 21 Fe ellipses with lateral size 50 nm \times 150 nm and thickness in the range 10–50 nm. For these the thickness dependence of the field was calculated at different positions, in the center and at the edges, and for varying periodicity while keeping the aspect ratio 1 : 3 of the grid. In this particular grid the interactions promote the onset of switching, as was clearly demonstrated in both experiments and micromagnetic simulations; the switching field of arrays was in all cases lower than that of the corresponding single ellipses. For the smallest particles the interaction field is of the order of 10 mT. For 50-nm-thick 100 nm \times 300 nm ellipses with 200 nm \times 600 nm separation, the calculated interaction field 22.6 mT at the center of the array agrees well with the average interaction field $\approx (18 \pm 2)$ mT, determined by FORC analysis.

Micromagnetic simulations were made for arrays of 15 \times 5 and 54 \times 18 ellipses with lateral size 50 nm \times 150 nm and 10 nm thickness. The switching fields are about the same for the two arrays, thus showing the same tendency of saturation as found for the calculated interaction field. We compared the switching fields obtained by simulations with periodic boundary conditions and arrays with the value B_{sw} obtained for corresponding single ellipse. Whereas the

shift obtained with periodic boundary conditions is in good agreement with the calculated interaction field, the shift for the arrays is significantly larger. We suggest this to be an effect of interactions on the magnetic domain states during switching of the ellipses. It is appropriate to here point out the limitations of the quasistatic treatment, since it cannot give full account of the reversal processes. Thermal fluctuations and statistical processes in the magnetization reversal are always present, but were not considered in our calculations. In another work [30] the magnetization dynamics of the samples was also investigated. In ferromagnetic resonance (FMR) the behavior is dominated by the properties of the single Fe ellipses, without significant influence of interactions.

V. CONCLUSIONS

The experimental and numerical results yield a consistent picture of the studied arrays of Fe ellipses: the magnetization reversal, occurring in the range 100–400 mT, is mainly

determined by the properties of the corresponding single Fe ellipses, and the interaction fields determined by the array configuration are of the order of tens of mT. For the actual arrays the interactions promote switching. For film thicknesses below the wall width parameter of Fe, about 20 nm, magnetization reversal occurs without formation of domain walls or vortices. In this range an array might be tuned to obtain a well-defined switching field. Another parameter to consider is the size of the array. The finite arrays with 54×18 and 61×21 ellipses are only $5 \mu\text{m} \times 5 \mu\text{m}$ and $6 \mu\text{m} \times 6 \mu\text{m}$ large. The interaction effects are already stabilized and the majority of ellipses feel the same interaction field as the central particle. This implies that it could be possible to arrange several substructures of arrays with different well-defined switching fields, within limited areas on one chip.

ACKNOWLEDGMENT

M.H. is grateful for the support of Prof. Peter Apell.

-
- [1] See, e.g., the review by B. D. Terris and T. Thomson, Nanofabricated and self-assembled magnetic structures as data storage media, *J. Phys. D* **38**, R199 (2005).
- [2] V. V. Kruglyak, S. O. Demokritov, and D. Grundler, *Magnonics*, *J. Phys. D* **43**, 264001 (2004).
- [3] *Magnonics*, Topics in Applied Physics No. 125, edited by S. O. Demokritov and A. N. Slavin (Springer-Verlag, Berlin, Heidelberg, 2013).
- [4] V. Kapaklis, U. B. Arnalds, A. Farhan, R. V. Chopdekar, A. Balan, A. Scholl, L. J. Heyderman, and B. Hjörvarsson, Thermal fluctuations in artificial spin ice, *Nat. Nanotechnol.* **9**, 514 (2014).
- [5] R. L. Stamps and R. E. Camley, Magnetization processes and reorientation transition for small magnetic dots, *Phys. Rev. B* **60**, 11694 (1999).
- [6] M. A. Kayali and W. M. Saslow, Hysteresis of finite arrays of magnetic nanodots, *Phys. Rev. B* **70**, 174404 (2004).
- [7] Y. Takagaki and K. H. Ploog, Magnetization of two-dimensional square arrays of nanomagnets, *Phys. Rev. B* **71**, 184439 (2005).
- [8] M. Alcántara Ortigoza, R. A. Klemm, and T. S. Rahman, Comment on “Magnetization of two-dimensional square arrays of nanomagnets”, *Phys. Rev. B* **74**, 226401 (2006).
- [9] M. Ewerlin, D. Demirbas, F. Brüssing, O. Petravic, A. A. Ünal, S. Valencia, F. Kronast, and H. Zabel, Magnetic Dipole and Higher Pole Interaction on a Square Lattice, *Phys. Rev. Lett.* **110**, 177209 (2013).
- [10] R. Lutge, Massively parallel fabrication of repetitive nanostructures: Nanolithography for nanoarrays, *J. Phys. D* **42**, 123001 (2009).
- [11] See, e.g., the review by K. Yu. Guslienko, Magnetic vortex state stability, reversal and dynamics in restricted geometries, *J. Nanosci. Nanotechnol.* **8**, 2745 (2008).
- [12] V. Novosad, K. Yu. Guslienko, H. Shima, Y. Otani, S. G. Kim, K. Fukamichi, N. Kikuchi, O. Kitakami, and Y. Shimada, Effect of interdot magnetostatic interaction on magnetization reversal in circular dot arrays, *Phys. Rev. B* **65**, 060402(R) (2002).
- [13] Y. Wang, W. H. Shi, H. X. Wei, D. Atkinson, B. S. Zhang, and X. F. Han, Manipulation of magnetization reversal of $\text{Ni}_{81}\text{Fe}_{19}$ nanoellipse arrays by tuning the shape anisotropy and the magnetostatic interactions, *J. Appl. Phys.* **111**, 07B909 (2012).
- [14] M. Pardavi-Horvath, Interaction effects in magnetic nanostructures, *Phys. Status Solidi A* **211**, 1030 (2014).
- [15] M. Hanson, C. Johansson, B. Nilsson, P. Isberg, and R. Wäppling, Magnetic properties of two-dimensional arrays of epitaxial Fe(001) submicron particles, *J. Appl. Phys.* **85**, 2793 (1999).
- [16] M. Hanson, O. Kazakova, P. Blomqvist, R. Wäppling, and B. Nilsson, Magnetic domain structures in submicron-size particles of epitaxial Fe(001) films: Shape anisotropy and thickness dependence, *Phys. Rev. B* **66**, 144419 (2002).
- [17] M. Hanson, R. Bručas, and O. Kazakova, Effects of size and interactions on the magnetic behaviour of elliptical (001)Fe nanoparticles, *J. Magn. Magn. Mater.* **316**, 181 (2007).
- [18] MicroMagus, supplied by MATESY, Magnetic Technologies and Systems GmbH.
- [19] A. Hubert and R. Schäfer, *Magnetic Domains: The Analysis of Magnetic Microstructures* (Springer-Verlag, Berlin, Heidelberg, 1998).
- [20] W. Rave and A. Hubert, Magnetic ground state of a thin-film element, *IEEE Trans. Magn.* **36**, 3886 (2000), and references therein.
- [21] J. E. Miltat and M. J. Donahue, Numerical micromagnetics: Finite difference methods, in *Micromagnetism*, Handbook of Magnetism and Advanced Magnetic Materials Vol. 2, edited by H. Kronmüller and S. Parkin (Wiley-Interscience, Chichester, 2007), pp. 742–764.
- [22] J. M. D. Coey, *Magnetism and Magnetic Materials* (Cambridge University Press, Cambridge, 2010).

- [23] O. Kazakova, M. Hanson, P. Blomqvist, and R. Wäppling, Interplay between shape and magnetocrystalline anisotropies in patterned bcc Fe/Co(001) multilayers, *Phys. Rev. B* **69**, 094408 (2004).
- [24] L. Tauxe, T. A. T. Mullender, and T. Pick, Potbellies, wasp-waists, and superparamagnetism in magnetic hysteresis, *J. Geophys. Res.* **101**, 571 (1996).
- [25] C. R. Pike, A. P. Roberts, and K. L. Verosub, Characterizing interactions in fine magnetic particle system using first order reversal curves, *J. Appl. Phys.* **85**, 6660 (1999).
- [26] R. K. Dumas, C.-P. Li, I. V. Roshchin, I. K. Schuller, and Kai Liu, Magnetic fingerprints of sub-100 nm Fe dots, *Phys. Rev. B* **75**, 134405 (2007).
- [27] D. A. Gilbert, G. T. Zimanyi, R. K. Dumas, M. Winklhofer, A. Gomez, N. Eibagi, J. L. Vicent, and K. Liu, Quantitative decoding of interactions in tunable nanomagnet arrays using first order reversal curves, *Sci. Rep.* **4**, 4204 (2014).
- [28] L. H. Bennett and E. Della Torre, Analysis of wasp-waist hysteresis loops, *J. Appl. Phys.* **97**, 10E502 (2005).
- [29] O. Fruchart, J.-P. Nozières, W. Wernsdorfer, D. Givord, F. Rousseaux, and D. Decanini, Enhanced Coercivity in Submicrometer-Sized Ultrathin Epitaxial Dots with In-Plane Magnetization, *Phys. Rev. Lett.* **82**, 1305 (1999).
- [30] V. Flovik, F. Macià, J. M. Hernández, R. Bručas, M. Hanson, and E. Wahlström, Tailoring the magnetodynamic properties of nanomagnets using magnetocrystalline and shape anisotropies, *Phys. Rev. B* **92**, 104406 (2015).

10.2 Paper VII

Vegard Flovik, Santanu Sinha, Alex Hansen

Dynamic Wettability Alteration in Immiscible Two-phase Flow in Porous Media: Effect on Transport Properties and Critical Slowing Down.

Front. Phys. 3, 00086 (2015).



Dynamic Wettability Alteration in Immiscible Two-phase Flow in Porous Media: Effect on Transport Properties and Critical Slowing Down

Vegard Flovik^{1*}, Santanu Sinha^{2*} and Alex Hansen^{1*}

¹ Department of Physics, Norwegian University of Science and Technology, Trondheim, Norway, ² Department of Physics, University of Oslo, Oslo, Norway

OPEN ACCESS

Edited by:

Renaud Toussaint,
University of Strasbourg, France

Reviewed by:

Piotr Szymczak,
University of Warsaw, Poland
Peter Lehmann,
ETH Zurich, Switzerland

*Correspondence:

Vegard Flovik
vegard.flovik@ntnu.no;
Santanu Sinha
santanu.sinha@ntnu.no;
Alex Hansen
alex.hansen@ntnu.no

Specialty section:

This article was submitted to
Interdisciplinary Physics,
a section of the journal
Frontiers in Physics

Received: 23 July 2015

Accepted: 23 October 2015

Published: 10 November 2015

Citation:

Flovik V, Sinha S and Hansen A (2015)
Dynamic Wettability Alteration in
Immiscible Two-phase Flow in Porous
Media: Effect on Transport Properties
and Critical Slowing Down.
Front. Phys. 3:86.
doi: 10.3389/fphy.2015.00086

The change in contact angles due to the injection of low salinity water or any other wettability altering agent in an oil-rich porous medium is modeled by a network of disordered pores transporting two immiscible fluids. We introduce a dynamic wettability altering mechanism, where the time dependent wetting property of each pore is determined by the cumulative flow of water through it. Simulations are performed to reach steady-state for different possible alterations in the wetting angle (θ). We find that deviation from oil-wet conditions re-mobilizes the stuck clusters and increases the oil fractional flow. However, the rate of increase in the fractional flow depends strongly on θ and as $\theta \rightarrow 90^\circ$, a critical angle, the system shows critical slowing down which is characterized by two dynamic critical exponents.

Keywords: wettability, porous media, porous media flow, fluid transport, two-phase flow in porous media, two-phase flow, capillary forces, critical slowing down

1. INTRODUCTION

The world's primary energy demand is predicted to increase by one-third between 2011 and 2035, where 82% of it comes from fossil fuels [1]. In this scenario, the fact that some 20–60% of the oil remains unrecovered in a reservoir after the production is declared unprofitable, is a challenge of increasing importance [2]. The main reason for this loss is the formation of oil clusters trapped in water and held in place by capillary forces, which in turn are controlled by the wetting properties of the reservoir fluids with respect to the matrix rock. The production from complex oil reserves that today are considered immobile or too slow compared to the cost is therefore an important area of research. In this context, the role of formation wettability is a focus area within the field of Enhanced Oil Recovery (EOR) [3].

Different reservoir rocks have widely different wetting characteristics [4]. Wettability may vary at the pore level from strongly oil wet through intermediate wetting to strongly water wet. Carbonate reservoirs contain more than half of the world's conventional oil reserves, but the oil recovery factor (a number between zero and unity representing the fraction of recoverable oil [5]) is very low compared to sandstone reservoirs [6]. This is due to the complex structure, formation heterogeneity and more chemically active wettability characteristics of the carbonate reservoirs, which leads to uncertainty in the fluid flow and oil recovery [7]. Sandstone is strongly water wet before oil migrates from a source rock into the reservoir. When oil enters a pore, it displaces the water which leaves behind a water film sandwiched between the oil and rock surface. This happens as a result of balancing van der Waals and electric double layer forces, capillary pressure and grain

curvature [8]. A permanent wettability alteration is then believed to take place by adsorption of asphaltenes from the crude oil to the rock, and leads to high but slow recovery through continuous oil films [9, 10]. As the oil saturation drops, these films can become discontinuous, leaving immobile oil clusters held in place by capillary forces.

After drilling a well into a reservoir, the natural pressure inside can force only around 10% of the total available volume of oil to reach the surface, which is called the primary recovery stage [5]. To maintain the pressure for further recovery, water or gas is injected by another injection well which is known as secondary recovery. This allows around 30% further production of oil depending on fluid properties and reservoir parameters. To recover the huge amount of oil left inside the reservoir after the secondary recovery, different techniques beyond the simple secondary injection are implemented, which constitutes the tertiary or EOR stage. In this stage wettability is the most important petrophysical property which plays a key role in the fluid transport properties of both conventional (permeabilities in milli-Darcy to Darcy range) and unconventional (low porosity and low permeability in nano to milli-Darcy range, e.g., shale) reservoirs [11] and there is great potential to improve the oil recovery efficiency by altering the wetting properties [12]. Main factors which can alter the pore wettability are: lowering the salinity [13, 14], adding water-soluble surfactants [15, 16] or adding oil-soluble organic acids or bases [17]. Increasing the reservoir temperature also increases water-wetness [4, 18]. There are some correlations with the wetting behavior to the electrostatic forces between the rock and oil surfaces [19], but there is no consensus on the dominating microscopic mechanism behind the wettability alteration. It is known from laboratory experiments and field tests that a drift from strongly oil-wet to water-wet or intermediate-wet conditions can significantly improve the oil recovery efficiency [17]. The amount of change in the wetting angle is a key factor here [20, 21] which not only decides the increase in oil flow but also the speed of the process. An improper change in the wetting angle can also make the recovery very slow and not profitable.

Given there is a certain change in the wetting angle due to a brine, the next important factor is the flow pathways in the matrix rock which transports the oil and brine. One cannot expect any change in the wetting angle of a pore if there is no flow of the brine through it. The flow pathways depend on several different factors: the porous network itself, oil saturation, capillary number and also on the present wettability conditions. A change in the wettability will cause a perturbation in the flow distribution of the system. This will in turn again affect the wettability change through the altered flow pathways, causing further changes in the flow distribution. The dynamics of wettability alterations is therefore controlled by a strongly correlated process.

There are some studies of wettability alterations in two-phase flow by equilibrium-based network models [22] for capillary dominated regimes where viscous forces are negligible. Wettability alterations by network models with film-flow has been studied [23] to find residual oil saturation as functions of contact angle. However, investigation of the time-scale of dynamics lacks attention in such models which is extremely

important for practical reasons. In this article, we present a detailed study of wettability alterations in two-phase flow considering a network model of disordered pores transporting two immiscible fluids where a dynamic wettability alteration mechanism, correlated with the flow-pathways, is implemented. We will focus on the transport properties due to the change in the wettability as well as on the time scale of the dynamics.

We study in the following the effect of wettability changes on immiscible two-phase flow based on a network model [24–26]. In Section 2, we present the model and how we adapt it to incorporate the dynamic wettability changes. In Section 3, we present our results. Initially, we let the two phases settle into a steady state where the averages of the macroscopic flow parameters no longer evolve. At some point, we then introduce the wettability altering agent, so that it starts changing the wetting angle. The wetting angle alteration depends on the cumulative volume of the wettability altering fluid that has flowed past a given pore. This induces transient behavior in the macroscopic flow properties and we measure the time it takes to settle back into a new steady state. We find that there is a critical point at a wetting angle of 90° and we measure its dynamical critical exponents; the exponents are different whether one approaches the critical point from smaller or larger angles. In Section 4 we summarize and conclude.

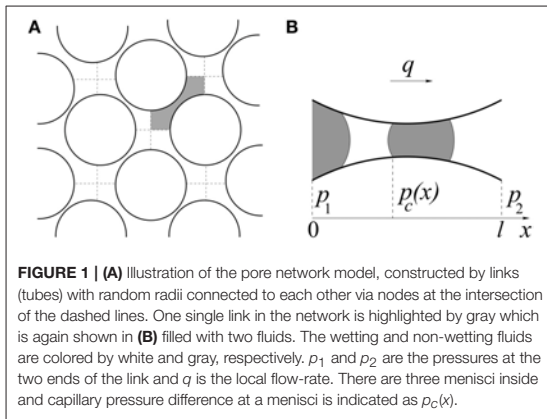
2. MODEL

We model the porous medium by a network of tubes (or links) oriented at 45° relative to the overall flow direction. The links contain volumes contributed from both the pore and the throat, which then intersect at volume-less vertices (or nodes). Any disorder can be introduced in the model by a proper random number distribution for the radius r of each link, and we choose a uniform distribution in the range $[0.1l, 0.4l]$ here, where l is the length of each tube. It is possible to consider any other distribution of pore sizes without any further change in the model. The network transports two immiscible fluids (we name them as oil and water), one of which is more wetting than the other with respect to the pore surface. The pores are assumed to be in between particles, and the pore shape is thus approximated to be hour-glass shaped, which introduces capillary effects in the system. The model is illustrated in **Figure 1**.

Due to the hour glass shape of the pore, the capillary pressure at a menisci separating the two fluids is not constant, and depends on the position x of the menisci inside the pore. The capillary pressure $p_c(x)$ at position x inside the i th pore is then calculated from a modified form of the Young Laplace equation [24, 27],

$$p_c(x) = \frac{2\gamma \cos \vartheta_i}{r_i} \left[1 - \cos \left(\frac{2\pi x}{l} \right) \right]. \quad (1)$$

where γ is the interfacial tension between the fluids and ϑ_i is the wetting angle for that pore. As an interface moves in time, $p_c(x)$ changes. The capillary pressure is zero at the two ends ($x = 0$ and l) and it is maximum at the narrowest part of the pore. It makes the model closer to the dynamics of drainage dominated flow, where the film flow can be neglected. When there are multiple



menisci in a pore, the total capillary pressure inside the *i*th pore is obtained from the vector sum ($\sum_i p_c(x)$) over all the menisci in that pore. The flow is driven by maintaining a constant total flow rate *Q* throughout the network, which introduces a global pressure drop. The instantaneous local flow rate q_i inside the *i*th link between two nodes with pressures p_1 and p_2 follows the Washburn equation of capillary flow [28],

$$q_i = -\frac{\pi r_i^2 k_i}{\mu_i^{eff} l} \left[\Delta p_i - \sum_i p_c(x) \right], \quad (2)$$

where $\Delta p_i = p_2 - p_1$. $k_i = r_i^2/8$ is the permeability of cylindrical tubes. Any other cross-sectional shape will only lead to an additional overall geometrical factor. $\mu_i^{eff} = \mu_o s_i + \mu_w(1 - s_i)$, is the volume averaged viscosity of the two phases inside the link, which is a function of the oil saturation s_i in that link. Here μ_o and μ_w are the viscosities of oil and water, respectively.

The flow equations for the tube network are solved using a conjugate gradient method [29]. These are the Kirchhoff equations balancing the flow, where the net fluid flux through every node should be zero at each time step, combined with the constitutive equation relating flux and pressure drop across each tube. The system of equations is then integrated in time using an explicit Euler scheme with a discrete time step and all the menisci positions are changed accordingly. Inside the *i*th tube, all menisci move with a speed determined by q_i . When any menisci reach at the end of a tube, new menisci are formed in the neighboring tubes. Consequently, wetting and non-wetting bubbles are snapped-off from the links having flow toward a node and enters in neighboring links having outward flow. Here, the total volume of the fluids entering to a node are distributed according to the flow rates of the neighboring tubes. Moreover, it is not allowed to increase the number of menisci inside any tube infinitely and therefore we implement coalescence process by merging two nearest menisci. In this article, we considered a maximum of four menisci inside one pore which can be tuned depending on the experimental observations. When this maximum number is exceeded, the

two nearest menisci are merged keeping the volume of each fluid conserved. In this way bubble snap-off and coalescence are introduced in the model. The absolute details of these processes in the simulation can be found in Knudsen et al. [25]. We did not consider film-flow in the present study. This is because wettability alteration techniques are important for reservoirs with low oil-saturation and when oil-saturation drops, the continuous oil films [9, 10] in a oil-wet network are expected to become discontinuous leaving immobile oil clusters stuck due to capillary forces.

The simulations are started with an initial random distribution of two fluids in a pure oil-wet network. Bi-periodic boundary conditions are implemented in the system, which effectively makes flow on a torus surface. The flow can therefore go on for infinite time, keeping the saturation constant and the system eventually reaches to a steady state. In the steady state, both drainage and imbibition take place simultaneously and fluid clusters are created, merged and broken into small clusters. One can consider this as the secondary recovery stage. Once the system reaches the steady-state in a oil-wet network, the dynamic wettability alterations are implemented, which may be considered as the tertiary recovery stage or EOR. In the following we discuss this in detail.

2.1. Dynamic Wettability Alteration

We now introduce a dynamic wettability alteration mechanism to simulate any wetting angle change, decided by the oil-brine-rock combination and the distribution of the flow channels in the system. In a previous study [26], a simplified static wettability alteration mechanism was studied, where the alteration probability was considered equal for all pores without any correlation with the flow of brine inside a pore. However, for wettability alterations to occur, the wettability altering agent (e.g., low-salinity water or surfactant) needs to be in contact with the pore walls. Thus, the wettability alteration should follow the fluid flow pathways and any change in the wetting angle inside a pore should depend on the cumulative volumetric flow of brine through that pore. This claim is rather trivial, as one can not expect any wettability change in a pore if the altering agent is not present. This means that if a certain pore is flooded by large amounts of brine, the wetting angle should change more in that pore than the one which had very little water flooded through. This is implemented in the model by measuring the cumulative volumetric flux $V_i(t)$ in each individual pore with time *t*,

$$V_i(t) = \sum_{\tilde{t}=t_0}^t q_i(\tilde{t})(1 - s_i(\tilde{t}))\Delta\tilde{t}, \quad (3)$$

where t_0 is the time when the injection of low salinity water is initiated, $\Delta\tilde{t}$ is the time interval between two simulation steps and $(1 - s_i(\tilde{t}))$ is the water saturation. $V_i(t)$ is then used to change the wetting angle for each tube continuously, updated at every time step after $t = t_0$. The wetting angle ϑ_i of the *i*th pore can change continuously from 180° to 0° as $V_i(t)$ changes from 0 to ∞ . Correspondingly, the $\cos \vartheta_i$ term in Equation (1) will change from -1 to 1 continuously. This continuous change of the

wetting angle with the variation of $V_i(t)$ is modeled by a function $G_i(t)$ given by,

$$G_i(t) = \frac{2}{\pi} \tan^{-1} \left[C \left(\frac{V_i(t)}{V_i^{\text{th}}} - 1 \right) \right] \quad (4)$$

which replaces the $\cos \vartheta_i$ term in Equation (1). As, to our knowledge, there is no consensus in the literature about the exact functional dependence of the wetting angle on the volumetric flow of brine at the pore level, we have chosen a function which starts the wetting angles from oil-wet conditions ($\vartheta_i \approx 0^\circ$) at $V_i(t) = 0$ and then asymptotically approaches to water-wet conditions ($\vartheta_i \approx 180^\circ$) as $V_i(t) \rightarrow \infty$. The pre-factor $2/\pi$ is a normalization constant to set the range of the function. The parameter C can be tuned to adjust the slope during the transition from oil wet to water wet and can also change the initial wetting angle from 180° . As our model does not include film flow, the wetting angles are not likely to reach either 0 or 180° for circular cross-section of pores. We have chosen $C = 20$ for our simulations which sets the starting wetting angle $\vartheta_i = 165.5^\circ$ when $V_i(t) = 0$. This leads to the change in the wetting angle as a function of $V_i(t)$ as shown in **Figure 2**.

As a larger pore will need more brine to be flooded in order to have a similar change in the wetting angle than a smaller pore, a threshold value V_i^{th} is introduced, which is proportional to the volume of that pore,

$$V_i^{\text{th}} = \eta \pi r_i^2 l. \quad (5)$$

At $V_i(t) = V_i^{\text{th}}$, the wetting angle reaches to 90° in that pore and $p_c(x)$ essentially becomes zero. Here η is a proportionality

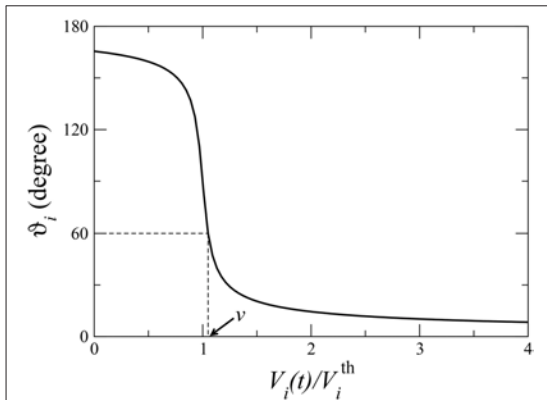


FIGURE 2 | Variation of the wetting angle ϑ_i in the i th link given by $G_i(t)$ (Equation 4) as a function of the cumulative volume of water $V_i(t)$ (Equation 3) passed through that link. V_i^{th} is the water volume needed to reach the wetting angle to 90° in that pore. When there is a cut-off (θ) in the maximum change in the wetting angle, ϑ_i is not allowed to change anymore as soon as $\vartheta_i = \theta$. An example of a cut-off 60° is shown by dashed lines, in this case as soon as $\vartheta_i = 60^\circ$ or $V_i(t) = vV_i^{\text{th}}$, ϑ_i is not changed anymore. The time (t) needed to reach the cut-off value therefore varies from pore to pore and depends on the value of V_i^{th} .

constant which decides how many pore volumes of water is needed to reach $V_i(t) = V_i^{\text{th}}$ for the i th pore. This parameter can possibly be adjusted against future experimental results, but is considered as a tuning parameter in this study. The expression for the capillary pressure at a menisci from Equation (1) then takes the form,

$$p_c(t) = \frac{2\gamma G_i(t)}{r_i} \left[1 - \cos \left(\frac{2\pi x}{l} \right) \right]. \quad (6)$$

The maximum amount of wetting angle that can be changed depends on the combination of brine, oil and rock properties [20, 21]. We therefore set a cut-off θ in the wetting angle change, such that any pore that has reached to a wetting angle $\vartheta_i = \theta$, can not be changed further. The model thus includes all the essential ingredients of wettability alteration study—it is a time dependent model where the wettability alteration is correlated with the flow pathways of the brine, and can be used to study any oil-brine-rock combination decided by θ .

3. RESULTS

Simulations are started with a random distribution of oil and water in an oil-wet network, where $\theta = 165.5^\circ$ for all links. First, the oil-wet system is evolved to a steady state before any wettability alteration is started. This will allow us to compare the change in the steady-state fractional flow of oil (F) with a change in the wetting angle. The oil fractional flow (F) is defined as the ratio of the oil flow-rate (Q_{oil}) to the total flow-rate (Q) given by, $F = Q_{\text{oil}}/Q$. The flow rate (Q) is kept constant throughout the simulation, which sets the capillary number $Ca = \mu_{\text{eff}}Q/(\gamma A)$, where A is the cross-sectional area of the network. A network of 40×40 links are considered, which is sufficient to be in the asymptotic limit for the range of parameters used [25]. An average over 5 different realizations of the network has been taken for each simulation. As the simulation continues, both drainage and imbibition take place simultaneously due to bi-periodic boundary conditions and the system eventually evolves to a steady state, with a distribution of water and oil clusters in the system. In **Figure 3**, F is plotted against the number of pore volumes passed (N) through the network. As we run the system with constant flow-rate, N is directly proportional to the time t , $N = tQ/v$ where v is the total volume of the network. The initial 200 pore volumes are for an oil-wet network, where it reaches to a steady state with $F \approx 0.235$. We then initiate the dynamic wettability alteration which resembles the flow of a wettability altering brine and F starts to drift. Here we run simulations for different values of η , defined in Equation (5), and the results are plotted in different colors. $\theta = 0^\circ$ in these simulations, which means any pore can change to pure water-wet depending upon the flow of brine through it. One can see that F approaches to a new steady-state with $F \approx 0.308$ due to the wettability alteration. The initialization of steady state is defined as the instant when the average fractional flow stops changing with time and essentially stays within its fluctuation. The time (τ) required to initialize the steady state after wettability alteration is started is measured in terms of the pore-volumes and plotted in the inset of **Figure 3**

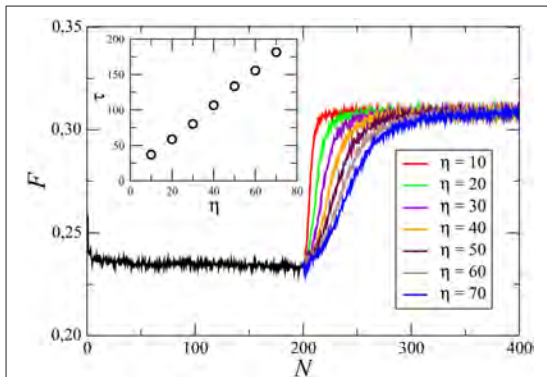


FIGURE 3 | (Color online) Change in the oil fractional-flow (F) during the simulation as a function of the number of network pore-volumes (N) of fluids passed through any cross-section of the network. Here the network is of size 40×40 links with oil saturation $S = 0.3$ and $Ca = 10^{-1}$. The initial part of the plot ($N < 200$) shows the change in F in an oil-wet system where it approaches to a steady state with $F \approx 0.235$. The wettability alteration starts at $N = 200$, where results for different simulations with different values of η (the number of pore volumes of water needed to pass through one pore to reach the wetting angle to 90° in that pore) are plotted in different colors. The system evolves to a new steady-state where F fluctuates around a higher average value. Different values of η only affects the rate of change in F but leads to the same average F . In the inset we plot τ , the number of network pore-volumes of fluids passed through the network to reach the steady-state after wettability alteration is initiated, as a function of η . τ is proportional to the total time to reach steady state which increases linearly with η as seen in the inset. A higher value of η results in a longer time to reach the new steady-state.

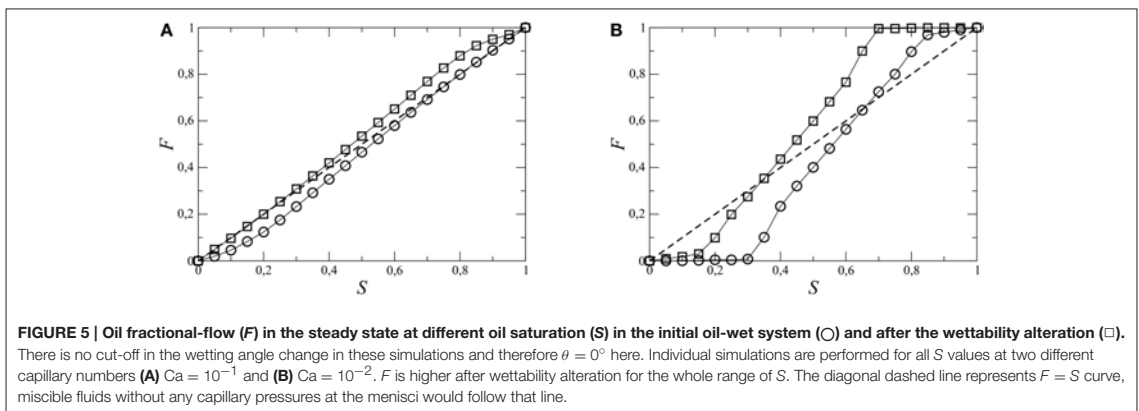
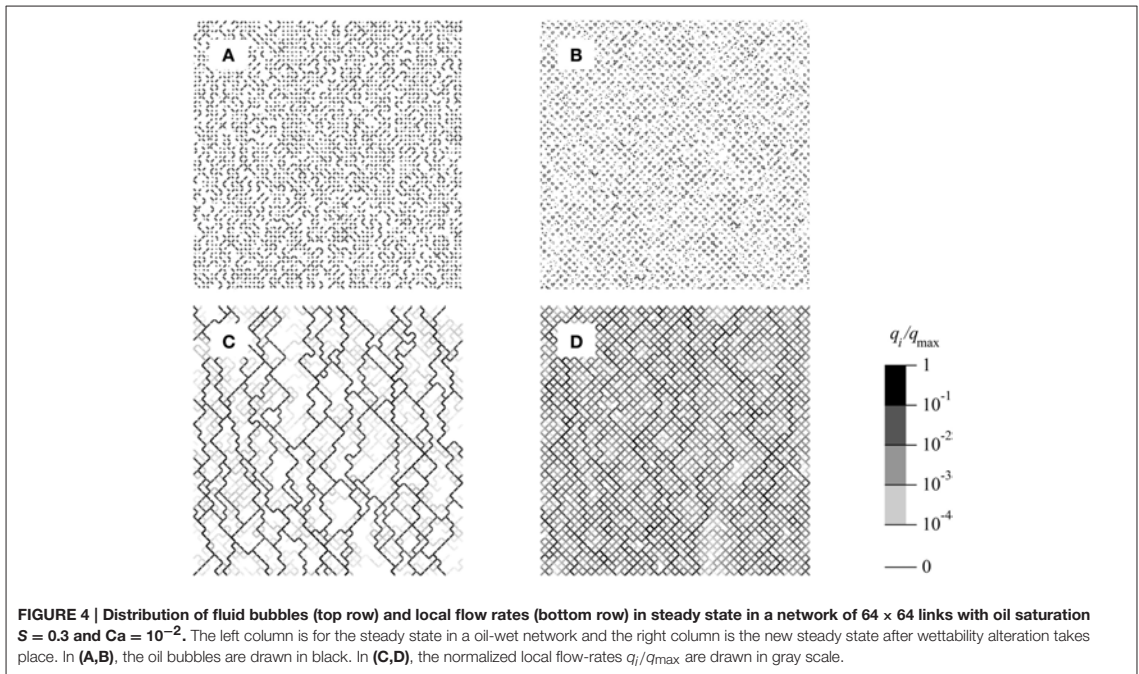
as a function of η and a simple linear dependency is observed. Therefore, different values of η only make the simulation faster or slower, but it reaches to the same steady state. In order to save computational time, we therefore use $\eta = 10$ in all our following simulations.

How the two fluids and the local flow-rates are distributed in the network in the two steady-states before and after the wettability alteration are shown in **Figure 4**. The network size is 64×64 links here with an oil-saturation $S = 0.3$ and the capillary number $Ca = 10^{-2}$. All the links are hour-glass shaped in the actual simulation with disorder in radii, but shown as a regular network for simplicity in drawing. The upper row shows the distribution of oil bubbles drawn in black. The left column (**Figure 4A**) shows the steady state in an oil-wet network and the right column (**Figure 4B**) shows the steady-state after the wettability alteration is initiated with maximum possible wetting angle change $\theta = 0^\circ$. A closer look in these bubble distributions shows more clustered oil bubbles in **Figure 4A** than in **Figure 4B** where they are more fragmented. A more interesting picture can be seen in the local flow-rate distribution in the bottom row, which shows a more dynamic scenario. The left (**Figure 4C**) and right (**Figure 4D**) figures are for the same time-steps before and after wettability alteration as in **Figures 4A,B**, respectively. Here the local flow-rates in each pore, normalized in between 0 and 1, are shown in gray scale. Interestingly, in the oil-wet system (**Figure 4C**), the flow is dominated in a few channels (black lines)

where the flow-rates are orders of magnitude higher than the rest of the system. Other than those channels, the system has negligible flow, indicated by white patches which means the fluids are effectively stuck in all those areas. This situation happens when the difference in the saturation of the two fluids is large, where the phase with higher saturation (water here) tries to percolate in paths dominated by a single phase with less number of interfaces. This is not favorable in oil-recovery, as it leaves immobile fluid in the reservoir. In the flow distribution after the wettability alteration (**Figure 4D**), the flow is more homogeneous and distributed over the whole system, indicating higher mobility of the fluids. However, one should remember that when the wettability alteration is started in a system shown in **Figure 4C**, the wettability alteration starts taking place only in those pores with active flow. But then it perturbs the flow-field and starts new flow paths and eventually the system drifts toward a more homogeneous flow with time, as shown in **Figure 4D**.

We now present the results when the wetting angle of any pore can change all the way down to zero degree ($\theta = 0^\circ$). In **Figure 5** the steady-state oil fractional-flow in an initial oil-wet system (F) is compared with that in the steady-state after wettability alteration (F'). Results are plotted as a function of S for two different capillary numbers, (**Figure 5A**) $Ca = 10^{-1}$ and (**Figure 5B**) $Ca = 10^{-2}$. The diagonal dashed line in the plots corresponds to $F = S$. If the fluids are miscible and there is no capillary forces at the menisci then both the fluids will flow equally and F will be exactly equal to S . But the presence of capillary forces at the interfaces lead to the deviation of the fractional-flow curve from the diagonal line. A lower capillary number (higher capillary forces) therefore results in more deviation from the $F = S$ line. For low oil saturation, the oil fractional-flow is lower than S , i.e., under the diagonal and for high S , F is higher than S , i.e., above the diagonal. Roughly, the phase with higher volume fraction gains and it flows faster than the other. At some point, the curve crosses the diagonal and it is the point where no phase gains. The crossover point is not at 50% saturation which clearly shows the asymmetry between the two phases [30]. As F stays below the $F = S$ line for low S , the flow of oil becomes lower and lower as oil saturation drops resulting small but stuck oil clusters. Interestingly, when wettability alterations are implemented, a significant increase in F can be observed for the full range of oil-saturation. Moreover, increase in F is higher for the lower capillary number, indicating that wettability alteration is very significant in the case of oil recovery, as Ca can go as low as 10^{-6} in the reservoir pores. Fractional flow also obeys the symmetry relation $F'(S) = 1 - F(1 - S)$ [26] which implies that, if the wetting angle of any pore is allowed to change all way down to zero degree ($\theta = 0^\circ$), the system will eventually become pure water-wet with time.

As noted earlier, the maximum change in wetting angle for a system, depends on the properties of the reservoir rock, crude oil and brine, and also on the temperature. Existing wettability alteration procedures generally turns the oil-wet system into intermediate wet, rather than to pure water-wet. Some examples of the change in the wetting angle for different rock materials and brine can be found in Kathel and Mohanty [20] and Nasralla et al. [21]. In our simulation this is taken care of by the parameter



θ , which decides the maximum change in the wetting angle ϑ_i for any pore. One should remember that, we are not forcibly changing the wetting angles ϑ_i to θ , rather the change in ϑ_i is decided independently for individual pores by the amount of brine passed through it (by Equations 3–6), and there is a maximum allowed change in any ϑ_i . As before, simulations are started with a pure oil-wet system to reach a steady state and then wettability alteration is started and simulation continues until the system reaches to a steady state again. Independent simulations have been performed for different values of θ . The proportionate change in the oil fractional-flow due this wettability change from

the oil-wet system, $\Delta F/F = (F' - F)/F$ is measured for different simulations and plotted in **Figure 6** against θ . There are a few things to notice. First, as one can immediately see, fractional flow increases with the decrease of oil-wetness, $\theta \rightarrow 0^\circ$. The maximum increase in F is higher for lower Ca , about 86% for $Ca = 10^{-2}$ and about 32% for $Ca = 10^{-1}$. This is because the change in wetting angle affects the capillary pressures at the menisci, so the change in F is larger when the capillary forces are higher. Secondly, the major change in F happens in the intermediate wetting regime, upto $\theta \approx 60^\circ$, and then it becomes almost flat afterwards. Moreover, this increase in F is

more rapid for lower value of Ca . All these facts points toward an optimal range of wetting angle change to increase the oil flow. This is an important observation for practical reasons, as it is not necessary to change the wetting angle further. Thirdly, there is a discontinuity in the curve exactly at $\theta = 90^\circ$, as we will discuss later.

Increase in the oil fractional-flow with the increase in the water-wetness may seem to be obvious and reported by many experiments and field tests. But, the most important concern for the oil industry is the rate of increase, or the time required to achieve a significant increase in the oil production. If the increment in oil flow is very slow compared to the cost of the process, then the oil recovery is declared as not profitable and the reservoir may be considered to be abandoned. As per our knowledge, there are very few systematic studies reported in the literature predicting the time scale to change the oil flow due to the wettability change by two-phase flow of brine and oil in a porous media. We observe that, due to the correlations between the flow paths and the wetting angle change, the time scale of the process varies dramatically with θ . This is illustrated in **Figure 7**, where F is plotted as a function of pore volumes (N) of fluid passed through the system. The initial 400 pore volumes are for an oil-wet system and then results of few different simulations with $\theta = 85, 88, 89, 90, 91, 92$ and 94° are plotted. Interestingly, the rate at which the system reaches a new steady-state, varies significantly depending on the value of θ . For example, after the wettability alteration is started, it needs to flow less than 100 pore volumes to reach the new steady state for $\theta = 94^\circ$ whereas more than 300 pore volumes are needed to reach a steady state for $\theta = 91^\circ$. Therefore, even if the final steady-state fractional flow is higher for $\theta = 91^\circ$ than for $\theta = 94^\circ$, it might not be profitable to alter the wetting angles to 91° because of the slow increase in F . In general, the process becomes slower and slower as $\theta \rightarrow 90^\circ$ from both sides. Such kind of slow increase in oil recovery as $\theta \rightarrow 90^\circ$ is also observed in experiments [20, 21]. This slowing down of the process is an combined effect of two factors. First, the fact that wettability only can change in the pores where there is flow of brine and the second is the value of θ . All the pores were initially oil-wet ($\vartheta_i \approx 165^\circ$) and when it reaches the steady state,

the flow finds the high mobility pathways depending on the mobility factor of the pores and the capillary pressures at the menisci. When the wettability alteration is started, the wetting angles of the existing flow pathways start decreasing. As a result, capillary pressures at menisci in those channels first decreases as $\vartheta_i \rightarrow 90^\circ$ and then it increase afterwards as $\vartheta_i \rightarrow 0^\circ$. This creates a perturbation in the global pressure field and correspondingly viscous pressures start changing with time which changes the flow field. However, capillary pressures at the zero-flow regimes are now higher than the high-flow regimes which makes it difficult to invade the zero-flow regimes causing a slower change in the flow field as ϑ_i approaches 90° . An interesting feature is observed exactly at $\theta = 90^\circ$, where the average fractional flow does not change at all after the wettability change. At exactly $\theta = 90^\circ$, capillary pressures in all the pores in the existing flow pathways essentially become zero, making them the lowest resistive channels with zero capillary barriers. As a result, the fluids keep flowing in the existing

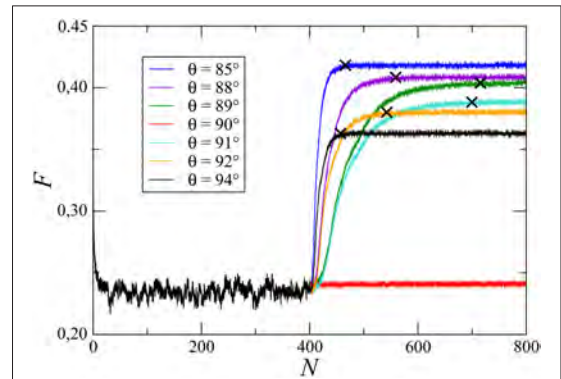


FIGURE 7 | Change in the oil fractional-flow F during the simulation for different values of maximum allowed wetting angle θ . The wettability alteration started at $N = 400$ pore-volumes. The initialization of the steady-states for different θ values are marked by crosses on the respective plots.

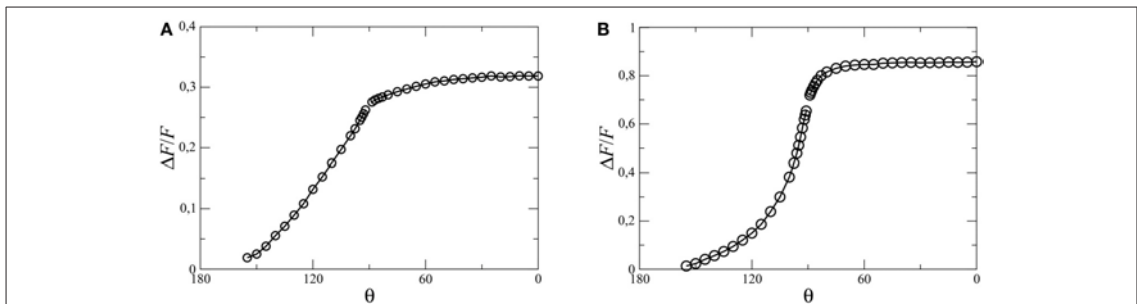
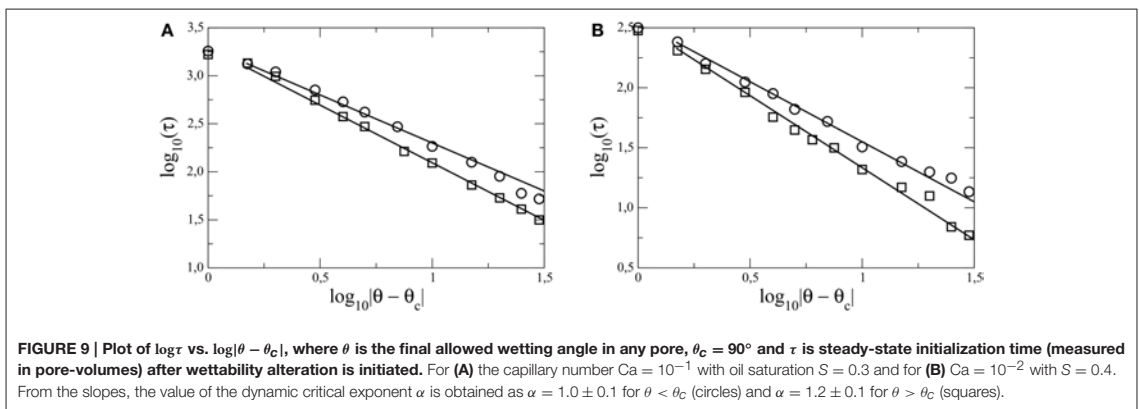
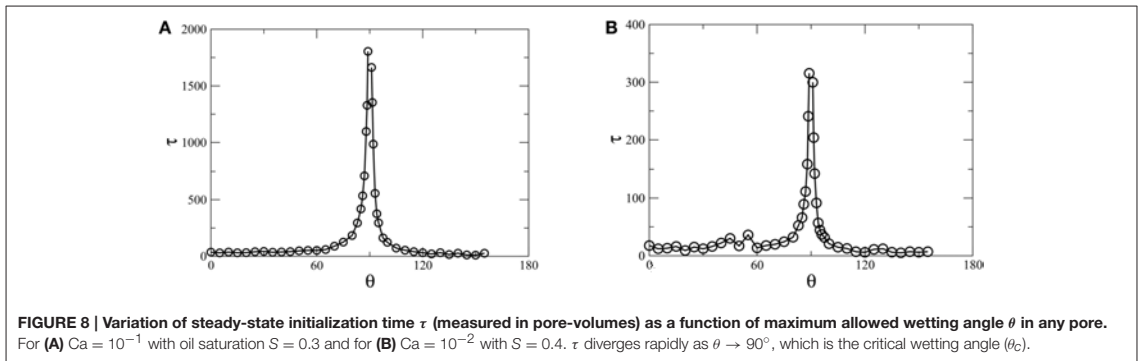


FIGURE 6 | Proportionate change in the steady-state oil fractional-flow ($\Delta F/F$) due to wettability alteration as a function of maximum wetting angle θ . For **(A)** the capillary number $Ca = 10^{-1}$ with oil-saturation $S = 0.3$ and for **(B)** $Ca = 10^{-2}$ with $S = 0.4$.



channels forever and the system stays in the same steady-state. The time taken to reach another new steady-state is therefore infinite at $\theta = 90^\circ$ and it therefore is a critical point for the system.

We now measure the steady-state initialization time τ , defined as the moment when the average of the fractional flow stops changing with time and becomes horizontal with the x axis. This is shown in **Figure 7**, where the initialization of steady states is marked by crosses on the respective plots. As the simulations are performed with constant Q , τ is proportional to the fluid volume passed through the system and therefore we measure τ in the units of N . τ for different simulations with different values of the maximum wetting angle (θ) is plotted in **Figure 8A** for $Ca = 10^{-1}$ with $S = 0.3$ and in **Figure 8B** for $Ca = 10^{-2}$ with $S = 0.4$. One can see that τ diverges rapidly as θ approaches $\theta_c = 90^\circ$ from both sides, $\theta > 90^\circ$ and $< 90^\circ$. This divergence of the steady-state time τ as $\theta \rightarrow \theta_c$ indicates the *critical slowing down* of the dynamics, which is a characteristics of critical phenomena. The critical slowing down is the outcome of the divergence of correlations at the critical point and can be characterized by a dynamic critical exponent z defined as $\tau \sim \xi^z$, where ξ is the correlation length [31]. As $\theta \rightarrow \theta_c$, the correlation length ξ diverges as $|\theta - \theta_c|^{-\nu}$ where ν is the correlation length

exponent. The divergence of the steady-state time τ can therefore be expressed as $\tau \sim |\theta - \theta_c|^{-\alpha}$, where $\alpha = zv$. In **Figure 9**, τ is plotted vs. $|\theta - \theta_c|$ in log-log scale which gives two different slopes for $\theta > \theta_c$ and $\theta < \theta_c$. We then find the value of the dynamic exponents α as $\alpha = 1.2 \pm 0.1$ for $\theta > \theta_c$ and $\alpha = 1.0 \pm 0.1$ for $\theta < \theta_c$. However, they are the same within error bar for different capillary numbers and saturations (**Figure 9**). The value of the dynamic critical exponents depend on the underlying dynamics and on the model [32]. In this case, wettability alteration was started from an oil-wet system with $\vartheta_i = 165^\circ$ for all the pores. So for the simulations with $\theta < 90^\circ$, the wetting angles cross the critical point (90°) when the capillary forces change directions. This might cause the system to mobilize the clusters somewhat faster than for $\theta > 90^\circ$ when the capillary forces does not change any direction. As a result, α becomes smaller for $\theta < 90^\circ$ than for $\theta > 90^\circ$.

We like to point out that a 2-dimensional (2D) pore network is considered in this study, but the model is equally applicable to any 3-dimensional (3D) network without any further change. However, as critical exponents depend on the spatial dimensionality of the system, values of the exponents measured for a 3D network are expected to be different.

4. CONCLUSIONS

In this article we have presented a detailed computational study of wettability alterations in two-phase flow in porous media, where the change in the wetting angle in a pore is controlled by the volumetric flow of the altering agent through it. When the wetting angles are allowed to alter toward water-wetness, the stuck oil clusters start to mobilize and oil-fractional flow increases. However, due to the correlations in the wetting angle change with the flow pathways, the time-scale of the dynamics strongly depends on the maximum allowed change in the wetting angle. We find that, as the final wetting angle is chosen closer to 90°, the system shows a critical slowing down in the dynamics. This critical slowing down is characterized by two dynamic critical exponents. The critical point we are dealing with is an equilibrium critical point as the system is in steady state. The dynamical critical exponents measure how long it takes

to go from one steady state to a new one. To our knowledge, this is the first example of there being *different values* for the exponents on either side of the critical point. Our findings are in agreement with experimental observations reported in literature, and are extremely important for application purposes like oil recovery, where the time scale of the process is a key issue.

ACKNOWLEDGMENTS

We thank E. Skjetne for introducing us to the subject of this study. We have benefited from discussions with D. Bideaux, E. G. flekkøy, S. Kjelstrup, and K. J. Måløy. This work has been supported by the Norwegian Research Council. We furthermore thank the Beijing Computational Sciences Research Center and its Director, H. Q. Lin for hospitality during the final stages of this work.

REFERENCES

- International Energy Agency. *World Energy Outlook*. Paris: IEA (2014). doi: 10.1787/weo-2013-en
- Roberts P. *The End of Oil: On the Edge of a Perilous New World*. New York, NY: Houghton Mifflin (2005).
- Abdallah W, Buckley JS, Carnegie A, Edwards J, Herold B, Fordham E. Fundamentals of wettability. *Schlumberger Oilfield Rev.* (2007) 19:44. Available online at: http://www.slb.com/resources/publications/industry_articles/oilfield_review/2007/or2007sum04_wettability.aspx
- Skauge A, Spildo K, Høiland L, Vik B. Theoretical and experimental evidence of different wettability classes. *J Pet Sci Eng.* (2007) 57:321–33. doi: 10.1016/j.petrol.2006.11.003
- Dake LP. *Fundamentals of Reservoir Engineering*. Amsterdam: Elsevier (1998).
- Sheng JJ. Comparison of the effects of wettability alteration and IFT reduction on oil recovery in carbonate reservoirs. *Asia-Pac J Chem Eng.* (2013) 8:154. doi: 10.1002/apj.1640
- Chilingar GV, Yen TF. Some notes on wettability and relative permeabilities of carbonate reservoir rocks. *II. Energy Sources* (1983) 7:67. doi: 10.1080/00908318308908076
- Israelachvili J. *Intermolecular and Surface Forces, 3rd Edn*. Amsterdam: Academic Press (2011).
- Kovscek AR, Wong H, Radke CJ. A pore-level scenario for the development of mixed wettability in oil reservoirs. *AIChE J.* (1993) 39:1072. doi: 10.1002/aic.690390616
- Kaminsky R, Radke CJ. Asphaltenes, water films, and wettability reversal. *SPE J.* (1997) 2: 485. doi: 10.2118/39087-PA
- Kidnay AJ, Parrish WR, McCartney DG. *Fundamentals of natural gas processing, 2nd Edn*. Florida, FL: CRC Press; Taylor & Francis Group (2011).
- Alvarez JO, Neog A, Jais A, Schechter DS. Impact of surfactants for wettability alteration in stimulation fluids and the potential for surfactant EOR in unconventional liquid reservoirs. *Soc. Pet. Eng.* (2014). doi: 10.2118/169001-MS
- Tang GQ, Morrow NR. Salinity, temperature, oil composition, and oil recovery by waterflooding. *SPE Reserv Eng.* (1997) 12:269. doi: 10.2118/36680-PA
- Tang GQ, Morrow NR. Influence of brine composition and fines migration on crude oil/brine/rock interactions and oil recovery. *J Pet Sci Eng.* (1999) 24:99. doi: 10.1016/S0920-4105(99)00034-0
- Standnes DC, Austad T. Wettability alteration in chalk: 2. Mechanism for wettability alteration from oil-wet to water-wet using surfactants. *J Pet Sci Eng.* (2000) 28:123. doi: 10.1016/S0920-4105(00)00084-X
- Mohan K, Gupta R, Mohanty KK. Wettability altering secondary oil recovery in carbonate rocks. *Energy Fuels* (2011) 25:3966. doi: 10.1021/ef200449y
- Tweheyo MT, Holt T, Torsæter O. An experimental study of the relationship between wettability and oil production characteristics. *J Pet Sci Eng.* (1999) 24:179. doi: 10.1016/S0920-4105(99)00041-8
- Schembre JM, Tang GQ, Kovscek AR. Wettability alteration and oil recovery by water imbibition at elevated temperatures. *J Pet Sci Eng.* (2006) 52:131. doi: 10.1016/j.petrol.2006.03.017
- Buckley JS, Takamura K, Morrow NR. Influence of electrical surface charges on the wetting properties of crude oils. *SPE Reserv Eng.* (1989) 4:332. doi: 10.2118/16964-PA
- Kathel P, Mohanty KK. EOR in tight oil reservoirs through wettability alteration. *Soc. Petro. Eng.* (2013). doi: 10.2118/166281-MS
- Nasralla RA, Bataweel MA, Nasr-El-Din HA. Investigation of wettability alteration and oil-recovery improvement by low-salinity water in sandstone rock. *Soc. Petro. Eng.* (2013). doi: 10.2118/146322-PA
- Blunt MJ. Physically-based network modeling of multiphase flow in intermediate-wet porous media. *J Pet Sci Eng.* (1998) 20:117. doi: 10.1016/S0920-4105(98)00010-2
- Ryazanov AV, van Dijke Mij, Sorbie KS. Two-phase pore-network modelling: existence of oil layers during water invasion. *Transp Porous Med.* (2009) 80:79. doi: 10.1007/s11242-009-9345-x
- Aker E, Måløy KJ, Hansen A, Batrouni GG. A two-dimensional network simulator for two-phase flow in porous media. *Transp Porous Med.* (1998) 32:163. doi: 10.1023/A:1006510106194
- Knudsen HA, Aker E, Hansen A. Bulk flow regimes and fractional flow in 2D porous media by numerical simulations. *Transp Porous Med.* (2002) 47:99. doi: 10.1023/A:1015039503551
- Sinha S, Grøva M, Ødegården TB, Skjetne E, Hansen A. Local wettability reversal during steady-state two-phase flow in porous media. *Phys Rev E* (2011) 84:037303. doi: 10.1103/PhysRevE.84.037303
- Dullien FAL. *Porous Media: Fluid Transport and Pore Structure*. San Diego, CA: Academic Press (1992).
- Washburn EW. The dynamics of capillary flow. *Phys Rev.* (1921) 17:273. doi: 10.1103/PhysRev.17.273
- Batrouni GG, Hansen A. Fourier acceleration of iterative processes in disordered systems. *J Stat Phys.* (1988) 52:747. doi: 10.1007/BF01019728

30. Knudsen HA, Hansen A. Relation between pressure and fractional flow in two-phase flow in porous media. *Phys Rev E* (2002) **65**:056310. doi: 10.1103/PhysRevE.65.056310
31. Bellac ML, Mortessagne F, Batrouni GG. *Equilibrium and Non-Equilibrium Statistical Thermodynamics*. Cambridge: Cambridge University Press (2004).
32. Nightingale MP, Blöte HWJ. Dynamic exponent of the two-dimensional Ising model and Monte Carlo computation of the subdominant eigenvalue of the stochastic matrix. *Phys Rev Lett*. (1996) **76**:4548. doi: 10.1103/PhysRevLett.76.4548

Conflict of Interest Statement: The authors declare that the research was conducted in the absence of any commercial or financial relationships that could be construed as a potential conflict of interest.

Copyright © 2015 Flovik, Sinha and Hansen. This is an open-access article distributed under the terms of the Creative Commons Attribution License (CC BY). The use, distribution or reproduction in other forums is permitted, provided the original author(s) or licensor are credited and that the original publication in this journal is cited, in accordance with accepted academic practice. No use, distribution or reproduction is permitted which does not comply with these terms.